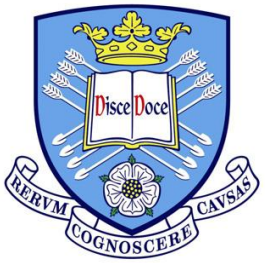


The University Of Sheffield.

# Study of Oxidation Steelmaking Reactions of Blast Furnace Hot-metal

**By:**
Efosa Curtis Obasohan (B.Eng., ProfGradIMMM)

A thesis submitted in partial fulfilment of the requirements for the degree of Doctor of Philosophy

The University of Sheffield
Faculty of Engineering
Department of Materials Science and Engineering

September 2015

# Abstract

Means of utilising low quality high phosphorus ores and coals is the focus of much research within the steelmaking industry due to the high cost and decreasing availability of premium quality raw materials. Practices such as double converter practice are used in some steel plants to drive HM phosphorus levels down to low levels, but even then costs and time constraints are associated with such practice. To tackle this issue, a HM dephosphorisation pre-treatment process was proposed by Tata Steel R&D featuring the refinement of desulphurised HM droplets.

To determine the feasibility of dephosphorisation reaction occurring within the HM droplets as it descended down the reactor, kinetic experiments were conducted using a purpose built levitation melting furnace featuring electromagnetic coils for melting the sample. Experiments conducted included free fall and stationary levitation kinetic experiments where oxidising gas mixture and/or slag-making material was introduced into the reaction system and quenched samples were analysed for change in composition and surface morphology.

Results indicated whilst no dephosphorisation took place within the short fall time (~0.32 seconds) or during the extended reaction time (60 seconds), liquid surface oxides formed as oxidation of carbon, silicon, manganese and iron occurred. Shifted focus onto analysing the composition and growth of the surface oxides with respect to parameters such as droplet size and gas phase oxygen content showed that such factors had limited effect on oxide growth and composition. Whilst lime was unable to flux into the liquid oxide, low liquidus basic synthetic slag was able to but with no change in HM phosphorus levels. HM silicon and manganese content were however significantly lowered in the presence of the basic slag indicating mass transfer of these elements from the metal to the slag.

Whilst the significance of the experimental results is that the suggestion of extensive dephosphorisation occurring during the fall of desulphurised HM droplets within the pre-treatment process has been disproved, the study improves understanding of droplet steelmaking reactions as well as offering a new experimental technique not previously available to Tata Steel for investigating reactivity or surface properties of metal droplets.

## Acknowledgement

I wish to thank both Dr Richard Thackray and Dr Stuart Millman for their continued encouragement and guidance throughout this study. Notably I am forever grateful to Dr Richard Thackray for being an ever present from my very first day at The University of Sheffield when he dedicated an extended period of time to me and my family to discuss the Materials Science & Engineering course and potential future industrial opportunities. The knowledge and experiences I have gained would not have been possible without your strong mentorship.

I also wish to offer my deepest gratitude to Christopher McDonald and the Teesside Technology Centre Researchers for the many learning opportunities that they have provided me with, as well as their extensive contribution not only to this body of work but also to my time spent within the Teesside area. A special thanks to Dr Neil Jones for his honesty, patience and source of constant motivation. I will always remember with great fondness the unique pep talks and the many times you set me on the right path.

The financial support of the Engineering and Physical Sciences Research Council, Tata Steel and Materials Processing Institute is gratefully acknowledged.

***To my Obasohan Family…***

It is said 'count your blessings and name them one by one'. You have given me so much support, encouragement and motivation throughout this research project and life in general. I especially wish to thank my parents for being a source of strength and wisdom throughout my studies. To my brother and sisters, thank you for your love and thank you for your prayers; this thesis is dedicated to you. Finally, I wish to extend a special thank you to my partner for her devotion, patience and care.

**To God be the Glory**

## Table of Content

## List of Figures

## List of Tables

## Nomenclature

$a_i$: activity of element i
A: Surface area ($cm^2$)
Ci: Concentration of component i ($g.moles/cm^3$)
$C_p$: Heat capacity (cal/g.°K)
D: Diffusivity ($cm^2/s$)
$e_x^y$: Interaction parameter; the effect of element y on the activity coefficient of element x
$f$ : Henrian activity coefficient
ΔG°: Standard free energy of formation (J/mol)
$J_n$: Nucleation rate ($cm^{-3}s^{-1}$)
K: Equilibrium constant
$k$: Mass transfer coefficient ($g.mole/cm^2s$)
k: Boltzmann Constant
M: Molar mass (g/mole)
N, n: Diffusion flux ($g.mole/cm^2s$)
P: Gas pressure (atm)
R: Gas constant ($cm^3atm/Kmol$)
r: radium (cm)
t: Time (s)
T: Temperature (°K)
X: Mole fraction
W= Sample weight (g)

α: Thermal diffusion factor
μ: Gas viscosity (g/cm.s)
δ: Boundary layer thickness (cm)
φ: Function of contact angle ψ
ρ: Density ($g/cm^3$)
σ: Surface tension at liquid gas interface
λ: Accommodation coefficient
U: Average flow velocity on a surface (cm/s)
ν: Approaching velocity of gas (cm/s)

Sh: Sherwood number (dimensionless)
Re: Reynolds number (dimensionless)
Sc: Schmidt number (dimensionless)
Pr: Prandtl number (dimensionless)
Gr: Grashof number (dimensionless)

**Superscript and Subscript**
m: Metal
s: Slag
g: Gas
g-m: Gas-metal interface
e: Equilibrium
o: Initial
b: Bulk
*: Reaction interface
f: film
RS: reference states of the oxide activities based on the regular solution model [25, 26]
$_{AB}$: Gas mixture of gas A and gas B

# 1. Introduction

Steelmakers face a challenge to meet the demand for lower phosphorus steels due to reduced availability and high cost of premium quality raw materials (iron ore and coal). Whilst high phosphorus raw materials are abundantly available, existing European steel plants are currently not designed to cater for such high phosphorus loads.

In 2008, Tata Steel R&D proposed a dephosphorisation pre-treatment process to be integrated between the desulphurisation and Basic Oxygen Steelmaking (BOS) converter. Based on atomisation of the desulphurised hot-metal (HM) stream into molten droplets, the process aimed to maximise the reaction surface area in contact with a controlled ambient condition (comprising of oxygen and lime) in order to maximise phosphorus transfer from the HM to slag. By dephosphorising before charging the BOS converter, it was suggested that cheaper and readily available high phosphorus raw materials could be utilised, and shorter blowing time in the BOS converter could occur as mainly carbon would be in need of oxidation. Through such practice, quality of the final steel product could be improved as lower phosphorus content would exist in the metal hence less likelihood of phosphorus related defects such as surface embrittlement.

In the 1960's-1970's the commencement of levitation melting studies by British Iron and Steel Research Association (BISRA), coincided with the development of a continuous steelmaking process, Spray Steelmaking, which as time has shown was inferior to the now dominant BOS process. Due to the ability of levitation melting technique to closely simulate the gas/metal reaction of HM droplets falling through an oxygen-bearing gas, the technique found use in conducting laboratory kinetic experiments. The proposed dephosphorisation pre-treatment by Tata Steel R&D was derived from spray steelmaking and as such, it was felt that for the present study, adopting a similar experimental apparatus would be ideal to simulate the process.

In the present study, a series of gas/metal/slag experiments were carried out by levitation melting technique, where the kinetic effects of various parameters such as oxygen potential, temperature and metal composition on oxidation steelmaking reactions of molten HM droplets were investigated. Unlike in previous work by various researchers who studied droplet reactions on a laboratory scale [49-53, 54-56, 63-72, 74, 75]; all of which are presented in Chapter 2, in this study slag-making material was introduced into the system to investigate phosphorus removal, whilst surface analytical techniques; Energy

Dispersive X-ray Spectroscopy (X-EDS) in Backscattered mode, and Electron Probe Micro-Analysis (EPMA) were applied to observe the effects of theses controlled conditions on droplet surface composition and morphology, as this area of study was found to be greatly limited from the results of sourced literature.

As well as general literature review on steelmaking process and reactions, Chapter 2 comprises a detailed section (Section 2.6) on apparatus design considerations as this area of study occupied a considerable period of time during the project given that the apparatus was fully designed, manufactured and commissioned before experimental use. The design process is heavily covered, whilst reasoning and justification of key design decisions as well as comparison with existing techniques/apparatuses are also highlighted.

Chapter 3 lists the 'Experimental Procedures' whilst Chapter 4 ('Results and Discussion') features apparatus design results (reasoning and justification of key design decisions as well as comparison with existing techniques/apparatuses are also highlighted) and experimental results which explicitly details and evaluates the quantitative analysis results and observations of metal surface evolution with experimental parameters. Kinetic theoretical considerations derived from literature and the experimental work are also presented, discussed and further applied to the findings of the study in this chapter. The thesis is rounded off in Chapter 5 and Chapter 6 with the 'Conclusion' and 'Recommendation of Future Work' respectively. As a spin-off from the main study, Appendix 1 presents results from the supplementary work done on statistical analysis of metal droplet size distribution and population density within BOS converter emulsion as the data derives from IMPHOS [3] which effectively forms the basis of the present study.

The project objective was initially aimed at providing fundamental evidence that dephosphorisation of falling HM droplets occurred under favourable conditions; namely high oxygen basic atmosphere and low droplet temperature, in order to justify the effectiveness of the proposed pre-treatment process. However, as the study evolved, scope for investigating the oxidation kinetics of other elements within the HM multi-component system (C, Mn, Si) became apparent and was equally pursued because along with the advanced surface analysis techniques which had not been extensively employed in historic studies for one reason or another, improved understanding of the reaction kinetics with respect to the evolution of metal surface reactions could be gathered. Other novel aspects of this study are:

- Through review of studies where levitation apparatus was used (Chapter 2 – Section 2.6), it became clear that the different studies were done on different apparatus and are therefore susceptible to different experimental errors. A design consideration that stemmed from this was to design an apparatus where both free fall and stationary experiments could be conducted. The ability to conduct series of experiments all on a single apparatus would have allowed for improved comparison of results
- Levitation studies reviewed in Chapter 2 – Section 2.5.3 focused primarily on decarburisation reactions. None of these studies investigated HM dephosphorisation and only a few [57, 73] introduced slag into the reaction system. The present investigation did both of this and whilst HM dephosphorisation results were not forthcoming, it opened up the potential of analysing reaction interface as presented in Chapter 4 - Section 4.3.3
- The majority of levitation melting steelmaking studies focused on decarburisation and also noted the occurrence of liquid oxides at the metal surface, whereas the present study conducted a comprehensive surface analysis investigation focused wholly on the oxide properties such as composition and growth and how these were affected by operational parameters. The use of X-EDS (backscattered mode) and EPMA were fully applied to extend on the findings of other researcher [51, 52, 64, 66, 70]

# 2. Literature Review

## 2.1 Overview of Steelmaking Practice

The integrated steelmaking route is a compilation of several steelmaking processes where high impurity raw materials are fed from the ironmaking stage and refined through the steelmaking processes to produce crude steel which is then alloyed to the desired composition during secondary steelmaking before then being cast into sellable products such as billets and slabs. Impurity elements such as sulphur, silicon and phosphorus are detrimental to the quality of the final product, with phosphorus known to segregate upon solidification leading to surface embrittlement and high levels of carbon within steel causing it to be hard and highly brittle. The following chapter aims to provide an insight into the importance of these steelmaking processes whilst touching upon the constraints faced by the integrated steelmaking route. The present section (Chapter 2 – Section 2.1) is referenced largely from DeO and Boom [1] and Tata Steel Steelmaking & Casting Course notes. [2]

The raw materials used to produce iron within the blast furnace are iron ore (i.e. haematite), metallurgical coal and coke; the latter two, effectively acting as heat source and fuel respectively. During the 'smelting' process comprising hot air being blown into the furnace, the metal within the ore is separated from the 'gangue' material and forms a carbon saturated liquid metal solution classed as Hot Metal (HM). Because impurity elements such as phosphorus and silicon reside within the raw materials, these are carried through to the liquid metal formed. To counteract this, lime is charged into the furnace to form basic liquid oxide (slag) where acidic oxides of these impurity elements dissolve into. The basic slag serves a dual purpose as it also acts to minimise refractory wear caused by the acidic oxides. The slag and HM are tapped separately with the HM then undergoing continued refining in the desulphurisation ladle and Basic Oxygen Steelmaking (BOS) converter. End product slag generally comprises oxides such as CaO, $SiO_2$, $Al_2O_3$, MgO and FeO. A typical HM analysis and temperature upon arrival to the BOS plant is as follows:

Table 1: Tap blast furnace Hot-metal composition

| %C | %Si | %Mn | %P | %S | Nitrogen | T (°C) |
|---|---|---|---|---|---|---|
| 4.3 - 4.8 | 0.1 - 1.0 | 0.2 - 0.6 | 0.06 – 0.11 | 0.01 – 0.10 | 80ppm | 1300-1400 |

These levels are unacceptable within end steel product and as such must be removed from the HM before being casting with the final composition. The underlying difference between the conditions required to remove sulphur and phosphorus from the HM is oxygen. Whilst dephosphorisation is favourable within an oxidising basic slag environment, desulphurisation requires reducing basic slag environment for its removal to be optimised. For this reason, desulphurisation stage occurs prior to the oxidising BOS converter process where oxidation and removal of phosphorus occurs. A common method of HM desulphurisation pre-treatment is Deep Injection. A refractory lined lance is submerged into the HM and pelletized reagents (i.e. magnesium, calcium carbide, lime) are injecting into the HM by a nitrogen carrier gas. Whilst final sulphur level is determined by the steel grade, a final HM sulphur level of 0.002% is achievable by the three mentioned reagents and bubbling caused by nitrogen introduced through the lance helps to promote mixing and faster reaction kinetics. Depending on the reagents used, the desulphurisation reactions that take place are as follows:

$$Mg + S = MgS \quad (1)$$

$$CaC_2 + S = CaS + C \quad (2)$$

$$CaO + S = CaS + O \quad (3)$$

The less dense metallic sulphides floats to the top of the metal bath and transferred into the basic slag through the reactions detailed above. To prevent slag carry over into the BOS converter where its oxidising atmosphere would cause sulphur reversion back into the HM, the sulphur rich slag is skimmed off by a mechanical skimming arm from the transfer ladle before the desulphurised HM is charged into the BOS converter for further refining. A typical desulphurised HM composition is as follows:

Table 2: End-desulphurised/Charge BOS converter HM composition

| %C | %Si | %Mn | %P | %S | T (°C) |
|---|---|---|---|---|---|
| 4.3 - 4.8 | 0.1 - 1.0 | 0.2 - 0.6 | 0.06 – 0.11 | 0.001 - 0.02 | 1250 - 1400 |

After the desulphurisation stage, the main impurity elements remaining in the HM are silicon, phosphorus and manganese, also, the HM is still carbon saturated with levels of

approximately 4.5wt%. Further refining of the HM occurs within the BOS converter where gaseous oxygen and dissolved oxygen oxidises above listed elements. The processing steps are as follows. Scrap metal is charged into the BOS converter primarily to act as coolant when the highly exothermic oxidation reactions are taking place, but also to prevent the molten HM directly contacting the basic refractory walls during initial oxidation as the acidic oxide products attack the refractory lining. The converter is then charged with the desulphurised HM from the transfer ladle before the water cooled lance is inserted into the converter ~3m above the metal bath and then pure oxygen is blown onto the metal surface at supersonic speed (Mach 2) leading to the formation of a jet impact zone where oxidation reactions are initiated.

During blow the blowing procedure, lime is charged into the furnace and a basic slag is formed as a layer on top the metal bath which absorbs the oxidised impurities such as silica and phosphorus pentoxide. Once the desired composition is reached, the steel is tapped into a transfer ladle in preparation for secondary steelmaking processes. The charge-to-tap time (the elapsed time from the desulphurisation HM being charged into the BOS converter and the crude steel being tapped out of the BOS converter into the transfer ladle) generally takes between 30-40 minutes, with the main blow sequence taking approximately 17 minutes [2]. A typical HM analysis and temperature after oxidation within the BOS converter and tapping into a transfer ladle for secondary steelmaking is as follows:

Table 3: BOS converter tap metal composition

| %C | %Si | %Mn | %P | %S | T (°C) |
|---|---|---|---|---|---|
| 0.03 – 0.06 | 0 | ~ 0.15 | 0.008 – 0.015 | 0.001 – 0.01 | 1600-1740 |

The main reactions taking place within the BOS converter are iron, silicon, carbon, and manganese and phosphorus oxidation. Due to its abundance, iron is readily oxidised to form iron oxide which initially combines with $SiO_2$ to form an early slag (fayalite). This then assists in the dissolution of CaO for the formation of early basic slag. Silica, an acidic oxide, formed from oxidation of silicon in the HM is absorbed into the basic slag and reduces the basicity generally measured by the $CaO/SiO_2$ ratio commonly known as the V-ratio.

After approximately 30% blowing time, silicon is fully oxidised and transferred into the basic slag, this is followed by increased rate of decarburisation once the energy barrier associated with CO bubble nucleation has been exceeded; at which point the Carbon oxygen product consist of approximately 90% CO and 10% $CO_2$. During this stage, the slag/metal emulsion volume may increase as CO bubbles form and expand rapidly causing further mixing between the slag and metal. Simultaneously, as the oxygen from the water cooled lance impinges the slag/metal surface, an abundance of metal droplets are formed and suspended within the slag/metal emulsion.

As already established in the preceding chapter, oxidation reactions occur within the BOS converter and the possibility of sulphur reversion is minimised having refined the HM under reducing atmosphere in the transfer ladle to remove the HM sulphur beforehand. Also, in terms of the order of reaction iron oxidation is prevalent as it is the most abundant element within the HM and the iron oxide aids dissolution of CaO to form a basic slag which is quickly populated by oxidised HM silicon (silica) hence reducing the basicity of the slag. This reaction if followed by decarburisation having overcome the CO bubble nucleation barrier and then significant dephosphorisation follows given the increased availability of oxygen and oxygen potential slag necessary for dephosphorisation to occur. As the reaction within the BOS converter takes place the conditions favourable for such reactions to take place are constantly changing. For example, CO nucleation is favoured by high oxygen availability and high HM temperatures, but considering the abundance of iron and presence of silicon, initial oxygen is utilised by these elements therefore minimising the amount of reactants for CO nucleation to occur. Also, dephosphorisation is favoured by low temperature HM and high oxygen potential slag, but within the middle part of the blow procedure, the exothermic heat given off by silicon and carbon oxidation causes increases in HM temperature, whilst both gaseous and dissolved oxygen in the slag is being consumed by the dominant decarburisation reaction, hence dephosphorisation is less favourable within this segment of the blow. These dynamics have been found in an extensive study of BOS converter practice by Millman [3] who through sampling metal, slag and emulsion in a 6 tonne converter was able to quantitatively show the dynamic state of reactions within the converter.

In the mentioned study, five different dephosphorisation behaviours were identified comprising rapid initial dephosphorisation followed by a combination of slower dephosphorisation rates or phosphorus reversion from the slag back into the metal. The

period of rapid dephosphorisation occurred at rates of approximately 0.007%P/min during the early stages of blow. Within this time period, temperature within the converter was below 1500°C and slag consisted of high levels of FeO (> 20 wt.%) which supported lime dissolution into the slag. Increased dissolve slag at the early stages of blow corresponded to a peak in slag P2O5 content before reaching a minimum midway through blow prior to rising again towards the end of blow [84]. The changes in slag chemistry and temperature were modelled using MTDATA to determine the evolution of slag phases (Amorphous liquid slag, C2S, Spinel and Halite) given the chemical component of CaO-$SiO_2$-FeO-$Fe_2O_3$-MgO-MnO-$Al_2O_3$-$P_2O_5$ with the researcher concluding that only the Amorphous liquid slag and C2S phases were able to take up phosphorus. It was further concluded that almost all phosphorus was contained in the C2S phase at the start of the blow, whilst at the end of blow, most phosphorus was contained within the amorphous slag phase for most of the five dephosphorisation profiles.

Comparison of the emulsion metal and the bulk bath metal composition throughout blow showed that generally, the carbon, phosphorus, silicon and manganese levels within the emulsion metal was less than their concentrations within the bulk bath metal, especially during the early stages of the blow as similar concentration levels were measured at the end of the blow. This led the research to conclude that metal droplets in the emulsion plays a major role in refining of the overall HM within the BOS converter given the fast circulation rate of metal between the emulsion and bulk bath. Smaller droplets (<500μm) were also repeatedly measured to be greatly refined compared to large droplets, with respect to dephosphorisation reaction; hence further supporting the argument that HM droplet dephosphorisation drives the overall dephosphorisation reaction.

As a supplement to the present study of 'Kinetics of Oxidation Steelmaking of Blast Furnace HM Droplets', analysis of droplet size distribution and population density from the IMPHOS project conducted by Millman [3] were conducted on samples collected from the emulsion layer within the 6 tonne BOS converter. The work is initially reviewed in the literature review (Section 2.3) and is further presented and discussed in Appendix 1.

### 2.2 Overview of HM Dephosphorisation Pre-treatment and Spray Steelmaking

Phosphorus in blast furnace iron (also known as hot metal), may be removed through BOS converter practice or dephosphorisation pre-treatment methods such as torpedo ladle practice', 'double converter practice' and 'multi-refining converter practice'

(MURC) as commonly practiced in Japan, Korea and more recently China. Current pre-treatment processes are able to produce final steel with phosphorus levels as low as 0.005wt.% phosphorus in comparison to 0.008wt.% phosphorus achievable by conventional BOS converter low phosphorus practice. Issues surrounding such practices include longer processing time than standard BOS converter practice, as well as use of multiple converters in the case of double converter practice. Specifically for double converter practice and MURC, the pre-treatment methods suffer from greater loss of yield due to double de-slagging – initial skimming of phosphorus rich slag then followed by removal of final slag which has an even higher capacity for phosphorus though metal phosphorus levels should be low at the second stage of blow. Unlike the Japanese who could practice near 100% hot metal charge, existing charging crane allowances within European steel plants were designed for 15%-25% scrap and 75%-85% hot metal at charge [94]. Therefore, to adopt similar practice, capital intensive plant upgrade would be necessary.

Historically, hot metal dephosphorisation was initially carried out in the torpedo ladle which had a relatively confined free volume. Blast furnace iron was first desiliconised in the blast furnace runner (<0.15wt.% silicon) and then charged into the torpedo ladle. Initial desiliconisation was required in order to prevent slag foaming and slopping in the torpedo ladle during dephosphorisation. Injectable grade flux agents CaO, fluorspar and iron ore were deep injected to initiate a fluid, basic and oxidising slag (limited amounts of gaseous oxygen was later introduced in order to reduce the extent of thermal losses). Low temperature, fluid slag, relatively high basicity and high lime activity (due to the large surface area of the powders) meant that significantly low hot metal phosphorus levels could be achieved [94, 95].

Where iron raw material prices were increasingly expensive and scrap prices less so and also in abundance, this provided an incentive to charge more scrap into the BOS converter along with the dephosphorised HM. However, scrap is a coolant; hence the HM needed to be high in thermal energy. To tackle this, 'Torpedo' HM dephosphorisation practice can be carried out in a ladle where low levels of $O_2$ in addition to FeO is blown into the ladle to promote the occurrence of the highly exothermic decarburisation reaction; hence providing the HM with the required thermal energy needed for the charging of higher scrap ratio in the BOS converter.

Much research has covered two stage blowing processes such as double converter and multi-refining converter practice (MURC) [94, 96]. Unlike the double converter process, the two stage oxygen blowing (soft and hard blowing) occurs within a single converter.

The initial soft-blowing procedure is done at lower temperatures and with an early basic slag; conditions ideal for phosphorus removal. With intermediate de-slagging of the phosphorus-rich slag, followed by de-slagging of the highly basic slag at the end of the second stage blow, not only is low HM phosphorus levels achieved, but the second slag can be used as a fluxing agent instead of lime for the initial soft blowing procedure; potentially decreasing slag volume by up to 50%, whilst the high phosphorus slag may find use in fertilisers for the agriculture industry [94]. The above mentioned pre-treatment methods suffer from several drawbacks; one common to both is loss of hot metal yield through multiple de-slagging. It is expected that the more frequent the removal of slag, the increased fraction of hot metal loss. The use of two converters suggests that the double converter practice is logistically demanding particularly when fitting such a procedure to an existing steel plant. Although this issue is addressed by the multi refining converter practice, intermediate de-slagging associated with both these practices further reduces plant productivity; approximated to be up to 20% for the multi refining practice [97].

Increased reactivity of phosphorus has been demonstrated with powdered lime (<500µm) by the Linz-Donawitz ARBED Centre Method (LD-AC) practice [98, 99, 100, 101]. The LD-AC process featured pneumatic injection of lime powder conveyed by the oxygen stream into the oxygen jet impact region. The lime and oxygen created a high basicity slag and oxidising conditions, both favourable for the removal of phosphorus. The basic slag was created relatively early in the blow at lower temperatures, thereby increasing the capability for phosphorus removal and ensuring that a large amount of the phosphorus was transferred from the hot metal into the slag. To prevent phosphorus reversion resulting from deterioration of optimised ambient conditions (increase in temperature), the highly basic, -phosphorus rich early slag was removed before blowing was continued with an addition of fresh lime. It however must be noted that the LD-AC method is not commonly practiced, if at all practiced, at present; with issues with agglomeration of lime powders within the lime injection system but more significantly, the superiority of the BOS converter process, contributing to its demise.

Phosphorus removal from hot metal was also found during Spray Steelmaking trials conducted by British Iron and Steel Research Association (BISRA) between the late 1960's and early 1970's, when investigating decarburisation as part of a potential continuous steelmaking process. Due to the increasing dominance of the BOS process at that time, further development of the spray steelmaking process was discontinued. However, the limited public literature [90, 92, 93] illustrates that significant levels of dephosphorisation occurred with relatively non optimised dephosphorising conditions such as low basicity slag.

Having established that metal (i.e. droplets) within the BOS converter slag/metal emulsion was greatly refined compared to bulk bath metal through the IMPHOS study, the HM dephosphorisation process was proposed by Tata Steel R&D derived from British Iron and Steel Research Association (BISRA) Spray Steelmaking process [90-93]. The spray steelmaking process (illustrated in Figure 1) was initially designed as part of a continuous steelmaking route mainly aimed at pre-treating (desiliconisation, dephosphorisation) blast furnace HM and then later considered for decarburising blast furnace HM. The process comprised initially filling a tundish with HM from a bottom pouring ladle followed by teeming a stream of HM into the reactor. The stream was then broken up into large surface area metal (droplets) by high velocity jets of oxygen [90]. Where lime powder was introduced through injection into the stream, some dephosphorisation (based on the analysis of the steel collected in the ladle at the bottom of the reactor) occurred, although further studies were proposed to investigate the possibility of achieving suitable levels of dephosphorisation [91].

Whilst BISRA conducted several pilot scale and plant scale production in the 1960's and 1970's the publically published results are not available due to patenting of the process. However several laboratory based experiments with respect to spray steelmaking were carried out around the time of the spray steelmaking technology. These studies [54-56, 63-65, 78]; all of which apply levitation melting technique; have been reviewed further in Chapter 2 – Section 2.5.

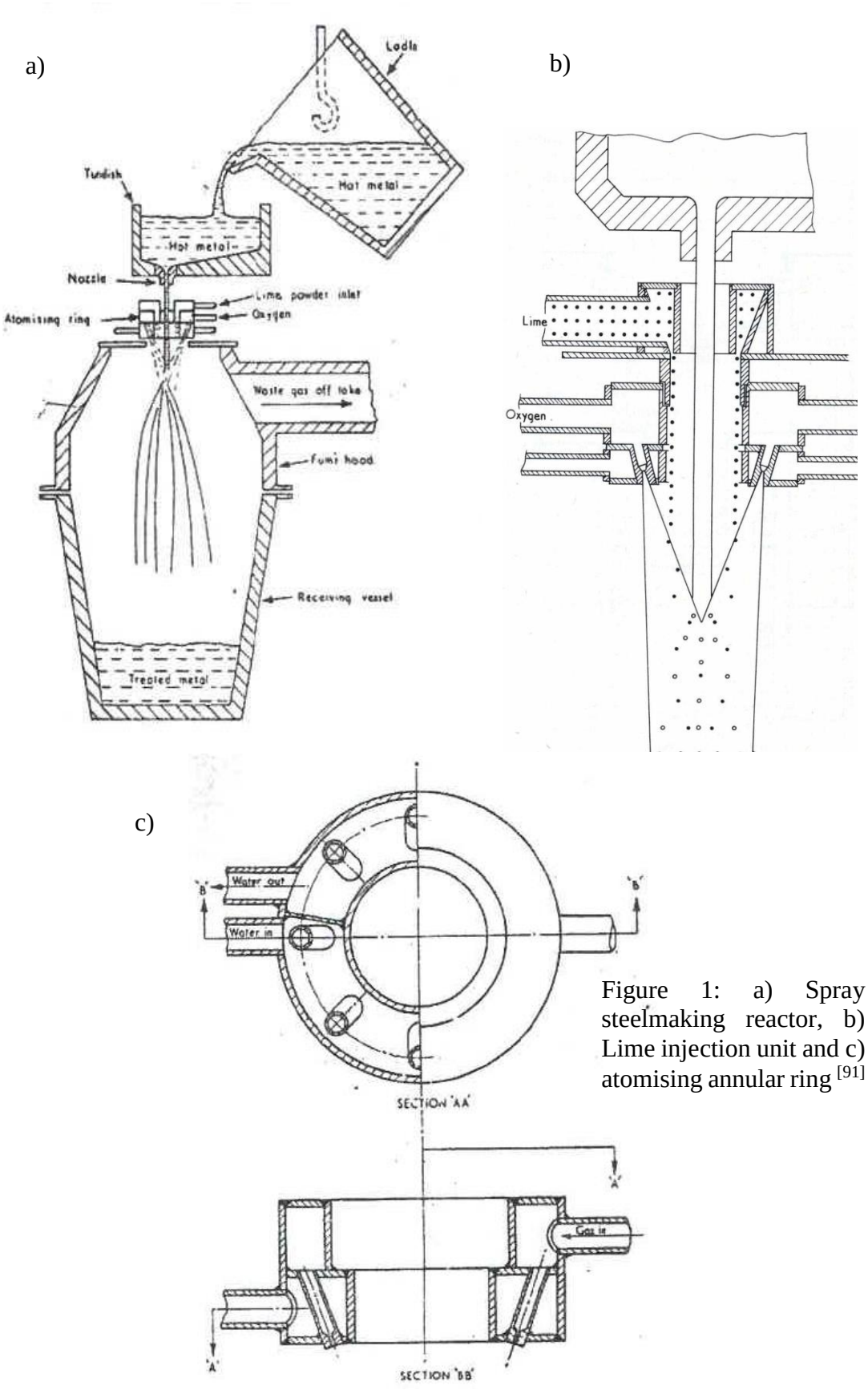


Figure 1: a) Spray steelmaking reactor, b) Lime injection unit and c) atomising annular ring [91]

### 2.3 Overview of Kinetics of Steelmaking Droplet

An interfacial area is one where two or more surfaces are in contact. Subagyo [4] has shown that the surface areas of metal droplets are larger than that of bulk bath metal. The IMPHOS study by Millman [3] further demonstrates that metal droplets drives the overall oxidation reaction through faster oxidation reactions compared to the bulk. The difference in metal chemistry between metal droplets and bulk bath metal is particularly observable at the early stages of the blow procedure. Three parameters associated with droplet kinetics in the BOS converter are droplet generation, droplet residence time and droplet size distribution; all of which are further reviewed below.

Within the BOS converter, droplets are formed primarily when pure oxygen jet from the water cooled lance impinges on the liquid surface causing shearing of the liquid surface and the generation of droplets. Through droplet generation studies [5-7, 103], a transition from dropping to swamping mechanism was observed whereby the former comprised shallow but stable cavity within the liquid surface and the latter comprised shallow cavity but with greater amount of metal droplets sheared from the liquid surface. Droplet generation is influenced by two overbidding factors; momentum of the oxygen jet (inertial forces) and physical properties of the liquid metal (i.e. surface tension, viscosity and density) [4, 6]. These characteristics that describe droplet generation is expressed through the nominal Weber number [6] as the criterion determines the transition of droplet generation mechanism from dropping to swamping, noted to change when $We_n \approx 10$ [6].

From water modelling results, Molloy [7] proposed 3 profiles of impinged liquid surface by the oxygen gas jet; 'Dimpling' characterised by low jet velocity resulting in a shallow and stable cavity at the surface of the bulk bath liquid, 'Swamping' characterised by an increased gas velocity whilst maintaining a shallow cavity, induces splashing (droplet generation) and finally 'Penetrating' which features yet higher gas velocities causing deeper penetration of the jet into the liquid surface which generates less splashing. The onset of splashing (droplet generation) hence the deviation of the system from stable conditions is defined by Kevin-Helmholtz (K-H) Instability criterion (Equation 4) which determines the number of times the critical K-H criterion is exceeded [8]. The criterion was further named as dimensionless parameter $N_B$ (Blowing Number) by Subagyo [9] who also derived the following empirical equation expressing the volumetric flow of blown gas ($R_G$) and droplet generation rate ($R_B$) as a function of the blowing number ($N_B$).

(4)

$$\frac{\rho_g u_g^2}{2\sqrt{\sigma g \rho_l}} = 1.0$$

Another parameter associated with droplets in the BOS converter is the residence time; the length of time the droplets are suspended in the emulsion/slag layer before re-entering the bulk bath metal. Whilst several studies such as those described below have focused on determining the residence time within the BOS converter, difficulty in measuring this parameter during blow has meant that discrepancies exist between several of the published results. For this reason such studies have been through laboratory based physical water modelling and computational modelling also. From these studies, droplet residency time is found to range between 0.25s – 120s. Much work has been done at Swinburne University where x-ray fluorescence has been used to observe droplet behaviour within a basic slag [10, 11]. The results of these studies show that depending on factors such as blow time and the physical properties of slag, droplet residence time was affected as proposed by Dogan [11].

In a process model of oxygen steelmaking, Dogan [11] evaluated the decarburisation kinetics of metal droplets within the slag/metal emulsion and in doing so, drew several conclusions about droplet residence time. From a metals perspective, during the stages of the decarburisation reaction, initially dense metal droplets are rich in carbon and once in contact with sufficient oxygen for CO to nucleate at the surface of the droplet, the metal 'bloats' and becomes less dense. As the metal is rich in carbon, as the reaction self-propagates, the droplet continues to swell. As the droplet becomes increasingly less dense, its residence time with the emulsion extends accordingly. Equally so, at the end of blow, where metal droplets contain less carbon compared to the start of blow, the droplets are denser and residence time would be expected to be less than that of a 'bloated' droplet. From a slag perspective, towards the end of blow, because the metal at this stage has been highly decarburised and desiliconised, further iron oxidation takes place which in turn decreases the slag viscosity and density, hence further contributing to the lowering of droplet residence time.

Metal droplet size distribution is required for kinetic calculation given the variation in the droplet interfacial area depending on the droplet size. Table 4 shows studies that have measured droplet size distribution in the BOS converter through plant measurements and

non-plant measurement techniques such as cold modelling [6] where water represents the hot metal and glycerine-Mercury represents the slag material.

Meyer [12] investigated the metal droplet size distribution of slag-metal emulsion from a 230t converter. Ejected emulsion material was rapidly cooled on large steel pans positioned outside the converter. Metal droplet size distribution was then measured by a sieving process after the emulsion material underwent mechanical crushing, screening and magnetic separation processes. Droplet size ranged between 14-100 mesh and the emulsion was recorded to accommodate up to 80% metal droplet by weight at a particular period of blow; however, some of the droplets had cavities, caused by CO nucleation within the droplets. Skewing of droplet size distribution towards finer sizes was further noted to have occurred due to fracture of larger droplets during the physical analysis (crushing) procedure.

A study of slag-metal reactions in an LD-LBE converter was conducted by Cicutti et al [13]. Samples of slag; metal and emulsion were collected simultaneously from a 200t converter during full operation using a special designed lance allowing for sampling at different times of blow. Having separated and analysed the metallic component of emulsion, it was found that droplet size ranged from 230μm to 3350μm, and the droplet size distribution generated during the BOS process obeyed the Rosin-Rammler-Sperling (RRS) function. As with Meyer [12], Cicutti reported droplets being more decarburised than the metal bath and, that the extent of decarburisation was greater for smaller droplets; a factor thought to contribute significantly to global decarburisation.

Millman [14] investigated the processing events of a 6t BOS converter with special emphasis on phosphorus behaviour. Samples of slag, bath metal and slag/metal emulsion were simultaneously collected at 2 minutes intervals during a 16 minute blowing cycle. Emulsion samples for specific BOS experimental heats were microscopically (optical and electro) image analysed to produce size distributions of emulsion metal droplet and voids. Independent of blow time and measured across a limited size range of 0-400μm, the majority of sampled metal droplets had diameters below 100μm. Furthermore, by comparing CFD modelled (calculated) metal droplet size distribution and actual (measure) droplet size distribution of an experimental BOS heat, the modelled results correlated well with measured results for lower slag/metal emulsion levels. However, the modelled results over predicted the size distribution at higher emulsion levels.

Price [14] further studied the significance of emulsion in carbon removal by sampling an industrial BOS converter using an ‘in-blow bomb’ device capable of collecting slag and emulsion samples simultaneously. Droplet size largely ranged from 1000μm-2000μm, although it was noted that agglomeration of the metal droplets on the sampler support chain may have affected the credibility of the droplet size distribution.

Tokovoi [16] sampled slag/metal emulsion by collecting droplets from the upper layer of slag/metal emulsion. Block [17] and Urquhart [5] collected samples from inside the converter with the former using a specially designed lance to sample the slag/emulsion. Both Resch [18] and Baptizmanskii et al [19] also sampled the slag/metal emulsion; Resch, by tilting the converter and Baptizmanskii, by cutting a hole in the crucible.

Table 4: Metal droplet size distribution from steelmaking studies

| | **Researchers** | **Place of collection** | **Droplet size (μm)** |
|---|---|---|---|
| **Converter Studies** | Meyer [12] | Outside converter through tap hole (230t converter) | 150 - 3320 |
| | Price [15] | Bath Sampling (90t converter) | 1000 - 2000 |
| | Schoop[80] | Bath Sampling (200t converter) | 50 - 2000 |
| | Cicutti [13] | Inside converter using a special lance (200t converter) | 230 - 3350 |
| | Millman [14] | Bath sampling (6t converter) | 16 to 6000 |
| **Non-converter Studies** | Tokovoi and co-workers [16] | Upper layer of slag/metal emulsion | 1000 - 2500 |
| | Block and co-workers [17] | Inside converter, 50mm or 150mm above metal bath | 500 - 4000 |
| | Urquhart and co-workers [5] | Inside converter with special lance | 63 - 2000 |
| | Resch [18] | By tilting the converter | 50 - 2000 |
| | Baptizmanskii and co-workers [19] | By cutting a hole in the crucible | 50 - 1800 |
| | Koria and Lange [20, 21] | Outside crucible from splashed liquid | 40 - 70000 |
| | Standish and He [6] | Cold Model (Glycerine-Hg and water model) | 1000 - 5000 |
| | Present work | Bath sampling (6t converter) | 16 - 6360 |

Koria and Lange [20, 21] sampled oxidised drops by using a combination of high speed filming (to observe impingement region) and collection of 'splashed' emulsion samples from the top of the crucible. Smaller droplets were spherical whereas larger droplets (>2000μm) appeared flattened. Droplet size distribution obeyed the Rosin-Rammler-Sperling (RRS) distribution function (Equation 5). Droplet sizes ranged between 500μm-5000μm, although larger 'metal pieces' were also collected (the largest equivalent droplet diameter being 70,000μm). It was concluded that larger droplets (>2000μm) decarburised less because of their inherent smaller surface area to volume ratio and reduced emulsion residence time given their larger weight.

$$R = 100 \exp\left[ -\left( \frac{d}{d'} \right)^{n} \right]\% \tag{5}$$

$R$ = Cumulative weight of droplets retained in the sieve
$d$ = Upper limit of class diameter in a given class (μm)
$d'$ = Size parameter – mean particle size (dimensionless)
$n$ = Distribution parameter – measure of spread of particle sizes (dimensionless)

Koria and Lange [22] further experimentally investigated the disintegration of Fe-5%C droplets falling vertically through a high-velocity jet. Results showed that having been fragmented initially by the high velocity jet into secondary droplets, further breakup did not occur; an event which led the authors to conclude that droplet size distribution was solely a characteristic of the Weber Number ($W_e$) expressed in Equation 6. As in latter studies [20, 21], the authors further mentioned the insignificance of initial droplet diameter ($d_i$) on final droplet size distribution.

$$W_e = \frac{\rho_g U_m^2 d_i}{2\sigma_i} \tag{6}$$

Nordqvist [23] conducted metal droplet size distribution experiments within a 30kg induction furnace. Analysis of emulsion samples by EPMA technique showed the majority of metal droplets had diameter of 360μm or less, and were predominantly spherically shaped.

Particle size distribution function is used to quantitatively define how the value of the property is distributed among the overall population [24]. Empirical methods commonly used to represent particle size distribution includes Rosin-Rammler-Sperling (RRS) distribution function, Gaussian distribution function and Logistic distribution function; all of which are two parameter function which have been found to represent particle size distribution accurately [25]. Brezani [26] argued that an advantage of the double *log 100/R (d)* versus *log d* (characteristic of the RSS) compared to log-log plots (characteristic of Gaussian and Logistic), is that the size and distribution parameters (*d'* and *n)* could be obtained, from which, material coarseness and spread of size distribution could be acquired.

Although RRS was initially derived for representing powdered coal particle size, its wide applicability has seen various steelmaking researchers, [14, 16-22] apply the approach to represent the droplet size distribution of metal droplets sampled from industrial and laboratory BOS slag/metal emulsion, with droplet size distribution found to obey the distribution function. An empirical equation for characteristic distribution parameter was further developed by Subagyo [9] containing his blowing number ($N_B$), and correlates well with both his and Koria & Lange's studies [9].

### 2.4 Refining Reactions

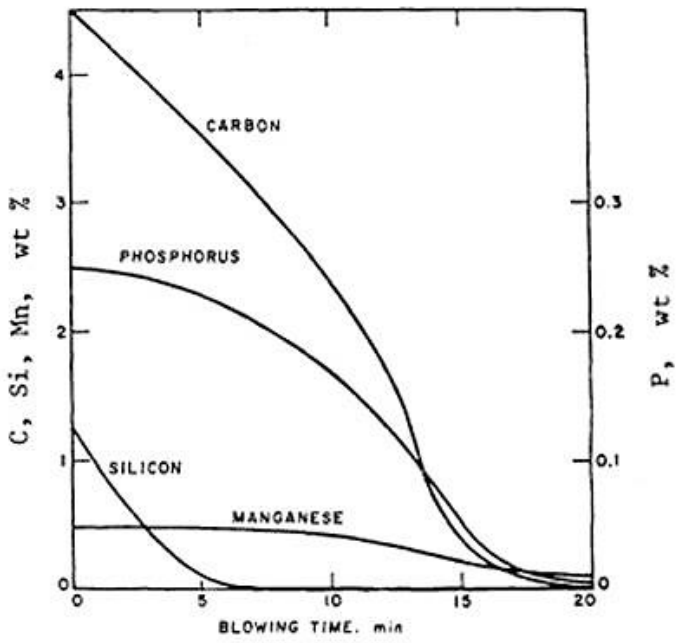


Figure 2: Evolution of bath composition with blowing time [1]

Refining of hot metal (HM) within the Basic Oxygen Steelmaking (BOS) converter occurs via injection of high purity oxygen from a water cooled lance and fluxing of lime to form a basic slag. Metalloids which are oxidised include carbon, silicon and manganese whilst iron oxidation also takes place. Phosphorus removal from the HM has been found to be dependent on the presence of basic slag of high oxygen potential [15, 27]. Figure 2 shows the changes in concentration of elements within the HM during BOS blowing procedure. As can be seen, oxidation of silicon, carbon and manganese occur simultaneously however whilst this may be the case, during the initial periods of blowing rapid silicon and manganese oxidation occur as CO nucleation is presumably slow [15. 28]. This leads to an initial liquid slag primarily made up of silica and iron oxide suitable for fluxing of CaO necessary to aid dephosphorisation.

As silicon oxidation nears completion (in fact silicon is fully oxidised within ~40% of the blow [15]), carbon begins to oxidise and this is very exothermic. Fe oxidation also happens and this is also very exothermic. At this time, most carbon oxidation takes place in the slag/metal emulsion and therefore CO generation aids slag/metal mixing but does not contribute significantly towards bath agitation. Only later in the blow does substantial CO generation take place in the metal bath.

Due to rapid fluxing of CaO into the slag, initial HM dephosphorisation is fast as phosphorus is transferred from the metal into the slag, however as the slag becomes increasingly rich in CaO, FeO becomes increasingly dilute and as such lowers the slag oxygen potential, and simultaneously with the increasing bath temperature (unfavourable to dephosphorisation due to instability of high phosphorus capacity phase such as dicalcium silicate), results in phosphorus reversion [3]. Towards the end of the blow procedure when HM carbon levels have dropped, increased iron oxidation takes place leading to increased oxygen potential in the slag again but at the same time diluting the slag constituents such as CaO and MnO, hence potentially making the slag less favourable for phosphorus uptake (as further discussed in Chapter 2.1.1) and affecting the manganese oxide activity in the slag in a way that increases transfer of manganese from the metal to the slag occurs [15]. However, MTDATA thermodynamic models by Millman[84], indicate the dilution effect of increased slag FeO is perhaps limited given that the thermodynamic model calculates increased phosphorus uptake towards the end of blow.

### 2.4.1 Basics of Dephosphorisation Reaction

#### 2.4.1.1 Phosphorus Activity in Metal

Phosphorus is removed from HM iron under oxidising conditions as a phosphate ion ($PO_4^{3-}$). The simplest representation of the oxidation reaction is given by Equation 7.

$$2[P]_{1\%} + 5[O]_{1\%} = (P_2O_5) \qquad (7)$$
$$\Delta G^0 = -168600 + 133.0T \qquad (Cal)$$

where, [ ] and ( ) denotes component in metal and slag phase respectively. The activities of the reactants and the products of the phosphorus reaction can be found using the equilibrium constant (K) expressed by Equation 8:

$$K = \frac{a(P_2O_5)}{[a_p]^2[a_O]^5} \qquad (8)$$

The solution of phosphorus in liquid iron is represented by the following equation

$$\frac{1}{2}P_{2(g)} = [P]_{1\%} \qquad (9)$$
$$\Delta G^0 = -29200 - 4.6T \qquad (Cal)$$

Considering that the presence of other species affects the activity of phosphorus, interaction parameters are applied when calculating the activity of any given species. Therefore the activity of a species can further be defined as shown in Equation 10, where, $f_i$ is the activity coefficient and $X_i$ is the mole fraction of species $i$ [29].

$$a_i = f_i X_i \qquad (10)$$

And the activity coefficient, $f_P$ is given by

$$\log f_P = e_P^P[\%P] + \Sigma e_P^X[\%X] \qquad (11)$$

A list of interaction parameters for dephosphorisation at 1600°C is given in Table 5 [29]:

Table 5: Interaction Parameters

| $e_y^x$ | C | Mn | O | P | S | Si |
|---|---|---|---|---|---|---|
| **C** | 0.124 | -0.012 | -0.340 | 0.051 | 0.046 | 0.080 |
| **P** | 0.130 | 0.000 | 0.130 | 0.62 | 0.028 | 0.120 |
| **Si** | 0.180 | -0.021 | -0.230 | 0.110 | 0.056 | 0.110 |
| **O** | -0.450 | 0.002 | -0.200 | 0.070 | -0.133 | -0.131 |

#### 2.4.1.2 Phosphate Capacity

Phosphate capacity can be defined as the dephosphorising power of a basic slag (oxide system). The most useful expression of this property is associated with the ionic model phosphorus reaction [30].

$$\frac{1}{2}P_{2(g)} + \frac{5}{4}O_{2(g)} + \frac{3}{2}(O^{2-}) = (PO_4^{3-}) \tag{12}$$

$$C_{PO_4^{3-}} = \frac{(\%PO_4^{3-})}{pP_2^{1/2}\,pO_2^{5/4}} \tag{13}$$

$C_{PO_4^{3-}}$ is related to the equilibrium constant (K) of *Equation 6* as follows:

$$C_{PO_4^{3-}} = \frac{Ka_{O^{2-}}^{3/2}}{f_{PO_4^{3-}}} \tag{14}$$

where, $f$ is the Henrian activity coefficient of $PO_4^{3-}$.

#### 2.4.1.3 Mechanism of Dephosphorisation

Dephosphorisation of blast furnace HM occurs under basic and oxidising conditions. Phosphate ion ($PO_4^{3-}$) is formed at the slag/metal interface due to dissolved oxygen in the metal and oxygen ions in the basic slag, which under favourable conditions precipitates high phosphorus capacity phases such as dicalcium silicate ($C_2S$) and tricalcum phosphate ($C_3P$). When sufficient CaO has dissolved locally to form these temperature dependent phases, $PO_4^{3-}$ dissolves into them to facilitate phosphorus removal. The dephosphorisation reaction can be expressed using the molecular or ionic model as illustrated in Equations 7 and 12 respectively.

Various industrial studies [31-36] have specifically investigated the slag phases that contribute towards dephosphorisation. Preßlinger et al [31, 32] conducted micro-analytical investigations of solid BOS converter slag to identify process parameters influenced by the refining process. Using EPMA technique, dicalcium silicate, wustite and dicalcium ferrite phases were identified within the sampled slags. Phosphorus was incorporated in the dicalcium silicate phase as a solid solution, whilst wustite mixed crystals were found as bivalent ions ($Mg^{2+}$, $Mn^{2+}$ and $Ca^{2+}$); these occupied the octahedral sites of the wustite cubic close packed crystal structure, usually accommodated by $Fe^{2+}/Fe^{3+}$ ions.

Similar phases were found by Waligora et al [33] having coupled several analytical techniques (XRD, EPMA, SEM, TEM-EDS and Raman Micro spectrometry) to characterise un-weathered steel slag. By using the Raman microscopy technique, the researcher was able to further differentiate between a homogenous dicalcium silicate phase ($CaO/ (SiO_2 + P_2O_5) = 2$) and heterogeneous silicate phase ($CaO/ (SiO_2 + P_2O_5)$ = 1.9 to 3.2) present in the sampled slag. Chemical composition analysis obtained by EPMA technique showed more phosphorus was captured in the homogeneous dicalcium silicate phase (3.68-6.95 wt.%) compared to the heterogeneous silicate phase (1.46-2.64 wt.%). The significance of this observation is however questionable given that on cooling, the liquid slag solidifies to dicalcium silicate, wustite and dicalcium ferrite phases. Therefore it is not usually possible to differentiate the dicalcium silicate phase originating and present at steelmaking temperature from the solidified $C_2S$ phase.

Maxl et al [34] analysed industrial and laboratory steelmaking slag in order to describe phosphorus bonding phases present. Microanalysis of the slag showed dicalcium silicate was present in the industrial slag but not in the laboratory slag; in which case, calcium phosphate ($C_nP$) was the phosphorus bonding phase. Although acknowledging the presence of wustite and dicalcium ferrite within the industrial slag, optical microscopy and EPMA showed phosphorus was incorporated within the matrix of the (precipitated) dendritic dicalcium silicate and that wustite incorporated the least phosphorus within its structure. As proposed by several other researchers [37, 38], the dephosphorisation reaction for this study was considered in terms of ionic theory, and a series of ionic equations were presented by the researchers.

Metal-slag reaction

$$[P] = (P)^{5+} + 5e^{-} \quad (15)$$

$$[Si] = (Si)^{4+} + 4e^{-} \quad (16)$$

Anion complex formation

$$(P)^{5+} + 4(O)^{2-} = (PO_4)^{3-} \quad (17)$$

$$(Si)^{4+} + 4(O)^{2-} = (SiO_4)^{4-} \quad (18)$$

$$(CaO) = 2(Ca)^{2+} + (O)^{2-} \quad (19)$$

Polymerisation

$$x(SiO_4)^{4-} + y(PO_4)^{3-} = (Si_xP_yO_{3x+3y+1})^{(2x+y)^-} + (x+y-1)(O)^{2-} \quad (20)$$

Crystallisation

$$2(Si_xP_yO_{3x+3y+1})^{(2x+y)^-} + (2x+y+2)(Ca)^{2+} = (Ca_{2x+y+2}Si_{2x}P_{2y}O_{6x+6y}+2) \quad (21)$$

Basic oxides (CaO) were considered as oxide ion donors with predominantly ionic bonding, whist acidic oxides ($SiO_2$, $P_2O_5$) were considered as oxide ion acceptors with predominantly polar-covalent bonding. At the metal/slag interface, under oxidising conditions, hot metal phosphorus ($P^{5+}$) and silicon ($Si^{4+}$) are transferred to the slag as tetrahedral complex ions ($PO_4^{3-}$ and $SiO_4^{4-}$). These ions polymerise to form structural 'chains'. When enough CaO is dissolved in the slag, stable compounds of C2S are formed and crystallise. $PO_4^{3-}$ in the slag is then taken up by the dicalcium silicate phase through partial substitution of $SiO_4^{4-}$ by $PO_4^{3-}$, forming a solid solution.

#### 2.4.1.4 Order

For steelmaking reactions to take place and a high level of metal refinement to occur whereby phosphorus, silicon and manganese levels are significantly lowered having undergone oxidation reactions and transfer from the metal phase into a basic slag, several steps are required as follows [15]:-

I. Transfer of the reaction species between the bulk phase and the interface
II. Reaction at the interface between reaction species to form reaction products
III. Transfer of the reaction products between the interface and the bulk phase

where, one of which is the rate determining step (RDS). Assuming Equation 7 to be representative of the dephosphorisation reaction, the reaction steps are as follows [39]

I. Metal phase mass transfer of [P] to the slag/metal interface
II. Metal phase mass transfer of [O] to the slag/metal interface, or supply of [O] from the slag to the interface via the reaction: (FeO) = Fe + [O]
III. Slag phase mass transfer of ($O^{2-}$) to the interface
IV. Slag phase mass transfer of ($PO_4^{3-}$) away from the interface into the slag
V. Chemical reaction for the formation of ($PO_4^{3-}$)

Although the kinetics of dephosphorisation are widely accepted to be first order with respect to phosphorus in the metal [29], the rate controlling mechanism for the reaction remains debatable, although the general consensus is that of mass transfer being the rate determining step (RDS) and not chemical reaction. Having fitted the experimental results to Equation 16 to conclude that the rate of dephosphorisation was first order, Monaghan [29] proposed that the likely rate limiting steps to be one of chemical reaction (Equation 23), mass transport control in the metal phase (Equation 24) or mass transport control in the gas phase (Equation 25). Through further derivation of integrated rate equations and application of the experimental data into these equations, the rate controlling step for dephosphorisation reaction was classed as mass transport control in the slag phase.

$$\frac{[\%P]_b - [\%P]_e}{[\%P]_o - [\%P]_e} = \exp(-kt) \qquad (22)$$

$$\ln\left[\frac{[\%P]_b - [\%P]_e}{[\%P]_o - [\%P]_e}\right]\left(\frac{[\%P]_o - [\%P]_e}{[\%P]_o}\right)\left(\frac{W_M}{\rho_M A}\right) = -k_f t \quad (23)$$

$$\ln\left[\frac{[\%P]_b - [\%P]_e}{[\%P]_o - [\%P]_e}\right]\left(\frac{[\%P]_o - [\%P]_e}{[\%P]_o}\right)\left(\frac{W_M}{\rho_M A}\right) = -k_m t \quad (24)$$

$$\ln\left[\frac{[\%P]_b - [\%P]_e}{[\%P]_o - [\%P]_e}\right]\left(\frac{[\%P]_e}{[\%P]_o}\right)\left(\frac{W_s}{\rho_s A}\right) = -k_s t \quad (25)$$

Subscripts *b, e, o* denote phosphorus concentrations (*%P*) in the bulk metal, metal equilibrium phosphorus concentration and initial metal phosphorus concentration respectively and subscripts *m* and *s* denote metal and slag respectively.

Manning [39] conducted a series of laboratory experiments to determine the rate controlling mechanism of phosphorus transfer from Fe-P alloy to CaO-$SiO_2$-MgO-FeO slag at 1600°C, where CaO/$SiO_2$ ratio ranged between 1.4-1.9, FeO content ranged between 18-25 Wt.%, and oxygen from FeO reaction controlled the dissolved oxygen in the metal. The results showed rapid initial dephosphorisation rates (0.07 $cm^3/s$) followed by decreased rate (0.007 $cm^3/s$) towards the end of the reaction. This finding was in agreement with that of Mori [40] and Nasu [41] who also reported a decrease in mass transfer as the reaction proceeded.

Having adopted a sessile drop technique to determine the effects of slag/metal interfacial tension on kinetics of dephosphorisation using CaO based slags of $Fe_2O_3$ content ranging from 10-30 wt.% and Fe-P alloys (0.06-0.10 wt.% P), Nasu [41] concluded that the rate of dephosphorisation was at least partially governed by mass transfer in the slag phase. Dephosphorisation rate was found to increase with increasing slag basicity and increasing initial $Fe_2O_3$ slag content (up to a critical point). The rate was also found to be limited by slag viscosity, where slags interfacial tension rapidly decreased and stabilised at a low level during the early rapid mass transfer period, and then increased again afterwards; providing further support to the argument that mass transfer in the slag phase is a contributing factor to the RDS.

Monaghan [29, 42] established that mass transfer in the slag was the "most likely" RDS having fitted experimental data to show the effect of slag weight on dephosphorisation at 1330°C, on an integrated plot for mass transport control in the slag. The data correlated well on a straight line, suggesting the reaction was controlled by mass transport in the slag phase. A similar fit was not observed when mass transport control in the metal with respect to [P] was plotted.

#### 2.4.1.5 Control

HM temperature, HM composition, slag basicity and slag oxygen potential have been found to influence phosphorus control. These factors have been the source of few kinetic studies. Mori [43], investigating the rate of dephosphorisation of high carbon (> 3.5 wt.% C) Fe-C alloys by CaO-$SiO_2$-FeO slags at temperatures ranging between 1300°C - 1460°C and initial metal phosphorus levels of 0.1 wt.%. Whilst decarburisation and dephosphorisation reactions took place simultaneously at the start of the experiments, dephosphorisation decreased with increasing temperature, and decreasing slag FeO content at latter stages of the experiment resulted in phosphorus reversion. Once rapid decarburisation had ceased increase in slag FeO content was further found to accelerate dephosphorisation.

The effect of oxygen potential on dephosphorisation kinetics of carbon saturated iron was further studied by Monaghan [42], who conducted a series of experiments at 1330°C with oxidising slags of FeO content ranging up to 50 wt.%, and metal phosphorus content ranging between 0.01 - 0.04 wt.%. Dephosphorisation rate was found to be a function of the initial metal phosphorus content, with metal of higher phosphorus content showing a faster dephosphorisation rate. As in the study by Mori [43], increasing slag FeO content up to a critical amount increased the rate and extent of dephosphorisation accordingly. Beyond the critical point (50 wt.% in this study), the rate and extent of dephosphorisation decreased. This phenomenon has been credited to two competing factors, where increased slag FeO content increases the oxygen potential but dilutes the slag basicity, hence lowering the slag phosphate capacity [44].

The effects of oxygen potential on the transfer of phosphorus between FeO containing slag and high carbon iron alloys under Ar-$O_2$ atmosphere was investigated by Wei [45] at temperatures of approximately 1300°C. Results showed that dephosphorisation rate was strongly influenced by atmospheric oxygen partial pressure of Ar-$O_2$, where the rate

increased with higher atmospheric partial pressures and higher slag FeO content; the latter, further leading to lower end phosphorus levels in the metal. It was suggested that where the atmospheric oxygen partial pressure exceeded that of the slag (FeO), the oxygen supply rate surpassed the consumption rate, hence leading to high FeO levels in the slag at latter stages of dephosphorisation reaction.

In an earlier separate study by Wei [46] the effect of metal phosphorus content (4.4 wt.% C, 0-1.8 wt.% P) on the reduction rate of FeO (4.6-20 wt.%) in a similar FeO containing slag was monitored. Higher initial metal phosphorus levels resulted in lower rates of FeO reduction whilst phosphorus in the slag phase was found to lower the rate of carbon oxidation considerably.

Based on the kinetic and thermodynamic findings of these and various other researchers, the ideal conditions for dephosphorisation are well established; low temperature, high slag oxygen potential and high slag basicity. The ionic theory proposed by Flood [37] can be used to justify this. By increasing the FeO slag content or the gas oxygen concentration, the oxide ions (LHS of Equation 12) within the slag increases; causing the reaction to shift to the RHS of the equation forming more phosphate ions and hence greatly contributing to dephosphorisation reaction at the slag/metal interface. Further implied by the ionic theory is that CaO (basic oxide) is effectively an oxide ion donor and, the acidic oxides ($SiO_2$, $P_2O_5$), oxide ion acceptors. Therefore by increasing the amount of CaO, the slag basicity increases and creates a greater driving force for phosphorus transfer out of the HM.

### 2.4.2 Hot-metal/ Fe-alloy Droplet Oxidation Studies

It is common practice that a study of HM/ Fe-alloy dephosphorisation on a laboratory scale comprises the use of crucible technique where a bulk slag is in contact with a bulk metal forming an interface to facilitate phosphorus transfer; in most cases the slag composition is partly governed by the crucible material. Droplet studies with respect to HM/Fe-alloy dephosphorisation has been limited in comparison to 'bulk' studies; although the importance of droplets in the role of dephosphorisation is well acknowledged, as shown in the work by Millman [3].

Gaye and Riboud [47] studied the kinetic reaction of Fe-X and Fe-C-X (X = C, P S) alloys and its effects on decarburisation rate. Kinetics of the dephosphorisation reaction was

obtained by conducting chemical analysis of water quenched samples. At a slag $CaO/SiO_2$ ratio (V-ratio) of 9.6, for Fe-P alloy droplets (2.5 wt.% C and 1.5 wt.% P), phosphorus content reached a minimum of 0.006 wt.% within 60 seconds. Similar end-phosphorus content was achieved within 10 seconds for Fe-C-P alloy droplets; with the significant difference in dephosphorisation rate concluded to be a consequence of metal agitation caused by gas evolution during simultaneous decarburisation reaction.

Identical experiments were conducted by Gare and Hazeldean [28] with higher carbon (3.9 wt.%) Fe-C-P alloy, and lower V-ratio of approximately 1.2. Using a Constant Volume Pressure Increase (CVPI) technique to measure decarburisation rates and x-ray fluorescence to observe slag/metal interfacial behaviour, phosphorus was found to slow down the overall decarburisation process by up to a minute; with the finding credited to the high affinity of oxygen by phosphorus inhibiting the availability of oxygen for decarburisation reaction to proceed at a faster rate. Total reaction time was 3 minutes, with rapid dephosphorisation occurring within the first few seconds of the overall decarburisation reaction.

Inhibition of decarburisation (for Fe-C alloys) and the resultant decrease in FeO reduction rate was further found by Murthy [48] when investigating the effect of $P_2O_5$ in lime based slags. It was noted that addition of $P_2O_5$ to the slag decreased FeO reduction rates by 15-18% at studied temperature of 1773K.

Stationary levitation technique was applied by Jahanshahi [49] to investigate dephosphorisation of Fe-P and Fe-C-P alloys by formation of volatile phosphorus products, within oxidising gaseous atmospheres in the absence of basic slag, at 1600°C. Metal phosphorus contents ranged between 0.1 wt.% - 2 wt.%. No phosphorus removal occurred in either alloys irrespective of initial carbon content and oxygen partial pressure ranging between $2.3x10^{-6}$ atm to 1 atm. A similar study was conducted by Kaplan [50] where carbon saturated Fe-C-1.76 wt.% P alloys droplets were levitation melted and exposed to gaseous oxidising atmosphere ($He-O_2$) at temperatures ranging from 1850°C - 2050°C. In the absence of basic slag, no phosphorus transfer from the metal to gas phase was found, although decarburisation rate was lowest for Fe-C-P alloys compared to Fe-C alloy.

Simultaneous oxidation of metalloids in a Fe-C-X alloys (where X = Si, Mn etc.) within an oxidising gas atmosphere has been investigated by few researchers [49-53, 66-72]. Sun and Pehlke [51, 52] noted that decarburisation occurred preferentially over silicon and manganese removal at elevated temperatures (1574°C – 1715°C), until the droplet's carbon level diminished to <1 wt. % C. At lower experimental temperatures (1360°C), an evenly distributed viscous silica-rich oxide layer coated the droplet's surface, consequently preventing further oxidation of the metalloids (C, Mn, Si). In agreement with the experimental observations of similar decarburisation (levitation) studies [51-56], Widlund [53] observed a decrease in decarburisation rate and simultaneous onset of silicon removal at a critical droplet carbon level (0.5wt%C), independent of initial carbon and silicon concentration and oxidising gas flow rate. A significant finding of this study was the presence of an oxygen gradient ranging from 10% (2μm beneath the drop surface) to 40% (at the drop surface), during the first 3 seconds of the experiment. This indicated oxygen enrichment of the drop surface occurred even at the early stages of decarburisation; a phenomenon which is characteristic of latter stages of droplet decarburisation process (leading to CO nucleation) [54-56].

## 2.5 Levitation Melting

### 2.5.1 Theory

Physics state that when a conductive specimen is passed through an external magnetic field, current is induced within the specimen. These same principles state that where current flows in alternating directions in two parallel conductors, they repel each other; it is for these reasons that a levitation force is produced, [57].

Levitation melting is a process of melting a conductive specimen by means of interaction with an external magnetic field [58]. When a conductive load is placed in an alternating magnetic field, eddy currents are induced in the metal. The current interacts with the induced and applied magnetic fields to generate electromagnetic forces (i.e. Lorentz forces), within the specimen. Levitation occurs if the applied magnetic field is greater than the gravitational force; this is further accompanied by heating/melting effect (Joules heating) by the induced eddy current [60].

Heating or melting is achieved through a skin effect, where frequency and load type dictates the skin depth. For smaller loads to induce a current, the skin needs to be thin,

hence a larger frequency is required. However, if the load is too small, the induced alternating current could potentially cancel itself out. Load influences frequency by changing the inductance of the capacitor according to Equation 26, where f is frequency (unit: kHz), L is inductance (unit: H) and C is capacitance (unit: F).

$$f = \frac{1}{2\pi\sqrt{LxC}} \tag{26}$$

If the input power matches the power used to heat/melt the load, then there is a 100% match percentage. Lower match percentages represent loss of heating efficiency. This can be overcome by using a smaller coil or a larger load to minimise the amount of space between the coil and load. On a steady state generator, the "Tap" mode can be changed also, effectively distributing the ratio of power given to the load from the generator [61].

Key components of a levitation unit include annealed copper coil and a power supply that controls power input which directly influences the external magnetic field strength, levitation force and, to an extent the specimen temperature. When input power is reduced, there is a reduction in coil current (and hence strength of external magnetic field) which decreases the levitation force. This causes the droplet to lower its positional height, drawing it closer to the region of high magnetic field density, thus increasing the droplet temperature [62]. Equally, increasing the positional height of the droplet away from the high magnetic field density region decreases the temperature. Inert gas can further be used to moderate droplet temperature.

### 2.5.2 Technique

There are two distinct levitation experiment techniques; 'Stationary' and 'Free fall'. The stationary technique is mainly used to study reactions for times greater than 2 seconds. The sample levitates and melts simultaneously and undergoes its reaction in-situ under the influence of an external magnetic field, prior to being quenched either in situ (gas quench) or on a water cooled mould. Free-fall technique is used to study reactions for times less than 2 seconds. The apparatus has two distinct sections; 'levitation melting chamber' and 'reaction column'. Having isothermally stabilised the levitated droplet, the coil is de-energised causing the droplet to fall down the reaction column of a known height.

### 2.5.3 Studies

Watkins [57] has presented the most comprehensive summary of kinetic studies on reactions of levitated molten metal droplets for metal/gas and metal/gas/slag systems. Having reviewed the limited number of studies available, there were no specific studies which examined the dephosphorisation kinetics of blast furnace HM; a potential reason being the complexity of introducing powdered reagents such as lime into the system to facilitate phosphorus removal. Nevertheless, these studies provide fundamental information regarding apparatus design, experimental preparation and setup.

Baker [54] measured the rate of decarburisation of an Fe-alloy droplet with carbon content between 0-5.5 wt.% (0.006 wt.% P, 0.002 wt.% Si, 0.026 wt.% S, 0.11 wt.% Mn) at 1660°C. The droplet was exposed to either pure or diluted (CO, He) $CO_2$ reactive gas. Dependent on gas flow rate, reaction times ranged between 2 seconds (high flow rate; 5 l/min) and 20 minutes (low flow rate; 1 l/min and diluted $CO_2$). The rate of decarburisation was found to be independent of carbon concentration, leading the author to conclude that gaseous diffusion (in the gas boundary layer) was the rate controlling step. This finding was further supported by strong correlation between the calculated and experimental decarburisation rates, as well as preliminary runs of similar experiments in a different binary reactive gas mixture of $O_2$-He.

In a follow up study by Baker [55] a mass transfer correlation equation was set up to predict the diffusion of oxygen through the gas layer into the metal. It was concluded that for high carbon concentrations, decarburisation was controlled by gaseous diffusion, but at lower carbon concentration (<1.0 wt.%), decarburisation rate was significantly slower

and was controlled by carbon diffusion in metal. During the latter, oxygen diffused into the droplet's surface due to oxygen enrichment of the gas boundary layer, resulting in a carbon gradient within the droplet. Consequently, at regions within the droplet where concentrations of oxygen and carbon were high, homogeneous nucleation of CO occurred. Although the effect of other alloying elements, notably silicon, manganese and phosphorus were not recorded in these studies [54, 55], the author proposed that studies of silicon and manganese oxidation using the levitation technique were to be conducted. Furthermore, the consumption of oxidants by Fe was recorded negligible compared to carbon consumption.

Further studies were done by Baker [56], this time adopting a 'free falling' levitation technique. The apparatus was made up of 3 sections (inert melting zone, reaction column and cooling zone) separated by a 'Saranwrap diaphragm'. The experimental setup allowed for use of different gaseous atmospheres and extended studies into the effect of eddy stirring on decarburisation rate. Samples were levitation melted to 1600°C in He/Ar atmosphere before free falling through pure oxygen in the reaction column and quenched by nitrogen (20 l/min) within the cooling section. Initial carbon content of the Fe-alloy ranged between 0.8 - 4.5 wt.%. During these free-falling levitation experiments, CO nucleation was found to occur beneath the droplet surface at higher carbon concentrations compared to static levitation experiments [54, 55]; indicating carbon diffusion control for the majority of decarburisation period.

Through mass transfer calculations, Baker [56] identified that the rate of decarburisation for free-falling technique, and simply by gaseous diffusion alone, was twice that of static levitation. From previous studies [54, 55], considering that carbon control would slow the decarburisation rate significantly, this led the author to conclude that gas diffusion remained predominantly rate controlling even at higher carbon concentrations, but a mixed control existed within the metal. Two mechanisms of homogeneous nucleation (surface removal by eddy diffusion and molecular diffusion) were further proposed by the researcher.

Oxidation reactions of binary (Fe-Si, Fe-C) and ternary (Fe-Si-C) iron alloys were investigated by Baker [63] within a 5 ft 'free falling' levitation apparatus. CO nucleation (at high carbon concentrations 4-4.9 wt.% C) occurred in carbon saturated droplets falling through pure oxygen at an initial temperature of 1600°C. It was concluded that at silicon

levels lower than 3 wt.% of the binary and ternary alloys, over 80% of the metalloids was oxidised during the 5ft drop through pure oxygen. With less silicon oxidation taking place in ternary system, the amount of exothermic heat (favourable for decarburisation) given off specifically by the reaction would have been less than the binary system, therefore subsequently limiting the onset of carbon removal.

Distin [64] studied decarburisation of carbon saturated Fe-C drops at temperatures between 1700°C - 1850°C, using the stationary levitation technique. Having subjected the droplet to various oxidants ($O_2$, $CO_2$, $O_2$+$H_2O$ and Ar+$H_2O$) within a series of experiments (300 ml/min, 500 ml/min and 1200 ml/min gas flow rates), the formation of oxides on the droplet surface was observed at low carbon concentrations (around 0.8 wt.% C). It was further concluded that carbon boil (CO nucleation) began only once the surface oxide had formed, irrespective of oxidant flow rate. A similar argument to that of Baker [54, 55] and Baker [56, 63] was made by Distin regarding the cause of CO nucleation; saturation of droplet surface with oxygen, causing diffusion of oxygen into the surface, resulting in oxygen and carbon rich regions within close proximity of each other leading to CO nucleation.

Roddis [65] proposed that carbon removal from Fe-C (0.44 wt.% - 4.8 wt.%) binary alloy occurred via surface and subsurface reactions, and that the transition between these reaction modes were dependent on the droplet temperature, oxidant composition and carbon concentration. It was further concluded that gaseous diffusion control was dominant during surface reactions for droplets of greater than 4 wt.% C, and carbon diffusion control for lower carbon content droplets, until a critical level had been reached whereby subsurface reactions occurred; influenced by diffusion of oxygen into the droplet.

Sulphur in Fe-C-S alloys was found to retard the reaction rate of decarburisation within decarburisation kinetic experiments conducted by Lee and RaO [66], but like in prior studies, decarburisation rates were independent of initial carbon content but affected it by increasing oxidant ($CO_2$-CO) flow rates. A deviation from constant decarburisation rate was observed at a certain point during the reaction, accompanied by formation of oxide on the droplet surface, although carbon boil was not witnessed.

Stationary levitation technique was applied by Jahanshahi [49] to investigate dephosphorisation of Fe-0.1 wt.% P and Fe-3.5 wt.% C-0.1 wt.% P alloys within an oxidising gaseous atmospheres and at 1600°C. No phosphorus removal occurred in either alloys irrespective of initial carbon content and oxidant ($CO_2$, He-$O_2$). Carbon boil was observed for the ternary alloy after a period of rapid decarburisation (~ 0.2wt.%/s) during the first 15 seconds of being exposed to oxygen. The onset of carbon boil was accompanied by a slower rate of decarburisation (0.02 wt.%/s).

Sun [51] investigated the simultaneous oxidation of carbon, silicon and manganese in an iron alloy by carbon dioxide and at temperatures ranging between 1575°C – 1715°C. Oxidation of carbon occurred preferentially to silicon and manganese until metal carbon level was low enough (< 1 wt.% C), whilst decarburisation rates were found to increase with increasing oxidant flow rate.

Further experimental study by Sun [52] was conducted to verify a model developed around the initial and new set of low temperature experiments. At high temperatures (1600°C), desiliconisation within low carbon (0.4 wt.% C) metal occurred instantaneously once exposed to the oxidising gaseous atmosphere. However, at lower temperatures (1360°C), for high carbon (> 3.4 wt.% C) iron alloys, there was no removal of carbon, silicon or manganese during the initial 2 minutes. It was further observed that a silica-rich oxide layer coated the droplet's surface, consequently preventing further oxidation. Suppression of further oxidation reactions by the oxide layer was not witnessed at elevated temperatures as the oxide was less viscous and subsequently gathered at the bottom of the droplet.

Similar work to that of Lee and RaO [66], which comprised studying decarburisation of Fe-C-S drops in an oxidising gaseous atmosphere, was conducted by Simento [67, 68]. Whilst desulphurisation was found to retard decarburisation by reducing the surface reaction rate of the oxidants, gaseous diffusion of the oxidants was identified as the rate controlling step. These findings were further validated by a mixed control model which corroborated with the experimental results.

Widlund [53] investigated the decarburisation of Fe-C-Si melts containing 4 wt.% C and 0.37-0.71 wt.% Si. The experiments were conducted within the temperature range 1400°C – 1600°C, and in a gaseous atmosphere comprising helium and oxygen (10% and 20%).

Decarburisation reaction proceeded at a constant rate for most of the process until a critical carbon level (0.5 wt.% C) was reached at which point metal silicon levels began to drop. A significant finding was the presence of an oxygen gradient at the droplet's surface (in the absence of a visible oxide layer) having conducted X-EDS analysis. The oxygen level ranged between 10% (2 μm below surface) to 40% (at the surface), during the first 3 seconds of the experiment; suggesting that oxygen enrichment of the surface occurred even at the early stages of decarburisation; a phenomenon which is characteristic at latter stages of decarburisation, generally leading to carbon boil/ CO nucleation.

Slag/metal equilibrium was studied by Caryll [69] using the stationary levitation technique. Iron specimens were drilled and packed with electrolytic Mn and then sealed with oxide scale by an oxygen flame. At operating temperatures between 1650°C – 1870°C, slag material (presumably formed by oxide scale) gathered at the bottom of the droplet. Hammer quenching was favoured over gas or copper mould quenching as this was found to give a higher cooling rate, hence suppressing potential changes of slag/metal Mn distribution. The levitation technique produced similar results to that of crucible melting techniques, with the added advantage of improved equilibrium measurement attainable at a wider range of temperatures.

The (stationary) levitation melting technique was further applied by Watkins [57] to investigate the growth of oxide layers on titanium deoxidised steel and pure iron. These metals were subjected to vaporised calcium metal and lime powder (CaO) to observe calcium modification of oxides formed on the deoxidised steels. Phosphorus levels within these metals were extremely low, ranging between 0.00007 wt.% to 0.009 wt.%. Lime was packed into a pre-drilled hole and formed 'cylindrical islands' at the surface of molten droplets, and remained so throughout the duration of the experiment as no lime dissolution took place.

See and Warner [70] studied reactions of Fe-C-Si alloy drops in free fall through oxidising gases and observed the formation of slag layer on the droplets surface using high speed photography. Although the slag material was not analysed, it was thought to be a FeO layer rich in $SiO_2$, similar in composition to that of Robertson and Jenkins [71]. In a similar set of experiments by Radzilowski [72] where the gaseous oxygen absorption by Fe-Si alloy was investigated at 1600°C, oxygen absorption rate was found to decrease when the initial silicon content was higher than 3 wt.% in iron. Changes in oxygen absorption rate

with increasing silicon content was found to be caused by increased growth of surface oxide film with increased amount of the alloying element (e.g. silicon) in the metal. Whilst the interfacial tension of the proposed silica-rich slag was not measured in the respective study, it was argued that because of the complex structure of Si/O network, the viscosity of the slag increased with silicon content to form a viscous slag film around the droplet, inhibiting uptake of oxygen at the metal surface.

### 2.6 Apparatus Design

An apparatus design review was conducted to compare various apparatus setups used for metal droplet studies and to identify the key components of levitation melting apparatus. On a laboratory scale, high temperature investigations involving metal droplet have traditionally been conducted using either crucible technique whilst more historic studies relating to spray steelmaking specifically used the contactless levitation melting technique as has studies investigating surface tension related behaviour. Table 6 summarises several of the studies where these techniques have been applied.

By using refractory crucibles, slag/metal reactions are able to be investigated however the drawback is contamination of slag as the refractory material may dissolve in the basic slag therefore changing the reaction system. To prevent such happening, researchers tend to add to the slag, reagent of the crucible material to saturate the slag and hence prevent uptake from the crucible. With the contactless nature of the levitation melting technique, such practice is not required as there is no scope for slag contamination from crucible erosion hence confidence can be had from the fact that all slag material comes entirely from the slag making material introduced into the reaction system.

An added advantage of the crucible technique is the ability to use as much/little of the reactants as required and in doing so, the ability to conduct equilibrium based experiments through sampling of the crucible content at time intervals. Several of these studies that have investigated droplet reactions and change in droplet physical property within slag material have also used x-ray fluorescence measurement to monitor droplet behaviour throughout the period of reaction, hence encasing of the crucible within the tube furnaces used for such studies do not restrict real time observation/measurements from within the crucible whereas this is more of a constraint for ‘contactless’ levitation melting technique.

Historically, the levitation melting technique within steelmaking industry was used to investigate decarburisation reaction kinetics of HM droplets and Fe-C based alloys. In the 1960's-1970's, the technique found use in laboratory based studies supplementing plant operation of spray steelmaking. Laboratory apparatus comprised several fundamental design features such as electromagnetic coil for heating and levitating the metal droplet, pyrometer viewing window for measuring droplet temperature, gas ports for introduction of inert and oxidising (reaction) gas and an enclosed glass volume for contain the metal droplet and seal it from atmospheric conditions. Table 7 details several laboratory studies where levitation melting apparatus has been used.

As shown in Table 7, the majority of levitation melting studies have mainly been metal/gas reactions between metal droplets and gaseous reaction atmosphere. As with the present study where stationary levitation melting technique was used, the oxidising reaction gas was diluted to similar levels of between 70-90% inert gas mainly to prolong reactions in order to measure kinetic effects and also for safety concerns as prolonged exposure of HM droplet to pure oxidising atmosphere would have resulted in droplet explosion as witnessed within free fall experiments of researchers such as Baker [56].

With respect to reaction system, the present apparatus further differentiates itself by studying metal/slag/gas system by initially coating the metal droplet with slag material before introducing it to the electromagnetic coil. Whereas Burtsev [73] encapsulated slag within a drilled cavity of his solid metal sample and potentially suffered sintering of the slag and poor slag dissolution at the molten metal surface, with the metal/slag arrangement employed in this study, even distribution of thin layer of slag around the 2g solid sample ensured quicker slag dissolution hence promoting increased level of slag/metal reaction. The ability to coat the solid metal sample further meant that smaller droplet size (2g) could be used in the study compared to the minimum droplet sixe of 4g used by Burtsev [73] presumably because this was the smallest weight sample which a slag-packed cavity could be drilled into.

The development of induction furnace generators has also seen increased heating efficiencies associated with steady state generators such as the one used in the current study, compared to history valve generators used in the majority of studies listed in Table 7, and as such, less power is required to heat samples to a desired temperature. For this reason, the number of turns on a levitation coil such as that used in the present study is

notably reduced although the requirement for alternating set of top and bottom turnings is still required to ensure droplet levitation. However, a similar 30° conical angle between the top turning and the bottom turning such as that adopted by Burtsev [73] and Widlund [53] presumably to increase magnetic field flux density within the bottom turn also featured in the coil of the present study for the same reason. Also, power being transferred to the EM coil was controlled to within +/- 1V with a remote control dial which as may be expect would have offered improved power control and consequently better temperature control than historic induction furnace valve generators.

Evident from Table 7, there are many similarities between the current setup and those listed in literature such as the use of two colour pyrometer and internal location of EM coil, however a further differentiation of the current apparatus is its ability to apply both stationary and free fall levitation technique on the same apparatus as discussed below; owing this function largely to its modular design. Further design considerations and design results are presented in Chapter 4 – Section 4.1.

Table 6: Laboratory techniques used to study steelmaking metal droplets

| Researcher | Area of study | Apparatus type | Container | Droplet weight (g) | Real-time measurement system | Reaction time | Reaction System |
|---|---|---|---|---|---|---|---|
| Gare and Hazeldean [28] | Decarburisation rates | Vertical tube furnace | $Al_2O_3$ tube | <2g | X-ray Fluorescence | 2-5mins | Metal/slag |
| Krishna Murthy [48] | Decarburisation rates | Induction furnace | $Al_2O_3$ crucible | 1-2g | X-ray Fluorescence/ pressure transducer | <25mins | Metal/slag |
| Chen [10] | Droplet swelling | Vertical tube furnace | MgO crucible | 0.5 – 3g | X-ray Fluorescence/ pressure transducer | 10s | Metal/slag |
| El-Kaddah [74] | Decarburisation reaction kinetics | Induction furnace | None (stationary levitation) | 1g | Pyrometer | <20mins | Metal/gas |
| Sun [25, 26] | Oxidation reactions | Induction furnace | None (stationary levitation) | 1-3g | Pyrometer | <2mins | Metal/gas |
| Distin [64] | Decarburisation reaction kinetics | Induction furnace | None (stationary levitation) | 1-2g | High speed camera/ Pyrometer | <3mins | Metal/gas |
| R. Baker [56] | Oxidation reactions | Induction furnace | None (free-fall levitation) | 1-2g | Pyrometer | ~1sec | Metal/gas |
| Burtsev [73] | Equilibrium sulphide distribution | Induction furnace | None (stationary levitation) | 4g | Pyrometer | <16mins | Metal/slag |

Table 7: Levitation melting studies

| Researcher | Type of Levitation Apparatus | Reaction system | Glassware | Coil design (top: bottom) | Coil location | Temperature measurement | Cooling method |
|---|---|---|---|---|---|---|---|
| El Kaddah [74] | Stationary | Metal/gas | $Al_2O_3$ tube | 4:4 | External | Two-colour pyrometer | Gas quench |
| Sun [25, 26] | Stationary | Metal/gas | Silica tube | 2:6 | External | Two-colour pyrometer (+/- 15°C) | Gas quenched in Cu mould |
| Distin [64] | Stationary | Metal/gas | Pyrex cell | 3:4 | Internal | - | Water quench |
| Kaplan [50] | Stationary | Metal/gas | Silica tube | 2:5 (co-planar bottom 2 turns | External | Two-colour pyrometer (+/- 7°C) | In situ Gas (He) cooling |
| Widlund [53] | Stationary | Metal/gas | Silica tube | 1:3 (30° conical) | External | Two-colour pyrometer | In situ Gas (He) cooling |
| Roddis [38] | Free-fall (81cm) | Meta/gas | Perspex Cell/Pyrex drop tube | - | Internal | Two-colour pyrometer | Water quenched |

| | | | | | | | |
|---|---|---|---|---|---|---|---|
| Jahanshahi [49] | Stationary | Metal/gas | Silica tube | 2:5 (co-planar bottom 2 turns | External | Two-colour pyrometer (+/-5°C) | Gas quenched in Cu mould |
| Distin [78] | Stationary | Metal/slag | Pyrex tube | 2:7 (co-planar bottom 2 turns) | External | - | Gas (He) quenched in Cu lined Pyrex mould |
| See [70] | Free-fall | Metal/gas | Pyrex cell | 2:5 (co-planar bottom 2 turns) | Internal | Two-colour pyrometer (+/-5°C) | - |
| Caryll [69] | Stationary | Metal/slag | Silica tube | 2:5 (co-planar bottom 2 turns) | External | Two-colour pyrometer (+/-10°C) | Anvil quench |
| Burtsev [73] | Stationary | Metal/slag | - | 1:3 (30° conical) | Internal | Pyrometer | Cu mould/liquid nitrogen |
| Present study | Stationary and Free fall | Metal/slag/gas | Silica cell and tube | 1:4 (30° conical) | Internal | Two-colour pyrometer (+/-16°C) | Water quench |

## 2.7 Summary of Literature Review

A review of the literature concerning oxidation steelmaking reactions has been conducted. The majority of studies have focused on decarburisation reaction kinetics and have found rapid surface decarburisation to be the dominant oxidation reaction until a critical carbon level of approximately less than 1 wt.% was reached, at which point, subsurface decarburisation took place and surface oxides became evident. Whilst metalloids such as silicon and manganese were only found to react after the critical carbon level had been reached, dephosphorisation did not occur within the gas/metal reactions either by mass transfer into the oxide/slag or via formation of volatile phosphorus product. It was concluded by the majority of researchers that the rate determining step for decarburisation was gas phase mass transfer, as increases in gas flow rate and gas phase oxygen content were seen to increase the rate of decarburisation accordingly.

Through reviewing the various studies, scope for further work which could be developed within the proposed research were highlighted such as in depth investigation into the effect of experimental parameters on oxide growth and metal surface morphology as this is likely to affect potential slag composition and as already mentioned in the literature, affect oxygen behaviour at the metal surface. The studies fall short of conducting slag/metal/gas experiments which would provide information of droplet dephosphorisation behaviour which is highly important considering dephosphorisation is an interfacial reaction. Again this is an area of potential work necessary to quantitatively compliment the extensive studies of carbon and limited studies of silicon and manganese oxidation by levitation melting technique.

The use of modern advanced surface analysis techniques such as X-EDS and EPMA coupled with the just as effective methods of bulk composition analysis; ICP-MS and combustion analysis is an added advantage of the proposed study compared to that of literature, as the ability to compliment qualitative observations such as those witnessed by various researchers, with quantitative results, is possible through analysis tools such as point and line scans which were used to identify surface metal surface, oxide and slag composition.

Understandably, comparison of experimental results from individual studies conducted on separate apparatus limits the accuracy of interpretation. With this in mind, the

opportunity of conducting a series of levitation melting experiments on a single apparatus such as that designed for the current investigation could help to limit any apparatus-specific experimental bias when comparing results. Controlled error analysis has also been conducted for this study as displayed in Chapter 4 – Section 4.4.

While levitation melting technique offers the advantage of no crucible contamination, its main setback is temperature control, however, various studies that have applied this technique have used a combination of special coil designs, inert gas flow rate and power setting to control the temperature. Whilst evidently suitable for gas/metal study of single droplets, the technique has not been used for gas/metal/slag reactions in the limited literature found to adopt this technique for studying oxidation steelmaking reactions. Ability to do so holds promise for the potential of studying kinetics of slag/metal reactions such as dephosphorisation of HM metal droplet; representative of the proposed HM dephosphorisation pre-treatment process.

For this current body of work, levitation melting apparatus was designed to allow for both stationary and free fall experiments where slag making material could be added to form a metal/gas/slag reaction system. Whilst several design similarities was shared with other levitation apparatus designs sourced from literature, the present apparatus differentiates itself mainly through its dynamic and modular design, improved control of power and temperature through the use of modern steady state induction furnace generator compared to traditional valve generators. Furthermore, the increased efficiency of steady state generator meant that coils used in the present study consisted of fewer coil turnings in comparison to various other studies [49, 54, 69, 77] which adopted the Harris & Jenkins [77] coil design having argued that the design offered improved droplet stability.

With regards to introduction of slag making material into the setup, several methods were attempted, however all of these methods had their drawback as discussed in the present section. An underlying reason for the lack of slag/metal reaction was the limited contact time between the metal and slag making material. In BOS converter practice where reaction times are much longer (> 16 minutes), refining of the HM droplets is aided by constant recirculation of droplets between the bulk slag and the slag/metal emulsion and the creation of new reaction sites at the metal surface through mixing. Also, early formed FeO and $SiO_2$ further helps to flux the lime to achieve a high basicity early BOS slag.

Having selected a high basicity and lower liquidus slag making material compared to pure CaO to aid fluxing of the slag into the liquid surface oxide and hence promote slag/metal reaction, slag was applied to the HM by coating the solid sample with the selected slag material. The experimental results with respect to slag/metal reaction are discussed in Chapter 4 - Section 4.3.3.

Unexpectedly, the design and commissioning of the levitation melting apparatus proved time consuming, especially given the limited information found in the few literature that had conducted levitation melting studies. Significant amounts of time was spent identifying its limitations and even then, due to the nature of early experimental results and where the apparatus required modification and/or repairs, this also proved time consuming which consequentially restricted the volume of experiments carried out using the apparatus. Nevertheless, the results of the completed experiments are presented in Chapter 4.

# 3. Experimental Procedure

## 3.1 Apparatus

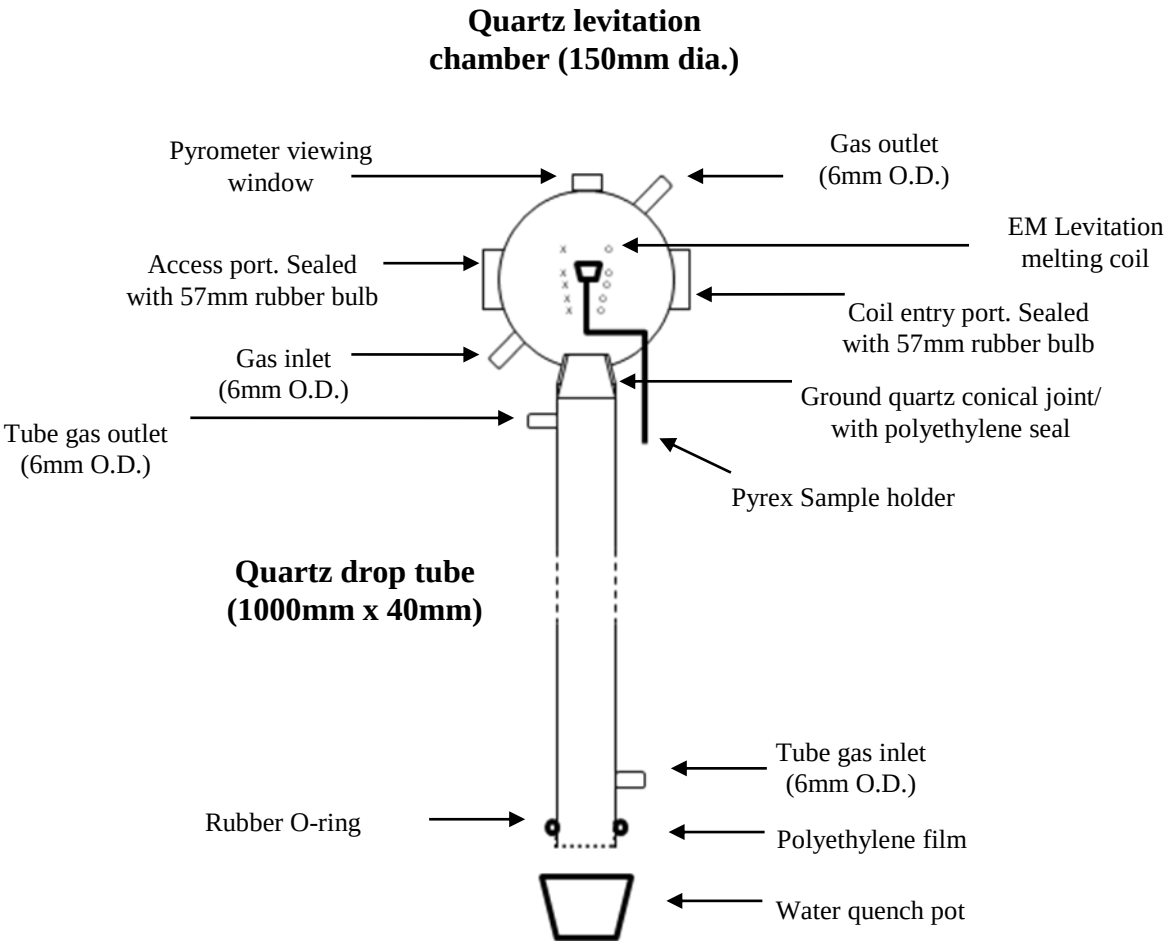


Figure 3: Schematic of experimental equipment

In order to perform the proposed set of levitation experiments, it was important to design and construct an apparatus fit for purpose; where clean, dry gases and slag making material could be introduced into the reaction chamber, a solid metal could be located, heated and melted within a suitably designed levitation coil, and liquid HM droplets could be rapidly cooled for subsequent chemical analysis. It was important that the apparatus was suitable for conducting both stationary and free-falling levitation experiments; whilst also allowing for in-situ gas cooling and water cooling of the liquid metal droplet sample. Following a review of various levitation studies [49-56, 62-72] and critically analysing their experimental arrangements in Chapter 2, it was possible to incorporate most of these key features into a design for the proposed investigation into kinetics of oxidation steelmaking reactions of HM droplets. Several components which made up the apparatus were externally manufactured and then assembled on site such as the coils and glassware which

make up the furnace. It was important to ensure ease of cleaning and maintenance of the apparatus components such as the glassware, and this was achieved by adopting a modular experimental unit design, where specific sections could be dismantled and reassembled easily and quickly when necessary. A schematic of the apparatus is shown in Figure 3.

### 3.1.1 Levitation-Melting (Induction) Furnace

#### 3.1.1.1 Electromagnetic Levitation Coil

A set of four levitation coils were designed and supplied by Ambrell Induction Heating Limited (UK); each of which allowed for the levitation of a range of metal sample weights. Although initial attempts to levitate samples using the two large coils proved unsuccessful, the two smaller coils were able to levitate metal samples ranging from 2g-10g. For stationary levitation reactions, the coils were only capable of holding metal samples up to 4g in weight during the reaction procedure. Consequently, the smaller coils were employed and except where stated, Coil 1 (Figure 4) was used throughout the experimental study.

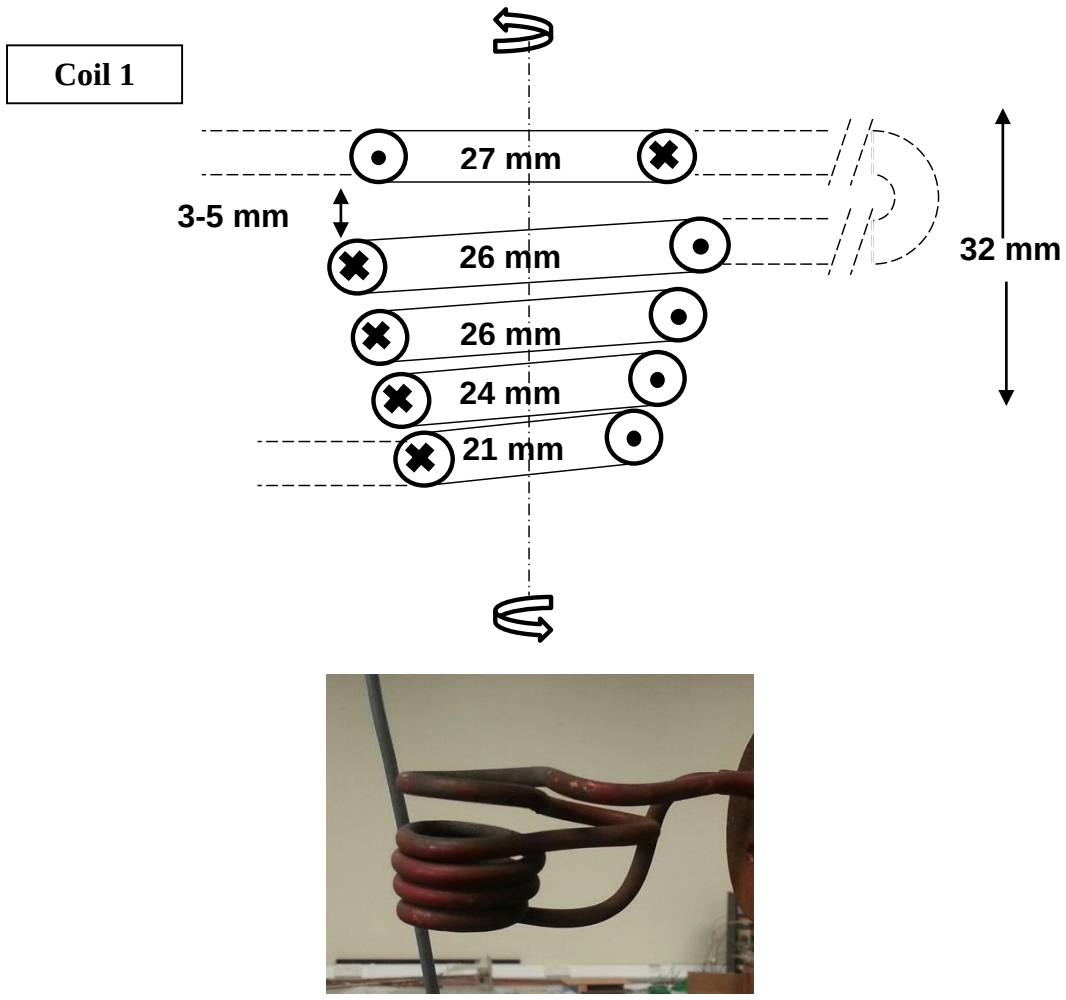


Figure 4: Schematic and photograph of EM levitation melting Coil 1

Coil 1 was designed as a conical shape featuring one upper turning and four reverse lower turnings, with a spacing of approximately 8mm between the top and bottom turnings (although this can be altered depending on the desired sample temperature). The water cooled copper tubing which made up the coils, had 4.9 mm outer diameter. At a height of 35 mm and internal diameter of 28 mm and 23 mm for the top turn and bottom turn of the coil respectively, the temperature of a solid HM droplet (initially at room temperature) could be raised to 1500°C within a few seconds with little levitation stability. In some cases, by further reducing the spacing between the top and bottom windings, temperatures greater than 1700°C could be achieved. Solid samples were introduced into the coil by gently lowering the sample holder (containing the sample), down through the coil. In some cases, a sample consisted of more than one piece of solid metal and for these instances; the individual pieces heated up and partially melted before joining together within the sample holder prior to levitation. This technique ensured improved droplet stability because the sample was already partially melted and therefore near spherically shaped before undergoing full levitation. To ensure that the droplet did no hit the copper tubing, the top turn was adjusted so that the magnetic field acted to centralise the sample in the coil. The coil was connected to a work-head by straight parallel copper tubing (6 mm O.D). The work-head was connected to a power supply unit (generator), and a water-chiller which controlled the cooling water temperature.

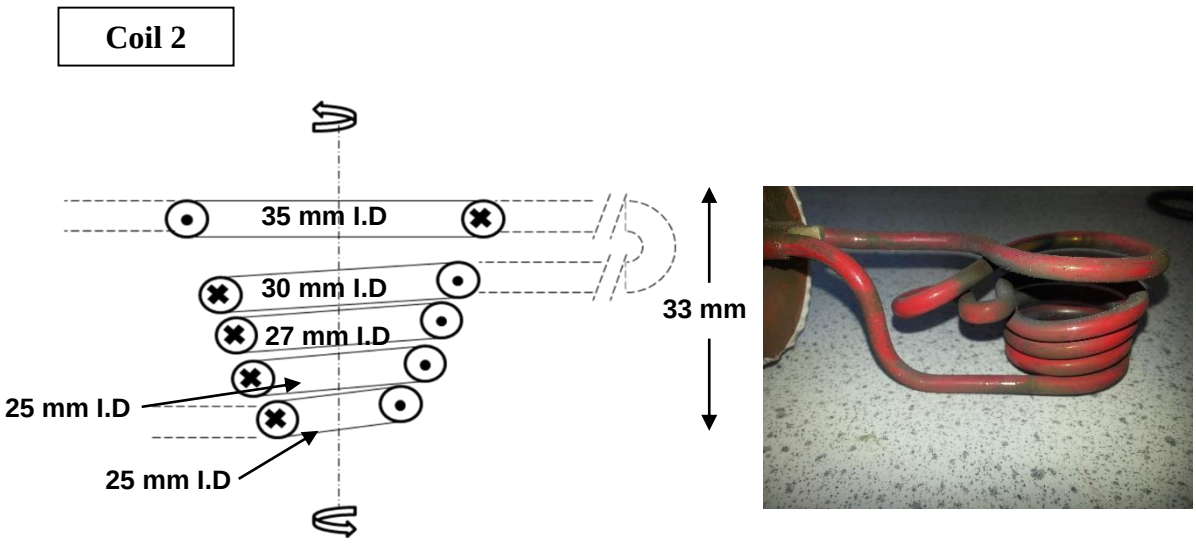


Figure 5: Schematic and photograph of EM levitation melting Coil 2

Coil 2 as shown in Figure 5 was also tested to determine the effect slight differences in design would have on the levitation and heating capabilities of the metal droplets. Whilst the number of top and bottom turnings was identical to Coil 1, the bottom turnings had a steeper angle from the bottom-upwards. Another distinct feature was that the top turning had a wider internal diameter than the top of the bottom turning. Therefore, if the spacing between the top and bottom turnings was the same as with Coil 1, upon levitating a sample there was less downwards force acting on the droplet, and at the same time a larger upward push exerted on the sample due to the higher concentrations of magnetic field generated within the steeper angled bottom turnings.

*Although the melting temperature of the HM samples was below 1200°C and HM temperature at the start of the BOS process is generally between 1200°C-1400°C, at such temperatures, with the coils available, droplet levitation stability could not be achieved. Attempts (discussed in Chapter 4 – Section 4.1.1) to achieve levitation stability and temperature control using a combination of power setting and inert cooling gas (Helium) identified 1600°C to be the lowest temperature suitable for the droplets and operation of coil design. Experiments were therefore conducted at this temperature whilst a new coil was being designed with the aim of improving droplet stability and temperature control according to literature [50, 54, 69, 77]. At such temperature (1600°C), whilst the study of dephosphorisation was perhaps hindered, reaction kinetics of other elements such as silicon, carbon and manganese formed a focus for the study as further shown in Chapter 4.*

Both Coil 1 and Coil 2 were able to achieve stable levitation melting at 1600°C. Whilst Coil 3 (Figure 6) and Coil 4 (Figure 7) were not used in the series of experiments (coils were too big to support levitation and melting of 2-4g droplets used in the study), the dimensions are given presented.

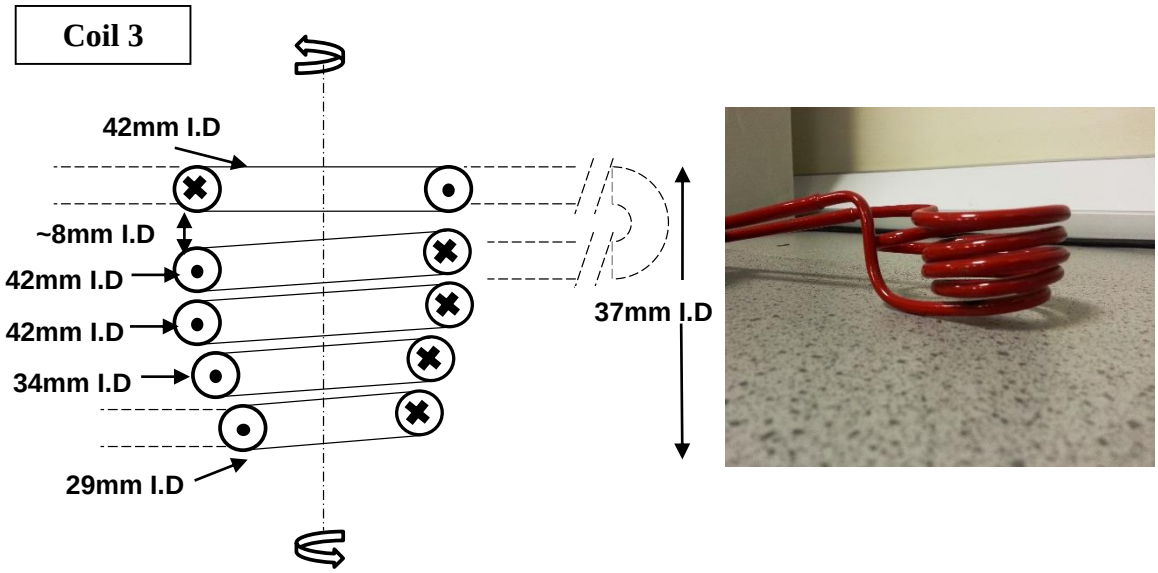


Figure 6: Schematic and image of EM levitation melting Coil 3

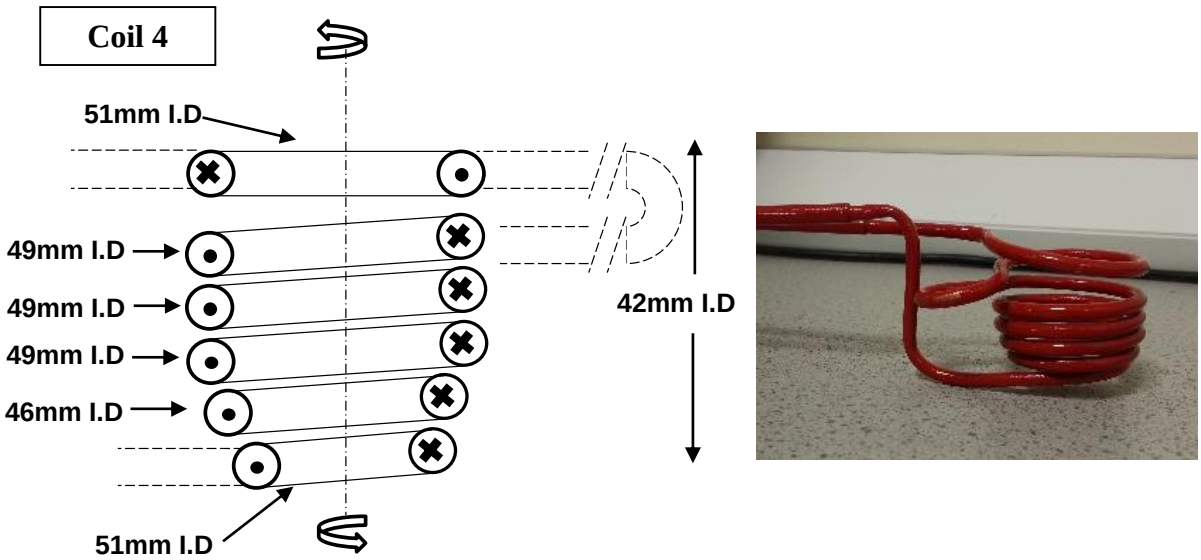


Figure 7: Schematic and photograph of EM levitation melting Coil 4

### 3.1.1.2 Melting (Levitation) Chamber and Reaction (drop) Tube

The levitation melting chamber and reaction tube were made of silica quartz primarily due to its low thermal expansion coefficient; making it less liable to crack when undergoing temperature changes. Ground silica quartz was used in parts which required a stronger and tougher surface such as gas inlets, outlets and joints. All glassware was manufactured by Yorlab (UK) and based on a design specification provided by the present

researcher. The spherically shaped levitation chamber as shown in Figure 8 was blown to an external diameter of 150mm. It featured the following:

- 6 mm O.D gas inlet and outlet at diagonally opposite ends
- 20 mm (diameter) pyrometer viewing window, centrally aligned with the centre of the levitation coil
- 2 x 60mm ports sealed with 57mm rubber bungs; one of which was used to feed the coil into the chamber
- Threaded port for manoeuvrable sample holder
- Female ground silica quartz conical joint to attach the drop tube to the bottom of the chamber

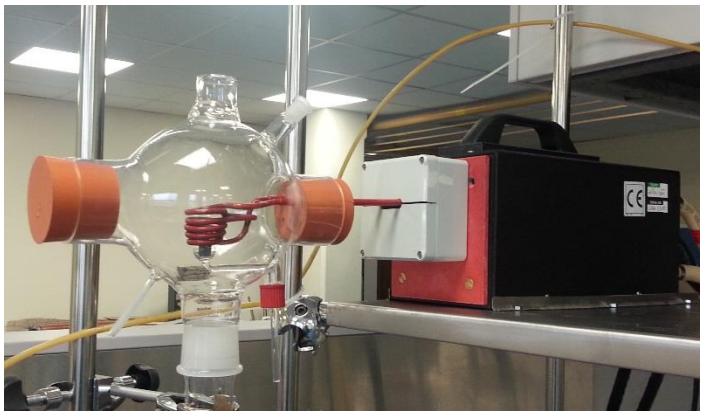

Figure 8: Quartz glass levitation chamber showing various ports for gas flow, coil entry and sample holder

The reaction (drop) tube (1000mm x 40mm) had male ground silica quartz tapered joint at one end, and a straight-through bottom at the other end. Gas inlet and outlet (6mm each) were further positioned towards the top and bottom of the tube, allowing for the separation and isolation of different gaseous atmospheres to that of the levitation chamber when necessary. Prestolok tube fittings (6mm I.D) were used to connect the gas lines to the inlets and outlets, creating a gas tight system. To create a gas tight reaction (drop) tube, polyethylene (cling) film was wrapped around the bottom of the tube and held in place by a silicon- greased rubber O-ring. The film was replaced after every experimental run because the film ruptured as molten metal droplet fell from the levitation melting chamber through the drop tube.

#### 3.1.1.3 Power Supply

Power was supplied to the levitation coil by an Ambrell EkoHeat 45kw/50-150kHz steady-state induction generator. Tap mode 10 (work-head transformer setting) was selected to ensure sufficient transfer of generated power into the sample for heating and levitation. By increasing the tap mode, the ratio of power transferred from the generator to the coils was reduced and therefore less external current was exerted from the coils to heat the droplet. When the tap mode was decreased, the ratio of power transferred from the generator to the coil (and hence the droplet) increased, thereby increasing the heating power to the droplet. A remote control was connected to the generator, allowing for remote operation of the power unit. A heating cycle could be started and ended using the remote control, whilst power input to the coils could also be controlled without the need to use the generator front panel. The levitation coil was connected to the work-head by 1/4" BSP knots. Copper olives (1/4") and high density PTFE tape were used to ensure water tight fitting.

#### 3.1.1.4 Water Chiller

A closed system water chiller (make: Kelvin, Model: KRA150A62651, 400V/50Hz, temperature range 0-45°C, fluid pressure 4.4-5.9 bar) connected to the work-head via the generator, cooled the levitation coil during heating operation. With a refillable tank of de-ionised water (~10L), water temperatures were maintained between 19°C and 23°C. Reinforced water pipes were fitted with jubilee clips at the inlets and outlets of the water chiller, generator and work-head, allowing for unrestricted flow of refrigerated water to the coils and warm water away from the coils and back into the chiller to be cooled. Both the water chiller and generator (Figure 9) were wired to separate power isolation switches to ensure safe deactivation of the units.

Figure 9: Induction furnace generator and water chiller for levitation induction furnace

### 3.1.1.5 Gas flow valves

Magnetic (solenoid) valves with an operating range of 0-16 bar were connected to the oxygen and helium gas line. Opening and closing procedure of the valves was controlled through LabVIEW programming software, having wired the valves to a 24Vdc power supply and an 8-channel 24Volt (direct current) National Instruments data logger. Alicat Scientific (model: MC Series 0-10SLPM) mass flow controller was also connected to the oxygen gas line to measure and moderate the set point oxygen flow rate into the levitation unit. The device comprised a 240V pin power jack, and an RS-232 input signal port which allowed for remote control of the device via a standard PC. A rapid response time (100ms) ensured quick changes in gaseous atmosphere during the levitation experiments, with a flow rate measurement accuracy of +/- 0.8% of the measured value, plus +/-0.2% of full scale (10SLPM) value. A gas filter was also integrated into the device to prevent build up and clogging of the inlet, whilst gas lines were secured onto the inlet and outlet ports using 6mm Prestolok fittings. Gas pressure, temperature and flow rates (0-10 SPLM range) were measured and displayed either on the device or on the PC. Although remote control of the device was achieved, remote logging of data on the PC was not, and therefore the device was fully controlled from the front panel.

### 3.1.1.6 Temperature

An Impac digital two-colour Pyrometer (Figure 10) was used to measure droplet temperature with an accuracy of +/-0.5% of the measured value for temperatures below 1500°C, and +/-1% of measuring value for temperatures above 1500°C. The two

wavelengths used were 0.9µm -1.05µm and the temperature range of the pyrometer was 700°C – 1800°C. The pyrometer was calibrated by the manufacturer and measured temperatures correlated well with the proposed HM liquidus temperatures calculated through MTData thermodynamic model. Temperature data was recorded every second on a compatible data logging software installed onto a standard PC. The pyrometer was securely clamped within the recommended distance from the hot-source in accordance with the instruction manual; 500mm - 1000mm. Sample temperatures were monitored through the pyrometer window located on top the levitation chamber and measured temperature was logged by the pyrometer software (Impac Infra-win software).

Figure 10: Two-colour pyrometer positioned above levitation chamber and in-line with the middle of the levitation coil

### 3.1.1.7 Computer Software

Several software programs were used during the experiments, primarily to record data and control operational parameters. Ambrell E-view software (Version 2.11) was used to capture data relating to the parameters controlled by the generator such as voltage, frequency and match percentage. The data was automatically saved in the form of plots and tabulated data (.csv format). The data was then extracted from the software into excel for data analysis if and when required. Impac Infra-win software was used to record droplet temperatures detected by the two-colour pyrometer (INFRATHERM ISQ 5). Results were displayed in the form of line graphs and tables which were saved automatically as ".txt" files. LabVIEW programming and data acquisition software was further used to control the opening and closing procedure of the magnetic valves.

### 3.1.2 Vertical Tube Furnace Layout

Figure 11 shows a detailed layout of the Isoheat vertical tube furnace. The furnace was heated by lanthanum chromite heating elements which surrounded an alumina work tube (O.D = 82mm, I.D = 72mm, Height = 1000mm). Both ends of the work tube were sealed with water-cooled stainless steel caps with O-rings installed within the caps to create a gas tight seal with the tube ends. The top cap featured a central hole (I.D = 30mm) with a slide gate allowing for input of components such as thermocouple, material feeder tube or gas bubbler line.

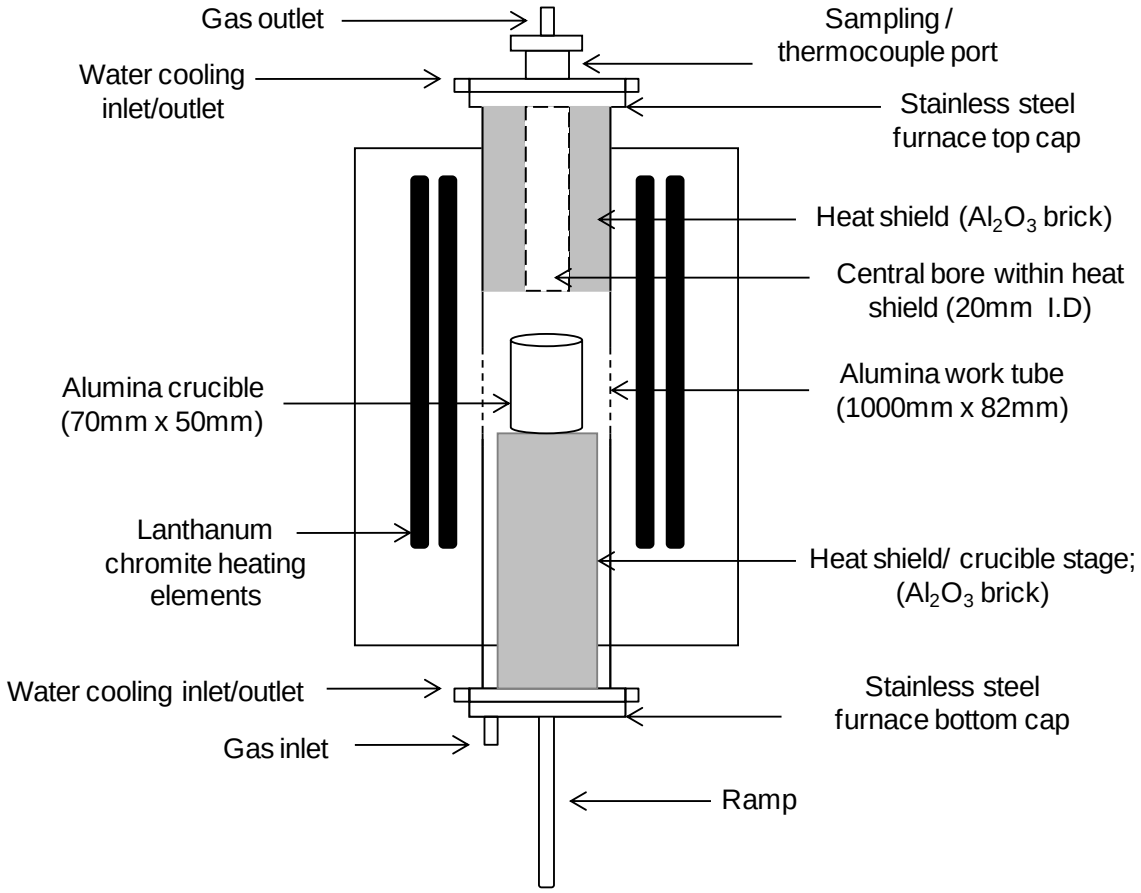


Figure 11: Schematic of Isoheat Vertical Tube furnace

The crucible (recrystallised alumina or magnesia crucible) containing metal or slag was placed in the work tube by positioning the crucible on the alumina platform directly below the furnace tube, and then slowly pushing the alumina platform upwards with a ramp to locate the crucible within the furnace hot zone (Figure 12) which had been determined in an earlier calibration study. The bottom end of the work tube was sealed with water cooled stainless steel cap prior to flushing it with Ar for approximately 1 hour in order to displace any air within the reaction zone. The central hole in the top cap was fitted with a gas

bubbler containing dibuthylphthalate to indicate inert gas flow through the work tube. Depending on experimental requirement, the furnace was programmed to undergo set heating and cooling profiles such as that given in Table 8. Temperature control was achieved using a EUROTHERM controller as shown in Figure 13.

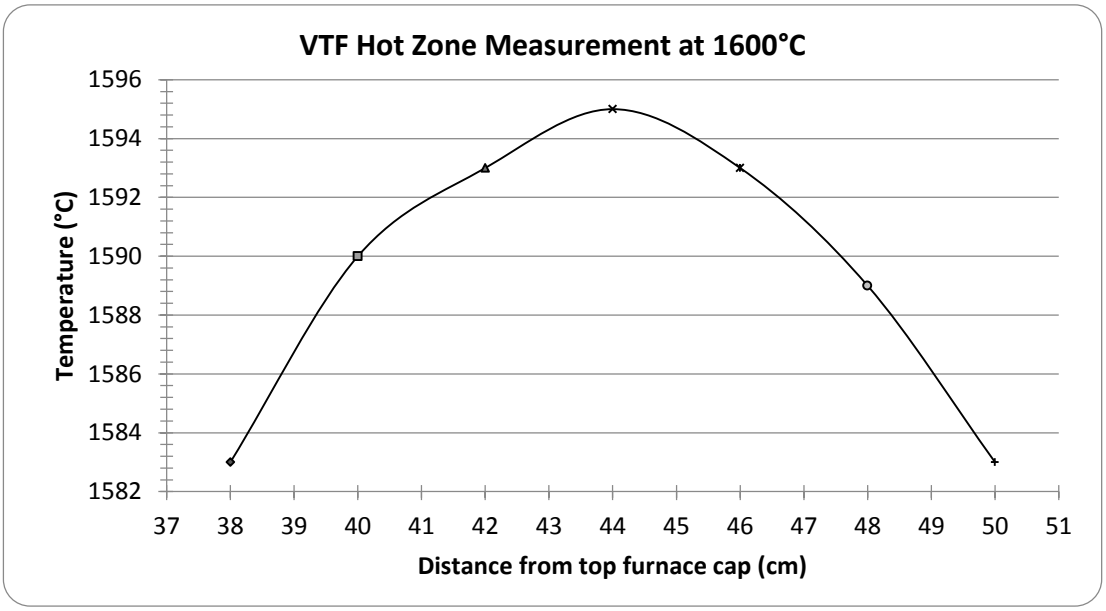


Figure 12: Measured temperature inside vertical tube furnace held at 1600°C. Type R thermocouple was used to measure temperature.

Figure 13: Isoheat Vertical tube furnace and Eurotherm controller

When the set temperature had been reached, the gas bubbler line was removed from the gas outlet, and a Type-R thermocouple (87% Pt/ 13%Rh/Pt) shrouded with recrystallised alumina sheath was introduced into the work tube via the central port in the top cap; the thermocouple was located close to the crucible for temperature measurements. Once the temperature had been confirmed, the thermocouple was slowly removed and the cap refitted with the gas bubbler. The furnace temperature was then left to equilibrate again before sampling the metal, making alloy additions or allowing the programme to dwell or ramp down in accordance with the set heating/cooling programme for material preparation. Considering that alumina is most susceptible to thermal shock within the temperature range of approximately 500-1000°C (due to phase transformation between its delta, theta and alpha phases; the latter the most temperature stable phase), a slower temperature ramp-up rate was used to prevent damage to the work tube; after which, a high furnace temperature ramp rate of 450°C per hour was used.

Table 8: Example of furnace heat/cooling programme

| **Programme** | **Ramp rate (°C/hour)** | **Target temperature (°C)** | **Dwell time (hour)** |
|---|---|---|---|
| 1 | 300 | 500 | 0 |
| 2 | 250 | 950 | 0 |
| 3 | 450 | 1610 | 2 or 'Hold' |
| 4 | 550 | 950 | 0 |
| 5 | 250 | 25 | 0 |

## 3.2 Materials and Preparation

### 3.2.1 Metal

#### 3.2.1.1 Hot-Metal

Desulphurised HM lollipop samples were sourced from Tata Steel Desulphurisation Plant, Scunthorpe, UK. Melting and casting graphite crucibles were sourced from Almath Crucibles Limited, UK. Desulphurised carbon saturated (>4wt% C) metal had phosphorus levels between 0.08-0.1 wt.%, 0.31-0.36 wt.% silicon, 0.36 wt.% manganese and 0.009 wt.% Sulphur. The lollipop samples were melted (100kw, 30kg capacity Radyne Induction Furnace) in a graphite crucible (I.D = 50m, O.D = 70mm and Height = 120mm) and stirred with a silica quartz rod to ensure homogeneity of melt. The HM was then poured into drilled holes (100mm x 10mm) in a cylindrical graphite block (120mm x

80mm) as shown in Figure 14, and then left to air cool to form cylindrical rods. After removing the rods from the graphite mould, they were then sectioned into cylindrical samples of up to 10g weight approximately, using a wheel saw cutter before being crushed into smaller weight (<2g) samples by single ball mill and mallet.

Figure 14: Pilot plant 30kg induction furnace used to melt HM lollipop samples and the graphite mould which the melt is poured and casted into.

### 3.2.2 Slag

#### 3.2.2.1 Pre-fused Slag

Synthetic slag was prepared by initially drying the reagent grade oxide component (CaO, $SiO_2$ and MgO) contained in individual alumina crucibles (O.D = 35mm, Height = 80mm), in a Carbolite chamber furnace at 950°C for 2 hours with a temperature ramp rate of 100°C/minute. The reagent grade $Fe_2O_3$ was also dried by undergoing the same drying out procedure but at 120°C for 2 hours. Properties of the reagent grades are listed in Table 9.

Table 9: Properties of slag making materials

| Material | Purity (Wt. %) | Size (mesh) | Source |
|---|---|---|---|
| CaO | 99.5 | - | Alfa Aesar (VWR) |
| $SiO_2$ | 99.5 | < 400 | Alfa Aesar (VWR) |
| MgO | 96 | < 325 | Alfa Aesar (VWR) |
| $Fe_2O_3$ | 97 | - | BDH |

Predetermined weights of the dried reagents were then thoroughly mixed together in a recrystallised magnesia crucible before being introduced into the Isoheat vertical tube furnace. The furnace was purged for an hour under Ar (200ml/min) and the material heated to 1600°C. To ensure chemical homogeneity, a magnesia rod was used to stir the slag before leaving it to cool overnight under Ar. Once the cooled slag had been separated from the crucible, it was crushed to fines in a Tema mill, rendering the material ready for experimental use.

XRF was used to determine the final synthetic slag composition (see Table 10) as it was expected that not all the $Fe_2O_3$ would reduce to form FeO given that the partial pressure of oxygen in argon used for slag preparation was $10^{-6}$ atm compared to the required value of $10^{-9}$ atm for complete conversion, whilst at the same time, MgO from the crucible walls may further dissolve into the slag. For both alloy and slag preparation, the tube furnace was equipped with a Type-R (87% platinum/rhodium, 13% platinum ) thermocouple for temperature measurement, and a gas bubbler as an indicator of inert gas flow through the otherwise sealed furnace.

Table 10: Composition of synthetic basic slag used to carry out slag/metal experiments within the present study

| Material | Concentration (wt.%) |
|---|---|
| CaO | 20.8 |
| $SiO_2$ | 13.1 |
| MgO | 11.2 |
| FeO | 51.3 |
| Residual oxides ($Al_2O_3$, $P_2O_5$) | 0.44 |

Based on the final slag composition determined through XRF, the aim basicity of around 1.5 was achieved ($CaO/SiO_2$ = 1.58). However, MgO slag content increased by 3.2wt.% over the 8wt.% initially added to the mix to prevent crucible erosion. Residual oxides of aluminium (0.31wt.%) and phosphorus (0.13 wt.%) were also detected. The extra MgO, $P_2O_5$ and $Al_2O_3$ came from the industrial Singleton Birch lime (commonly used in plant based BOS practice) used in the experiments. This presence of these oxides is evident in Table 11 which shows the measured (XRF) lime composition. This form of lime was chosen to be used over reagent grade lime to make it more representative of the proposed HM dephosphorisation process where such lime will be employed.

XRF results gave a total Fe wt.% of 39.9 wt.% within the analysed slag, and it was assumed that the $Fe_2O_3$ introduced into the slag had been reduced to form FeO during the pre-fusing procedure. Therefore, based on Equation 27, the reported total Fe wt.% was converted to FeO equivalent as shown below.

$$Fe_2O_3 \rightarrow 2FeO + \frac{1}{2}O_2 \qquad (27)$$

$$\left(\frac{55.8+16}{55.8}\right)x39.9 = 51.3wt.\%$$

### 3.2.2.2 Lime

BOS standard grade lime (< 70μm) was sourced from Singleton Birch, UK. In experiments where only CaO was used, it was used as delivered having been kept completely fresh and isolated from reactive atmosphere. Precautions taken to ensure the quality of lime was maintained included double sealing during storage, storage of lime in a dry and sealed environment and placing lime in a silica gel filled desiccator prior to experimental use. The composition of the Singleton Birch lime is listed in Table 11.

Table 11: XRF results of Singleton Birch CaO composition

| Components | Concentration (Wt. %) |
|---|---|
| CaO | 97.6 |
| $SiO_2$ | 1.7 |
| $Al_2O_3$ | 0.35 |
| MgO | 0.32 |
| $P_2O_5$ | 0.09 |

### 3.2.3 Gases and Gas Purification Reagents

High purity (>99.999%) argon, helium and oxygen gases were sourced from Air Products and BOC gases. The properties of these gases are detailed in Table 12. Oxygen bearing gases were fed through dehydrating agents; Silica beads (2-5mm) and Magnesium Perchlorate Hydrate to absorb moisture from the gases before entering the levitation melting chamber and drop tube. The gas purification reagents were packed in separate columns of a Pyrex glass purification unit which comprised 6mm O.D. inlet and outlet. Gas lines were connected to the inlet/outlet by 6mm Prestolock tube fittings and the columns were sealed with 20mm rubber bungs to ensure no entrainment of moisture or oxygen from the atmosphere, silicon grease also applied to ensure an air tight seal.

Higher purity (>99.9999%) argon gas was sourced from BOC gases (UK), and used for slag preparation in the Isoheat furnace. As illustrated in the Ellingham diagram for oxides (Figure 15), for the complete conversion of $Fe_2O_3$ to FeO at 1600°C, oxygen partial pressure lower than $10^{-9}$ atm was required. However such levels could not be achieved and the highest purity argon available was $10^{-6}$atm, therefore it was assumed that some $Fe_2O_3$ still existed in the prepared slag material.

Table 12: Properties of gases

| | | | Composition (ppm) | | | | | |
|---|---|---|---|---|---|---|---|---|
| **Gas** | **Source** | **Purity (%)** | **$O_2$** | **$H_2O$** | **TFC** | **$N_2$** | **$CO/CO_2$** | **$N_2$** |
| Helium | Air Products | >99.999 | <1 | <2 | <0.5 | <5 | - | - |
| Argon | Air products | >99.999 | <1.5 | <2 | <0.1 | <4 | - | - |
| Argon | BOC gases | >99.9999 | Total impurities <1vpm (H20, N2, O2) | | | | | |
| Oxygen | Air Products | >99.999 | - | <1 | - | <5 | <0.5 | <0.5 |

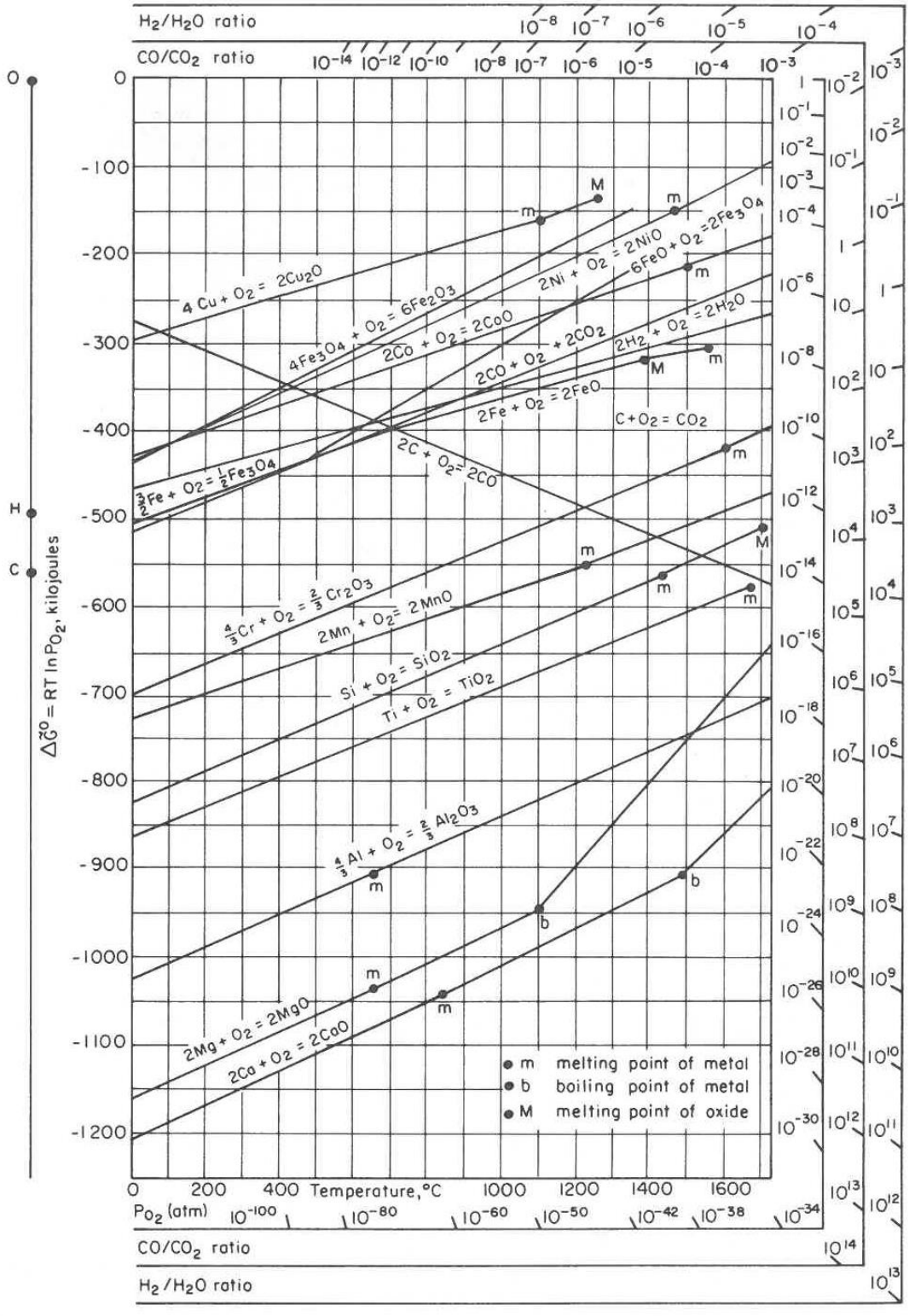


Figure 15: Oxides Ellingham diagram [81]

### 3.3 Procedure

### 3.3.1 Levitation Melting

#### 3.3.1.1 Assembly of Levitation Melting Unit

The apparatus was designed to aid easy assembly, disassembly and maintenance of the glassware. The sample cup/rod was attached onto the levitation chamber by a threaded plastic cap and permitted vertical and rotational movement of the rod within it. A 57mm rubber bung initially sectioned into two halves and with 8mm grooves to accommodate the 2 x 6mm O.D. coil leads, were fitted onto the coil leads and stuck together using super glue. The bung with the coil protruding at one end and the lead at the other was then wedged into one of the side ports on the levitation chamber as seen in Figure 8. The second side port was sealed by using a solid 57mm rubber bung (this was the port used to introduce the solid HM sample onto the sample holder); silicon grease was further applied between the bung/glass seal to ensure a gas tight seal. The levitation melting chamber was joined to the 1000mm x 40mm reaction tube by fitting the ground conical shaped female end of the chamber to the ground conical shaped male end of the reaction tube and Polyethylene (cling) film separated the atmosphere between the two units in order to prevent mixing of gases between both sections. Polyethylene film was further used to seal the bottom of the reaction tube and was held in place by rubber O-ring.

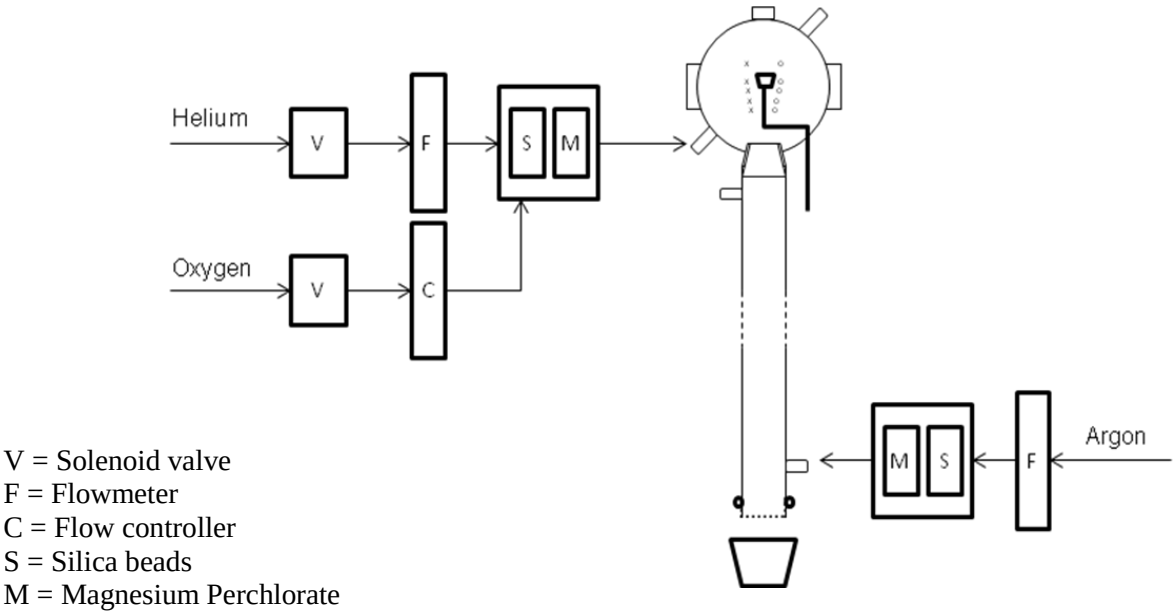


Figure 16: Schematic of gas flow within the levitation melting apparatus

PVC (6.35mm O.D) gas lines were fitted onto 6mm inlets and outlets of the levitation chamber, reaction tube, and purification glassware using 6mm tube fittings. Figure 16 illustrates the gas flow route during a typical experiment. High purity argon, helium and oxygen gases were sourced from separate gas cylinders which were fitted with 0-10 bar multi-stage gas regulators. Argon was fed into a separate purification unit, and, helium and oxygen were mixed whilst purified in a different purification unit. Both set of purification units contained silica gel and magnesium perchlorate to remove moisture from the gases, and 0-10SPLM flow meters were positioned on each gas line between the purification units and the levitation unit. The free-fall and stationary levitation techniques required different gas delivery regimes as highlighted in the operational experimental procedure in the following sections. Also gas tubes, fittings, regulator and mass flow controller on the oxygen gas line were degreased before experimental use.

#### 3.3.1.2 Free Falling Levitation Melting Procedure

For gas/metal/slag experiments, 2g of lime/synthetic slag was wrapped in polyethylene film and placed in the sample holder before assembling the levitation unit. Once assembled, 2g metal (HM or Fe-alloy) was charged into the levitation chamber via side ports using a tong. The side port was then sealed with a 57mm rubber bung. To completely seal of the atmosphere in the levitation chamber from the reaction drop tube, polyethylene film was wedged between the male and female conical joints of both components. Both the levitation chamber and the reaction drop tube were then purged for 3 minutes with their respective gases; argon (3 LPM) in the levitation chamber and $He/O_2$ (2LPM) mix in the reaction drop tube, to displace any oxygen in the system. Having activated the generator and achieved the droplet target temperature (1600°C), the sample holder was then lifted upwards to bring the lime or slag into contact with the bottom surface of the molten droplet, and was then withdrawn having deposited the slag making material on the droplet's surface. The droplet was left to stabilise at the target temperature again before then de-energising the generator and hence the levitation coil, resulting in the lime or slag containing droplet falling down the 1000mm length reaction drop tube and reacting with the oxygen rich (10% - 30% $O_2$) environment before being quenched in a water pot directly underneath the reaction drop tube. Gas/metal reactions were conducted in the same manner but without the presence of lime/slag material.

A single reaction drop tube (Height = 1000mm) was used for all free fall reactions and each sample weighed 2g +/- 0.2g. The time it took a single droplet to fall down the full

length of the tube and hence the droplet reaction time, was measured using a digital camera at 25 frames per second. During a fall procedure, the droplet was captured on 8 of the 25 frames within a second, therefore the drop time and reaction time was calculated to be approximately 0.32 seconds in an upward gas flow rate of 2LPM.

#### 3.3.1.3 Stationary Levitation Melting Procedure

The procedure was similar to the free falling procedure, but with a few distinct differences. The levitation chamber was purged with helium (as it forms part of the reaction gas) and the drop tube was purged with argon (3 LPM). Having achieved target temperature (1600°C), for metal/gas/slag experiments, the slag making material was deposited on the droplet's surface by the sample holder and then the droplet was allowed to recover its target temperature. Once at temperature, oxygen was introduced into the levitation chamber. The generator was then de-energised when a predetermined reaction time (0 - 60 seconds) had been reached. The droplet fell out of the levitation coil and through the drop tube containing an inert atmosphere before being quenched in the water pot directly below the drop tube. As with the free fall technique, oxygen levels within the $He/O_2$ mix ranged from 10% to 30%. However, for stationary levitation technique, as well as diluting the oxygen, helium also acted as a coolant. The amount of He used in the levitation chamber was therefore governed by the temperature of the droplet whilst the amount of $O_2$ was dictated by the helium quantity, although at all times the $He/O_2$ volume ratio was maintained.

#### 3.3.1.4 Slag Application Procedure

Application of CaO using the technique described above proved to be ineffective getting sufficient amount of material onto the surface of the molten droplet. This might be expected due to the high liquidus temperature of CaO and low wettability of the reagent as discussed by Watkins [57]. In subsequent experiments where synthetic slag material was used, the solid metal was initially coated with the slag material before commencing the experimental run. The sample was lightly dressed in PVA glue which behaved as a sticking agent for the slag powder that coated the solid HM surface. The metal/slag assembly was then stored in a desiccator to dry before experimental use. Through this technique, the entire surface of the metal was in contact with slag; and considering the slag had a low liquidus temperature (1500°), primarily due to its high FeO content, slag/metal interaction was promoted as detailed in Chapter 4.

### 3.4 Chemical Analysis

#### 3.4.1 Metal - Bulk Analysis

##### 3.4.1.1 Combustion Analyser (Eltra Elemental Analyser CS-800)

Metal carbon content was analysed using an Eltra elemental analyser (Model: CS-800), where the reacted sample was combusted in a ceramic crucible within an induction furnace. The resulting reaction gas $CO_2$ was then measured by solid-state IR detectors. The reacted sample was crushed into chips using a manual ball mill. 0.5g of the sample mixed with tungsten chips was weighed in a crucible before placing the crucible in the furnace to undergo carbon analysis. Analysis time ranged between 40-50seconds for optimum results, with the results displayed on the computer screen afterwards. Calibration of the high frequency furnace was done to calibration standard ZRM 478. For high carbon metals (0.1 wt.%-12wt.%) such as those of this study, measurement sensitivity was 0.1ppm carbon with an accuracy of +/-10ppm C (or +/- 0.5wt.% carbon).

##### 3.4.1.2 Inductively Coupled Plasma - Mass Spectrometry (ICP-MS)

Analysis of metal silicon, manganese and phosphorus was carried out by ICP-MS (Instrument: Thermo iCAP 6500 ICP). The sample was dissolved in a mixture of hydrochloric and nitric acids and diluted to a fixed volume before being analysed by ICP-MS technique. 1g (+/-0.01g) of the chipped reacted sample was weighed into a 250ml PTFE beaker and the weight recorded. 70ml of solvent acid derived from a mixture of 350ml demineralised water: 300ml nitric acid: 150ml hydrochloric acid (cooled and diluted to 1 litre with demineralised water) was then added to the beaker and the sample left to dissolve for a minimum of 2 hours. Once the dissolved mixture had cooled, it was transferred to a 200ml volumetric flask and diluted to 200ml with demineralised water. After mixing the diluted solution, it was then filtered through Whatman 540 paper to separate the non-dissolved solutes. Analysis of the samples was then carried out according to the procedure given in the ICP-MS operation instructions using calibrated programmes on the analysis instrument. Detection limits for Mn, P, Si was 0.05ppm, 0.5ppm and 0.5ppm respectively; all with a measurement sensitivity of <1ppb.

#### 3.4.2 Metal - Surface Analysis

##### 3.4.2.1 Energy Dispersive X-ray spectroscopy (X-EDS)

X-EDS (Backscattered mode) was used to analyse composition distribution at the metal cross section, and more specifically, the edges of the metal cross section consisting of oxide and slag. Quenched droplets were sectioned and mounted in non-conductive

Bakelite, ensuring that the cross sectional interface was exposed. Each sample was ground (80 grit and 220 grit), and polished (15μm and 3μm) using an electronic multi-mount grinder/polisher. Grinding was done using silicon carbide discs and polishing was done using diamond paste distributed on polish discs. Each stage of grinding and polishing lasted 5 minutes whilst the samples were manually cleaned with water, acetone and cotton wool (in order to prevent contamination of the grinding paper or polish disc pads) and then air dried by a dryer; before progressing to the next stage. The mounted sample was placed on a platform inside the SEM/X-EDS (Quanta 650 FEG SEM) chamber and once the chamber was sealed, it was put under vacuum. The sample was raised 10mm below the detector; a suitable distance for fast analysis and accurate results. Aztech Feature Software, compatible with the X-EDS machine was then used to conduct the point and line analysis, as well as process the resultant data.

#### 3.4.2.2 Electron Probe Micro Analyser (EPMA)

EPMA was used to map the concentration of elements (e.g. phosphorus, silicon, manganese, iron, calcium) across the metal cross section area. Gallium phosphide was used as a standard for phosphorus predominantly because of its high phosphorus content and high level of stability. Pure silicon, manganese and iron were also used as standards for detecting their respective elements.

### 3.4.3 Slag/Lime

#### 3.4.3.1 X-ray Fluorescence (XRF)

Lime powder and synthetic slag was analysed by XRF technique to determine the initial compositions. The material was heated in a Carbolite electric oven at 200°C to drive off moisture and carbon. 6g of lithium based flux (49.75% Lithium Tetraborate, 49.75% Lithium Metaborate and 0.50% Lithium Bromide) was placed into a platinum/gold crucible and mixed at a 10:1 ratio with 0.6g of lime powder. The powders were thoroughly mixed and then loaded into an electric fusion machine (Model: Katanox K1 Prime). The mixture underwent a heating and cooling cycle where it was heated to 1000°C at a rate of 100°C/minute before being held at that temperature for 5 minutes whilst being rocked back and forth to aid mixture of the molten material. After further heating to 1050°C at a lower rate of 25°C/minute, the material was then held for a further 1minute at 1050°C. The molten material was then automatically poured into a preheated platinum mould and subjected to initial air cooling (1 minute) and then eventual forced convection cooling by an embedded fan for 5 minutes; forming a fused bead suitable for XRF analysis. The bead

was loaded into the sample holder in the XRF machine (Model: Thermo Scientific ARL PERFORM'X Sequential 2.5kW XRF Spectrometer), after which, the chamber was put under vacuum and sample ionised with x-rays. Fluorescent x-rays were then analysed and intensities compared against calibration intensity profiles from certified reference material prepared under the same conditions as the experimental samples. The average composition (converted from intensity values) was calculated from a set of 3 identical scans via the XRF OXSAS software.

Table 13: Error of analysis

| **Area of analysis** | **Equipment** | **Analysis element / oxides** | **Error (+/- wt. %)** |
|---|---|---|---|
| **Metal bulk** | Combustion analysis | C | 0.1 |
| | ICP-MS | Si, Mn, P | 0.03, 0.03, 0.01 |
| **Metal surface** | EPMA | Si, Mn, P, Fe | 0.007 |
| | X-EDS | Fe, Si, Mn, P and $O_2$ | 0.1 |

The errors of analysis are given in Table 13. Although ICP-MS was capable of measuring bulk oxygen concentrations of the bulk metal sample, the set-up of the analysis equipment restricted its use as specific sample dimensions were needed to carry out the analysis. The samples needed to be rod shaped and of 4mm maximum diameter. Considering that there was no control over the quenched sample's final shape, this method of analysis could not be used. Although bulk oxygen content of the metals were not obtained by the analysis techniques used in the investigations, knowledge can be drawn from the reviewed literature to complement the experimental results present. Also, surface analysis technique (namely X-EDS maps) also provided a somewhat qualitative indication of oxygen concentration across the metal cross section, but more so at the droplet surface as shown in Chapter 4.

# 4. Results and Discussion

## 4.1 Apparatus Design

### 4.1.1 Design Considerations

A significant period of time within this study was dedicated to designing a suitable apparatus able to investigate the premise of the work detailed in Chapter 1. As part of the design stage, a literature review of methods used to investigate the oxidation reaction of iron alloy droplets was conducted.

Considering that the basis of HM dephosphorisation pre-treatment process (Figure 17) stemmed from Spray Steelmaking; a proposed continuous steelmaking concept founded by British Steel, and that levitation melting techniques proved successful in investigating gas metal reactions of carbon saturated iron alloy droplets, provided strong encouragement to tailor the technique for dephosphorisation studies and aiming to simulate the metal droplet behaviour in the proposed dephosphorisation pre-treatment process. The stages of apparatus design are detailed and discussed below.

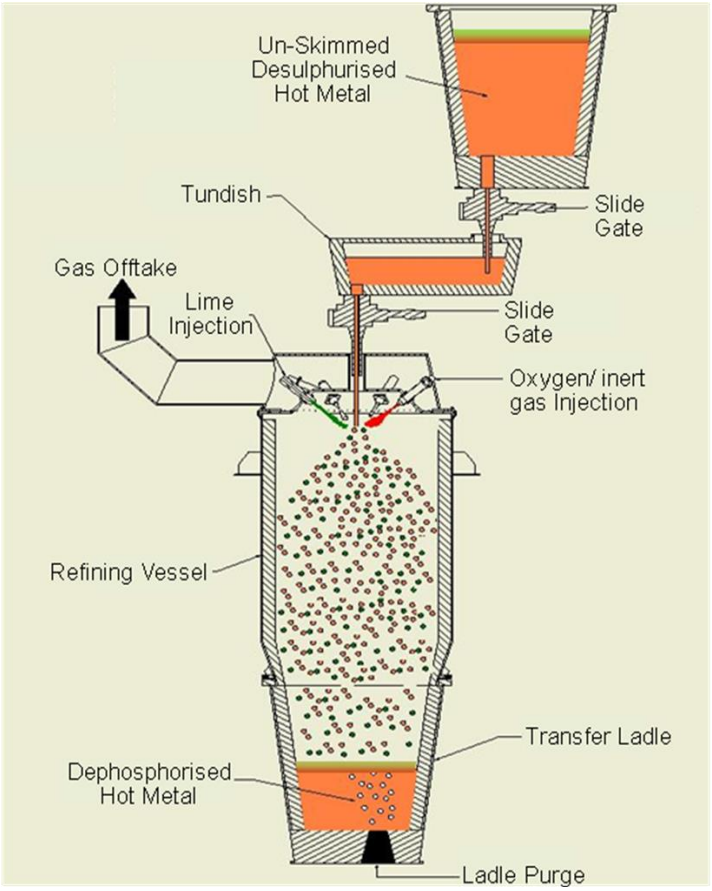


Figure 17: HM dephosphorisation pre-treatment reaction vessel [14]

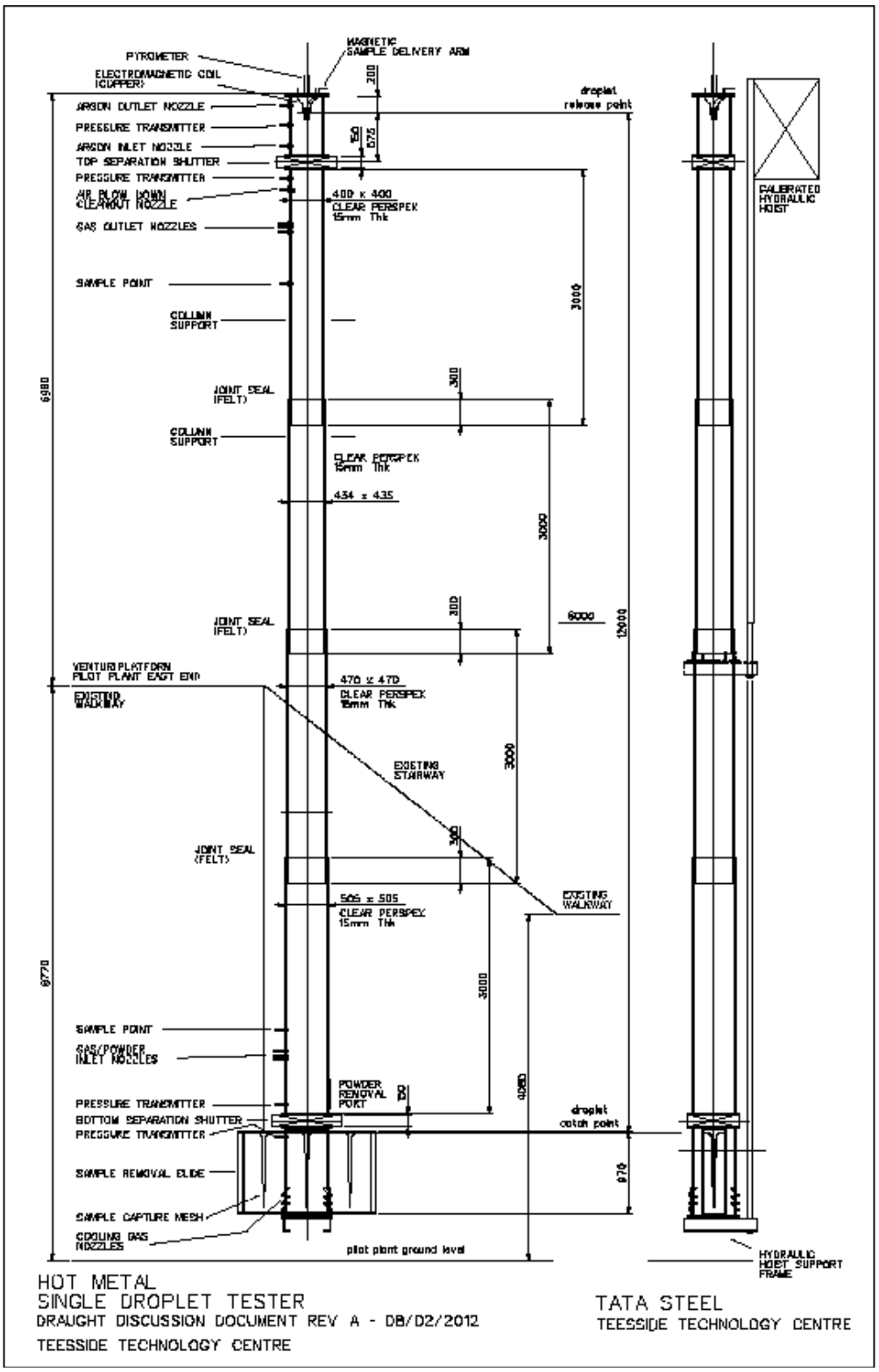


Figure 18: 1st pilot scale single droplet apparatus design

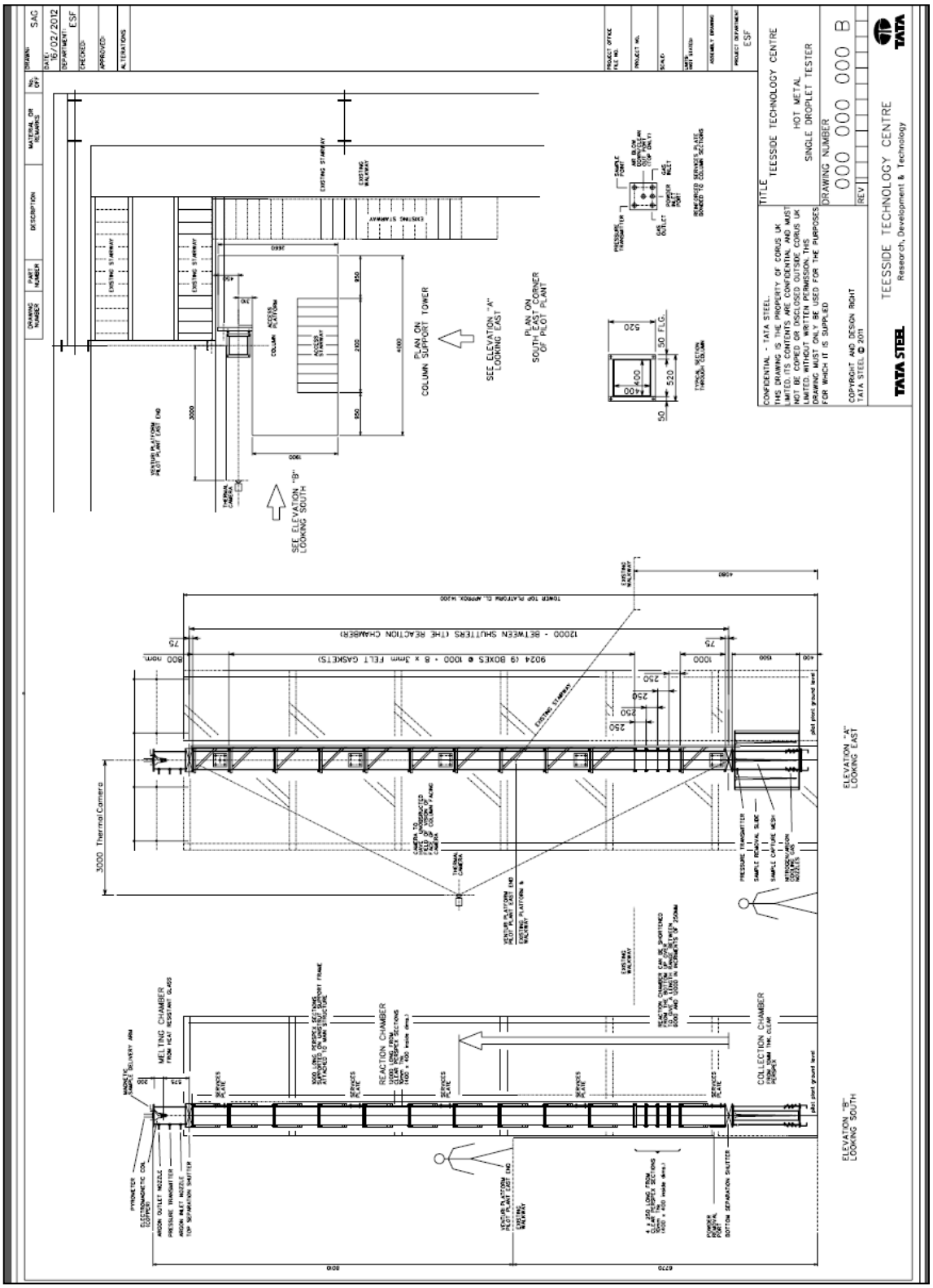


Figure 19: 2nd pilot scale single droplet apparatus design

The initial design idea was a proposed pilot plant scale structure comprising a 12m length (0.4m x 0.4m) Perspex reaction tube with a high frequency induction heater centrally located above the tube. The reaction tube comprised two 6m length sections with a joint seal between them. With the idea of being able to change the drop height and hence reaction time, the tubes were telescopic, where the bottom section could be moved vertically to alter the overall reaction height. The melting zone which featured the electromagnetic coil was sealed from the reaction tube by a polyethylene (cling) film housed in a cassette, therefore isolating different gas atmospheres in the levitation melting chamber and the reaction tube. The tube comprised several inlets and outlets at the top and bottom for gas and powder (lime and ferrosilicon) injection via the gas stream. Cooling of the droplet was to be achieved by helium gas jets at the bottom of the reaction tube when the reacted droplet would penetrate through another level of polyethylene film before being captured in a metallic mesh and immediately subjected to the inert (helium) cooling gas from the jets.

Further development of the initial design focused on making the apparatus modular so it would be relatively easy to change the tube height and reaction time. The reaction tube (still be made from Perspex) would be made up of 4 x 3.05m telescopic sections, attached to each other by side flanges as illustrated in Figure 18, hence also giving it increased structural strength. Although theoretically the design simulated the proposed dephosphorisation pre-treatment process relatively well with regards to the drop height, droplet temperature and reaction atmosphere, the time constraint in developing such a large scale apparatus could potentially have restricted the time necessary for conducting actual meaningful experiments in order to obtain fundamental results. In addition to the main levitating melting structure, steel frames would have been needed to support the Perspex unit, whilst sub-units such as lime powder dispenser system would have also been required for the controlled introduction of lime powder into the system. Figure 19 displays a similar design to that of Figure 18 as shorter sections of Perspex were considered in order to allow for easier moderation of the reaction height.

With these considerations, it was felt that to progress through to a stage where a pilot scale structure was to be developed, fundamental laboratory based investigation using a smaller laboratory scale apparatus was necessary to conduct equally as significant studies on the reaction kinetics and thermodynamics of HM droplets under controlled oxidising atmospheres. Having reviewed the different methods used to conduct studies on metal

droplets such as sessile drop [41] technique and crucible techniques [28, 47, 48], it was decided that levitation melting technique would be applied for the following reasons:

- No crucible contamination on the sample therefore analysis results are representative of the sample/reaction alone
- The technique has been applied in previous steelmaking studies to investigate similar subjects, therefore offering confidence that the technique was potentially applicable to the present study
- The ability to conduct experiments over a wide range of reaction times depending on the levitation melting technique employed; 'free fall' or 'stationary'

Having decided upon the technique to be applied in the present study, the apparatus which the experiments would be conducted on was then designed, manufactured and tested to the stage an experimental technique was developed, the limitations of the apparatus was understood and the errors posed by the apparatus on experimental results were identified (discussed below); in order to achieve accurate results and interpretation of results in preparation for the main series of studies.

Depending on the droplet sizes, metal composition and metal liquidus temperature, the amount of voltage needed to levitate and heat the droplet varied. The smaller the droplet, the less power (voltage) was required to levitate the droplet whereas more power was necessary to lift a larger droplet. From the V=IR relation it is clear to see that power is related to the current, hence the heating effect of the droplet, therefore when the power was reduced too much, there was less current passing through the coil therefore less induced current within the droplet. Although the droplet remained levitated, the target temperature of 1600°C was not reached. Also, when the droplet was at temperature but near the levitation power threshold, the gravitational pull force was strong enough to pull the droplet out of the coil. As well as observing the events described above, a reduction in levitation power also led to increase in droplet temperature to a certain extent as illustrated in Figure 20. Where the power was reduced, the droplet sunk lower into the coil where magnetic flux density was at its highest due to the higher number of bottom turnings compared to top turnings, therefore resulting in a higher number of magnetic flux line intersecting the sample (Case A), which led to greater induced current and increases in droplet temperature.

When a similar sized droplet occupies a smaller coil, more of the magnetic flux lines pass through the sample, therefore increasing the magnetic flux density and induced current within the sample, resulting in increased heating effect

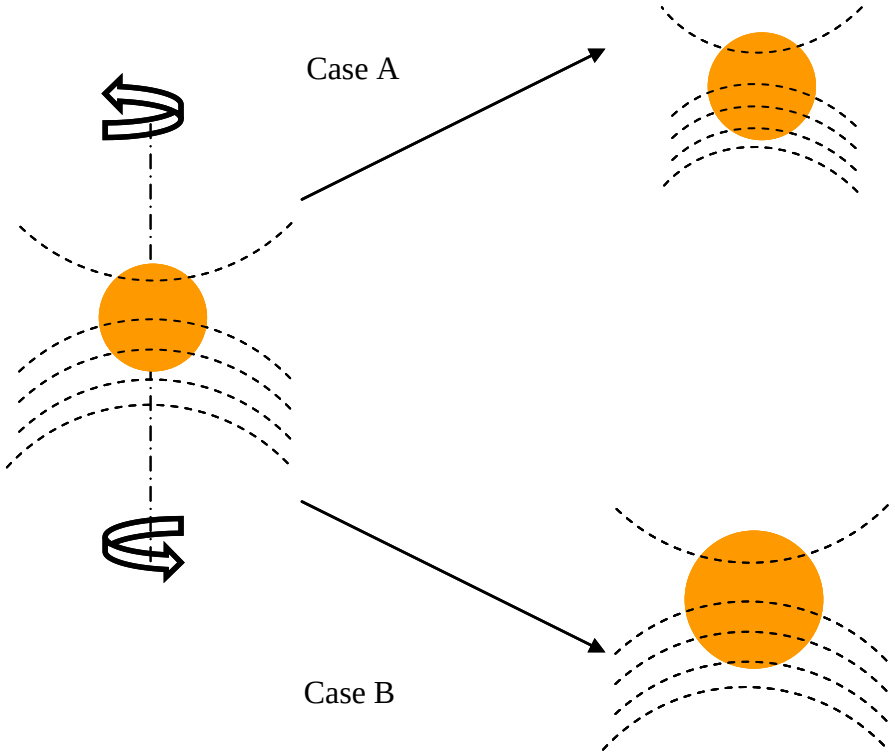


When using a similar larger droplet within a similar sized coil, the spacing between the droplet edge and the coil is reduced meaning the droplet is intersected by more of the magnetic flux lines resulting in increased heating effect and levitation stability.

Figure 20: Effect of coil size and sample size on heating of sample

Although the apparatus was made from silica quartz and benefitted from having a high softening temperature and high thermal shock resistance, caution was taken during ongoing experiments to ensure that the glassware did not fracture. Sparking and sputtering of the HM droplet during oxidation reaction was witnessed when the droplets were left to levitate under oxidising atmosphere (10-30% $O_2$) for a prolonged period of time; greater than 60 seconds, resulting in the sputtered parts hitting the levitation chamber glassware. Whilst such an event has been documented in literature [54-56, 63-65] to be due to subsurface decarburisation, it was decided to limit the experimental runs for HM droplets to 60 seconds as sputtering event occurred not long afterwards.

A further limitation to the experiments was the inability to analyse the cooled non-metallic oxide/slag that had formed at the surface of the droplet because of its minute quantity (<0.1g). Upon hitting the bottom of the water quench pot, the surface of the droplet quickly solidified, at this stage, some of the surface material became loose (as fine grains) and resided at the bottom of the pot. More surface material was lost upon crushing the sample in a ball mill in preparation for bulk metal analysis. The quantity was insignificant to conduct composition analysis such as XRF which required at least 0.6g of the test sample. Nevertheless the ability to analyse the metal/oxide interface and measure the elemental compositions by X-EDS and EPMA proved equally as effective in giving a true representation of the evolution of the droplet's surface with reaction time as presented in Chapter 4 - Section 4.3.2 (EPMA) and 4.3.3 (X-EDS).

As detailed in Chapter 3 - Section 3.1.1, the two colour pyrometer suffered from inherent measurement errors dependent on the distance from droplet and the temperature of the droplet. Considering the arrangement of the pyrometer relative to the molten droplet, only the top surface of the droplet was focused on and therefore temperature readings were of the top droplet surface only. Although there was likely to be temperature gradients [75] between the surface and centre of the metal due to cooling gasses blown onto the surface for the purpose of this study, the sample was considered small enough that the conductive properties of the metal overcame any significant difference in temperature. The positioning of the sample relative to the magnetic field was also considered to affect the heating of the sample, as increased magnetic field lines intersecting the droplet would have led to increased heating and increased droplet temperature. Again, it was assumed that the measured temperature at the droplet’s top surface was identical to that of the bulk metal.

Alignment of the pyrometer to capture droplet temperature was sensitive to droplet instability within the coil. Droplet stability was improved by altering the top turning of the coil so that the droplet was centrally aligned within the coil matching the pyrometer line of focus. If the temperature graph being displayed on the pyrometer software was found to be unstable in a sense that it suddenly varied widely in temperature, it suggested that the droplet surface was not entirely in focus and therefore if the droplet was already centrally aligned, the pyrometer needed to be adjusted along its horizontal plane, until a smoother temperature line was achieved. To further achieve accurate temperature measurement throughout the series of experiments, the pyrometer viewing window was

constantly cleaned with damp tissue cloth as deposited residues deposited on the inside of the glassware.

An area of potential analytical error was noted for surface analysis techniques (X-EDS and EPMA) where only a fraction of the reacted surface underwent analysis primarily due to time constraint posed by the technique. Also, to achieve excellent resolution and quality of composition intensity maps, the mapped area needed to be small, therefore further restricting the size of area which could be analysed at any one time. For example within a cross section of approximately 5mm diameter, only a section of 1mm x 0.5mm and 0.5mm depth was mapped by EPMA to determine the concentration of the elements at the surface of the droplet, whilst for X-EDS a line scan spanning 10µm in a 30µm x 30µm section covering the surface edge and bulk metal was qualitatively and partially quantitatively used to determine surface composition from bulk metal to the surface. It was evident that there could be significant error in taking the results of the analysed small areas as fully representative of the entire surface, especially considering the shape changes of the droplet during fall and also upon impact with other surfaces such as the water interface and the bottom of the water quench pot. Whilst surface analysis results had been quantitatively interpreted it was also used in conjunction with bulk analysis to provide a much more holistic view of reaction kinetics.

Statistical study of metal droplets in slag/metal emulsion during a BOS converter process conducted in the present body of work (Appendix 1) showed that droplet size distribution ranged from about 16µm to 6000µm. The results of the study provided only an indication of sampled droplet sizes within the emulsion, whilst the effects of droplet coalescence and breakup were not considered as part of the study, although proposed. However because larger droplets could exist in the emulsion and slag layer within the BOS converter the apparatus was designed to cater for this also.

### 4.1.2 Induction (Electromagnetic) Coil and Power Supply

Zinn [76] proposed several conditions to consider when designing an induction coil such as that used for simultaneous levitation and heating, these were as follows:

- The specimen must be coupled as closely to the coil as possible to maximise energy transfer; maximum number of magnetic flux lines intersecting the specimen

- The coil should be designed/shaped so that the maximum number of magnetic flux lines are concentrated towards the centre of the coil providing a maximum heating rate
- The coil must be designed to prevent the magnetic field cancelling each other; putting a loop in the inductor provides inductance

In the majority of studies reviewed, the induction coils were located externally, surrounding a glass tube within which the specimen was introduced and levitated. Various researchers [49, 54, 69, 77] have adopted a 7 turn coil featuring two top turnings and 5 bottom alternate turnings. The two lowest turnings on the bottom section were co-planar, with the upper 3 adopting a conical shape wound at a 30° semi-angle. The coil was noted to offer excellent droplet stability, with droplets of initial weights ranging from 0.7g-1g.

A series of levitation experiments at a range of temperatures conducted by Widlund [53] used a single 3-turn coil, where the bottom 2 turns formed a conical shape (30° semi-angle), whilst Sun [51, 52] used 3 different coils, each with distinct design features dependent on the target droplet temperature. For high (7-turns) and low (8-turns) temperature coils, a Y-shaped bottom turning and 2 alternately wound top turning were employed. For the high temperature coil, the separation between the top and bottom turnings was greater than that of the lower temperature coil, whilst an additional winding was added to the lower temperature coil. By increasing the bottom turning, the levitation force was stronger and resulted in the droplet being forced out of the high temperature zone (high magnetic flux region).

The apparatus used by Lee [66] featured a levitation coil sealed within a levitation melting chamber having been fitted through a rubber bung. The 5-turn coil had 3 conical shaped bottom turnings (with the two bottom turnings being co-planar), and 2 alternately wound top turnings, with a spacing of 8mm between the top and bottom turnings. An internally positioned coil was also employed by Distin [64], who suggested that droplet instability caused by droplet boiling during oxidation reactions, would have struck the wall of the glassware if the more common external coil setup was employed.

Apart from the coil used by Baker [54], all other coils were made from copper tubes ranging from approximately 3mm-8mm outer diameters, and levitated loads ranging from

approximately 0.7g – 2.3g. Power was supplied from RF valve generators with frequencies ranging between 315 kHz - 450 kHz.

Although the researcher did not have direct involvement in the design and production of the two coils used in this study as they were supplied by coil manufacturers Ambrell Precision Induction Heating, through use of the EM coils, an understanding of the effects coil design had on sample stability/sample alignment, heating efficiency and levitation size capability, were identified and where possible the coils were modified to improving the aforementioned parameters.

As a range of weighted (1g-15g) samples were initially considered for use during the series of stationary and free falling levitation experiments, the supplier offered 4 sets of coils; as discussed in Chapter 3 - Section 3.1.1. Initially, the levitation capability of each coil was tested by lowering a sample held on top of a quartz silica rod into the middle of the high magnetic field region. When there was sufficient levitation power, the droplet would lift off the sample holder and suspend under a helium flow rate of 2LPM, this would occasionally be followed by a premature drop of the sample due to droplet instability within the coil. In which case, attempts were made to adjust the top turning of the coil to align the droplet centrally where the magnetic flux density was highest. Because the flux density was highest in this region compared to closer to the coil turnings, the sample underwent increased heating. Further droplet stability/central alignment was improved by changing the spacing between the top and bottom turns; where the droplet was unstable in the vertical axis, the spacing between the two sections of turn was either decreased (closer together) to achieve stability and lower sample temperature, or increased (wider spacing) to achieve both stability and higher droplet temperature.

Misalignment in the horizontal plane was also easily resolved by altering the top turning, so the sample became centrally aligned. At times the sample would instantly be dislodged from the sample holder upon being introduced into the coil, but would not levitate. By repeating the practice again and identifying the direction of displacement, it became apparent which area of the coil needed adjusting, whilst the droplet's inability to levitate indicated increased power was required. High gas flows (>10LPM) within the levitation melting chamber was also found to contribute towards sample misalignment. The levitation chamber was designed so inwards gas flow from the bottom of the levitation melting chamber was directed at the coil/levitated sample; therefore, were there to be a

significantly high gas flow rate into the levitation melting chamber, the sample became unstable as it was forced away from its equilibrium levitation position. This resulted in the droplet falling from its suspended position prematurely. Gas flow was especially difficult to control as the flow rate was associated with the temperature of the sample, which was influenced by the externally applied field and induced current (eddy current; Joules heating); which in turn influenced the levitation capability of the sample through the amount of power put in by the generator. To minimise the amount of input gas, the minimum levitation power was determined; this generally ranged from 360V – 410V depending on droplet size.

Once levitation was achieved the next steps were to ensure the samples got up to temperature and then control of temperature predominantly by generator input power and gas flow rate. Effectively, the base power was the power at which stable levitation of the sample was achieved. If the temperature was too high, the flow rate of inert gas was then increased until the temperature was stable at target temperature (1600°C). Inert gas flow rate usually varied between 1LPM – 8LPM. The reason for the wide range is down to the varied amount of power having to be put in mainly depending on the sample size/weight. Where samples were unable to achieve the target temperature, several solutions were available. Firstly, the power from the generator was decreased by 5V increments and then left to see if the temperature being recorded by the pyrometer changed. By decreasing the temperature, the sample sunk lower into the high magnetic flux density region, therefore increased induced current within the sample which led to increased heating effect. However, continued decrease of the power without being able to achieve temperature also resulted in premature falling of the droplet as there was insufficient power to support the sample. In this case another solution employed was to increase the spacing between the top and bottom turnings, and also decrease the spacing between the set of turning that make up the bottom turnings as this offered higher flux line density with the lines closer together; so when the droplet sunk to the lower part of the coil, whilst still being suspended, greater amount of current was induced in the droplet hence increased droplet temperature. To affect temperature further if necessary, the ‘Tap Mode’ at the back of the generator was adjusted. The Tap Mode (which was usually set at Tap Mode 10) is effectively a setting which determines the amount of power being distributed to the heat sink (sample) from the generator. By decreasing the tap mode increased amount of power was distributed towards the sample due to increased external current within the coils.

Levitation melting of low carbon (<1wt.%) Fe-alloys such as FeSi and FeMn were attempted using the same coils which had been used for carbon saturated HM samples. Whilst the samples were able to achieve levitation, the target temperature was not reached. Low match percentage of 75% was recorded for these samples indicating low heating efficiency. Given that higher carbon HM droplets were able to achieve temperature, it was assumed that the inability of being able to attain similar temperature with low carbon Fe-alloys was perhaps due to the lower inductance of the metal. In comparison to similar studies detailed in the literature, smaller coils compared to the one of the present study was used to achieve levitation heating, and in hindsight, a similar coil design should have been used. With this in mind, a similar coil to that used by several researchers [50, 54, 69, 77] was designed and made available for use upon successful commission. Though the coil has not been used or tested in this particular study, the theory behind the design suggests that it will be able to support smaller droplets at lower temperatures (closer to early BOS temperature 1200°C – 1400°C) and at reduced power setting given the extra coil turns and reduced spacing between the coil edges and the metal sample; aimed at concentrating the magnetic field within the coil.

With respect to the capability of the coils used in this study, having developed the experimental technique, an understanding of how the coils operate and the effect of sample properties on heating capabilities, opportunities for improving the design to achieve the target temperature (1600°C) was achieved as clearly discussed in the preceding paragraphs.

The majority of experiments were conducted with 2g samples as these were the smallest samples which could be levitated with good stability whilst undergoing oxidation reaction via the stationary levitation melting technique. The low sample weight meant that the magnetic field was able to support and stabilise the droplet far better than larger samples and as such, was able to counteract the gravitational pull and reaction-led instabilities to remain levitated during exposure to an oxidising atmosphere.

An understanding of the different size ranges of droplets within the BOS converter was obtained in an early statistical study of droplet sizes suspended in slag/metal emulsion reported in Appendix 1. Whilst the study showed the presence of micro-scale droplets, the levitation melting apparatus was limited to investigating macro-scale droplets. While Coil 1 and 2 were both able to levitate and hold at a temperature samples ranging from

2g – 10g only samples of 2g-4g were able to undergo stationary levitation whilst reacting under oxidising atmosphere. Larger samples were less stable, presumably because of the extra weight and the gravitational pull being exerted on the droplet. Also, whilst the larger droplets filled the volume within the coil resulting in a higher match percentage (higher percentage of generated power being used to heat the sample), when oxygen was introduced to the droplet, when the droplet absorbed oxygen and swelled, it became increasingly unstable leading to the droplet being displaced and hitting the coil before falling out of the coil prematurely. This observation was regularly preceded by the build-up of a dark phase at the bottom of the droplet which caused distortion of the droplet's spherical shape into a tear-drop shape. The introduction of powdered CaO onto the droplet surface had a similar effect on larger droplets hence affecting the interaction of the magnetic field with the molten droplet and resulting in the droplet prematurely falling out of the coil.

The (non-conductive) CaO concentrated at the bottom of the droplet covered a small area of the overall droplet surface, and exerted even more of a gravitational pull on the droplet given the added weight. The shape distortion was not as prominent for smaller droplets and therefore managed to remain levitated within the coil. In addition to the reasons given above, the 2g sample was the main droplet size used in the conducted series of experiment because it presented the largest surface area to volume ratio which was of importance when considering surface reactions such as desiliconisation and dephosphorisation.

### 4.1.3 Glassware

Levitation experiments were commonly done in a setup similar to that of Widlund [53], where a glass tube (Silica Quartz or Pyrex), was positioned within an external coil. The internal tube diameters ranged from 12mm – 15mm, although the dimension was greatly influenced by the coil's internal diameter and droplet size. The glassware generally comprised of gas inlet and outlet near the top and bottom of the tube, in order to aid gas flow. In the majority of studies, silica quartz was favoured over Pyrex glass presumably due to its lower thermal expansion coefficient and higher resistance to thermal shock. In several studies [49, 53, 64], the push rod that supports the sample holder was made from glass due to its insulating properties, whilst the sample holders were made of alumina [53] and copper [51, 53] for quenching the sample within the cup, and glass (i.e. Pyrex) [78], where sample quench within the cup was not employed.

Distin [64], Lee [66] and Simento [67] positioned their coils inside the glass levitation chamber. In comparison to the smaller volume levitation tubes, the inlet gases were introduced through a silica lance directly above the top of the coil to ensure rapid gas homogeneity locally around the droplet when levitated. A cross sectional glass design was adopted in these three studies, as it allowed for the input of different components within the chamber, without affecting the coil set up. In the study by Lee [66], an interface consisting of a flat glass window; was used for temperature measurement (pyrometer), whilst the top interface was used to introduce the gas inlet lance. A separate interface was sealed with a rubber bung which had the coil leads fed through it to position the coil centrally within the levitation melting camber, and the bottom interface featured an outlet tube with a rapid quench copper mould at the end of it.

For this study, the apparatus glassware was designed to cater for both free fall and stationary levitation experiments. Potential design features were identified in the limited number of literature [49-56, 63-72] which had used levitation apparatus to investigate oxidation of iron-alloys, of which, only a further few [64-68, 70] had the EM coil positioned within the levitation chamber. Other design features included viewing port for the pyrometer to take temperature measurements of levitated droplet, gas inlet and outlet. The reaction (drop) tube was also made from silica quartz and featured gas inlet and outlet also. As the designed apparatus proved successful in levitating and melting HM droplets within a controlled atmosphere before exposing it to a reactive atmosphere during its falling procedure, it was deemed suitable for the proposed series of experiments.

A major factor affecting the glassware having decided to adopt a design whereby the coil was positioned inside a glass chamber instead of around a glass tube, was staining of the pyrometer viewing window. It was more so a factor when conducting stationary levitation experiments, due to gases such as CO, $CO_2$ and FeO fumes being given off and naturally rising upwards and coating the pyrometer viewing port. Whilst temperature measurement was not as important during the reaction procedure given that during the oxidation, reaction temperature was governed by the steelmaking reactions occurring and not solely by the current induced in the sample, staining of the pyrometer viewing window meant that further temperature readings were most likely inaccurate and therefore for this study, only the initial temperature (before oxygen was introduced into the apparatus) was considered. Prior to every run, the viewing port was cleaned with a damp cloth to ensure accurate initial temperature measurement.

As with the stationary levitation technique, under free fall experiments where the metal sample fell through an oxidising atmosphere within the reaction tube, the silica quartz tube also stained during the reaction procedure and at high oxygen atmospheres, sputtering of the droplet occurred and resulted in the sputtered parts hitting and adhering to the glass. Before conducting another run, the inside of the glassware was cleaned to ensure that all sputtered metal of a specific run was removed and gathered together to prevent mix-up of reacted products.

### 4.1.4 Cooling method

Methods used to quench or fast cool the droplets after levitation melting included water cooled mould quenching, water quench and in-situ gas cooling. Simento [67] used a combination of Helium gas and water cooled mould to achieve fast quench, ensuring that no mass transfer occurred during the cooling period. Lee [66] lifted the copper mould to within closer proximity of the coil to minimise the droplet travel distance onto the mould surface. Sun [51, 52] elected to quench samples in a copper mould, where after a reaction time, the mould was rapidly moved upwards through the coil, carrying the droplet out of the coil and effectively quenching and casting it in the mould. Baker [54] used a similar non-water cooled copper mould quenching technique, where the power was shut off, causing the droplet to fall and quench onto a copper mould beneath the coil.

Caryll [69] used a hammer quench technique to rapidly cool levitated droplets having concluded that the cooling rates of other quench techniques were not fast enough to preserve high-temperature slag-metal equilibrium distribution of elements within the levitated droplet. The hammer quench technique involved a copper anvil and copper faced piston. Once the droplet was discharged from the de-energised coil, a lead pendulum hammer was released simultaneously to drive the piston against the anvil, quenching the specimen between the piston and anvil; the specimen was quenched to a film of $10^{-4}$ cm thickness. The initial cooling rate ($10^{6}$ °C/s) of a droplet 1900°C, was found to be sufficient for suppressing any compositional change during quenching, whilst such changes during initial free fall of the droplet (prior to quenching) was accounted for through convection and radiation heat loss calculations.

In-situ gas cooling technique was applied by Widlund [53] to maintain a non-deformed droplet suitable for metal/slag interface analysis. The helium flow for cooling the droplet

was activated after an elapsed reaction period, and the sample cooled whilst levitating in the coil. Once solidified, the power was turned off, causing the non-deformed specimen to fall onto an alumina cup (initially used to charge the coil with the non-reacted specimen).

Water quenching was employed in the present study to facilitate rapid cooling and allow for a constant and repeatable cooling method between free-fall and stationary levitation melting techniques. In-situ gas quenching would not have been practical during a short time (~0.32s) free fall procedure whilst quenching on a silica quartz mould (sample holder) would not have provided superior heat conductive properties compared to a copper mould to facilitate fast mould quenching.

### 4.1.5 Measurement and control systems

As with the present study, temperature measurements were carried out by two colour pyrometer in the majority of studies. Prisms were positioned on top of the levitation glassware and focused on the droplet from a height above the coil; hence measuring the temperature of the droplet's top surface.

Distin [78] noted that temperature measurements of the metal would not be accurate with an optical or radiation pyrometer focused at the top of the droplet due to interference of iron vapour in the measurement path, and nor would it be accurate by measuring at the bottom of the droplet due to uncertainty regarding the emissivity of the slag. The researcher used a calorimeter to determine droplet temperatures by passing inert gases (He-Ar) over the levitated molten droplet and then releasing it into the calorimeter. Calibration curves relating the measured (two-colour pyrometer) droplet temperature to the specific temperature rise in the calorimeter was plotted to determine accurate droplet temperature.

Estimated temperature error within the study by Distin was +/- 15°C, while errors of +/- 7°C to 15°C were recorded for pyrometer measurements in similar studies[49-53], Jahanshahi [49] and Kaplan [50] calibrating their pyrometer against a platinum/platinum-rhodium (13%) thermocouple immersed in molten carbon saturated iron. Gas flow within the various levitation experiments were also controlled and monitored by rotameters and (stop clock/ solenoid) valves; where switch over times were recorded to be as fast as 1/10$^{th}$ of a second [53].

### 4.1.6 Application of slag-making material

A premise for this study was to investigate the capability of dephosphorisation under the controlled oxidising conditions using the levitation melting technique in order to identify the potential of such reaction occurring during the proposed HM dephosphorisation pre-treatment process shown in Figure 17. Although the techniques applied proved unsuccessful in achieving dephosphorisation as metal phosphorus content remained unchanged after both free fall and stationary levitation for longer periods of time, the method of application and findings are still discussed as follows.

Initial test comprised drilling a 5mm width hole at a depth (~5mm) into the face of the solid cylindrical metal sample, and packing the hole with lime or lime based slag making material (Method 1). There were several fundamental limitations of this technique. Because a hollow volume was required to pack the lime into, the solid metal sample needed to be large enough to contain a hole of that diameter, and through trial and error, the largest sample which this technique could be applied to, was found to be a 6g cylindrical HM sample; larger than the maximum weight sample which could achieve stable levitation melting. Although there was repeatability in the amount of slag lime packed into the void, fluxing of CaO was unsuccessful as the packed lime sintered into a block when the metal was fully molten; a similar occurrence was also observed by Watkins [57] even at higher droplet temperatures (~1900°C) to that of this study. This resulted in the sintered block positioning itself beneath the droplet, distorting the molten droplet shape and effectively pulling the droplet from the high magnetic field zone within the coil, causing the droplet to prematurely fall out of the coil. Following this observation, other techniques of lime application were trialled.

In order to maintain the operational similarities between the laboratory experiments and the proposed HM dephosphorisation pre-treatment process, means of further exposing a falling droplet to oxygen and lime powder were considered; a method which could be applied to a range of droplet sizes and be as consistent with regards to the coverage of the droplet's surface. A second lime application technique (Method 2) trialled was dropping the molten droplet at temperature through a container of fine (< 70μm) lime before the droplet entered the oxygen rich reaction column. The container (as shown in Figure 21) was simply a silica quartz tube (20mm I.D x 20mm height) with both ends wrapped in polyethylene film.

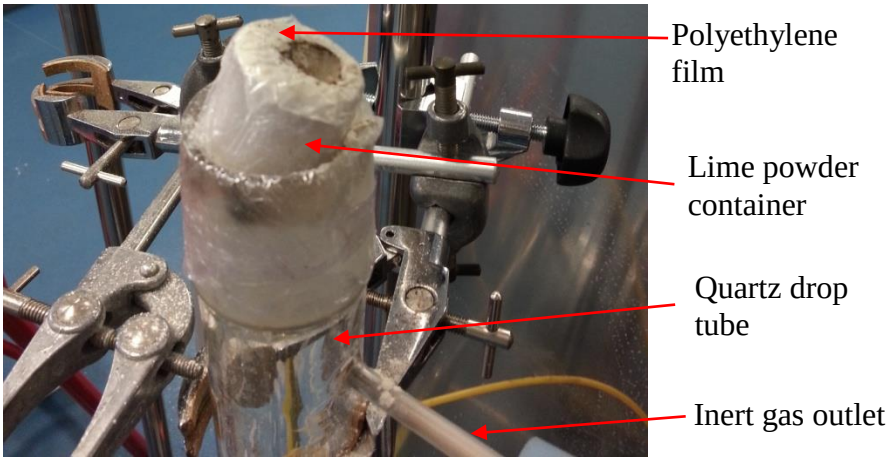


Figure 21: HM entry puncture of CaO filled silica quartz container

Polyethylene was a justifiable material to use because it had a low melting point (< 200°C) and was easily penetrated when it came into contact with the molten droplet and its radiant heat. The base of the container was securely wrapped with the film before loading 2g (+/-0.01g) lime into the container and then sealing the container with another coat of film. The enclosed container was placed on the (polyethylene film) seal between the levitation melting chamber and the reaction (drop) tube, and positioned directly beneath the levitation coil.

This technique could be applied to a range of droplet sizes, and although it restricted control over the amount of coating the droplet surface, the consistency and repeatability of the experiments were maintained by the initial weight of the lime, distribution of the lime once in the container, droplet weight and the droplet's initial temperature. However, this technique was only applicable to droplets undergoing free-fall levitation experiments and not stationary levitation experiments. When conducting surface analysis techniques (X-EDS and EPMA) on droplets which had undergone free falling procedure with the above mentioned lime application technique, identifying the lime regions on the metal's surface was difficult simply because very little if any remained at the metal surface during the falling procedure as the surface analysis results indicated in Chapter 4 - Section 4.3.3. Where lime was detected, it was of extremely low concentrations and was assumed to be in its initial solid state (free lime), due to its inability to flux at the metal surface into liquid oxide which consisted primarily of $SiO_2$, MnO and FeO. Factors such as short exposure time of lime to the droplet surface which would have limited the time where lime and the metal surface were in contact, coupled with insufficient amount of iron

oxidation produced at the metal surface within the short time, may have contributed to the lack of metal/lime reaction taking place.

From the failed attempts (Method 1 and Method 2) of promoting slag formation at the metal surface through lime dissolution into surface liquid oxides, it was concluded that exposure time was just as important as FeO formation, therefore a further technique was tried (Method 3). 1g (+/- 0.01g) of powdered lime was wrapped in polyethylene film and positioned inside the sample holder as shown in Figure 22. The sample holder was then positioned within the EM levitation coil, and the solid metal sample mounted on top of the polyethylene wrapped lime bed. Once the metal had reached temperature during levitation melting, the sample holder was then raised towards the sample. Upon approaching the sample, the radiant heat from the droplet melted and penetrated the polyethylene film and when contact was made between the sample and the loose lime powder in the sample holder cup followed by the sample levitating and spinning within the cup of lime, coating the sample as it did so.

An advantage of Method 3 was that the exposure time of the droplet to lime could be extended for as long as possible before introducing oxygen into the system whether during free fall or stationary levitation technique. Also, having observed sintering of the densely packed lime through Method 1, Method 3 aimed to prevent such an occurrence again by using a loose bed of CaO. Being smaller particles it was therefore more likely that more of the individual CaO particle surface area would be in contact with the surface of the HM/liquid oxide and therefore potentially promote CaO dissolution.

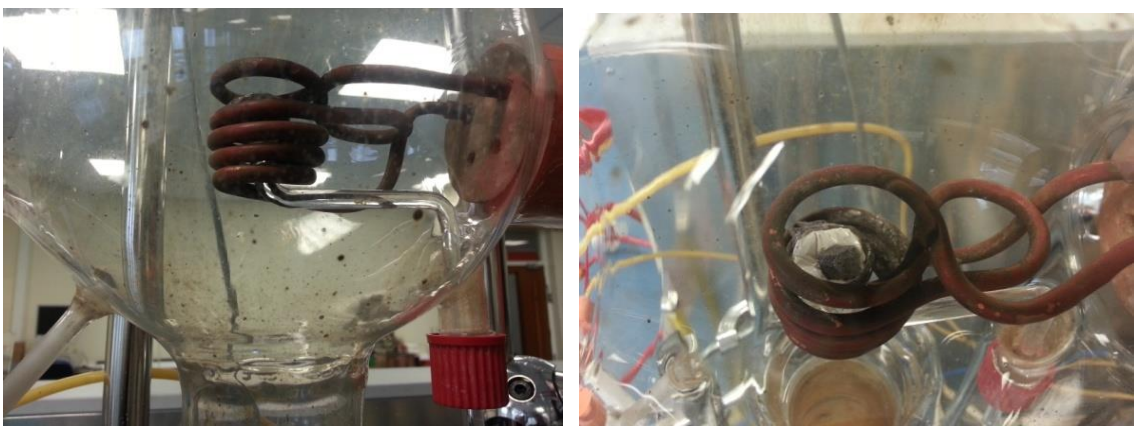

Figure 22: CaO wrapped in cling film and packed into sample holder, with solid sample positioned onto before levitation melting

Given the failed attempts (premature falling) to apply this technique for larger samples (> 4g), it was only applicable to smaller samples which restricted the scope of study with respect to investigating the effect of droplet size on the kinetics of steelmaking oxidation reactions. Method 3 was applied on several 2g HM samples (as these had the best levitation stability whilst reacting in the oxidising atmosphere) for reaction times extending between 10-60seconds. Although unable to differentiate between free lime and fluxed lime, the amount of the substance that was detected at the metal surface of reacted droplets increased with increasing reaction time as graphically displayed in Figures 23-25, but had no effect on HM phosphorus content. A significant drawback of this application, was that the amount of lime on the droplet surface was not repeatable. Also, it was clear that lime dissolution remained the underlying issue with regards to promoting slag/metal reaction at the droplet's surface.

Considering the aforementioned methods of lime application were unable to promote slag/metal reactions, premixed high phosphorus capacity basic slag was trialled. The Slag Atlas [79] compiled a table featuring different concentrations of constituents that made up $CaO$-$SiO_2$-$FeO$-$MgO$ quaternary slag. Along with the table of concentration ranges for the given slag composition, plots of phosphate capacities as a function of temperature and FeO concentration were further used to identify potential slag compositions and concentrations of the slag constituents. As the slag was to be pre-fused in magnesia crucible at 1600°C, 8 wt.% MgO was added to the slag to minimise crucible erosion. Whilst the inclusion of MgO meant that the slag was less like the targeted early BOS slag, it was necessary to prevent damage to the crucible. In hindsight, perhaps a platinum crucible would have been a better choice of crucible material as the crucible erosion would not have been a constraint.

The slags were also designed to have a slag basicity ($CaO/SiO_2$ v-ratio) ranging between 1.5 and 2; reflecting the v-ratio recorded during peak phosphorus content in the IMPHOS slags [84] during the early part of blow. 40 wt.% FeO slag content was selected as corresponded to the highest equilibrium phosphate capacity for this slag type [79]. These 'boundaries' offered guidelines for the selection of a suitable slag composition.

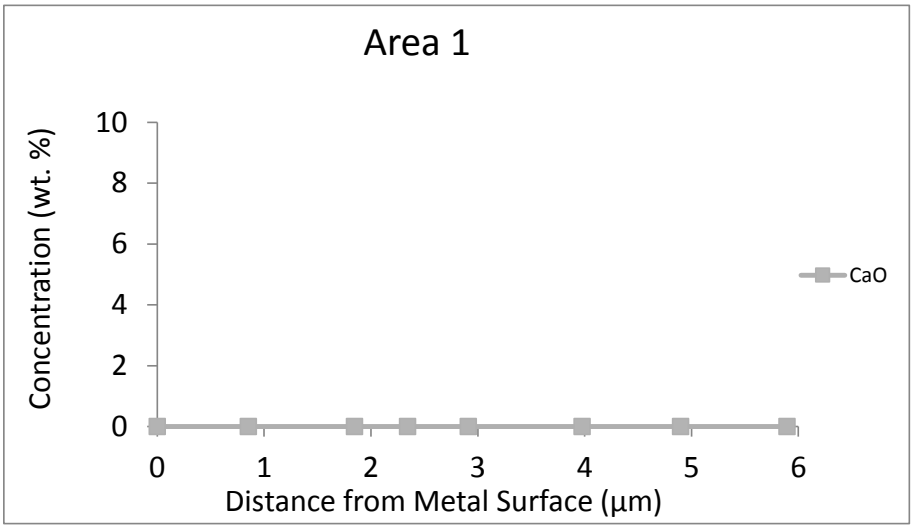


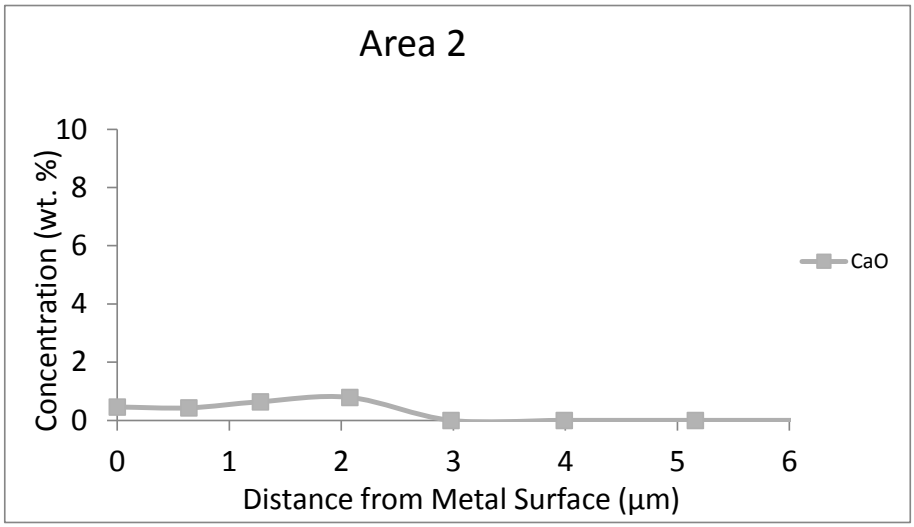


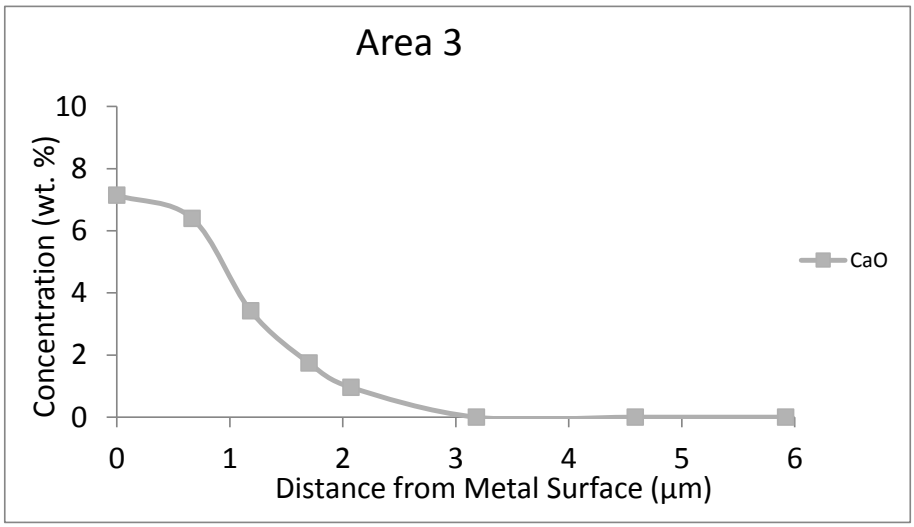


Figure 23: Concentration of unfluxed CaO at the surface of a 2g HM sample which had undergone stationary levitation reaction for 10 seconds in 20% $O_2$/80% He gas atmosphere. Area 1-3 are from various surface sites on a single HM sample.

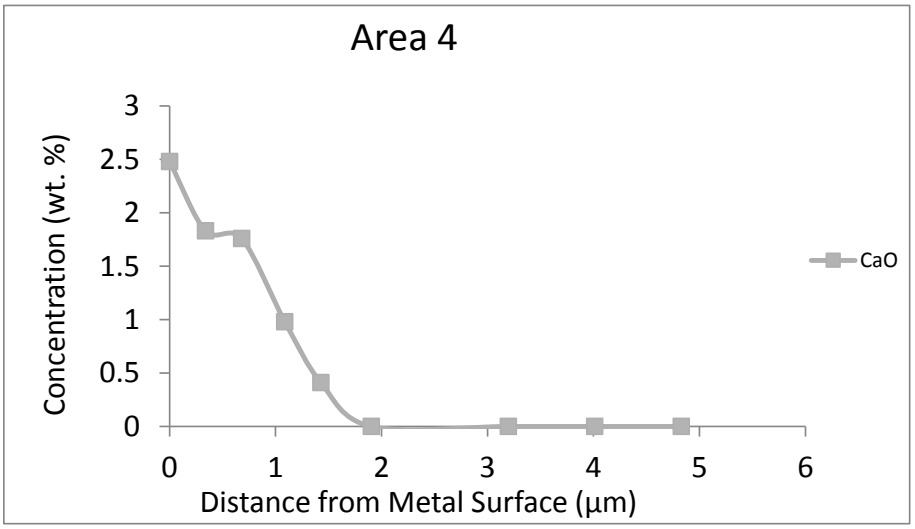


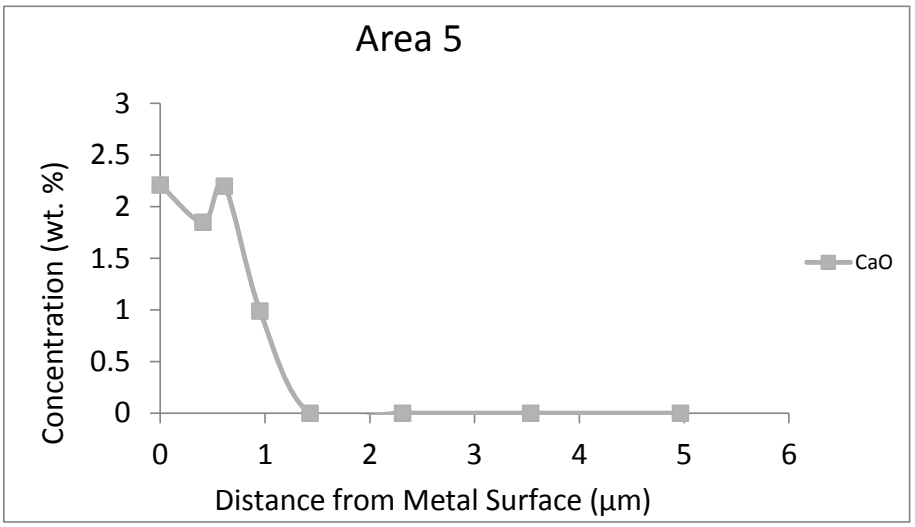


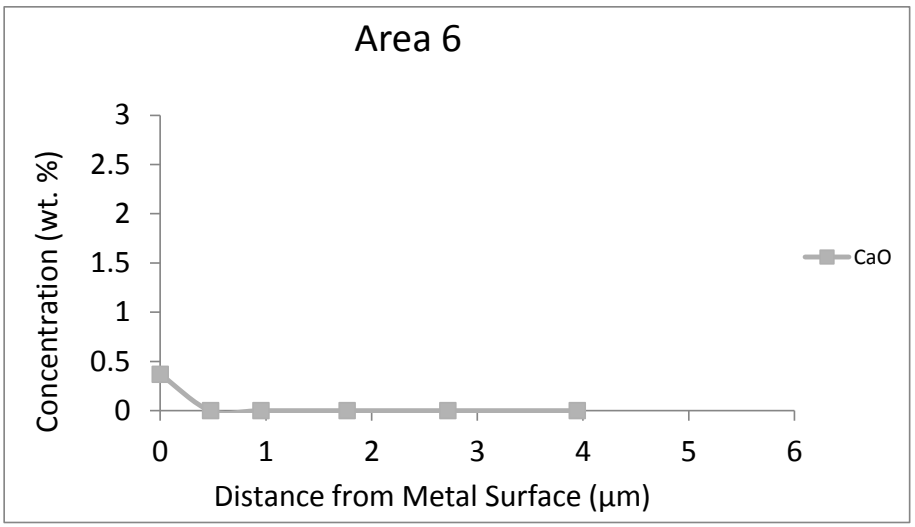


Figure 24: Concentration of unfluxed CaO at the surface of a 2g HM sample which had undergone stationary levitation reaction for 30 seconds in 20% $O_2$/80% He gas atmosphere. Area 4-6 are from various surface sites on a single HM sample.

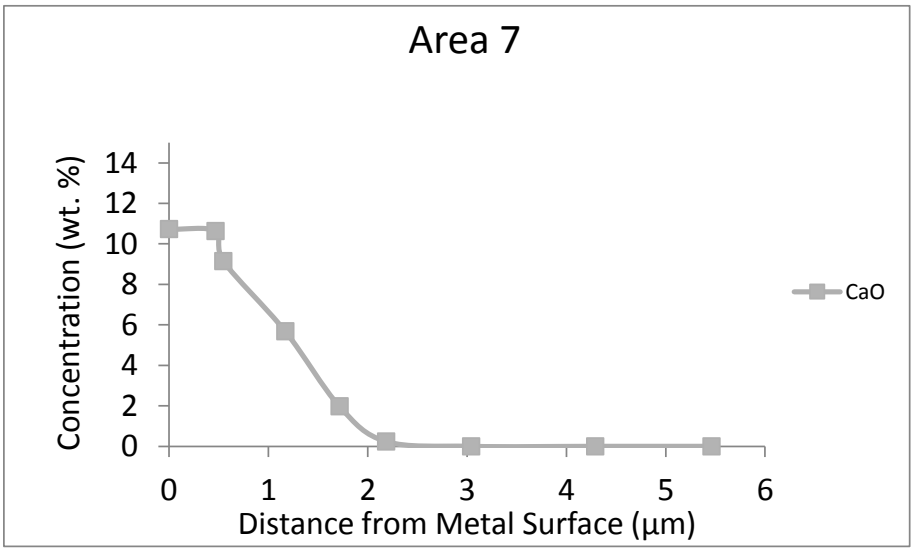


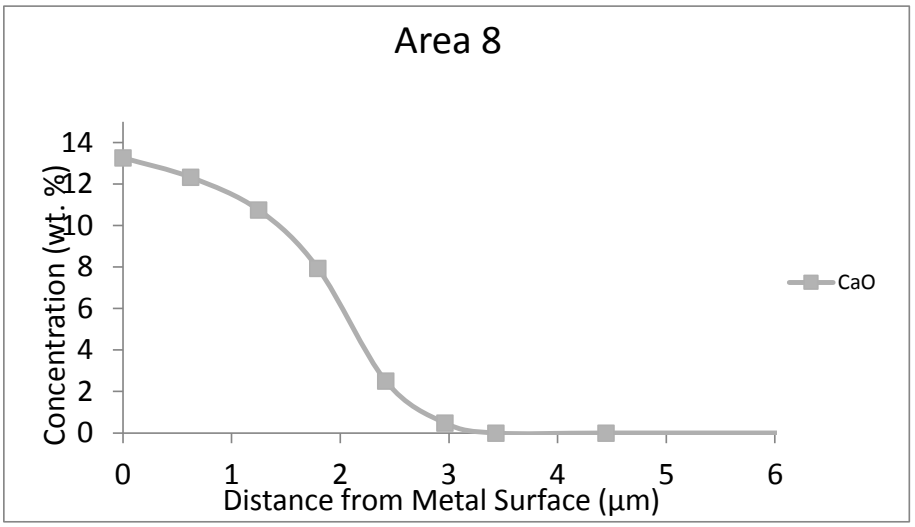


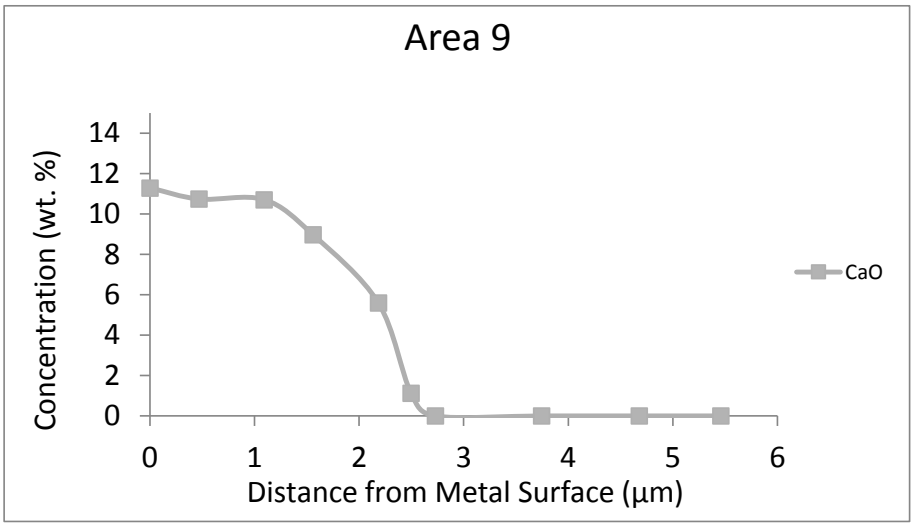


Figure 25: Concentration of unfluxed CaO at the surface of a 2g HM sample which had undergone stationary levitation reaction for 60 seconds in 20% $O_2$/80% He gas atmosphere. Area 7-9 are from various surface sites on a single HM sample.

Table 14: Concentration range for constituents of multicomponent slag suitable for achieving high equilibrium phosphate capacity at 1600°C [79]

| **Slag compositions** | **Concentration (wt.%) at 1600°C** |
|---|---|
| CaO | 0.2 – 41.8 |
| MgO | 6.32 – 27.9 |
| $SiO_2$ | 0.51 – 33.85 |
| FeO | 12.6 – 81.5 |
| $Fe_2O_3$ | 0.86 – 14.2 |
| $P_2O_5$ | 0.13 – 1.14 |

For the slags selected, FeO concentration was maintained at 40 wt.% and MgO at 8 wt.% for the reasons given above. The only variable was the ratio between CaO and $SiO_2$. For slag 1, a V-ratio of 2.1 was selected. The liquidus temperature which represents the temperature, above which all slag constituents was liquid, was approximately 1600°C. Slag 2 had a V-ratio of 1.7 and as a result of decreased amount of CaO in the slag compared to slag 1, the liquidus temperature decreased to approximately 1550°C. Slag 3, with an even lower V-ratio of 1.5 had a liquidus temperature approximating 1500°C. It must be noted that during modelling of these results, temperature steps of 20°C were used and as such the temperatures have a tolerance of +/-20°C, hence the calculated temperatures were considered as approximate indication of liquidus temperature.

Table 15: Concentration of 3 synthetic slags (modelled to identify liquidus temperature)

| **Slag material** | **CaO (wt.%)** | **$SiO_2$ (wt.%)** | **MgO (wt.%)** | **FeO (wt.%)** |
|---|---|---|---|---|
| **Slag 1** | 35 | 17 | 8 | 40 |
| **Slag 2** | 32.7 | 19.3 | 8 | 40 |
| **Slag 3** | 31.2 | 20.8 | 8 | 40 |

Based on the basicity alone and discounting slag mass and reaction time given their limitations in these series of experiments owing largely to the experimental technique, Slag 1 had the highest dephosphorising power, however having already highlighted exposure time as a factor behind slow CaO dissolution within the liquid oxide formed at

the metal surface, given the lower liquidus temperature of Slag 3, it was more likely to achieve a liquid state quicker than Slag 1 and 2, and in-turn, mix with the liquid oxide within the maximum reaction time period of 60 seconds and therefore most likely to promote dephosphorisation although perhaps not to the extent of Slag 1 or 2 were these slags to flux sufficiently at the metal surface. It must be noted that liquidus temperatures calculated by MTDATA are equilibrium values and it is clear (through bulk analysis of the reacted samples presented in Chapter 4 – Section 4.2) that the current system is non-equilibrium.

Whilst Method 3 proved an effective slag application technique, upon heating the solid sample, some of the visually observed initial adhered slag on the droplet's surface fell off whilst an immeasurable amount remained on the droplet's surface but concentrated at the bottom of the droplet. Although the remnant slag eventually fluxed into the liquid oxide, experimental results suggested HM dephosphorisation did not occur. Refer to X-EDS composition maps in Chapter 4 – Section 4.3.3).

As detailed in Chapter 3, the main technique of slag application employed in this study was coating (Method 4). The solid samples were initially coated with PVA glue and then further covered in Slag 1 and left to cool in a desiccator. This method proved effective in coating the metal surface of the metal was initially in contact with slag, therefore giving slag fluxing a greater opportunity to occur. This method offered the most positive outcome compared to other methods tried and further offered the distinct advantage (over other levitation studies [49-53, 57-56, 63-72, 75] of investigating slag/metal reactions using the levitation melting technique.

### 4.2 Chemical Analysis of Bulk Metal

Gas/metal reactions were conducted under oxidising gas atmospheres and with different size samples to determine the effect of these parameters on oxidation rate and change in elemental (C, Si, Mn, P) concentration within the reacted HM samples. The objective of this particular study was to determine whether the rate controlling step for decarburisation was indeed gas phase mass transfer as proposed in literature [50-56, 63-65]. As stated in Chapter 3, combustion analyser was used to measure carbon content in the metal samples whilst ICP-MS was used to measure concentrations of silicon, manganese and phosphorus within the metal. *Note that the error bars in Figure 31-45 represent analytical errors which are further given in Table 27, along with calculated random errors.*

Solid HM samples - 2g in weight were initially held under an inert gas stream (helium gas) and melted at 1600°C. Oxygen was then introduced into the inert gas steam at 30% concentration to promote oxidation reactions between the gas phase and the metal droplet for times ranging between 0-60 seconds. For this series of experiments (Table 16), liquid metal droplets were water quenched at 10s intervals. As with other experimental runs, fumes evolved from the metal surface as soon as oxygen was introduced into the gas stream and a distinct darker phase was observed at the molten metal surface. From the temperature profile of each metal droplet which was recorded by 2-colour pyrometer (+/- 16°C), the temperature of the droplets was observed to increase from the moment oxygen was introduced into the system. Considering the induction furnace power was not adjusted during this time, it can be assumed that the increase in droplet temperature was due solely to exothermic oxidation reactions such as formation of iron oxide on the droplet surface or decarburisation as shown in Figure 26.

Experiments were repeated using similar HM sample weights but with synthetic slag coated onto the solid HM sample surface; the composition of the slag is given in Chapter 3 - Section 3.2.2.1. The results show that the rate of decarburisation remained relatively similar irrespective of the presence of slag material at the droplet's surface. However, as the experimental run progressed, the rates began to differ and carbon levels in the metal which had been coated with slag material were lower than the set of samples without initial slag coating.

### 4.2.1 Change in HM element concentration with reaction time

Table 16: Experimental parameters for measuring the change in hot-metal C, Si, Mn and P concentration with reaction time under 30% $O_2$:70%He gaseous atmosphere (Run 1-4) and basic conditions (Run 5-8) at an initial temperature of 1600°C

| **Run** | **Reaction Time (s)** | **Sample Weight (g)** | **$O_2$/He Ratio (%)** | **Initial Temperature (°C)** | **Initial HM Composition** | **Slag** | **Final Metal Composition (wt.%)** | | | |
|---|---|---|---|---|---|---|---|---|---|---|
| | | | | | | | C (+/-0.1 wt.%) | Si (+/-0.03 wt.%) | Mn (+/-0.03 wt.%) | P (+/- 0.01 wt.%) |
| 1 | 0 | 2 | 0/100 | 1600 | 4.98 wt.% C<br>0.30 wt. % Si<br>0.36 wt.% Mn<br>0.09 wt.% P | No | 4.98 | 0.30 | 0.36 | 0.09 |
| 2 | 10 | 2 | 30/70 | 1600 | | No | 4.82 | 0.22 | 0.32 | 0.09 |
| 3 | 30 | 2 | 30/70 | 1600 | | No | 3.95 | 0.17 | 0.34 | 0.09 |
| 4 | 60 | 2 | 30/70 | 1600 | | No | 2.41 | 0.24 | 0.24 | 0.1 |
| 5 | 10 | 2 | 30/70 | 1600 | | Yes | 4.76 | 0.24 | 0.33 | 0.09 |
| 6 | 30 | 2 | 30/70 | 1600 | | Yes | 3.83 | 0.12 | 0.18 | 0.09 |
| 7 | 60 | 2 | 30/70 | 1600 | | Yes | 1.97 | 0.15 | 0.18 | 0.1 |

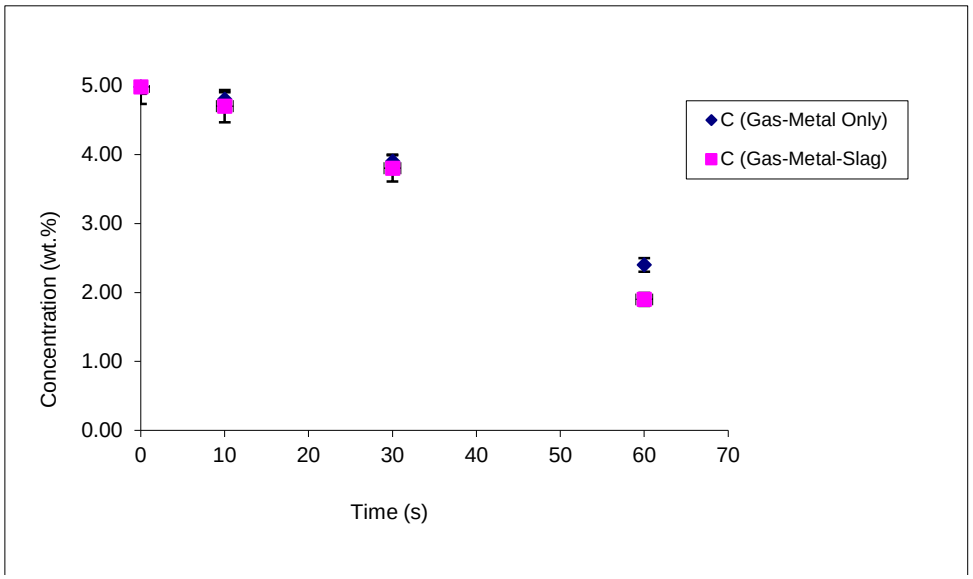


Figure 26: Change in HM carbon content of 2g HM samples between 0-60s reaction time and reacted under 30%$O_2$:70%He gaseous atmosphere with the HM at an initial temperature of 1600°C. (Run 1-7)

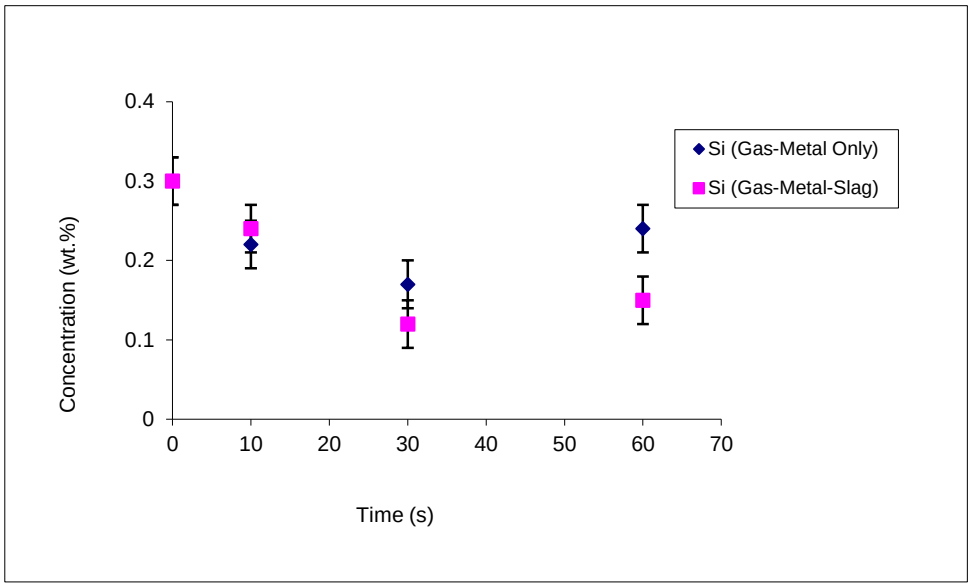


Figure 27: Change in HM silicon content of 2g HM samples between 0-60s reaction time and reacted under 30%$O_2$:70%He gaseous atmosphere with the HM at an initial temperature of 1600°C. (Run 1-7)

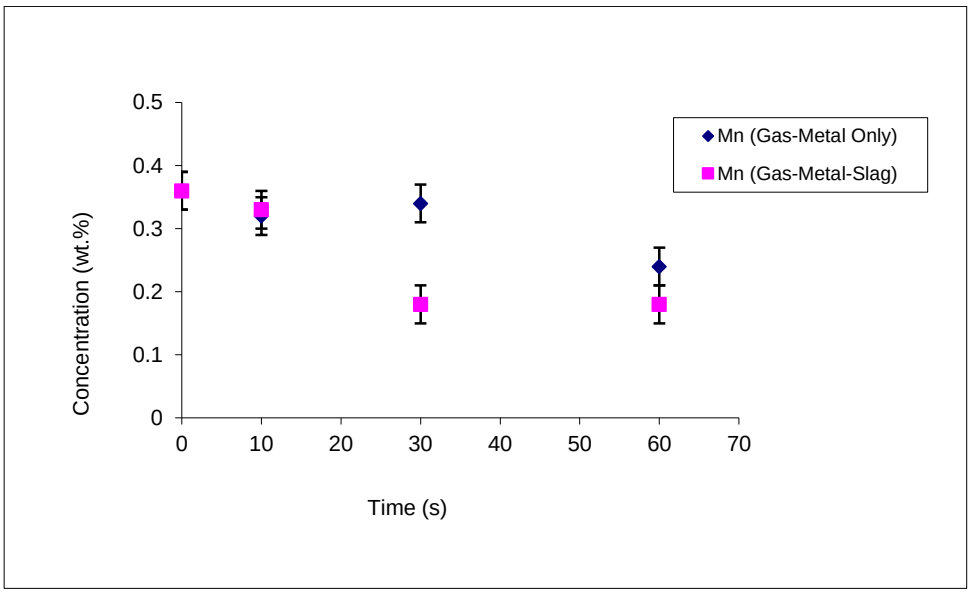


Figure 28: Change in HM manganese content of 2g HM samples between 0-60s reaction time and reacted under 30%O2:70%He gaseous atmosphere with the HM at an initial temperature of 1600°C. (Run 1-7)

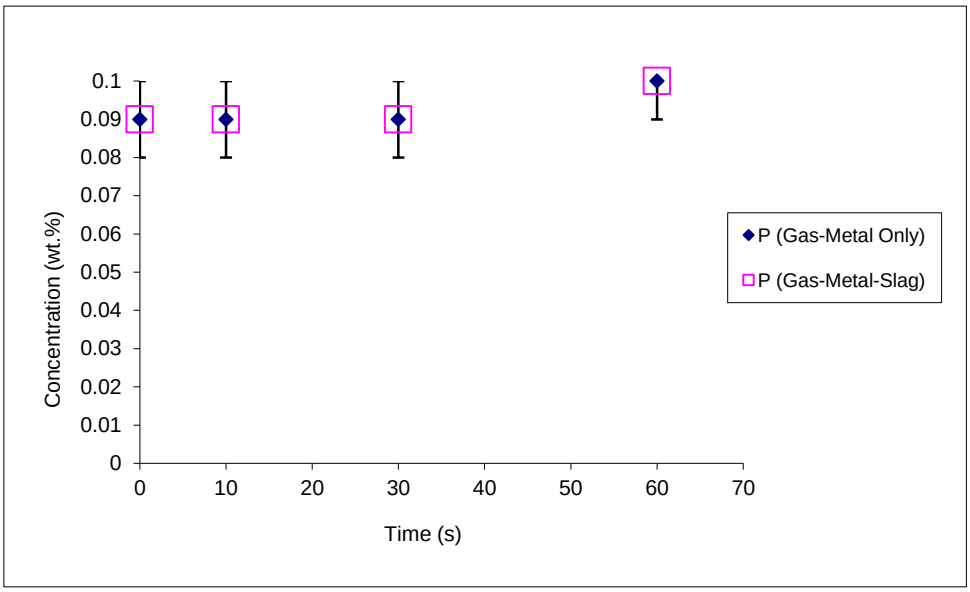


Figure 29: Change in HM phosphorus content of 2g HM samples between 0-60s reaction time and reacted under 30%$O_2$:70%He gaseous atmosphere with the HM at an initial temperature of 1600°C. (Run 1-7)

In addition to iron oxidation reaction taking place given its abundance within the metal phase, HM carbon (Figure 26), silicon (Figure 27) and manganese (Figure 29) content was found to decrease with reaction time when reacted under the experimental conditions listed in Table 16. Interestingly, the greatest change in concentration of silicon and manganese was within the first 10 seconds of reaction, which coincides with the time period where the change in HM carbon content was at its lowest. Measurement of slag/oxide chemistry from the reacted samples would have been ideal in order to determine whether there was indeed simultaneous slag chemistry changes especially within early stage of the reaction where silicon and manganese HM levels have been observed to drop significantly – silicon by almost 50% in the first 30 seconds and manganese by nearly the same ratio after 30 seconds of metal-gas-slag reaction. The reaction equations can be represented as follows:

$$C + O = CO \tag{28}$$

$$Si + O_2 = SiO_2 \tag{29}$$

$$Mn + O = MnO \tag{30}$$

$$Fe + O = FeO \tag{31}$$

The steps for such reactions to occur are as follows:

i) Transfer of HM elements from the bulk to surface of the metal
ii) Transfer of oxygen from the bulk gas phase to the metal surface
iii) Chemical reaction of HM elements and oxygen at the surface of the metal, effectively creating a reaction interface
iv) Diffusion of reaction product(s) away from the reaction interface

With respect to carbon oxidation, as the product is a gas, CO would simply be swept away into the gas phase more so by convection than diffusion given the forced flow of incoming reaction gas to the metal surface, hence ensuring that the C-O reaction sites on the metal surface are renewed for further HM decarburisation to take place. As shown in the reaction formulas above, products of silicon, manganese and iron oxidation would have formed liquid oxides at the surface of the droplet. Therefore new silicon, manganese and iron reaction products forming at the metal surface would add to the liquid oxide phase

initially formed, and with these reactions measured to take place simultaneously alongside iron oxidation, the oxide would consist of a mixture of $SiO_2$, MnO and FeO, hence decreasing their respective activity within the oxide, driving further oxidation of the HM elements to take place.

The free energy of oxidation of carbon, silicon, manganese and iron from the liquid metal to their oxide products at steelmaking temperatures such as that used in the present experiment is always negative meaning that the products can be formed in its pure state. The standard free energy of oxidation for these reactions can be represented as follows [51]:

$$[C]+[O]=CO \qquad (32)$$
$$\Delta G^o = -22{,}200 - 38.34T \quad (J)$$

$$[Si]+2[O]=SiO_{2(RS)} \qquad (33)$$
$$\Delta G^o = -576{,}440 + 218.21 \quad (J)$$

$$[Mn]+[O]=MnO_{(RS)} \qquad (34)$$
$$\Delta G^o = -288{,}200 + 129.3T \quad (J)$$

$$[Fe]+[O]=FeO_{(RS)} \qquad (35)$$
$$\Delta G^o = -177{,}700 + 49.83T \quad (J)$$

In its pure state, silicon oxidation is the most negative, hence the most thermodynamic favourable reaction, followed by carbon oxidation, iron oxidation and then manganese oxidation. This implies that gaseous oxygen should be tied with silicon more so than any other elements, as appears to be the case given the removal of nearly 50% of silicon within the first 30 seconds of reaction.

Upon introduction of basic slag material into the reaction system, HM silicon and manganese levels dropped even further compared to their concentration when only exposed to oxygen as the reactant. This can best be explained by considering the ionic theory proposed by Flood and Grjotheim[37] where the slag components are considered as cation and anions with basic oxides (CaO) as ion donors and acidic oxides ($SiO_2$, $P_2O_5$) as oxide ion acceptors.

$$CaO = Ca^{2+} + O^{2-} \quad (36)$$

$$FeO = Fe^{2+} + O^{2-} \quad (37)$$

$$MgO = Mg^{2+} + O^{2-} \quad (38)$$

Having already established that it is thermodynamically possible for oxide products of silicon and manganese to form in their pure state under such steelmaking temperatures, further oxidation of these HM elements is possible because of increased availability of free oxygen within the basic slag where the basic oxides (namely CaO) act as an oxide ion donors as shown in equation 36-38. The reason for rapid silicon and manganese oxidation within the first 30 seconds of reaction is because that the slag is initially at its most basic (greatest availability of oxide ions) before (acidic) oxide products of silicon and manganese mix with it. As this occurs, the basicity of the slag decreases hence there is less of a driving force to take up more acidic oxides, notably as CaO is not replenished to maintain favourable basicity levels as is the case in conventional BOS converter practice.

For phosphorus, as shown through equation 7 [27], the free energy of oxidation reaction is always positive at steelmaking temperatures, therefore it is thermodynamically unfavourable for the reaction to occur, hence the lack of dephosphorisation during metal-gas reactions, as was the case for these series of experiments. For dephosphorisation to occur, the activity of $P_2O_5$ needs to be lowered (or the activity of phosphorus and oxygen raised), achieved by increasing the basicity of the slag (i.e. addition of CaO). The lowering of activity of $P_2O_5$ can be shown as the phosphate formation:

$$4(CaO) + 2[P] + 5[O] = (4CaO.P_2O_5) \quad (39)$$

Given the absence of this third phase, no dephosphorisation occurred when the metal was simply reacted with oxygen from the gas phase. However, even when basic slag was introduced into the reaction system, dephosphorisation did not occur through the presence of the slag was seen to drive HM silicon and manganese levels lower than for gas-metal reaction. This suggests that the argument of there being insufficient time for the initial slag to flux with the liquid oxide is not entirely resonsible, even though reaction time was significantly less than would be the case in a BOS converter. This can however be best understood by considering the dissolution of phosphorus pentoxide in a basic slag such as that used in the present study. This is represented by the following equation:

$$(P_2O_5) + 3(O^{2-}) = 2(PO_4^{3-}) \quad (40)$$

Clearly, increasing the free oxygen ion in the slag favours the dissociation of $P_2O_5$ into the phosphate ion captured in high phosphorus capacity phases such as temperature dependent C2S slag phase. And as further shown in the equation 40, free ions are associated with CaO, suggesting that by increasing the basicity of the slag, the number of free ions increases, hence favouring dephosphorisation. With HM silicon and manganese content nearly halved within the first 30 seconds of the metal-gas-slag reactions conducted in this study, it follows that its acidic oxide products would have reduced the basicity of the initially basic slag. Further considering that the synthetic slag was not replenished with new CaO, hence unbounded oxygen, there would have been progressively less free oxygen ion available for dissociation of $P_2O_5$ to take place.

In BOS practice, upon injecting oxygen through the oxygen lance onto the bulk metal surface to form the jet impact zone, within the first few minutes of blowing, oxidation of silicon, iron and manganese occurs and consequently, liquid oxides of these elements flux CaO in order to create a basic slag predominantly rich in iron and silicon. The liquid oxide phase components as observed in the present study for HM droplets which had undergone gas/metal reaction also consisted of early silicon and iron constituents. It has further been noted that because of the formation of these CaO free oxides during the early stages of the blow, the flux rate of CaO during BOS practice was rapid therefore leading to increases in the slag basicity. As shown in the present study where CaO was introduced into the reaction system, fresh Singleton Birch lime was not able to flux totally into the liquid oxides formed at the droplet surface, and as such, a basic slag could not be formed consequently leading to no phosphorus removal.

As aforementioned, the strong dependency of slag basicity on phosphorus removal is justification as to why no phosphorus was removed from the HM droplets. However the inability for the CaO to sufficiently flux into the oxide may be credited to several factors. Insufficient oxide formation may be a reason for the lack of CaO fluxing into the liquid oxide especially considering that incoming oxygen was mostly used up by surface decarburisation reaction, the little that occurred was not sustainable, therefore limiting the availability of oxygen for further oxide formation to take place.

Another factor considered was the effect of oxide viscosity given that a cooler gas was being blown onto the surface of molten HM droplet. With the droplet temperature increasing as reaction procedure progressed (as shown in Figure 64), the oxide viscosity may have decreased as increased heat would have been expelled from the droplet surface. Taking this point into consideration, the initial liquid oxide may be considered more viscous than the latter liquid oxide which would suggest that fluxing of the slag would have been increasingly favourable towards the latter stages of the reaction were a continuous feed of slag material or CaO introduced to the metal surface.

High phosphorus capacity phases, notably dicalcium silicate (C2S) have been credited for being important in promoting HM dephosphorisation by precipitation of such phases within liquid slag, notably during the initial period of lime fluxing into the slag as the slag melting point increases more rapidly than that of the bulk metal [15, 43] . The reason for this is primarily due to the early formation of silica slag which aids rapid CaO dissolution which further causes the slag layer closest to the CaO to become quickly saturated in CaO and form a C2S phase for which metal oxides (i.e. $PO_4^{3-}$) infiltrate. The formation of the phase is strongly dependent on the continuous influx of CaO and low slag temperature so it can precipitate out of the liquid slag. In the present study, the slag temperature may be presumed close to that of the droplet given that it only thinly coated the droplet and as reaction procedure progressed, the droplet increased in temperature hence increasing the slag temperature also. Furthermore the absence of a continuous feed of CaO could have also restricted the formation of C2S phases especially given the short reaction time for any potential CaO to flux into the liquid oxide and then precipitate such high phosphorus phases.

### 4.2.2 Effect of droplet weight/size

Table 17: Experimental parameters for measuring the effect of HM droplet weight (2g, 3g, 4g) on oxidation reaction of C, Si, Mn and P under 20%$O_2$:80%He gaseous atmosphere (Run 8-10) and basic conditions (Run11-13)

| **Run** | **Reaction Time (s)** | **Sample Weight (g)** | **$O_2$/He Ratio (%)** | **Initial Temperature (°C)** | **Initial HM Composition** | **Slag** | **Final HM Composition (wt.%)** | | | |
|---|---|---|---|---|---|---|---|---|---|---|
| | | | | | | | C (+/-0.1 wt.%) | Si (+/-0.03 wt.%) | Mn (+/-0.03 wt.%) | P (+/- 0.01 wt.%) |
| 8 | 60 | 2 | 20/80 | 1600 | 4.98 wt.% C<br>0.30 wt. % Si<br>0.36 wt.% Mn<br>0.09 wt.% P | No | 1.6 | 0.23 | 0.23 | 0.09 |
| 9 | 60 | 3 | 20/80 | 1600 | | No | 2.6 | 0.21 | 0.29 | 0.09 |
| 10 | 60 | 4 | 20/80 | 1600 | | No | 3.2 | 0.15 | 0.31 | 0.09 |
| 11 | 60 | 2 | 20/80 | 1600 | | Yes | 1.8 | 0.02 | 0.12 | 0.09 |
| 12 | 60 | 3 | 20/80 | 1600 | | Yes | 2.3 | 0.013 | 0.13 | 0.09 |
| 13 | 60 | 4 | 20/80 | 1600 | | Yes | 2.9 | 0.006 | 0.12 | 0.09 |

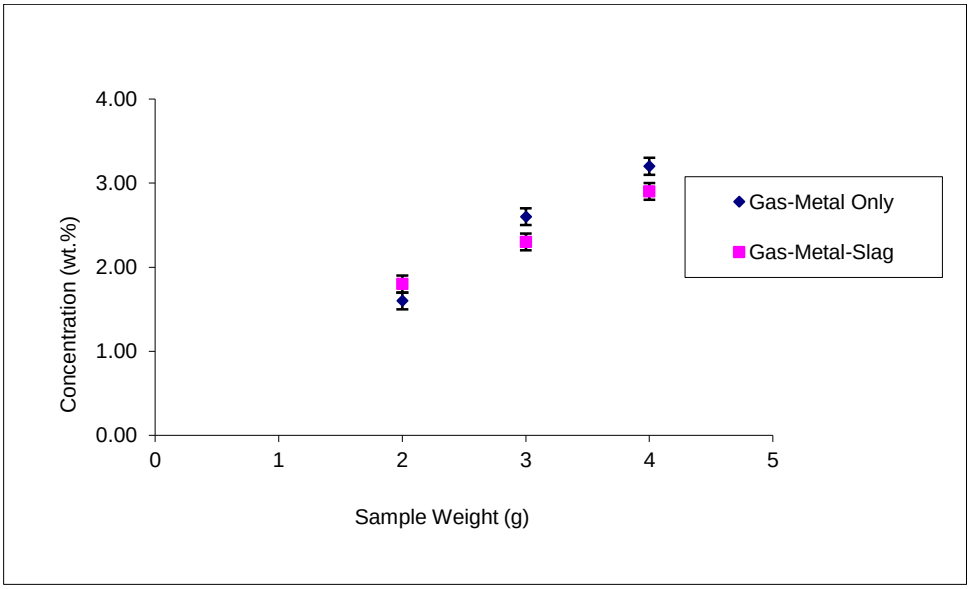


Figure 30: Final HM carbon concentration for 2g, 3g, and 4g HM samples with initial HM carbon content of 4.98 wt.%, reacted under 20%$O_2$:80%He gaseous atmosphere (Run 8-10) and basic conditions (Run11-13)

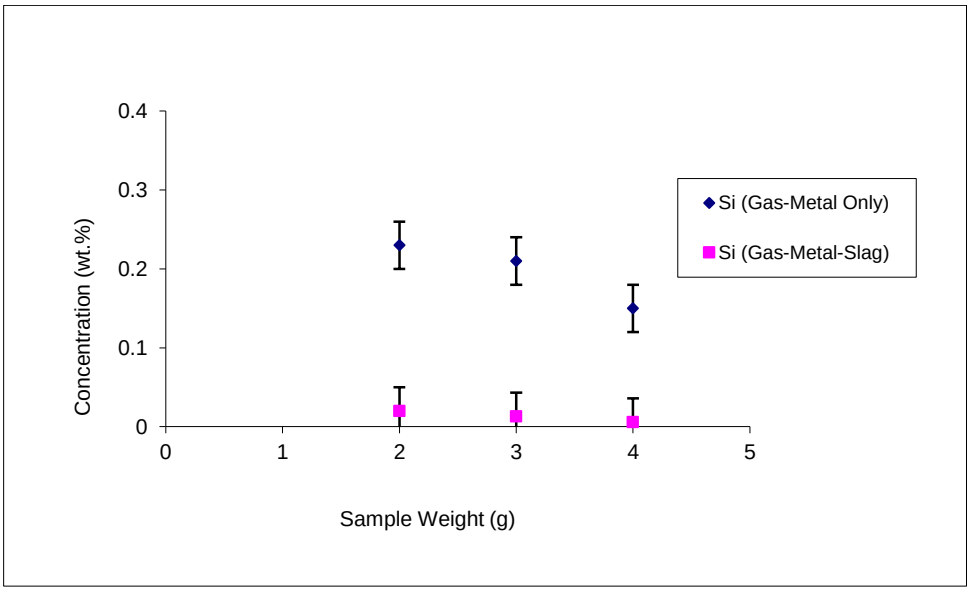


Figure 31: Final HM silicon concentration for 2g, 3g, and 4g HM samples with initial HM silicon content of 0.30 wt.%, reacted under 20%$O_2$:80%He gaseous atmosphere (Run 8-10) and basic conditions (Run11-13)

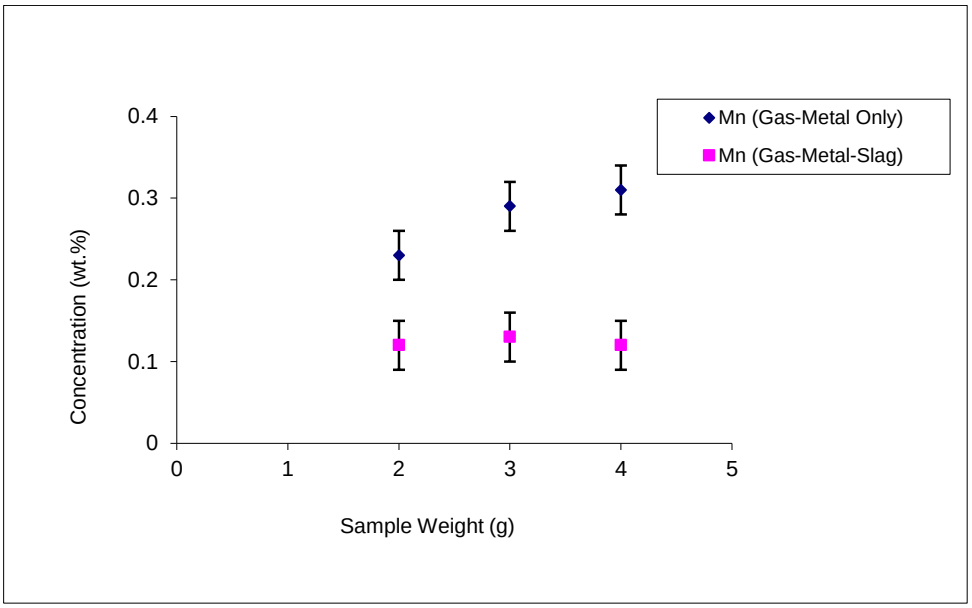


Figure 32: Final HM manganese concentration for 2g, 3g, and 4g HM samples with initial HM manganese content of 0.36 wt.%, reacted under 20%$O_2$:80%He gaseous atmosphere (Run 8-10) and basic conditions (Run11-13)

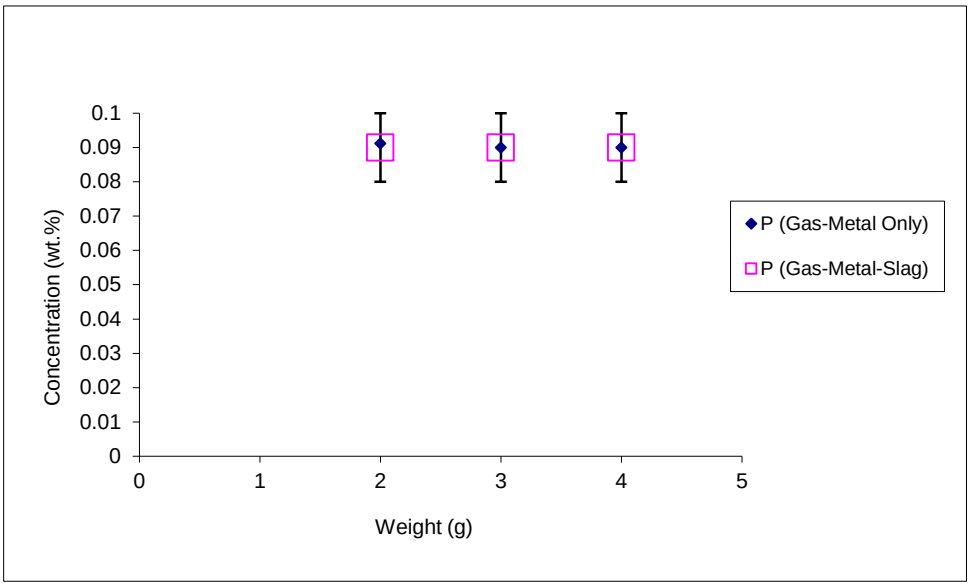


Figure 33: Final HM phosphors concentration for 2g, 3g, and 4g HM samples with initial HM manganese content of 0.09 wt.%, reacted under 20%$O_2$:80%He gaseous atmosphere (Run 8-10) and basic conditions (Run11-13)

Stationary levitation studies were carried out on 2g, 3g and 4g samples to monitor oxidation reactions under a 20% oxygen-helium gas stream (Table 17). Prior to the introduction of oxygen, the temperature of the droplets was maintained at 1600°C.

HM carbon (Figure 30), silicon (Figure 31) and manganese (Figure 32) concentration decreased with reaction time irrespective of sample weight whereas HM phosphorus concentration (Figure 33) witnessed no change. The greatest change in HM carbon and manganese concentration was witnessed by the smallest droplet (2g) and the least change by the larger droplet 4g) indicating that faster surface reaction occurred for smaller droplet given the larger surface area to volume ratio. The opposite was true for HM silicon as the greatest change in HM silicon concentration was experienced by the 4g sample and the least change by the 2g sample. This result goes against theory which suggests that given the larger surface area of smaller droplets, surface reactions should be quicker for smaller droplets. Whilst the samples which reacted with slag material displayed a similar trend, there is obviously scope for further work to be done in this area.

Similar experiments were repeated but with the solid samples initially coated with synthetic slag as detailed in Chapter 3 - Section 3.2.2.1. The presence of the slag at the metal surface had no effect on decarburisation as the final HM content remained relatively the same compared to the samples with no slag. On the other hand, silicon and manganese levels in the HM were significantly reduced in the presence of the basic slag. Initial HM silicon content was 0.30 wt.%, and it dropped to 0.02 wt.%, 0.013 wt.% and 0.006 wt.% for 2g, 3g, and 4g samples respectively. Given that the initial slag chemistry for the reacted samples was the same and the amount of slag coated onto the metal surface was primarily a function of the size of the metal, the effect of slag mass may have played a role in achieving the final HM Si content. However, droplet size is believed to have had a more marked effect of final HM Si levels as shown in the non-slag reaction results.

Final HM manganese levels in the 2-4g samples that simply underwent metal-gas reaction decreased as sample size decreased also. With slag, HM Mn content dropped to around 0.12 wt.% (+/- 0.01wt.%) irrespective of droplet size. Whilst there appeared to be no effect of droplet size on manganese removal with slag, it is clear that the presence of a basic slag had a strong influence on manganese reaction. This is further displayed through microscopic analysis of the reaction interface (Chapter 4 – Section 4.3.3) where

manganese is seen to populate the surface non-metal phase; indicating mass transfer of the element across the reaction interface.

The effect of slag on the different final HM content of C, Si and Mn, and lack of change in HM phosphorus content has been discussed in section 4.2.1 and holds true for these results also. Understanding of the effect of droplet size on the change in HM concentration can be achieved through equation 41 whereby the flux, $N$ (rate of mass transfer, mol/s) is a function of the mass transfer coefficient, $k$ (m/s), change in concentration, $\Delta X$ (mol/m$^3$) and the droplet surface area, $A$ (m$^3$).

$$N = kA\Delta X \tag{41}$$

Given that the mass transfer coefficient ($k$) is a constant, for the purpose/simplicity of explanation, this can be omitted from equation 41 simply leaving the following:

$$N = A\Delta X \tag{42}$$

This shows that an increase in the reaction surface area is proportional to an increase in the rate of mass transfer. For the HM droplet, the 'reaction' surface area comprise the immediate surface area and new surfaces replenishing the old ones, hence the volume of the droplet needs to be taken into account. For simplicity of argument, we assume that the molten droplet was spherical where its volume ($V$) and area ($A$) can be equated as such ($V=4/3\pi r^3$ and $A=4\pi r^2$), even though it was observed to form a tear-drop shape at times during levitation within the EM coil. Through application of these geometry equations to data recorded for experimental run 8-10, we can conclude that the 2g droplet has a larger surface area to volume ratio (7.55), it essentially has a larger 'reaction' surface area. Putting this in the context of equation 42 where $A$ is effectively the surface area to volume ratio, it shows that indeed, the rate of mass transfer does increase with increased reaction surface area, hence the effect of droplet size – this is further illustrated with respect to the change in HM carbon concentration in Figure 34 and 35.

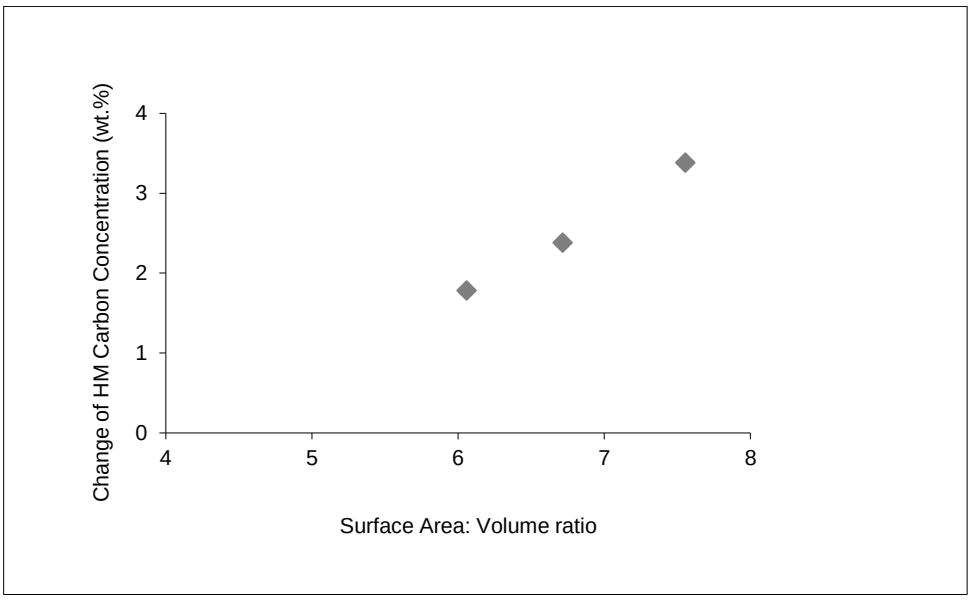


Figure 34: Change of HM carbon content for 2g, 3g, 4g samples of respective volume-surface area ratio, reacted under 20%$O_2$:80%He gaseous atmosphere (Run 8-10) and basic conditions (Run11-13)

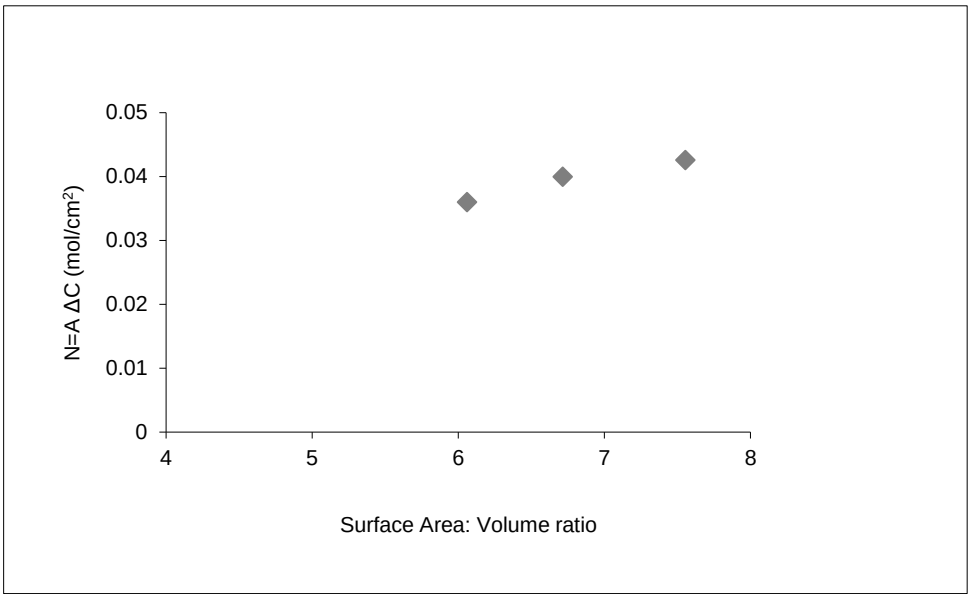


Figure 35: Effect of HM droplet surface area on rate of mass transfer for carbon, for 2g, 3g, 4g samples of respective volume-surface area ratio, reacted under 20%$O_2$:80%He gaseous atmosphere (Run 8-10) and basic conditions (Run11-13)

With respect to the other metalloids (silicon and manganese), although one might have expected manganese to follow a similar trend to silicon given that they are both oxide forming oxidation products, the change in HM manganese content was greatest for smaller droplets sizes, for gas/metal reaction. Assuming the argument presented for silicon was agreeable with manganese also, the trend in the change of HM manganese level could be due to vaporisation of the element from the metal surface given its low

vapour pressure ($10^{-2}$ atm) [105] in which case, the effect of surface area to volume ratio becomes important as the diffusion time of manganese from the bulk metal to surface is faster for smaller droplets therefore faster replenishment of surface manganese for vaporisation to occur simultaneously with rapid surface decarburisation.

Comparing the results of slag/metal/gas experiments displayed in Figure 28 and Figure 32, it is evident that the manganese level attained was at the level where no further manganese oxidation took place, irrespective of droplet size and increasing reaction time; as manganese level plateau between 0.12 wt.% - 0.18 wt.% after 30 seconds reaction time; presumably due to high oxygen utilisation by carbon and iron. This finding further supports the conclusions from literature [51, 52] which suggests that there was little/no change in HM manganese level until carbon was below a critical level (~1wt.%).

Confidence can be had in these set of results as the values recorded for the 2g HM samples which had undergone simply gas-metal reactions correlated well with the results of the control repeated experiments detailed in Chapter 4 - Section 4.4. Also note that whilst the final carbon content for the sample used in Run 8 recorded 1.6wt.% compared to the average of 2.15wt.% in the repeated control experiments (Table 26), when the upper analytical and random errors are accounted for, the result (1.88wt.%) still lays within the lower boundary (>1.80.wt%) of the error calculated for the repeated experiments therefore demonstrating consistency in the experimental technique.

### 4.2.3 Effect of gas phase oxygen content

Table 18: Experimental parameters – Effect of gas phase oxygen content

| Run | Reaction Time (s) | Sample Weight (g) | $O_2$/He Ratio (%) | Initial Temperature (°C) | Initial HM Composition | Slag*[1] | Final HM Composition (wt.%) | | | |
|---|---|---|---|---|---|---|---|---|---|---|
| | | | | | | | C (+/-0.1 wt.%) | Si (+/-0.03 wt.%) | Mn (+/-0.03 wt.%) | P (+/- 0.01 wt.%) |
| 14 | 10 | 2 | 10/90 | 1600 | 4.51 wt.% C<br>0.30 wt. % Si<br>0.36 wt.% Mn<br>0.09 wt.% P | No | 4.40 | 0.18 | 0.34 | 0.09 |
| 15 | 20 | 2 | 10/90 | 1600 | | No | 4.31 | 0.20 | 0.37 | 0.09 |
| 16 | 30 | 2 | 10/90 | 1600 | | No | 3.87 | 0.19 | 0.39 | 0.09 |
| 17 | 40 | 2 | 10/90 | 1600 | | No | 4.10 | 0.17 | 0.28 | 0.09 |
| 18 | 50 | 2 | 10/90 | 1600 | | No | 3.36 | 0.19 | 0.32 | 0.09 |
| 19 | 10 | 2 | 20/80 | 1600 | | No | 4.17 | 0.22 | 0.37 | 0.11 |
| 20 | 20 | 2 | 20/80 | 1600 | | No | 3.34 | 0.23 | 0.26 | 0.11 |
| 21 | 30 | 2 | 20/80 | 1600 | | No | 2.42 | 0.21 | 0.33 | 0.10 |
| 22 | 40 | 2 | 20/80 | 1600 | | No | 1.63 | 0.31 | 0.25 | 0.10 |
| 23 | 50 | 2 | 20/80 | 1600 | | No | 1.94 | 0.40 | 0.21 | 0.11 |
| 24 | 60 | 2 | 20/80 | 1600 | | No | 0.81 | 0.23 | 0.24 | 0.10 |
| 25 (FF) | 0.32 | 2 | 10/90 | 1600 | | No | 4.9 | 0.35 | 0.38 | 0.09 |
| 26 (FF) | 0.32 | 2 | 20/80 | 1600 | | No | 5.1 | 0.29 | 0.38 | 0.09 |
| 27 (FF) | 0.32 | 2 | 30/70 | 1600 | | No | 4.9 | 0.33 | 0.40 | 0.09 |

*[1]: CaO was introduced into the reaction system but did not produce a slag or promote slag/metal reactions
*[2]: Run 25, 26, 27 Carbon = 4.98wt.%
(FF): Free fall experiments

As detailed in Table 18, 2g HM droplets were exposed to gas atmosphere of 10%, 20% and 30% oxygen content in the oxygen-helium gas phase for reaction times of up to 60 seconds, having initially been held at 1600°C under inert atmosphere prior to introducing oxygen into the system. For 10% gas phase oxygen reaction at 40 seconds and for 20% gas phase oxygen reaction at 50 seconds, carbon level goes up to 4.10 wt.% and 1.94 wt.% respectively. These results lay outside the line of trend and their respective error bands given that carbon level is expected to decrease with reaction time. Therefore the results has been classed as anomalies. Other results listed in Table 18 lay within their errors bands listed in Table 27. Also, it should be noted that given that applied lime did not produce a slag to drive slag/metal reactions, the experiment results is therefore representative of metal/gas reaction alone. Figure 36 is therefore used to primarily show carbon change and not the influence of lime on reaction behaviour.

Decarburisation rate (Figure 36 and Figure 37) increased with increased gas phase oxygen content which is to be expected considering the availability of increased reactant to aid the reaction. A slower rate of decarburisation was witnessed during the first 10 seconds of reaction for samples that had reacted under 20% oxygen gas phase content, followed by rapid decarburisation up to about 40 seconds into the reaction which preceded another period of slow decarburisation; although at a slower rate than at the start of the reaction.

Whilst the transition from fast (surface) to slow (subsurface) decarburisation has been discussed by researchers such as Sun [51, 52] Baker [54] and Roddis [65] who have carried out similar work using Fe-C alloys, the initial slow rate of decarburisation experienced at the start of the reaction in these series of experiments has not been accounted for in those same studies when using this specific experimental technique. However, Gare and Hazeldean [28] have argued the phenomenon to be due to the slow process of initial CO nucleation at the gas/metal interface; noting the period to be an 'Incubation Period' where the nucleation energy barrier is being overcome. The average rate over the 60s reaction time for both reactions derived from the slope of the integrated rate plot was 0.0051 mol/cm$^2$s and 0.0264 mol/cm$^2$s for reactions conducted under 10% and 20% gas phase oxygen content respectively.

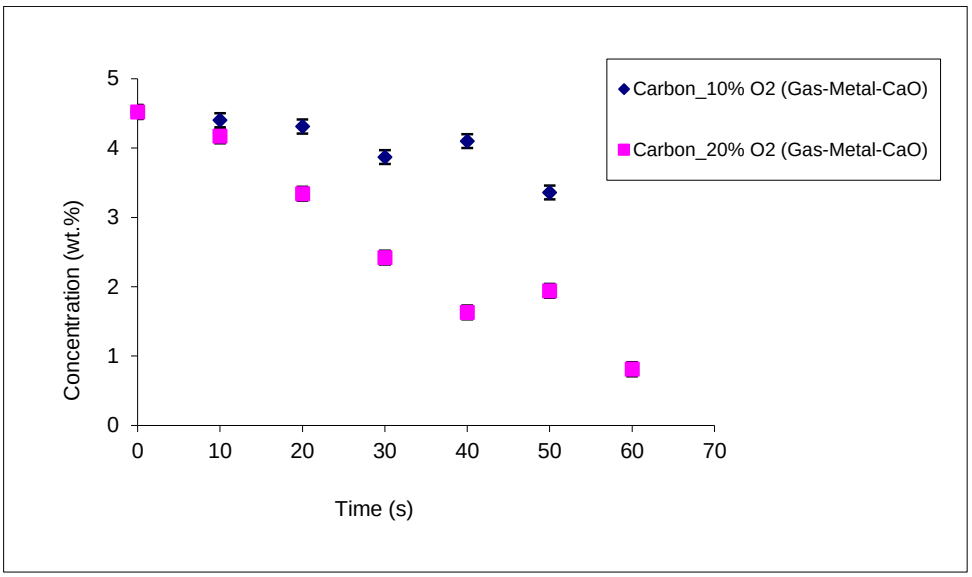


Figure 36: Change in HM carbon concentration for 2g HM samples reacted under 10%$O_2$:90% He and 20%$O_2$:80%He gas atmosphere from 0-60 seconds with Singleton Birch lime introduced into the reaction system

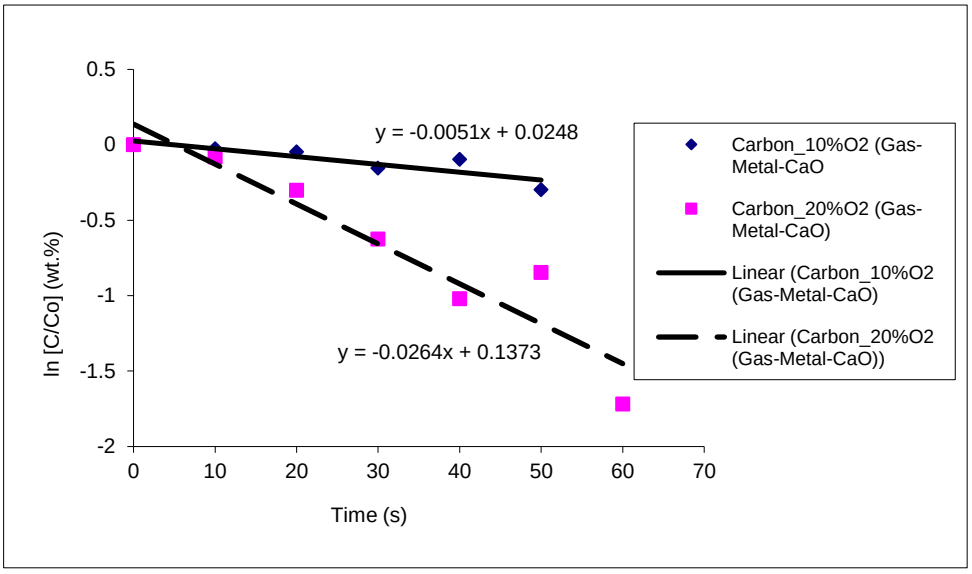


Figure 37: Rate of carbon oxidation for 2g HM samples reacted under 10%$O_2$:90% He and 20%$O_2$:80%He gas atmosphere from 0-60 seconds with Singleton Birch lime introduced into the reaction system

Figure 36 show that the difference in gas phase oxygen content from 10-20% had a marked effect on final HM carbon level. Worth noting is that whilst the change in the level of decarburisation was observed to differ, silicon and manganese final HM levels remained similar irrespective of gas phase oxygen content, with silicon levels recorded between 0.18-0.22 wt.% (anomaly result at 50s reaction for 20% gas phase reaction) and manganese, 0.21-0.39 wt.% between 0-50s reaction time. For both 10% and 20% gas phase oxygen the silicon content has approximately halved in the first 10 seconds also,

further supporting the argument of initial CO nucleation incubation period where oxygen utilisation at the reaction interface by silicon (and iron) has presumably limited its availability for decarburisation.

Comparing the bulk metal compositions measured by combustion analysis and ICP-MS techniques to surface and sub-surface (500 µm depth) measurements by EPMA analysis technique, it is evident that a silicon and manganese concentration gradients existed between the bulk metal and the metal droplet surface.

Given that gas phase mass transfer control was the rate controlling step and decarburisation occurred mainly through chemical reaction of carbon and oxygen at the metal/gas interface at the surface of the metal, it is conceivable that carbon would have displayed similar concentration gradient trend across the metal cross section as the oxygen products of these elements are thermodynamically more stable than the element form as shown by the increased negativity of the Gibbs free energy for their respective reaction products [82].

With an increased gas phase oxygen content at the reaction interface, the oxygen gradient between the bulk metal and the metal surface would have steepened, in which case, the driving force for metal phase mass transfer of HM elements such as carbon, would have been stronger and potentially led to the metal surface growing richer in HM elements quicker than it would have done under less gas phase oxygen content. This could have resulted in enrichment of surface oxide given that the increase of gas phase oxygen content could have brought about increased rate of oxygen supply to the surface compared to the rate of carbon diffusion to the metal surface as argued by See & Warner [70]; in which case, the excess oxygen could have contributed towards increased oxidation of oxide-forming elements such as silicon.

Due to rapid decarburisation, the concentration which researchers [50-53, 74] have identified the transition from surface to subsurface decarburisation to occur (~ 1 wt.%), was reached between the reaction times of 40s and 60s, with HM carbon concentrations of 1.63 wt.% and 0.81 wt.% recorded respectively for these times. This represents a switch from gas phase control (oxygen supply) to carbon diffusion control. Whilst droplet sputtering and explosion was not observed in the present series of experiments, a change in the slope of decarburisation was witnessed for reactions that took place under 20% oxygen gas phase

content. Given the slower rate of decarburisation for 10% oxygen gas phase reactions, the critical carbon level for the transition to occur was not reached and hence further silicon or manganese oxidation was restricted.

Note that for this particular series of experiment Run 10-24, a new batch of samples were prepared and used. Whilst having a lower initial carbon content, the HM remained carbon saturated with all else the same compared to previous samples used in the study. Unexplainably, for the samples which underwent reaction under 20% oxygen atmosphere (Run 19-24), prior to introduction of oxygen into the reaction chamber, temperature control was difficult and as such higher volumes of helium gas (> 6LPM) was necessary to cool the droplet to its reaction temperature and as such higher oxygen content was needed to make up the 20% $O_2$:80% He ratio. This may well explain the extremely low final carbon level recorded notably for Run 24 compared to the repeated controlled experiments as increased flow rate has been noted to increase decarburisation rate [54, 64]. A further contribution to this behaviour as already highlighted in Chapter 3 - Section 3.1.1.1 may be unsuitability of the EM coil for such small samples causing unprecedented heating behaviour. Nevertheless, whilst the actual valves may be questionable (notable samples reacted for 50 and 60 seconds), the effect of gas different gas phase oxygen content is evident.

Free fall levitation experiments of varying oxygen gas phase content have also been conducted with 2g HM samples initially at 1600°C falling down a 1m length silica quartz tube filled with upward-flowing (2LPM) oxidising gas. As displayed in Figures 38-41, during the 0.32s reaction time under 10, 20 and 30% gas phase oxygen content, there was little/no change in the concentration of carbon, silicon, manganese and phosphorus in the metal having been analysed by bulk analysis methods; ICP-MS and combustion analyser techniques. During the free fall experiments however, as with the stationary levitation experiments, iron fuming took place and it evolved from the metal surface at seemingly faster rates with increasing gas phase oxygen content. This was noted by the increasingly heavy staining of the inner silica quartz tube wall which required cleaning before each experimental run. Due to the speed of the fall and the inability to gather clear images of the metal surface, it was difficult to examine the metal surface to determine whether formation of surface oxide occurred. Were an oxide phase to exist at the metal surface, it may well have been highly rich in iron than other oxide forming elements as noted by

several researchers [66, 70, 72] considering that little/no silicon and manganese removal occurred, but iron fuming did take place.

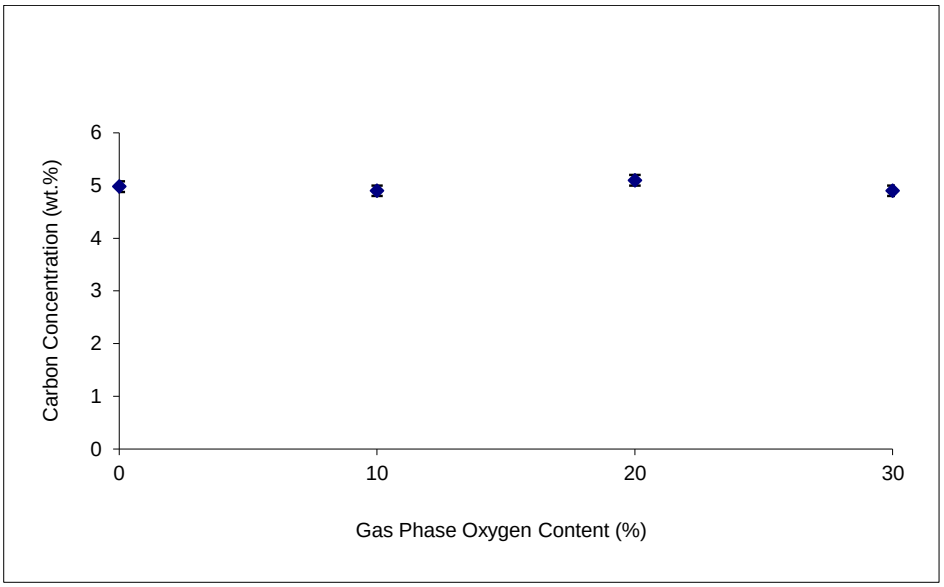


Figure 38: Effect of gas phase oxygen content on carbon oxidation of 2g HM droplets falling through 1m column of 10%, 20% and 30%$O_2$ gas (Run 25-27)

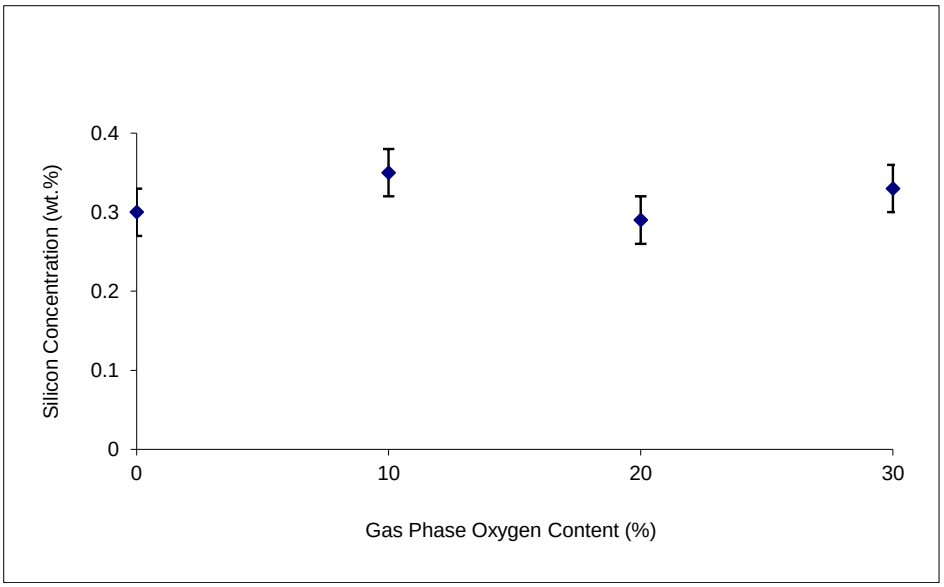


Figure 39: Effect of gas phase oxygen content on silicon oxidation of 2g HM droplets falling through 1m column of 10%, 20% and 30%$O_2$ gas (Run 25-27)

The lack of HM decarburisation when exposed to different gas phase oxygen content (10-30%) during the free fall experiments suggests that negligible amount of carbon oxidation took place as the metal remained saturated in carbon and at similar levels to that of its initial concentration. .

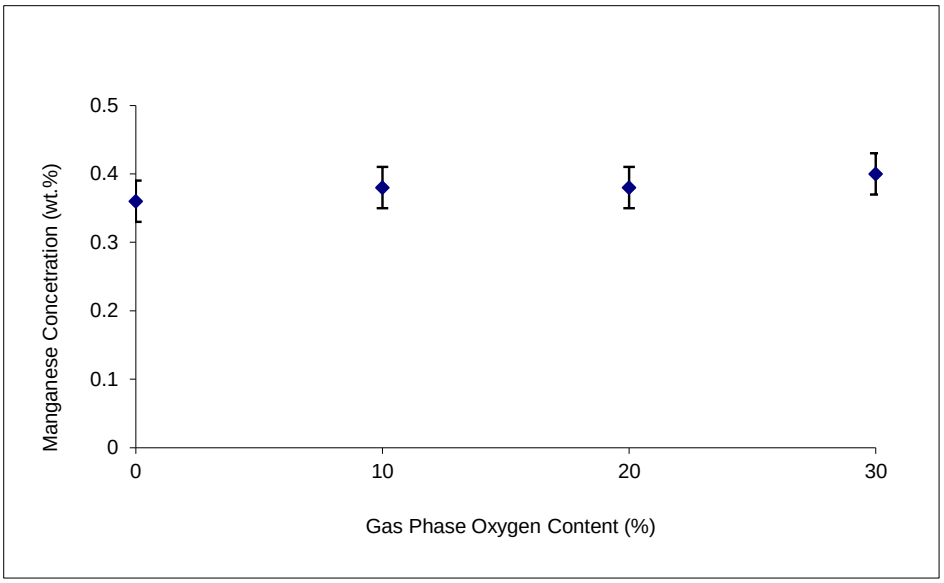


Figure 40: Effect of gas phase oxygen content on manganese oxidation of 2g HM droplets falling through 1m column of 10%, 20% and 30%$O_2$ gas (Run 25-27)

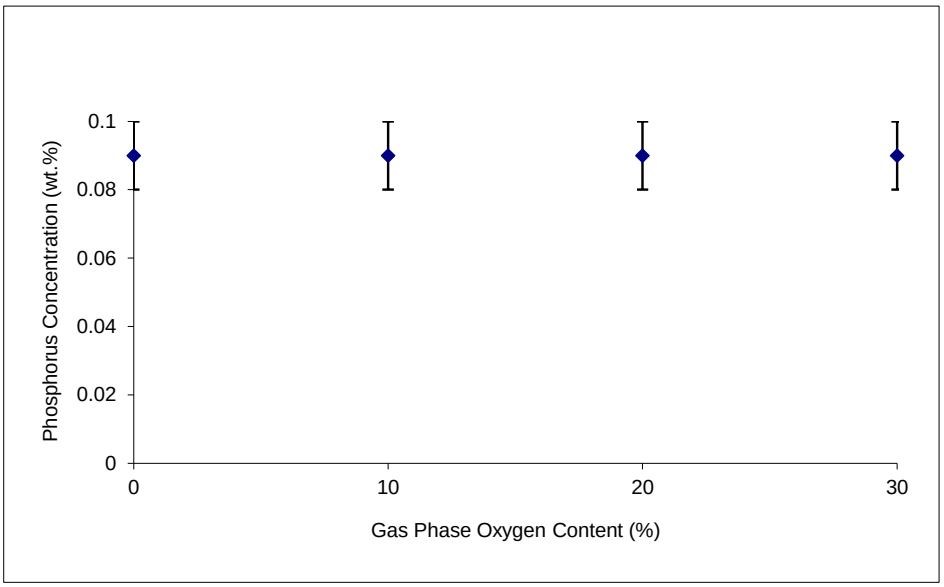


Figure 41: Effect of gas phase oxygen content on phosphors oxidation of 2g HM droplets falling through 1m column of 10%, 20% and 30%$O_2$ gas (Run 25-27)

Whilst gas phase mass transfer has been credited as the rate controlling step in the present study as well as in literature [50-56, 63-65], from the free fall experiments it was evident that the proposed rate controlling mechanism was not prevalent as no decarburisation took place during the short reaction time of 0.32 seconds even at increasingly higher gas phase oxygen content atmosphere of up to 30% oxygen, as shown in Figure 38. The lack of decarburisation may have been due to the fact that initial CO nucleation had not taken place during the short reaction time, and as such, propagation of the C-O reaction could not have taken place.

A factor known to govern the rate of CO potential and rate of CO nucleation is concentration of reactants [10, 27], and considering the short reaction time compared to that of stationary levitation technique, perhaps the lack of CO nucleation was a result of insufficient oxygen and carbon at the reaction interface; this claim is further supported when comparing the experimental results of similar free fall levitation studies by Baker [56, 63], Roddis [65] and See & Warner [70]. In these particular studies, the marked difference in the experimental set up compared to that of the present study was the use of undiluted oxygen within the reaction column as the reaction gas phase comprised 100% oxygen, and in turn recorded changes in HM carbon content. Adding to the fact that the reactions occurred during more or less similar reaction times, it becomes clear that the limiting factor contributing to the lack of HM decarburisation in the present study was indeed oxygen availability. The oxygen which was available was being used for oxidation of iron, silicon and manganese.

If HM decarburisation of free fall droplets were to have occurred, See & Warner [70] argued that it would have been due to surface decarburisation because for an Fe-4%C alloy subjected to pure oxygen, significant subsurface decarburisation would not occur until approximately 0.9 seconds; before which sputtering/ejection of metal mass (characteristic of subsurface decarburisation), would be less than 1%.

*By reviewing the bulk analysis results for the 20% and 30% gas phase oxygen stationary levitation experiments, there appears to be a lot of variance outside of the error band. This is more pronounced for carbon than any other metalloid in the HM system suggesting strong influence of interaction from other elements such as silicon and manganese on the carbon reaction. Whilst some of this variance may be attributed to the use of different HM batches also; two sets of HM batches were used; one of 4.98wt.% and the other of 4.51 wt.% initial HM carbon, the significant variance between end carbon levels suggest that the experimental technique was not optimised although efforts were made to ensure it was, as displayed through the tightness of control experimental results in Chapter 4 - Section 4.4. It is recommended that this should be kept in mind when reviewing the bulk analysis results and steps to address this is given in Chapter 6 – (Recommendation of Future Work).*

The experimental results for stationary levitation experiments of the present study agrees with the conclusions of other researchers [50-56, 63-65] that gas phase mass transfer of oxygen to the metal surface was the rate controlling step for decarburisation, as the rate of the reaction varied significantly with variation in gas parameters such gas phase oxygen content and can be further proven by application of gas phase mass transfer models. The two models frequently used to determine the mass transfer properties of a metal droplet/ gas system are the Ranz-Marshall and Steinberger-Treybal correlation [75]. The diffusion flux of a gaseous species (i.e. $O_2$) within a gas mixture (i.e. $O_2$-He) is a function of the mass transfer coefficient and the mole fractions of the primary species in the bulk gas phase.

$$N_A = k_{xm} X_{Abulk} \tag{43}$$

Dimensionless numbers can be used to work out the mass transfer coefficient ($k_{xm}$), and by definition the Sherwood number ($Sh_{AB}$) for mass transfer is as follows:

$$Sh_{AB} = \frac{k_{xm} d_p}{D_{AB} C} \tag{44}$$

$$C = \frac{P}{RT} \tag{45}$$

$$N_A = \frac{Sh_{AB} D_{AB} P X_{Abulk}}{d_p RT} \tag{46}$$

A film temperature ($T_f$) representative of the temperature gradient within the gas phase is described as follows:

$$T_f = \frac{T_{droplet} + T_{bulk}}{2} \tag{47}$$

The Ranz-Marshall correlation [75] for levitated and free fall drops only accounts for forced convection and does not take into consideration thermal or concentration gradients. It is expressed as follows:

$$Sh_{AB} = 2.0 + 0.60\,\mathrm{Re}^{0.5}\,Sc^{0.33} \tag{48}$$

$$\mathrm{Re} = \frac{v d_p}{\mu} \tag{49}$$

$$Sc = \frac{\mu}{\rho D_{AB}} \tag{50}$$

The Steinberger-Treybal correlation used by See[70], accounts for forced and natural convection which occurs when the density of gas phase is non uniform due to concentration and temperature gradients. The correlation is expressed as follows:

$$Sh_{AB} = 2.0 + 0.569(\bar{G}r'.Sc)^{0.25} + 0.347\,\mathrm{Re}^{0.62}\,Sc^{0.31} \tag{51}$$

$$\bar{G}r' = Gr' + (\frac{Sc}{\mathrm{Pr}})^{0.5} Gr \tag{52}$$

$$Gr' = \frac{\rho^2 g d_p^3 \alpha (X_{Abulk} - X_{Ainterface})}{\mu^2} \tag{53}$$

$$Gr = \frac{\rho^2 g d_p^3 (T_{droplet} - T_{bulk})}{\mu^2 T_f} \tag{54}$$

$$\mathrm{Pr} = \frac{C_p \mu}{k} \tag{55}$$

$$\alpha = \frac{1}{\rho}(\frac{\partial \rho}{\partial X_A}) \tag{56}$$

The thickness of the gas boundary layer as discussed by Kaplan [50] can also be expressed by Equation 57.

$$k_m = \frac{-PD_{AB}}{RT\delta_{O_2}} \tag{57}$$

The Steinberger-Treybal correlation [75] for gas phase mass transfer was used to determine the gas mass transfer coefficient of oxygen from the gas phase towards the reaction interface and was also used to identify the thickness of the gas boundary layer proposed by Kaplan [50] and Distin [64]. The presence of the oxide at the metal surface restricts direct contact between the metal and gas phase and by doing so, the flow of oxygen to the surface and CO away from the surface may be hindered as the gases diffuse across the oxides as proposed by Ehrlich[89]. The lack of oxygen availability would therefore reduce the rate of decarburisation as shown through the experiments of 10% and 20% gas phase oxygen content (Run 14-24), which in turn would reduce the onset of further silicon and manganese oxidation.

Due to difficulty in identifying a representative gas temperature because of temperature gradients between the metal surface and gas phase, a film temperature ($T_f$) described in Equation 47 was used. Bulk temperature was valued at ~ 1750°C as temperatures within this region was reached towards the end of the 60s oxidation reaction, as shown in the temperature profile in Figure 64.

$v = 5.01x10^{-5} cm^3 / s$
$P = 1atm$
$T_f = 1160.5^o K$
$\mu_{O_2} = 5.89x10^{-4} g / cm.s$
$\mu_{He} = 4.83x10^{-4} g / cm.s$
$\rho_g = 3.99x10^{-4} g / cm^3$
$D_{O_2-He} = 0.7361 cm^2 / s$
$R = 82.06 cm^3 atm / Kmol$

$$Sh_{O_2-He} = 2.0 + 0.60\,\mathrm{Re}^{0.5}\, Sc^{0.33} \tag{58}$$

$$\mathrm{Re} = \frac{v d_p}{\mu} \tag{59}$$

$$Sc = \frac{\mu}{\rho D_{O_2-He}} \tag{60}$$

$$Sh_{O_2-He} = 2.0 + (0.63x0.072^{0.5} x1.82^{0.33}) = 2.21 \tag{61}$$

$$\delta_{O_2} = \frac{d_p}{Sh_{O_2-He}} = \frac{0.78}{2.21} = 0.35cm \quad (62)$$

Therefore,

$$k_{O_2-He} = \frac{D_{O_2-He}}{RT\delta_{O_2}} = \frac{0.74}{82.06x1160.5x0.35} = 2.22x10^{-5} mol/cm^2 s \quad (63)$$

Having obtained the width of the gas boundary layer using Sherwood's dimensionless number, the parameter was then applied to derive the gas phase mass transfer coefficient; $2.22x10^{-5}$ mol/cm$^2$s. This represents the transfer of oxygen at the reaction interface between the metal and oxygen bearing gas. The flux of carbon in the liquid phase from bulk metal to the gas/metal reaction interface was calculated as follows. The rate of reaction for the series of experiments listed in Table 18 was derived by calculating the change in HM carbon content over the 60s reaction time from the experimental results plotted in Figure 37. Carbon diffusivity of $1.8x10^{-3}$mol/cm$^2$s proposed by Distin [64] was also employed for the following calculations as it was found to fit well for carbon saturated iron alloys.

$$Rate = kACb^* \quad (64)$$

$$Rate = -\frac{\Delta C}{t} = -\frac{0.00135 - 0.0075}{60} = 1.025x10^{-4} mol/s \quad (65)$$

$$N = \frac{Rate}{A} = kCb^* \quad (66)$$

$$N = \frac{Rate}{A} = \frac{1.025x10^{-4}}{4\pi\left(\frac{0.78}{2}\right)^2} = 5.36x10^{-5} mol/cm^2 s \quad (67)$$

$$k_C = \frac{5D}{A} = \frac{5x(1.8x10^{-3})}{1.91} = 4.71x10^{-3} mol/cm^2 s \quad (68)$$

$$Cb^* = \frac{N}{k_C} = \frac{5.36x10^{-5}}{4.71x10^{-3}} = 0.011mol \quad (69)$$

The mass transfer coefficient for oxygen gas phase transfer is less than that of carbon diffusion within the liquid metal therefore supporting the hypothesis of the rate controlling step being gas phase oxygen diffusion towards the reaction interface. The calculated mass transfer coefficient of carbon within the liquid metal and diffusion of oxygen at the metal/gas interface correlates well with Distin's who measured values of $3.2x10^{-4}$mol/cm$^2$s and $2x10^{-5}$ mol/cm$^2$s respectively.

The calculation of the gas phase mass transfer coefficient did not take into account the presence of liquid oxide forming at the metal surface therefore diffusion of oxygen to the reaction interface was assumed to be simply through the gas phase alone. However, from surface analysis conducted on numerous samples that have undergone gas/metal reactions under oxidising atmospheres, it has been shown that oxides do exist at the metal surface and further assumed that oxygen diffusion through these liquid oxides take place. Therefore, the actual gas phase mass transfer coefficient value may well be less than that calculated as diffusion of oxygen through the oxide towards the metal surface would be kinetically slower than diffusion of oxygen through the gas phase alone.

The mass transfer coefficient of carbon calculated using the effective diffusivity proposed by Distin [64] was a magnitude of power less than that of the actual mass transfer coefficient derived from the slope of the plot (0.0264cm/mol$^2$s) suggesting that carbon was diffusing to the metal surface quicker than predicted by Distin, but still at rates faster than that of oxygen diffusion to the reaction interface.

### 4.3 Microscopic Surface and Cross-Section Analysis of Hot-metal Droplets

Optical and Electron Microscopy analysis of the reacted metal droplet cross section and surface were conducted to determine the changes in elemental concentration between the bulk and surface of the metal, as well as observing whether the chemical reactions at the surface of the metal produced surface oxides. Optical Microscopy was primarily used to observe the changes in HM carbon content across the metal cross section and whilst this method was entirely qualitative, combustion analysis was used to provide quantitative data to support the interpretation of the qualitative observations to within 0.1wt% of the analysed carbon concentration whilst EPMA analysis provided both qualitative and quantitative (+/- 0.007 wt.%) of the elements and their concentration at the surface of the metal droplet.

### 4.3.1 Optical Microscopy Analysis of Hot-metal Droplet Cross Section

Figures 42a-c are optical images of Runs 2, 3 and 4 which had undergone gas/metal reaction for 10, 30 and 60 seconds respectively within a gas phase consisting of 30% oxygen, and had final metal carbon concentrations of 4.8, 3.9 and 2.4 wt.% respectively.

Figure 42a shows that the sample which had reacted for 10s (Run 2) contained large graphite nodules homogeneously distributed across the metal cross section. The presence of the nodules suggested the metal remained saturated with carbon after 10s reaction time, whilst there was no distinct difference between the distributions of the nodules in the bulk metal and metal surface. Similar homogeneous distribution of graphite nodules were observed for the droplet (Run 3) which had reacted for 30s; see Figure 42b, however, a marked difference to that of the sample which had reacted for 10s was a reduction in size of the nodules whilst maintaining equally as uniform distribution across the metal cross section. The sample which had reacted for 60s (Run 4, Figure 42c) and had a corresponding bulk metal carbon concentration of 2.4 wt.% (measured by combustion analysis) had no visible graphite nodules across the metal cross section even though bulk analysis suggested the droplet still had a high level of carbon within it. Porosity was however observed within the metal and in most cases, the various porosity network connected and extended to or from the metal surface.

Cross sectional optical images of 2g, 3g and 4g samples which had undergone gas/metal (Run 8, 9, 10) and gas/metal/slag (Run 11, 12, 13) reaction for the same length of time (60s) within 20% gas phase oxygen content were captured. For the 3g and 4g samples, no porosity was seen within the metal cross section irrespective of the presence of slag at the metal surface. However a significant amount of porosity was found for the 2g samples (Figure 43a-c) which had final metal carbon concentration of 1.6 wt.% for the droplet of gas/metal reaction (Figure 43a), and 1.8 wt.% for the droplet which included slag material (Figure 43b and 43c).

Qualitatively, a greater volume of porosity was observed to exist immediately beneath the metal surface compared to the bulk of the metal in all cases, suggesting that perhaps this was caused by early entrainment of oxygen and subsurface CO nucleation resulting in generation of gas bubbles beneath the metal surface as reported by several researchers [53-56, 63-65]. Further support for this argument that the observed porosities only represent initial subsurface entrainment of oxygen includes the fact that explosion/sputtering of the

droplet did not take place. Then again considering that the samples were water quenched, the porosities may well have been an effect of droplet shrinkage upon cooling. Nevertheless, the fact that such porosities were not seen for HM droplets of higher end-carbon concentrations (which underwent similar cooling regime) suggests otherwise.

a)

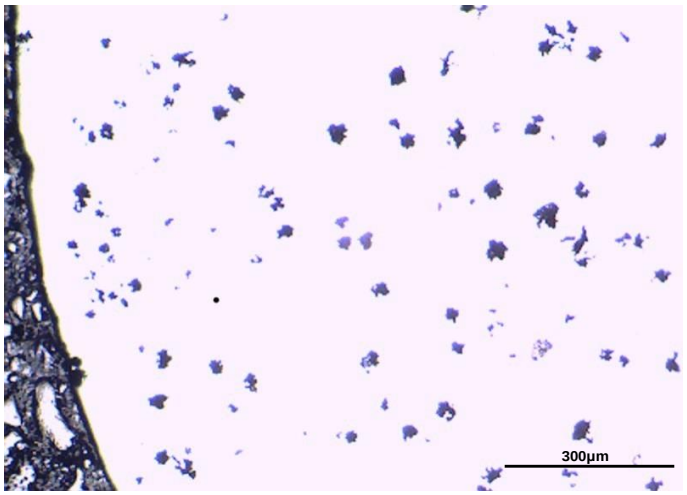


b)

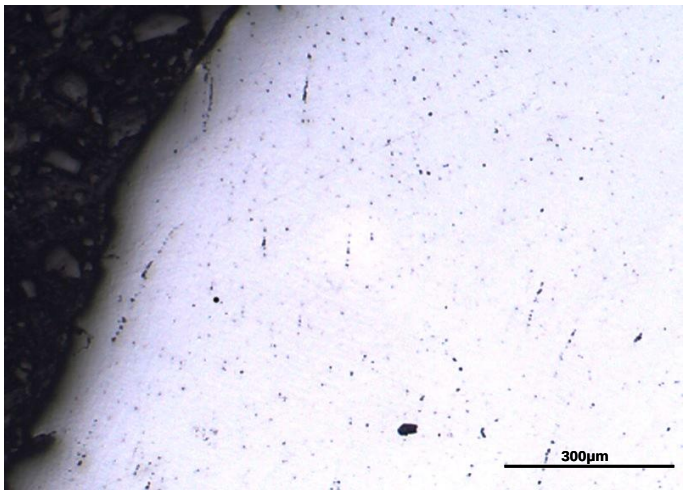


c)

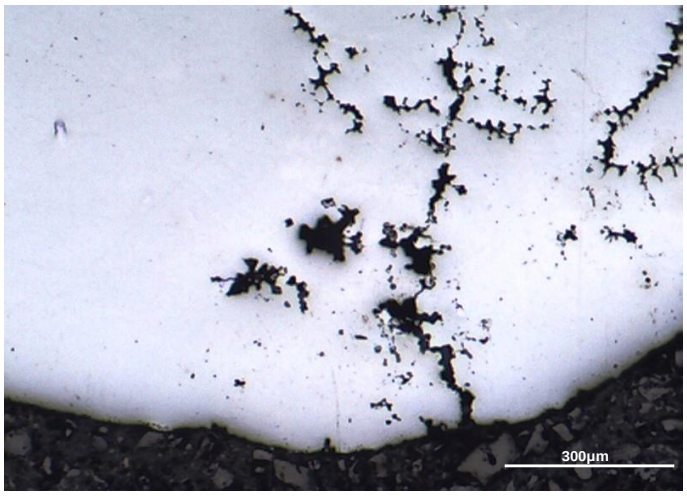


Figure 42: Light micrographs of reacted droplets at a) 10, b) 30 and c) 60 seconds showing graphite nodules and porosities

a)

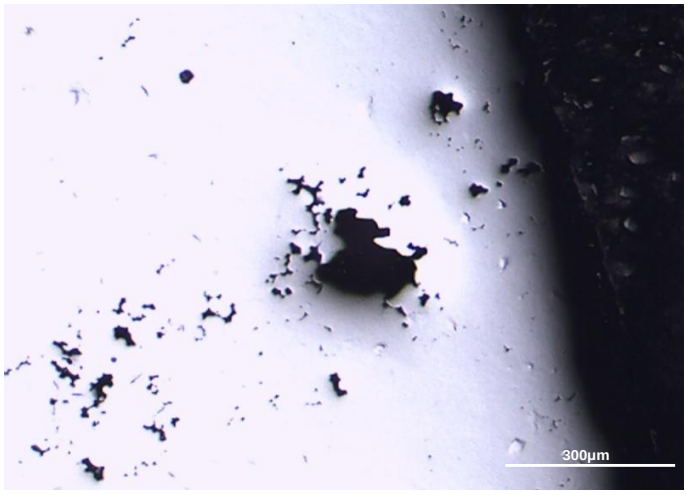


b)

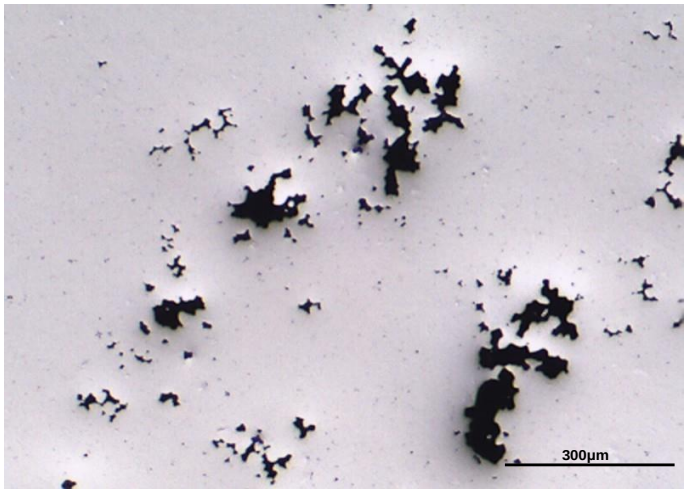


c)

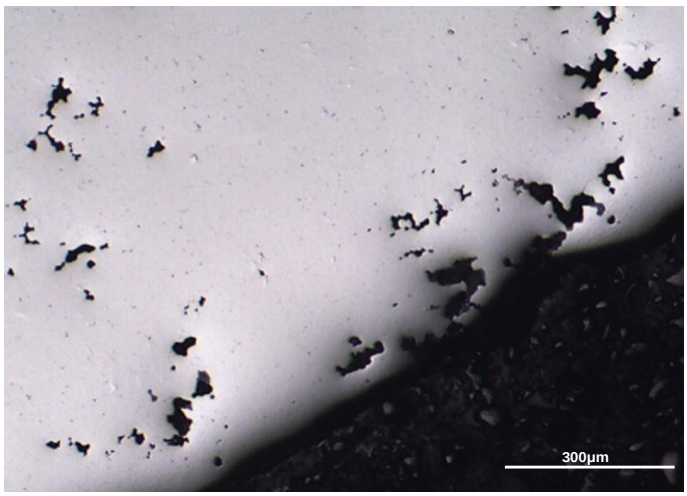


Figure 43: Light micrographs showing porosities in metal cross section for a) 2g, b) 3g and d) 4g samples

### 4.3.2 EPMA Surface Analysis of Hot-metal Droplets

Access to EPMA equipment was limited and as such, the analysis could only be conducted on a few samples; notably the early samples where CaO was introduced into the system (as this particular study formed the basis of moving from using CaO to synthetic basic slag to drive dephosphorisation). The samples analysed (Run 19, 21, 24) had reacted for 10, 30 and 60s respectively under 20% gas phase oxygen concentration at a flow rate of 3LPM with the initial droplet temperature at 1600°C; also, powdered CaO was introduced into the system by dipping the molten HM into the sample holder (cup) filled with CaO powder as described in Chapter 4 - Section 4.1.1. For this particular series of experiments, only stationary levitation experiments were conducted as it was reasoned that if no dephosphorisation was measured for these samples then the likelihood of the reaction occurring during the 0.32s fall would be extremely low. The analysed area was 1000μm x 500μm, and line scans (numbered 1-5 in Figure 46) were conducted to determine the elemental concentration beneath the metal surface.

X-ray intensities of manganese (Figure 44a and 44b) showed regions of high and low manganese concentrations with high manganese concentration at the droplet surface qualitatively identifiable by the bright red bands. The concentration gradient of manganese at the metal surface was qualitatively more evident for the sample which had reacted for 60 seconds (Figure 44c) compared to droplets that had reacted for short time periods.

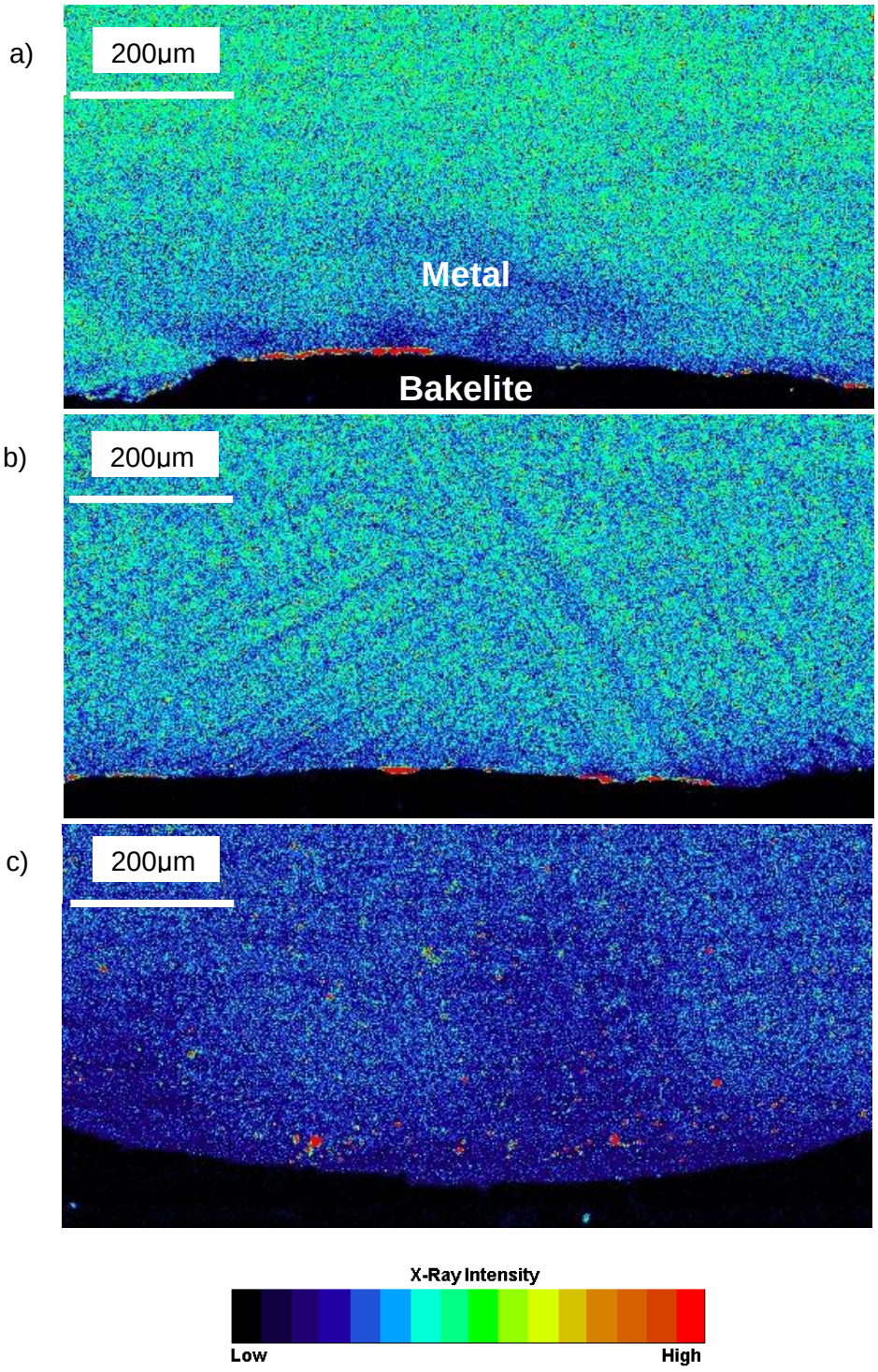


Figure 44: EPMA map of manganese concentration (X-ray intensities) across metal cross section for HM sample reacted in 20% gas phase oxygen for a) 10s, b) 30s and c) 60s

Phosphorus EPMA maps (Figure 45a-45c) showed homogeneous distribution of finely sized high phosphorus concentration regions for the 10s and 30s reaction samples. Higher concentration phosphorus regions were witnessed in the sample reacted for 60 seconds; although this may be due to phosphorus segregation at the grain boundaries/interfaces upon solidification.

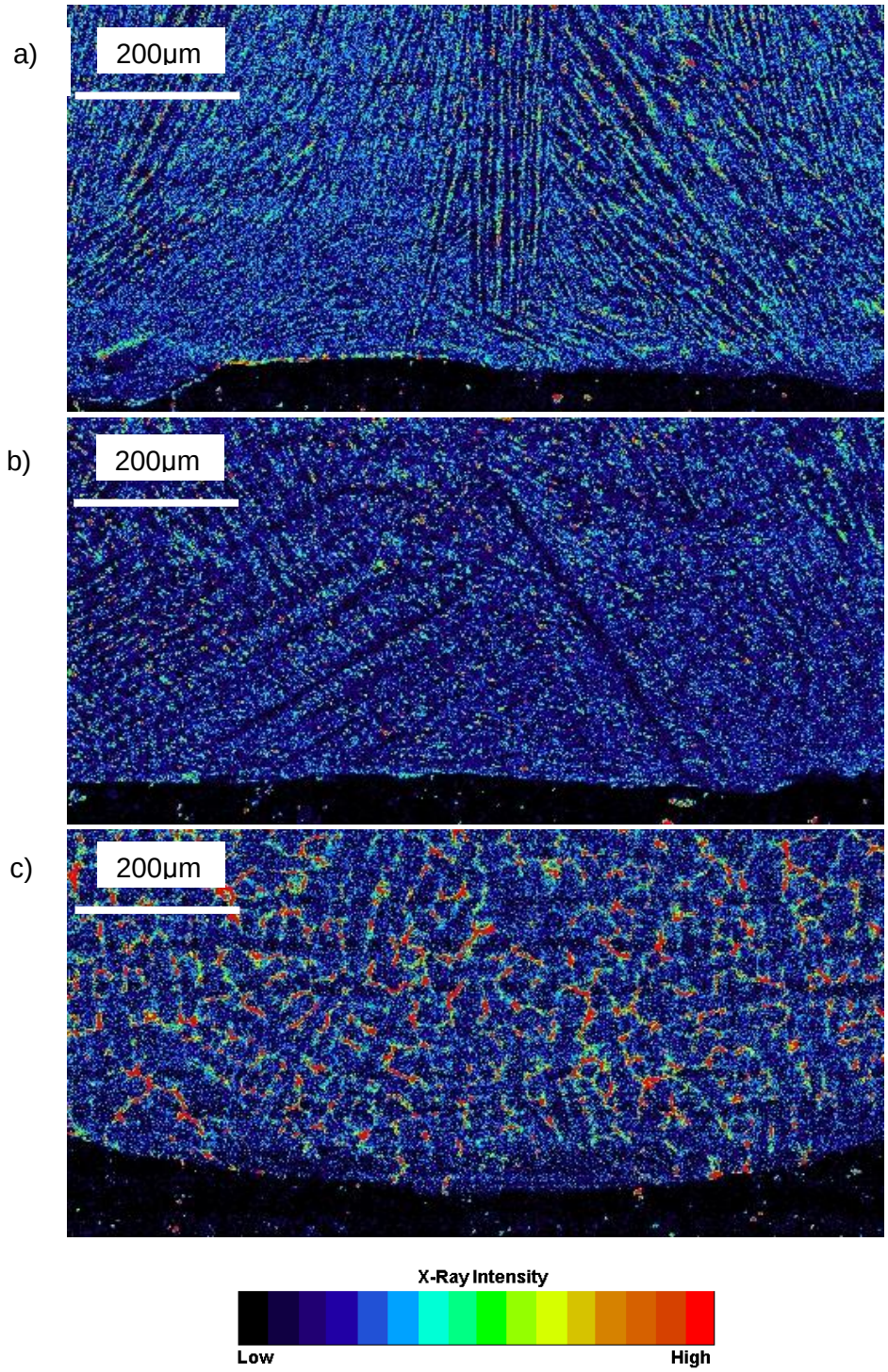


Figure 45: EPMA map of phosphorus concentration (X-ray intensities) across metal cross section for HM sample reacted in 20% gas phase oxygen for a) 10s, b) 30s and c) 60s

Silicon x-ray (Figure 46a-c) intensity was initially high but decreased with reaction time from 10 to 30 seconds. It remained relatively similar for the 30 and 60 seconds reacted sample, but a distinct difference was the metal which had reacted for 60 seconds (Figure 46c), had a wider band of low silicon x-ray intensity spanning along the immediate subsurface of the metal, implying surface depletion of silicon, a finding which correlates well with the plotted results (Figure 47a) of silicon concentration within the same region.

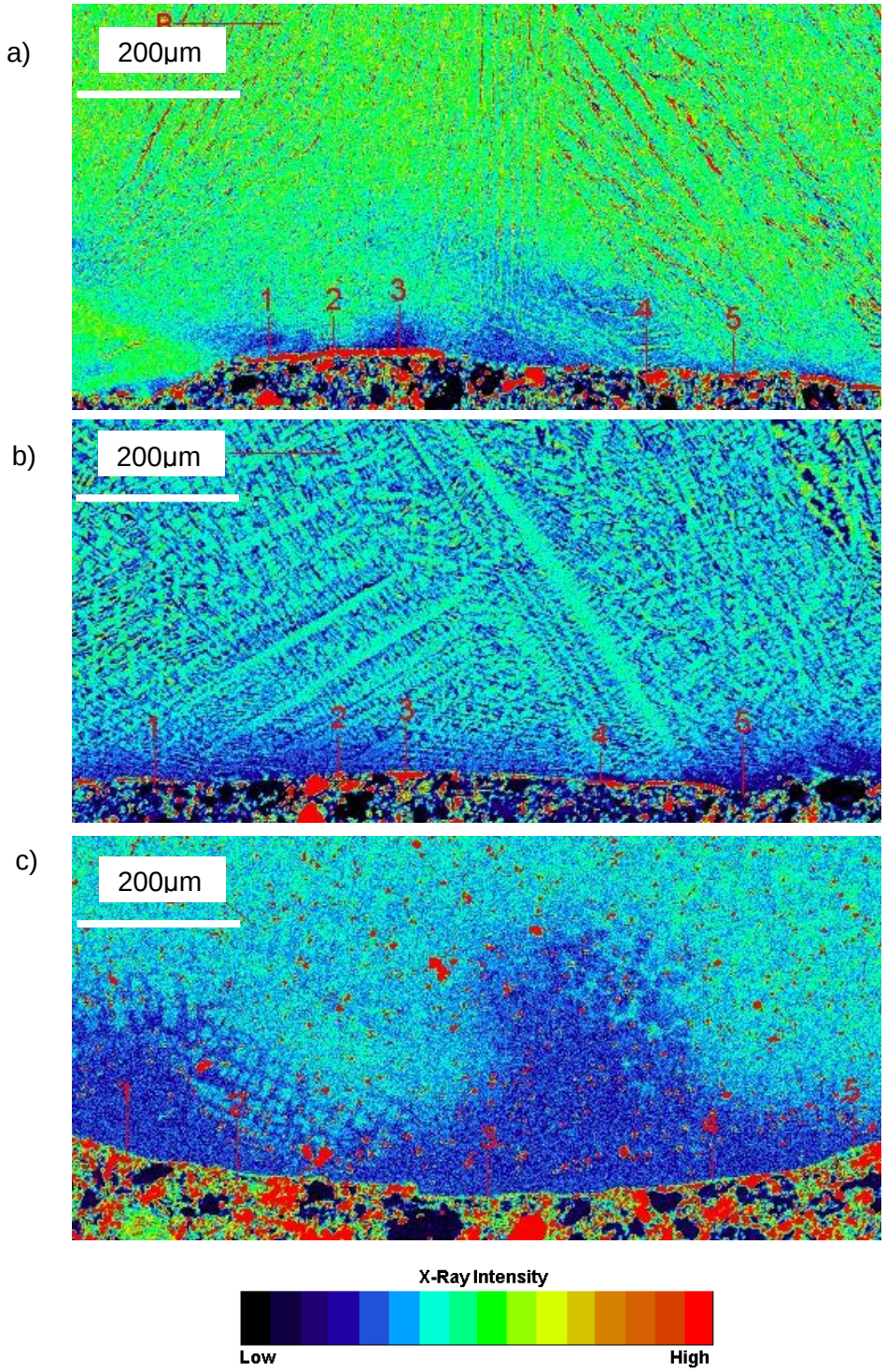


Figure 46: EPMA map of silicon concentration (X-ray intensities) across metal cross section for HM sample reacted in 20% gas phase oxygen for a) 10s, b) 30s and c) 60s

a)

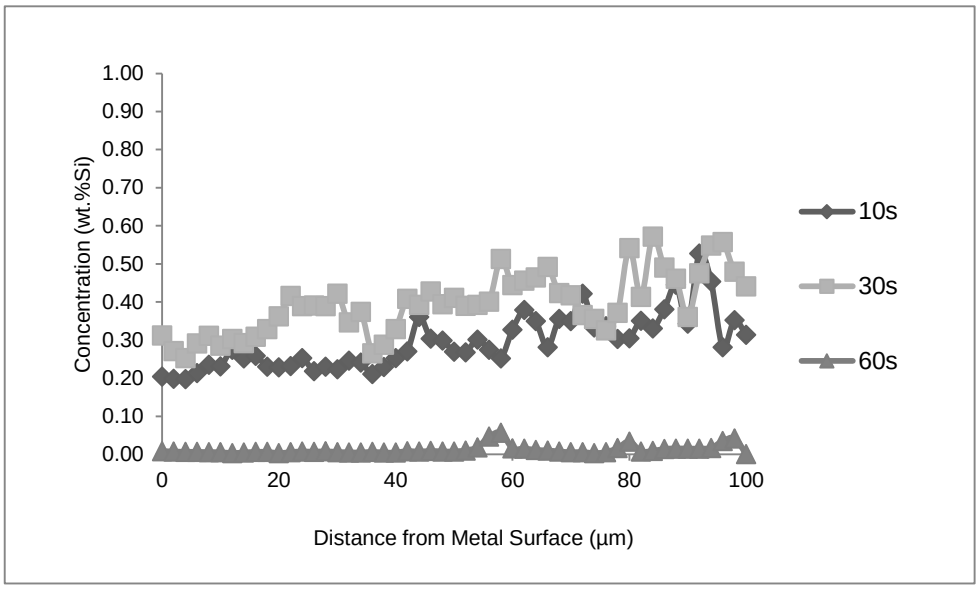


b)

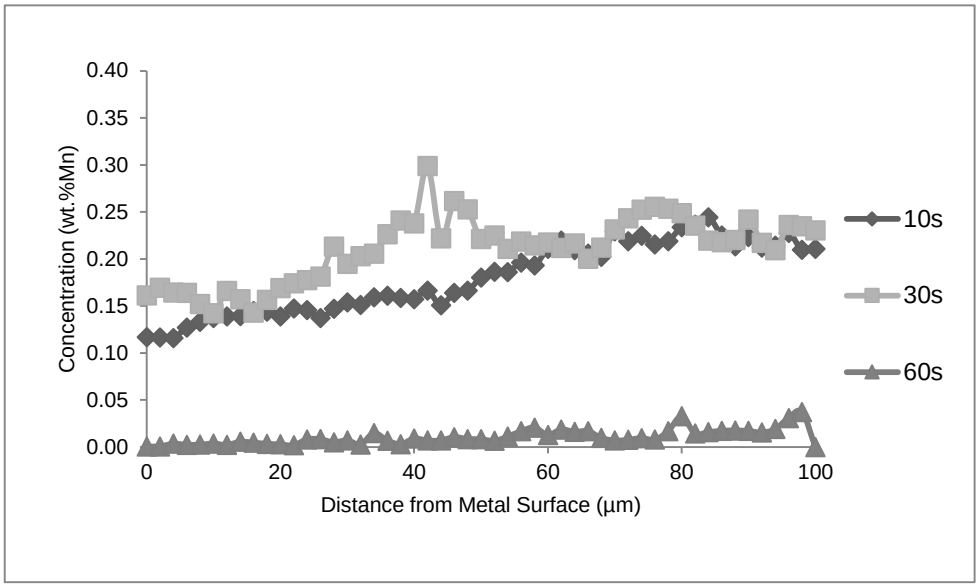


c)

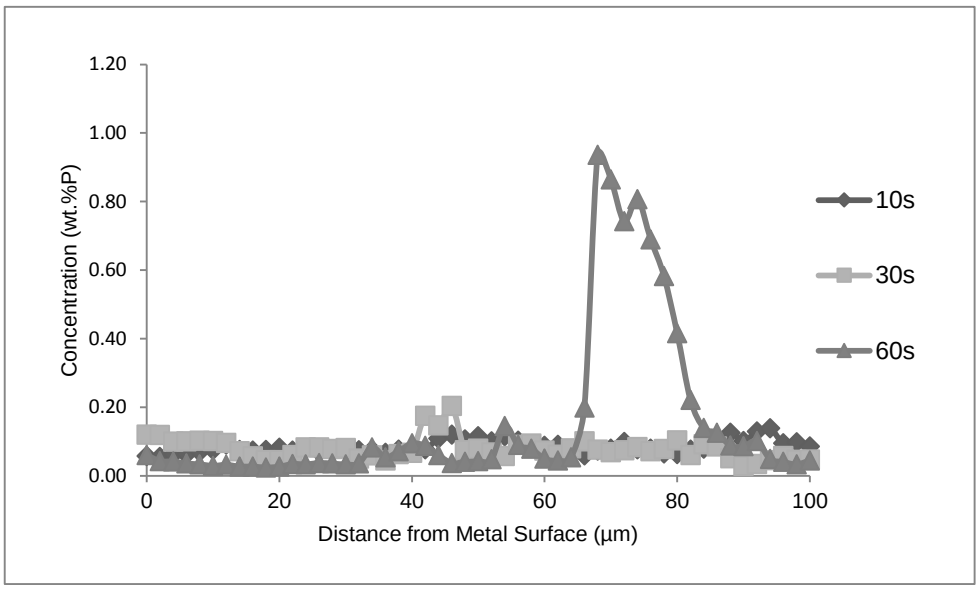


Figure 47: a) Silicon, b) manganese and c) phosphorus concentration gradient between HM surface and bulk for 2g samples reacting under 20%$O_2$:80%He for 10, 30 and 60 seconds reaction time (Run 19, 21, 24)

Silicon and manganese both experienced a concentration gradient with increasing depth into the sample; with the sample comprising lower concentrations at the metal surface, higher subsurface concentrations and even higher bulk HM concentrations measured by ICP-MS and combustion analysis technique. Within the short subsurface distance, this trend was seen for the samples which had reacted for different lengths of times but was most apparent for samples which had undergone shorter reaction procedure. The concentration of both silicon and manganese along the measured distance were higher for the 30 seconds reaction droplet compared to the 10 seconds reaction droplet as the metal surface/ subsurface became enriched in these elements before undergoing further refining leading to extremely low levels of these elements at the surface and subsurface, and also a reduced concentration gradient.

An explanation for this observation may be that the initial rate of mass transfer of these elements to the metal surface was greater than the rate of chemical reaction therefore resulting in the build-up of silicon and manganese at the metal surface. Considering that gas phase oxygen was mostly utilised by HM carbon (after rapid desiliconisation to nearly half the initial HM content) evident through rapid decarburisation compared to other HM elements, whilst oxygen at the surface created a concentration gradient between the metal subsurface and reaction interface, the limited distribution of oxygen to promote silicon and manganese oxidation meant that the chemical reactions were constrained and therefore remained in the metal.

With increasing depth into the subsurface, the concentration gradient reduced and began to plateau indicating that the bulk levels of Si and Mn were greater than 500 μm from the metal surface. Within the 100μm depth, after 60s of reaction time, Si and Mn levels at the surface and subsurface had diminished to near negligible amounts. This level was consistently maintained at longer subsurface depths compared to that of 10 and 30 seconds reaction which experienced concentration gradients away from the metal surface.

As aforementioned, although CaO was introduced into the system, bulk dephosphorisation did not occur as the metal phosphorus content remained at its initial level of 0.09 wt.%. This finding was further supported by the plot (Figure 47c) which showed phosphorus levels at the surface and immediate subsurface to be relatively consistent with distance into the metal. The single large peak in the plot was believed to be representative of a phosphorus segregated region and sized at approximately 25 μm.

If mass transfer of these elements (silicon and manganese) across the reaction interface occurred, then one might argue that the region of surface depletion should not exist because the sites at the surface which had been vacated by the reacted silicon elements would have been replenished with on-coming elements from the bulk metal; in which case a concentration gradient between the bulk and surface metal would not exist as argued by El Kaddah [74], who assumed the droplet behaved like static spheres as the atomic diffusivity ($60x10^{-9}m^2/s$) and effective diffusivity ($40x10^{-9}$ $m^2/s$) were comparatively similar. However, there was a distinct difference in concentrations between the analysed subsurface area and bulk metal concentrations obtained by ICP-MS analysis. Even within the depleted region, a concentration gradient still existed as shown in Figure 47a and Figure 47b, hence suggesting that the rate at which surface sites were replenished was slower than the rate of silicon and manganese oxidation.

Widlund [53] noted that an oxygen gradient of up to 1 μm depth existed at the metal surface, and the present study further showed through subsurface concentration gradients of HM elements (Si and Mn) that an oxygen gradient was also present, although at greater depths than that of Widlund's. More importantly if oxygen had diffused into the metal subsurface, this would suggest that the reaction interface had also extended into the metal subsurface.

Coupled with the fact that oxides (Chapter 4 – Section 4.3.3.) were measured to increase in thickness with reaction time (Figure 50-54), considering that the region of depletion was seen as early as 10seconds into the reaction procedure and grew as the reaction time increased, it could be argued that the oxide components were primarily formed from the elements which initially resided in the region of surface depletion. Were the reaction interface to be further into the metal subsurface, this would also have meant that oxygen from the gas phase would have had to travel greater distances initially through the gas phase and then beyond the metal surface to reach the deeper interface; a scenario which could have led to subsurface CO nucleation (and droplet explosion) which was not observed in the present study.

Having discussed the surface depletion region with respect to the bulk metal, further discussions relate to comparing the metal surface with the immediate subsurface where elemental concentrations have been quantitatively measured and displayed in Figure 47a-

c. It has already been established that within the depletion region, a higher concentration of manganese and silicon existed at 30 seconds compared to 10 seconds; inferring metal mass phase transfer from the bulk metal to the metal surface via the depletion region, followed by rapid removal of these elements from the surface to levels of extreme deficiency (~0wt.%). This can be interpreted by considering that within the first 10 seconds where decarburisation is limited because silicon and manganese oxidation are more favourable, the concentration gradient of silicon and manganese was caused by diffusion of these elements towards the metal surface adjacent to high oxygen concentration gas phase due to its thermodynamic tendency to want to oxidise into a more stable phase.

Within 30 seconds, as shown in Figure 36, carbon oxidation was the dominant reaction after early silicon oxidation and substantial iron oxidation has taken place; both of which are highly exothermic reactions. This would have contributed towards a temperature increase favourable to decarburisation and overall faster reaction kinetics such as mass transfer of silicon and manganese to the metal surface; justifying the increase in surface concentration of these elements during this particular time period.

Although experimental results from literature [50-53] suggested that the rate of decarburisation slows down after a critical carbon level had been reached, then accompanied by simultaneous oxidation of silicon and manganese, in the present study, there was no significant change in bulk Si and Mn content (Table 18) at such carbon levels, although HM Si and Mn levels were negligible (~0wt.%) at the measured subsurface after 60 seconds reaction time. The difference from observations made in literature is perhaps owing to the difference of reaction system whereby their reaction systems were predominantly binary or ternary Fe-C alloys compared to HM samples used in the present study, therefore less competition for oxygen between metal elements.

### 4.3.3 X-EDS Surface Analysis of Hot-metal Droplets

X-EDS analysis (Backscattered electron imagery mode) technique was further used to observe the metal droplet surfaces for samples of Runs 19, 21, 24 having undergone reaction with oxygen and CaO. The observed silicon and manganese concentration gradient (from the EPMA results) between the metal droplet surface and subsurface provided the motivation to conduct closer analysis of the metal surface (i.e. reaction interface), in order to gain further insight into the kinetics of oxidation steelmaking temperature occurring between the different phases.

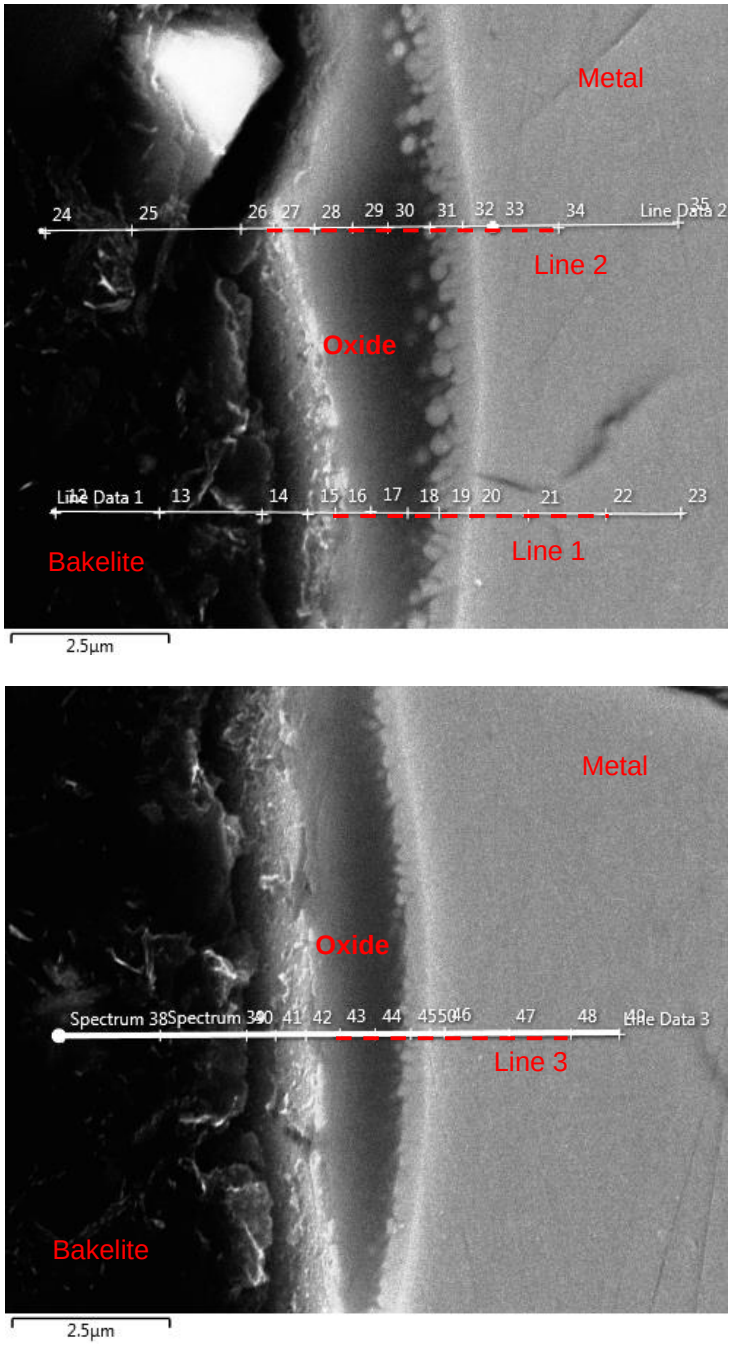


Figure 48: X-EDS image (BSE) of metal/oxide interface for 2g sample reacted with lime for 60 seconds under 20% gas phase oxygen content; Run 24

Table 19: Concentration of chemical elements across liquid oxide phase for 2g HM sample reacting under 20%$O_2$:80%He gas atmosphere for 60s and at an initial HM temperature of 1600°C (Run 24)

| **Line1** | | **Element Concentration (wt.%)** | | | | | | | | |
|---|---|---|---|---|---|---|---|---|---|---|
| **Points** | **Actual Distance (μm)** | **O** | **Mg** | **Al** | **Si** | **P** | **Ca** | **Mn** | **Fe** | **Total** |
| **16** | 0 | 11.75 | 0 | 0 | 12.19 | 0.28 | 9.52 | 6.8 | 59.45 | 100 |
| **17** | 0.63 | 21.33 | 0 | 0 | 12.06 | 0.28 | 7.37 | 4.88 | 54.08 | 100 |
| **18** | 1.13 | 18.17 | 0 | 0 | 9.02 | 0.19 | 4.62 | 3.49 | 64.51 | 100 |
| **19** | 1.75 | 13.28 | 0 | 0 | 4.14 | 0 | 1.63 | 1.77 | 79.17 | 100 |
| **20** | 2.13 | 3.76 | 0 | 0 | 0.64 | 0 | 0.22 | 0.34 | 95.04 | 100 |
| **21** | 3.13 | | 0 | 0 | 0 | 0 | 0 | 0 | 100 | 100 |
| **22** | 4.25 | | 0 | 0 | 0 | 0 | 0 | 0 | 100 | 100 |
| | | | | | | | | | | |
| **Line 2** | | **Element Concentration (wt.%)** | | | | | | | | |
| **Points** | **Actual Distance (μm)** | **O** | **Mg** | **Al** | **Si** | **P** | **Ca** | **Mn** | **Fe** | **Total** |
| **27** | 0 | 16.67 | 0 | 0 | 13.62 | 0.23 | 11.4 | 7.55 | 50.53 | 100 |
| **28** | 0.63 | 25.56 | 0 | 0 | 14.25 | 0.34 | 9.63 | 6.08 | 44.15 | 100 |
| **29** | 1.25 | 24.86 | 0 | 0 | 13.35 | 0.27 | 8.4 | 5.52 | 47.6 | 100 |
| **30** | 1.75 | 21.75 | 0 | 0 | 11.06 | 0.27 | 6.31 | 4.15 | 56.46 | 100 |
| **31** | 2.38 | 15.74 | 0 | 0 | 4.22 | 0 | 2.01 | 2.17 | 75.86 | 100 |
| **32** | 2.88 | 7.86 | 0 | 0 | 1.09 | 0 | 0.42 | 0.63 | 90 | 100 |
| **33** | 3.38 | 1.12 | 0 | 0 | 0 | 0 | 0 | 0 | 98.88 | 100 |
| **34** | 4.38 | 0 | 0 | 0 | 0 | 0 | 0 | 0 | 100 | 100 |
| | | | | | | | | | | |

Table 19 continued

| Line 3 | | Element Concentration (wt.%) | | | | | | | | |
|---|---|---|---|---|---|---|---|---|---|---|
| **Spectrum Label** | **Actual Distance (μm)** | **O** | **Mg** | **Al** | **Si** | **P** | **Ca** | **Mn** | **Fe** | **Total** |
| **42** | 0 | 15.45 | 0 | 0 | 12.41 | 0.33 | 9.25 | 6.23 | 56.33 | 100 |
| **43** | 0.63 | 20.91 | 0 | 0 | 12.09 | 0.29 | 7.26 | 4.97 | 54.47 | 100 |
| **44** | 1.13 | 17.75 | 0 | 0 | 9.23 | 0 | 4.58 | 3.37 | 65.07 | 100 |
| **45** | 1.50 | 11.65 | 0 | 0 | 2.6 | 0 | 0.94 | 1.46 | 83.35 | 100 |
| **46** | 1.75 | 1.85 | 0 | 0 | 0.25 | 0 | 0 | 0 | 97.9 | 100 |
| **47** | 2.75 | 0 | 0 | 0 | 0 | 0 | 0 | 0 | 100 | 100 |
| **48** | 3.63 | 0 | 0 | 0 | 0 | 0 | 0 | 0 | 100 | 100 |

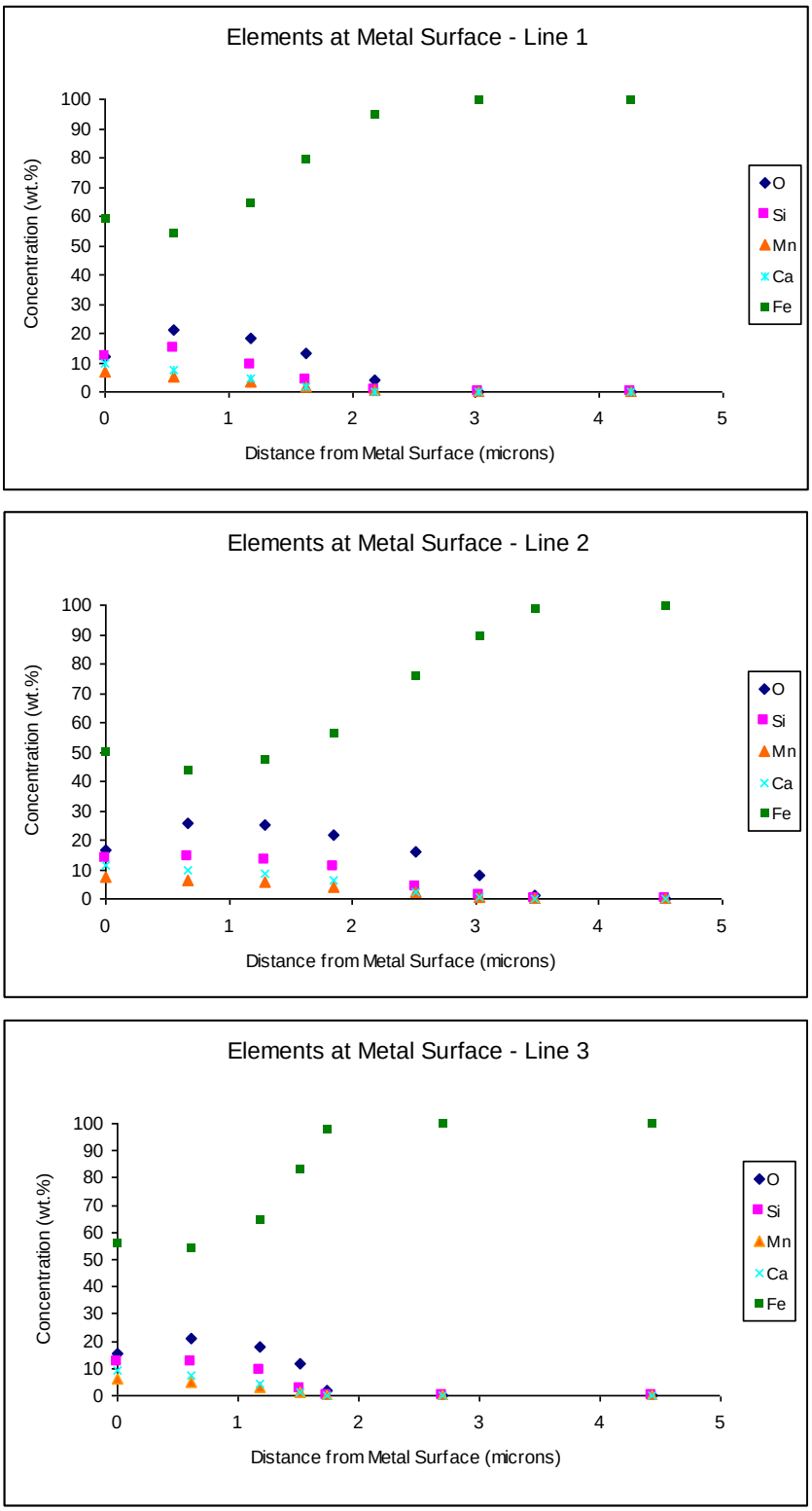


Figure 49: Concentration of elements across oxide phase for Run 24

The red dashed lines in Figure 48 represent the area of oxide analysis, and the concentrations of the elements are plotted in Figure 49. These areas were determined by identifying the point at which magnesium and aluminium (both from the Bakelite only) were no longer detectable (this was assumed to be the metal surface edge) and the point at which Fe was 100wt.% (assumed to be subsurface metal). This method of identifying the boundaries of the metal/oxide surface proved effective as only the Bakelite contained magnesium and aluminium. The scale bar at the bottom left of the X-EDS images were then used to approximate the width of the oxide band.

Whilst the line scans of the droplets that reacted at 10, 30 and 60 seconds measured a concentration gradient of silicon and manganese getting richer towards the metal surface from subsurface, oxygen was also measured at the subsurface and found to decrease with increased depth into the metal. What appeared to be liquid oxide given the levels of Si, Mn and Ca (from the CaO introduced into the system), was present at the metal surface for sample which had reacted for 60 seconds. The oxide band spanned approximately 2.5μm and the concentrations of the elements within the band are given in Figure 49.

Although CaO was detected in the liquid oxide, no change in HM phosphorus was recorded, and whilst a CaO concentration gradient was seemingly present, it remained questionable whether the CaO was fully dissolved in the liquid slag or remained as free-lime given the high liquidus temperature of CaO and the relatively short reaction time. Nevertheless, these results held promise for further work which was conducted by analysing the growth of the surface oxide and the effect of experimental parameters such as droplet weight/size and gas phase oxygen concentration on the development of the oxide.

Taking into consideration that poor CaO dissolution into the liquid oxide may have contributed to the lack of phosphorus removal, a low liquidus (1500°C) basic synthetic slag (composition of slag is detailed in Chapter 3 - Section 3.2.2.1) was prepared with the ratios of its constituent obtained from literature [79]. Its high initial FeO content (40 wt.%) ensured that the slag was liquid at the operational temperature of 1600°C therefore aiding mixing with the liquid oxide at the metal surface with the aim of promoting phosphorus transfer into the basic and high oxygen potential slag. Whilst acknowledging that FeO concentration is perhaps greater than that of BOS slag; notably early BOS slag where FeO concentration ranges between 20% and 30% [3], experimental constraints such as limited

contact time between the HM droplet and slag were factors which influenced the slag design; as would be the case if HM dephosphorisation is to occur within the falling procedure of the proposed HM dephosphorisation pre-treatment process [14]. The contribution of oxygen from FeO in the synthetic slag could not be quantified in the corresponding set of experiments, but given the importance of high oxygen potential slag necessary for dephosphorisation, its presence within the slag mix would suggest a greater likelihood of slag/metal reaction as further discussed below.

From the X-EDS image and concentration plots given in Figure 48 and 49 respectively, it is clear that an oxide band existed at the surface of the reacted HM sample which had been subjected to CaO in an attempt to instigate slag/metal reaction such as dephosphorisation. Although the dephosphorisation reaction was unsuccessful as no change in HM phosphorus content was recorded, oxides of silicon and manganese was measured in the liquid oxide phase, with greater concentrations closer to the metal/oxide interface compared to the gas/metal interface. It has already been shown through EPMA analysis that at such reaction times, HM concentrations of Si and Mn at the metal surface were extremely low, and this is further supported by the measurement of near 100% Fe concentration in the bulk metal by X-EDS analysis. Although the passivity of the oxide was not measured in the present study, one can expect that as the silicon content in the oxide increases, the passivity of the oxide may change and become increasingly restrictive to oxygen diffusion towards the metal surface and hence limit further oxidation reactions occurring, as noted by Radzilowski [72, 75].

The general consensus between studies that have observed oxide formation during such reactions is that the oxide consists of $SiO_2$ and FeO. See and Warner [70] noted that FeO-$SiO_2$ oxide existed for his Fe-C-Si reactions whilst Sun and Pehlke [51, 52] claimed the same but with a small manganese oxide constituent given its lower HM concentration in the metal; hence, both correlating well with that of the present study. Assuming the first oxide formed was FeO due to its abundance, upon further oxidation of HM Si and Mn and hence increased concentrations within the liquid oxide, their respective activities within the liquid oxide would have reduced, marking a change in their respective Gibbs free energy, which can be represented as follows:

$$\Delta G = \Delta G^{o} + RT \ln K \qquad (70)$$

As a result, a driving force would have been established causing the reaction to move towards the right of their respective chemical reaction equations, increase the activities of the individual oxides favourable for attaining a high equilibrium constant.

$$[C]+[O]=CO \tag{71}$$

$$\ln K_c = \ln \frac{P_{CO}}{a_C a_O} \tag{72}$$

$$[Si]+2[O]=SiO_{2(RS)} \tag{73}$$

$$\ln K_{Si} = \ln \frac{a_{SiO_2}}{a_{Si} a_O^2} \tag{74}$$

$$[Mn]+[O]=MnO_{(RS)} \tag{75}$$

$$\ln K_{Mn} = \frac{a_{MnO}}{a_{Mn} a_O} \tag{76}$$

$$[Fe]+[O]=FeO_{(RS)} \tag{77}$$

$$\ln K_{Fe} = \frac{a_{FeO}}{a_{Fe} a_O} \tag{78}$$

#### 4.3.3.1 Change in Oxide Composition and Thickness with Reaction Time

For gas-metal reactions of 2g droplets that reacted under 30% oxygen gas phase content (Runs 2, 3 and 4), distinct oxide bands were detected on the metal's surface; containing oxygen, silicon, manganese and iron.

Point analysis was taken along the line scans spanning the width of the oxide bands. Several line scans were done per droplet to give a good representation of the composition and dimensions of the oxide band. Figure 50 and Figure 51 shows that for 10s reaction, the oxide band already had a thickness of up to 4μm. Iron levels were found to increase in the oxide as the point of analysis in the oxide approached the metal surface, whilst silicon, manganese levels remained relatively stable across the width of the band. Oxygen content in the oxide band was higher at the oxide/gas interface and decreased along the gradient towards the metal surface.

For reactions at 30 seconds (Figure 52 and 53), the oxide band increased in thickness approximately two folds, but the concentrations of manganese and oxygen remained relatively identical to that of the droplet which had reacted for 10 seconds. Silicon levels were inconsistent between the 2 sites which were analysed as was the iron content. For the droplet which reacted for 60 seconds (Figure 54), whilst surface oxide proved difficult to locate; for reasons later discussed in this chapter, the single surface oxide that was detected spanned approximately 13μm in thickness, and consisted of relatively uniform manganese and silicon levels across the band. Iron concentration was at its lowest when compared to its concentrations for reactions of short time, and had similar concentrations with oxygen across the width of the oxide band.

Table 20: Concentration of elements across oxide phase (Refers to Fig. 50 and 51)

| **Site 1** | | **Element Concentration (wt.%)** | | | | | | | | | | |
|---|---|---|---|---|---|---|---|---|---|---|---|---|
| **Points** | **Actual Distance (µm)** | **O** | **Mg** | **Al** | **Si** | **P** | **S** | **Ca** | **Ti** | **Mn** | **Fe** | **Total** |
| 2 | 0 | 4.92 | 0 | 0 | 15.08 | 0.3 | 0 | 0.47 | 1.85 | 18.04 | 59.34 | 100 |
| 3 | 1 | 34.39 | 0 | 0.12 | 15.73 | 0.36 | 0 | 0.26 | 1.21 | 11.14 | 36.79 | 100 |
| 4 | 2 | 36.1 | 0 | 0.16 | 15.48 | 0.34 | 0 | 0.28 | 1.05 | 10.65 | 35.94 | 100 |
| 5 | 2.5 | 31.48 | 0 | 0.14 | 15.94 | 0.37 | 0 | 0.27 | 1.21 | 11.15 | 39.45 | 100 |
| 6 | 4 | 24.55 | 0 | 0 | 13.13 | 0.33 | 0 | 0.17 | 0.97 | 9.16 | 51.69 | 100 |
| | | | | | | | | | | | | |
| **Site 2** | | **Element Concentration (wt.%)** | | | | | | | | | | |
| **Points** | **Actual Distance (µm)** | **O** | **Mg** | **Al** | **Si** | **P** | **S** | **Ca** | **Ti** | **Mn** | **Fe** | **Total** |
| 3 | 0 | 17.87 | 0 | 0 | 12.68 | 0.14 | 0 | 0.24 | 1.12 | 12.67 | 55.28 | 100 |
| 4 | 0.416 | 29.8 | 0 | 0.11 | 14.59 | 0.16 | 0 | 0.23 | 0.9 | 10.64 | 43.58 | 100 |
| 5 | 0.832 | 33.45 | 0 | 0.17 | 14.86 | 0.16 | 0 | 0.17 | 1.11 | 9.7 | 40.38 | 100 |
| 6 | 1.456 | 32.78 | 0 | 0 | 16.22 | 0.15 | 0 | 0.17 | 1.03 | 11.61 | 38.03 | 100 |
| 7 | 2.08 | 30.14 | 0 | 0 | 15.49 | 0.18 | 0 | 0.15 | 1.1 | 12.08 | 40.86 | 100 |
| 8 | 2.704 | 26.36 | 0 | 0 | 14.14 | 0.16 | 0 | 0.16 | 0.89 | 10.45 | 47.85 | 100 |
| 9 | 3.328 | 20.28 | 0 | 0 | 10.44 | 0.16 | 0 | 0.12 | 0.57 | 6.95 | 61.46 | 100 |

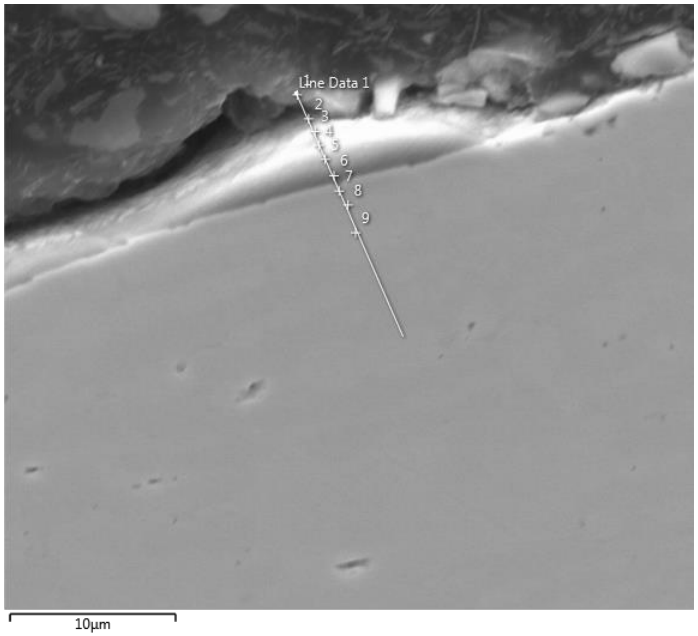


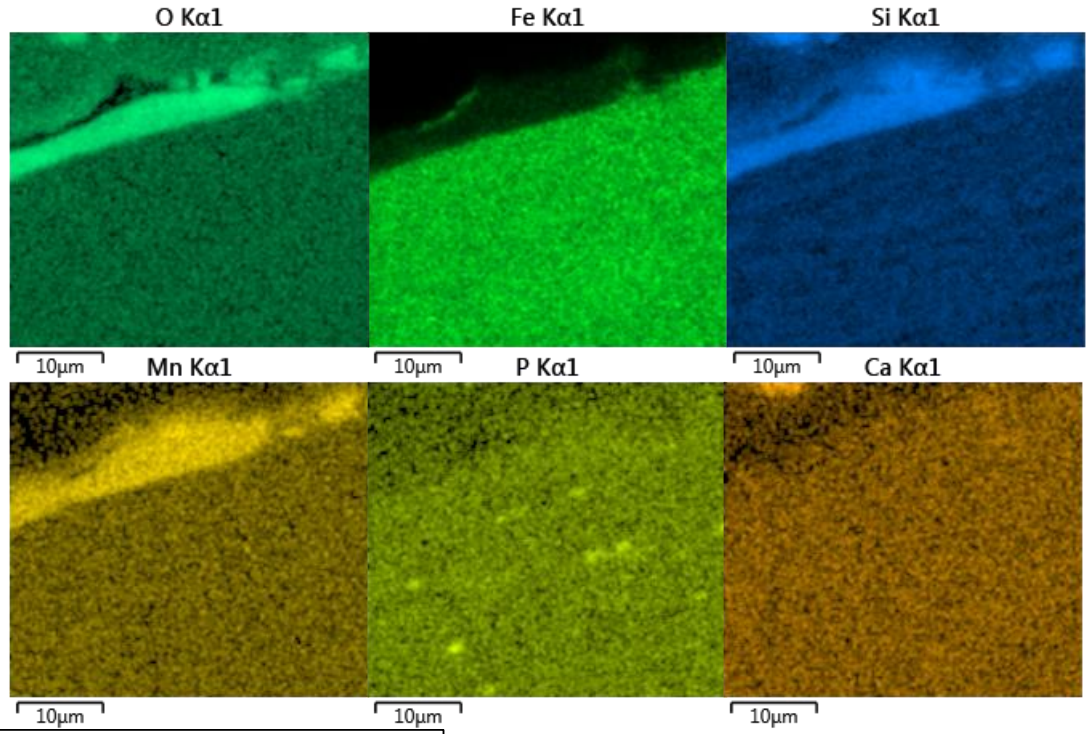


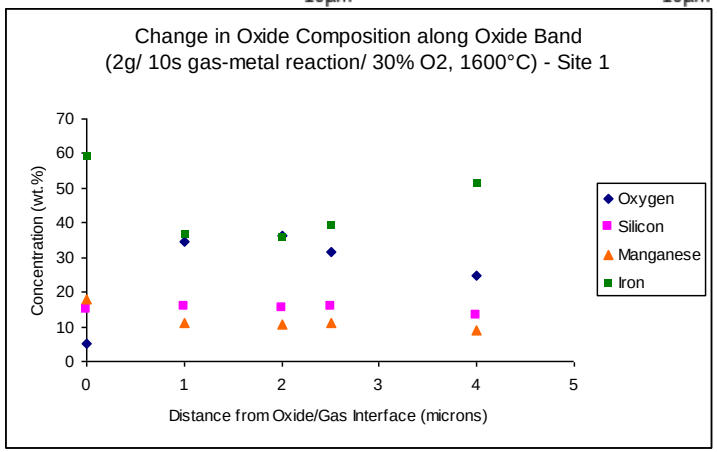


Figure 50: BSE/X-EDS image of surface oxide for 2g HM sample at 10s reaction time (Run 2) Site 1

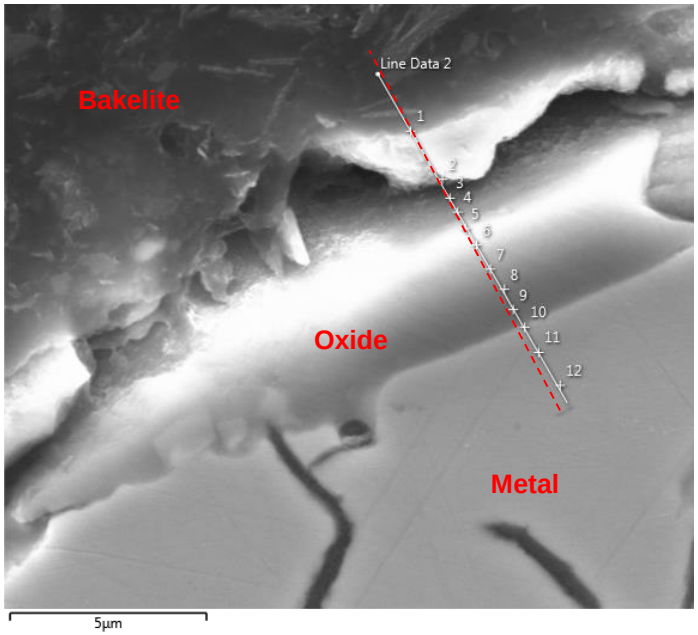


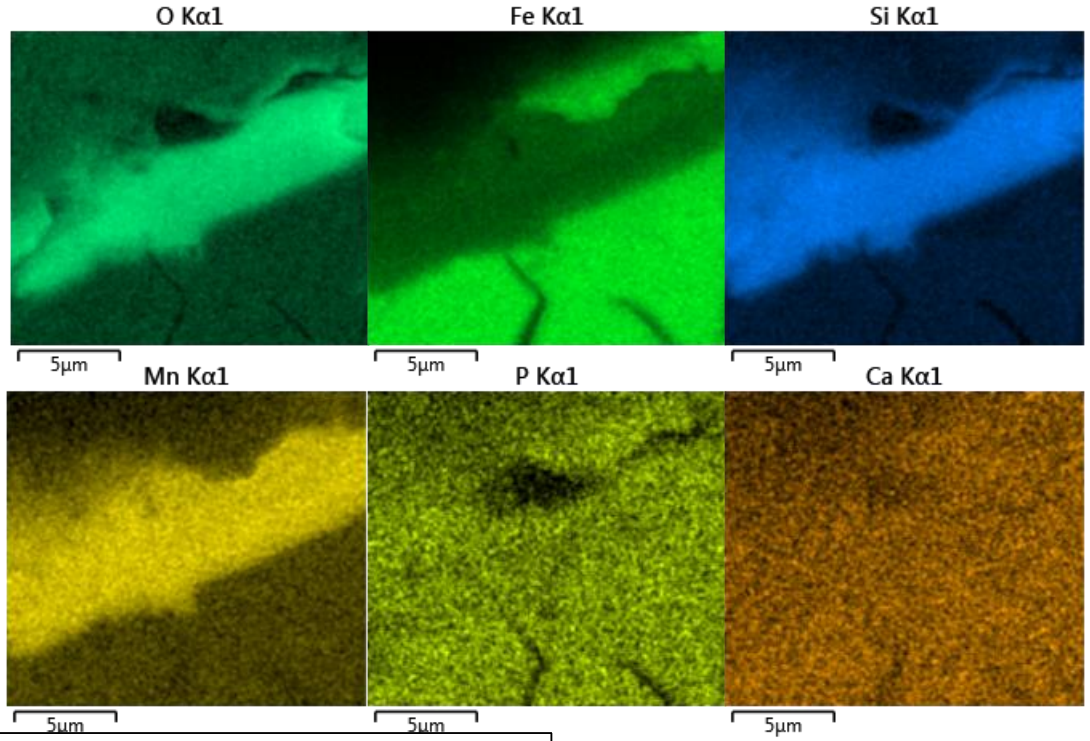


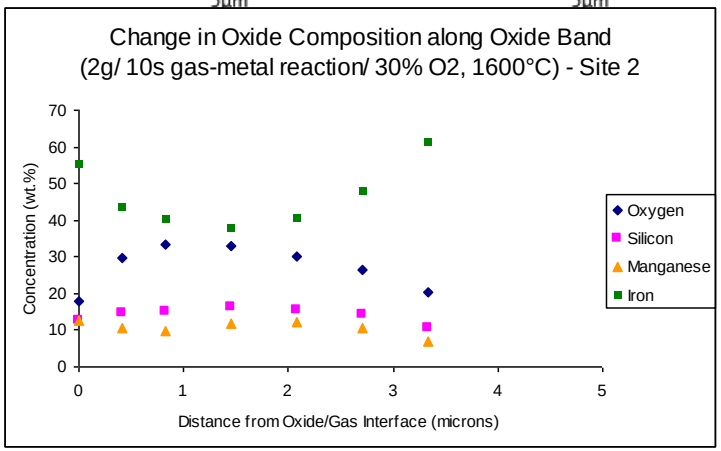


Figure 51: BSE/X-EDS image of surface oxide for 2g HM sample at 10s reaction time (Run 2) Site 2

Table 21: Concentration of elements across oxide phase (Refers to Fig. 52 and 53)

| **Site 1** | | **Element Concentration (wt.%)** | | | | | | | | | | |
|---|---|---|---|---|---|---|---|---|---|---|---|---|
| **Points** | **Actual Distance (µm)** | **O** | **Mg** | **Al** | **Si** | **P** | **S** | **Ca** | **Ti** | **Mn** | **Fe** | **Total** |
| 3 | 0 | 0.44 | 0 | 0.21 | 19.87 | 0.26 | 0 | 0.34 | 2.43 | 18.21 | 58.24 | 100 |
| 4 | 1.18 | 0.8 | 0 | 0.35 | 19.72 | 0.5 | 0 | 0.19 | 4.14 | 17.19 | 57.09 | 100 |
| 5 | 2.36 | 5.18 | 0 | 0.24 | 23.29 | 0.44 | 0 | 0.23 | 2.37 | 16.54 | 51.7 | 100 |
| 6 | 3.54 | 38.02 | 0 | 0.21 | 16.91 | 0.27 | 0 | 0.12 | 1.23 | 10.98 | 32.25 | 100 |
| 7 | 4.72 | 41.51 | 0 | 0.18 | 15.98 | 0.18 | 0 | 0 | 1.51 | 10.25 | 30.39 | 100 |
| 8 | 5.31 | 41.34 | 0 | 0 | 16.41 | 0.17 | 0 | 0.09 | 1.15 | 10.46 | 30.38 | 100 |
| 9 | 7.08 | 35.9 | 0 | 0 | 15.84 | 0.22 | 0 | 0.11 | 1.16 | 10.48 | 36.29 | 100 |
| | | | | | | | | | | | | |
| **Site 2** | | **Element Concentration (wt.%)** | | | | | | | | | | |
| **Points** | **Actual Distance (µm)** | **O** | **Mg** | **Al** | **Si** | **P** | **S** | **Ca** | **Ti** | **Mn** | **Fe** | **Total** |
| 3 | 0 | 3.83 | 0.24 | 0.32 | 11.97 | 0.4 | 0.3 | 0 | 7.75 | 11.8 | 63.4 | 100 |
| 4 | 0.82 | 19.57 | 0.22 | 0.24 | 8.09 | 0.24 | 0 | 0 | 9 | 9.92 | 52.72 | 100 |
| 5 | 2.05 | 31.32 | 0 | 0.2 | 7.81 | 0.2 | 0 | 0 | 8.42 | 8.67 | 43.38 | 100 |
| 6 | 3.075 | 32.04 | 0 | 0.17 | 11.95 | 0.24 | 0 | 0 | 1.79 | 9.94 | 43.87 | 100 |
| 7 | 4.305 | 33.01 | 0 | 0.16 | 10.85 | 0.27 | 0 | 0 | 1.47 | 8.42 | 45.83 | 100 |
| 8 | 5.74 | 28.72 | 0 | 0.2 | 9.51 | 0.19 | 0 | 0 | 0.71 | 5.57 | 55.11 | 100 |

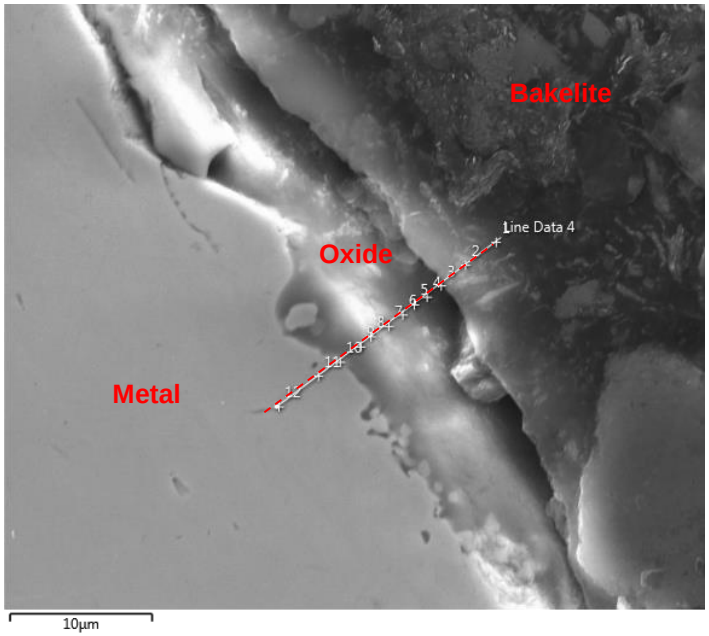


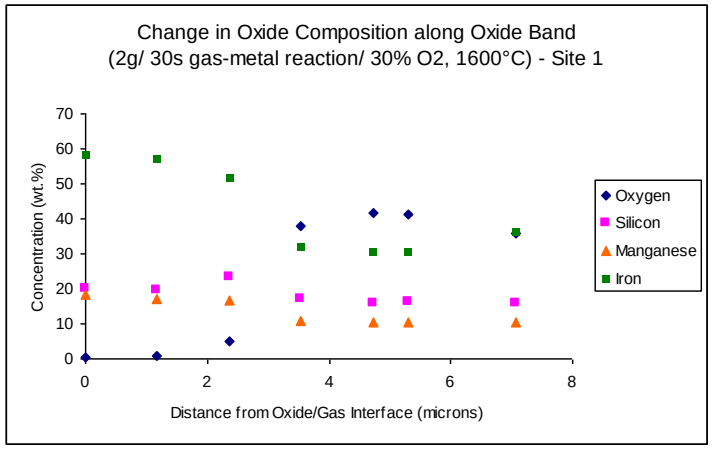


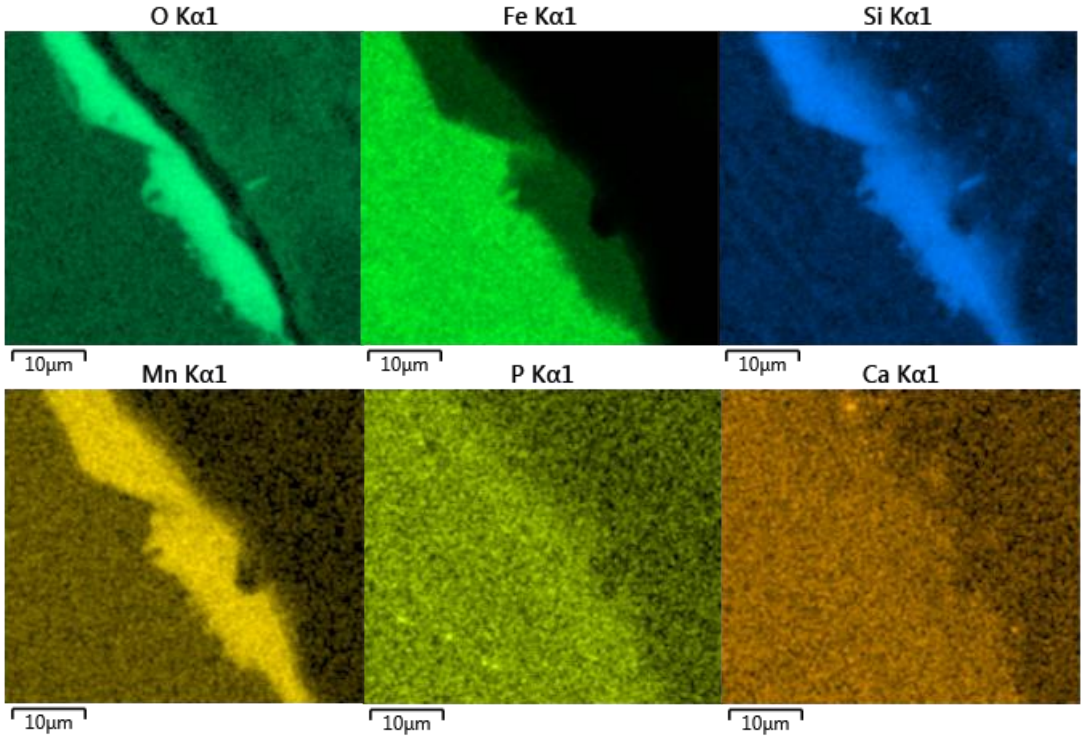


Figure 52: BSE/X-EDS image of surface oxide for 2g HM sample at 30s reaction time and change of oxide composition along its width. (Run 3)

Site 1


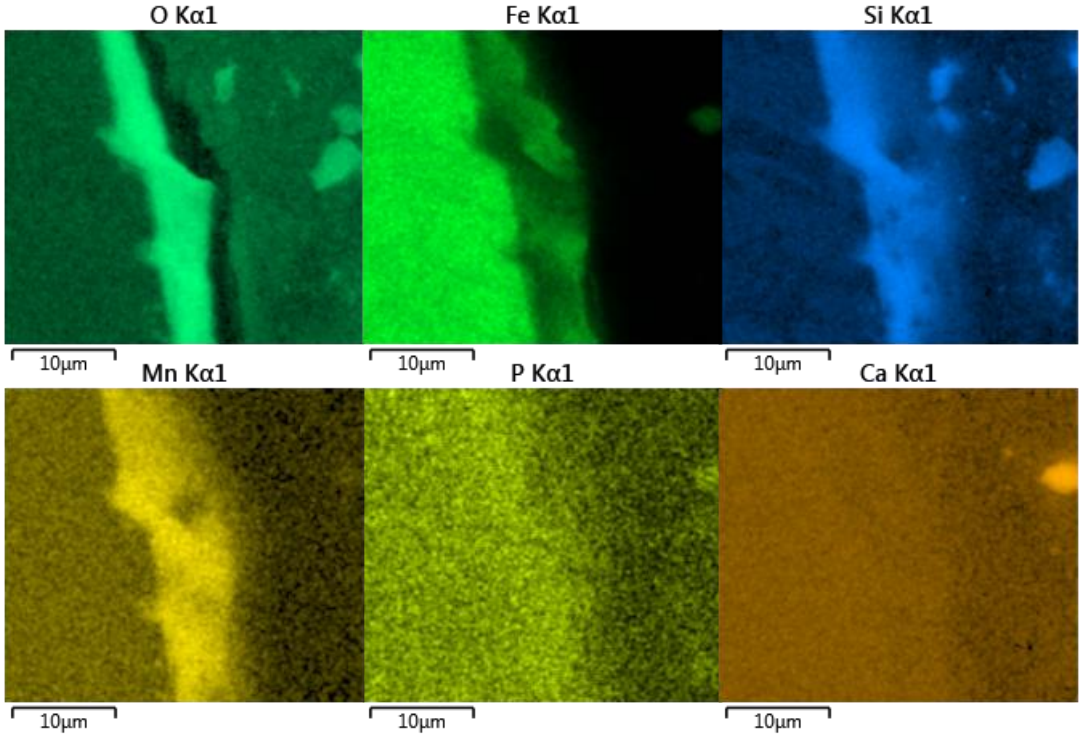


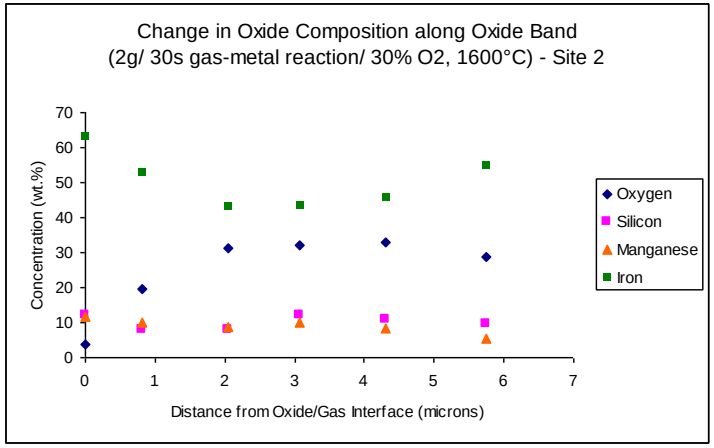


Figure 53: BSE/X-EDS image of surface oxide for 2g HM sample at 30s reaction time and change of oxide composition along its width. (Run 3) Site 2

Table 22: Concentration of elements across oxide phase (Refers to Fig. 54)

| | | Element Concentration (wt.%) | | | | | | | | | | |
|---|---|---|---|---|---|---|---|---|---|---|---|---|
| **Points** | **Actual Distance (µm)** | **O** | **Mg** | **Al** | **Si** | **P** | **S** | **Ca** | **Ti** | **Mn** | **Fe** | **Total** |
| 3 | 0 | 15.81 | 0 | 0.45 | 26.93 | 0 | 0 | 0.38 | 2.36 | 12.69 | 41.37 | 100 |
| 4 | 3.72 | 32.32 | 0 | 0.15 | 24.24 | 0 | 0 | 0.12 | 2.14 | 10.46 | 30.58 | 100 |
| 5 | 6.51 | 31.96 | 0 | 0 | 20.97 | 0 | 0 | 0 | 2.15 | 11.35 | 33.57 | 100 |
| 6 | 10.23 | 30.38 | 0 | 0 | 19.56 | 0 | 0 | 0 | 2.14 | 11.96 | 35.96 | 100 |
| 7 | 13.02 | 32.67 | 0 | 0 | 25.24 | 0 | 0 | 0 | 2.02 | 9.46 | 30.6 | 100 |

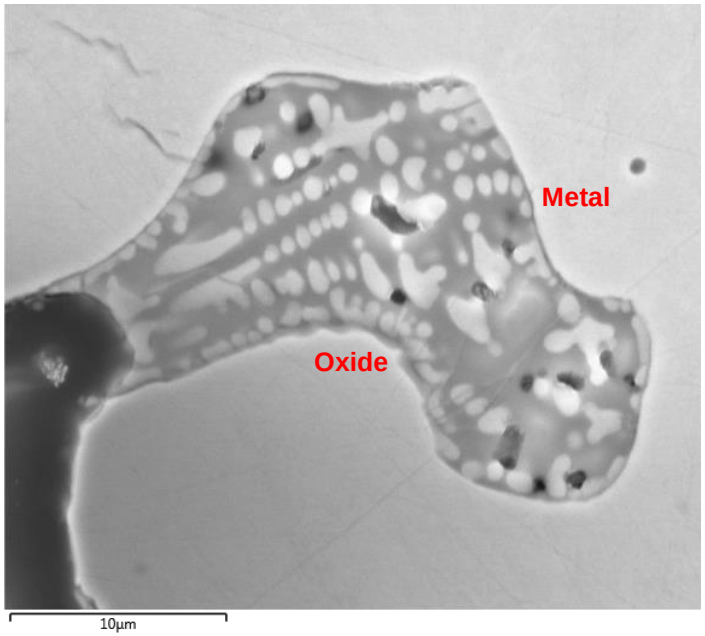


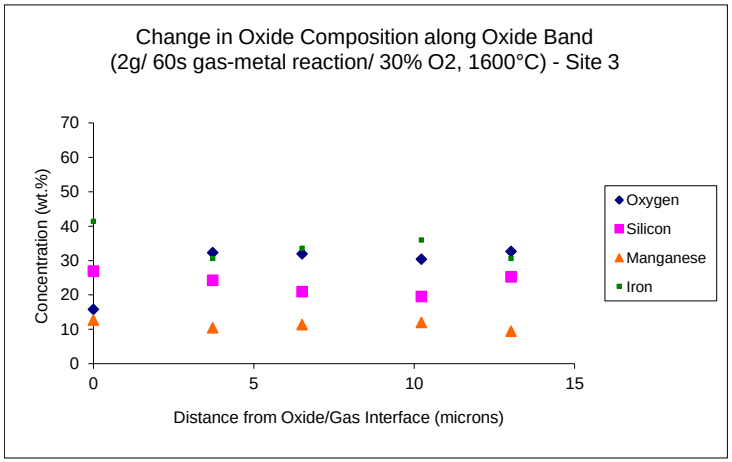


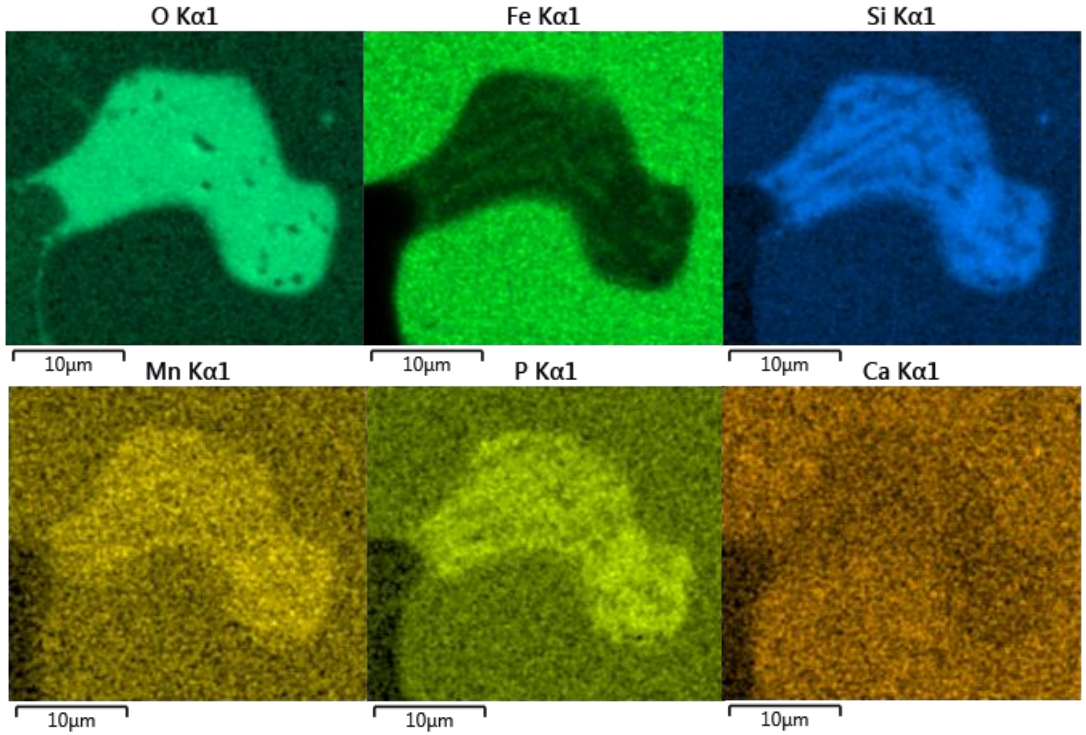


Figure 54: BSE/X-EDS image of surface oxide for 2g HM sample at 60s reaction time and change of oxide composition along its width. (Run 4) Site 3

High levels of iron were also recorded at the oxide/gas interface with the lowest concentration measured in the middle of the oxide phase. This finding perhaps lends further support to the argument discussed by Kaplan [50] and Distin [64] of FeO oxide formation through initial Fe vaporisation; which in turn would increase the amount of iron at the oxide/gas interface to levels perhaps higher than that in the middle of the oxide. Assuming oxidation of Fe vapour occurred and contributed to the oxide constituent, this further suggests that on-coming oxygen from the gas phase may have been shielded by Fe, and by doing so, effectively reducing the total amount of oxygen available for further oxidation reactions to take place. This is in partial agreement with the suggestion by Turkdogan [83] who stated that prior to decarburisation taking place, all vaporised Fe must first be oxidised. Whilst this was not the case in the present study as decarburisation was observed to occur simultaneously with fuming (presumably Fe vapour), the high iron content at the oxide/gas interface compared to the bulk oxide phase suggests that Fe vapour oxidation and deposition potentially did occur.

Silicon content was at its highest in the oxide phase for the HM droplet that underwent gas/metal reaction for 60 seconds (Run 4) compared to other samples which had reacted for shorter time periods. This coupled with the difficulty in locating surface oxides which led to X-EDS maps being taken of the bulk metal and revealing entrainment of oxides within the bulk metal, supports the theory of increased surface turbulence being the cause of entrainment and equally so, the onset of subsurface decarburisation being the cause of surface turbulence given that gas evolution may have occurred within the bulk metal.

Assuming the proposed argument to be true, then surface carbon levels would therefore have been significantly reduced by rapid surface reaction, in which case, increased distribution of oxygen to surface elements such as silicon could have taken place, which would explain the increase in oxide phase silicon content. Further considering that the metal surface was continually being refreshed by metal from the bulk; due to turbulence and eddy current stirring, new bare surfaces would have been available consisting of new HM silicon elements for continued oxidation to take place and therefore contributing towards enriching the oxide phase with silicon.

In summary, for 2g droplets which had undergone gas/metal reaction under 30% oxygen in the gas phase, oxides was found to exist at the metal surface. The oxides were rich in silicon, manganese and oxygen. Whilst no significant change in the oxide composition

with reaction time was recorded, the oxide band increased with longer reaction time; although there was less surface oxides on the droplet which had reacted for 60 seconds, having proven difficult to find using X-EDS technique. The X-EDS composition maps were used to further distinguish the metal from the oxide phase hence quantitatively showing mass transfer across the reaction interface into the liquid oxide.

#### 4.3.3.2 Effect of Droplet Weight/Size on Oxide Composition and Thickness

The effect of droplet size on liquid oxide formation was determined by subjecting samples of various weights (2g, 3g and 4g) to an oxidising atmosphere (20% gas phase oxygen concentration) for 60 seconds. Whilst oxides were located at the metal surface, they rarely existed as bands, but instead occupied 'pockets' on the metal surface which was believed to have formed due to metal surface turbulence presumed to be caused by a combination of impingement of gas from the gas phase on the droplet surface, and gas evolution from the droplet itself. Further evidence of gas evolution is the bubble-shaped dark areas within the oxide and extensive porosity seen in the metal by optical microscopy as shown in Figure 42a, 42b and 42c and further discussed below.

As shown in Figures 55 to Figure 60, there was limited concentration distribution within the bulk of the surface oxide. A potential reason for this may be good mixing/agitation of elements caused by movement of gas ($O_2$, CO) through the liquid oxide. Similar, elemental concentration levels were observed for samples which had been subjected to the similar experimental conditions but with higher gas phase oxygen content (30%), and similar analysis conditions; iron concentration was approximately 30 wt.% as was oxygen concentration, whilst silicon and manganese remained consistent throughout the oxide at around 20 wt.% and 10wt.% respectively; although silicon content at the interfaces were markedly higher (~ 30 wt.%) for reactions at 30% gas phase oxygen content.

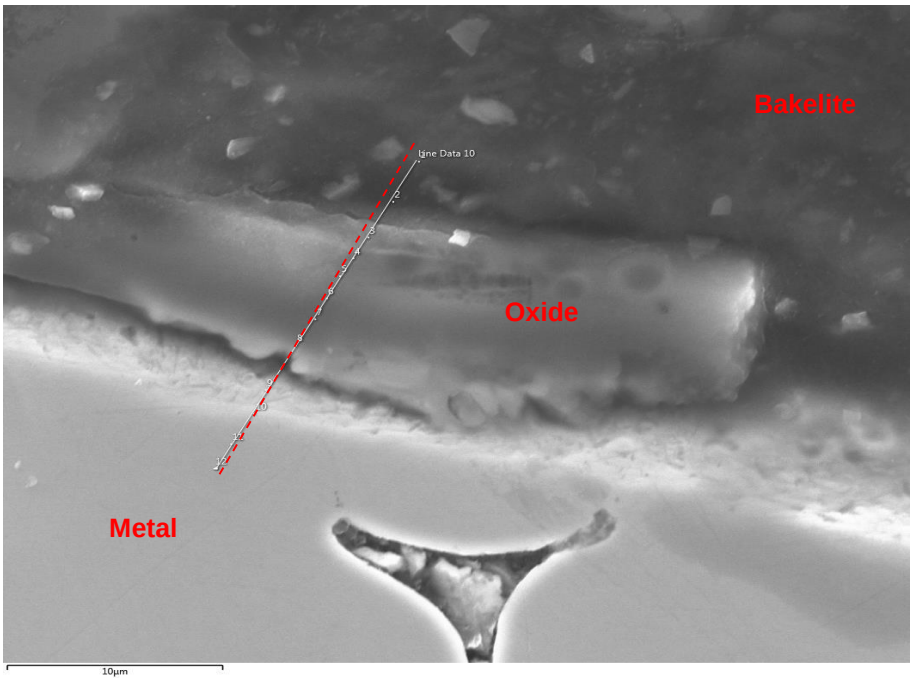


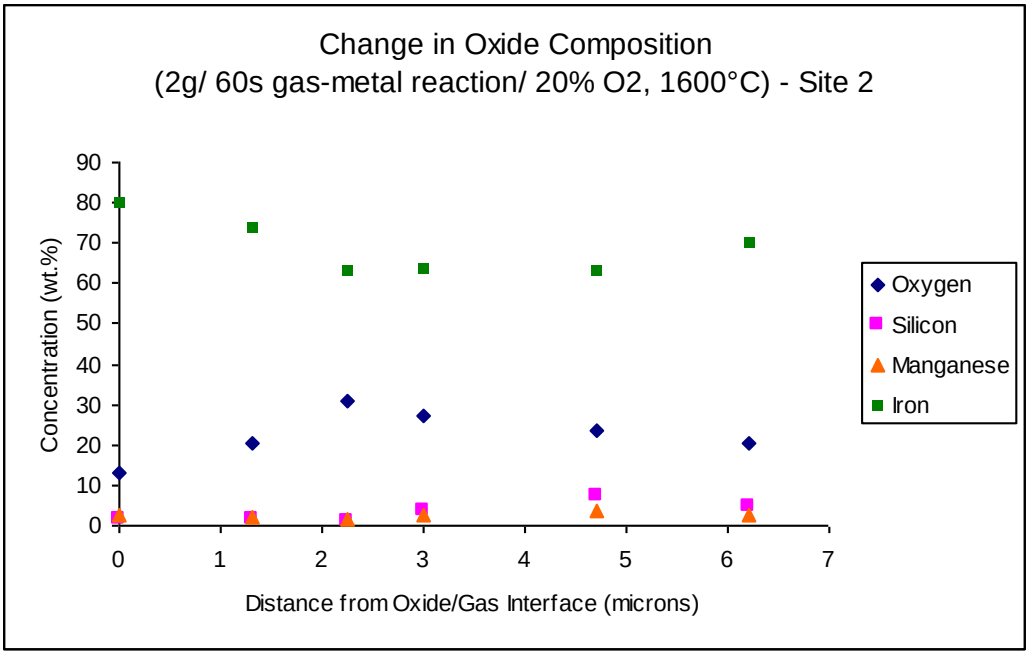


Figure 55: BSE/X-EDS image of surface oxide for 2g HM sample at 60s reaction time and change of oxide composition along its (Run 8) – Site 2

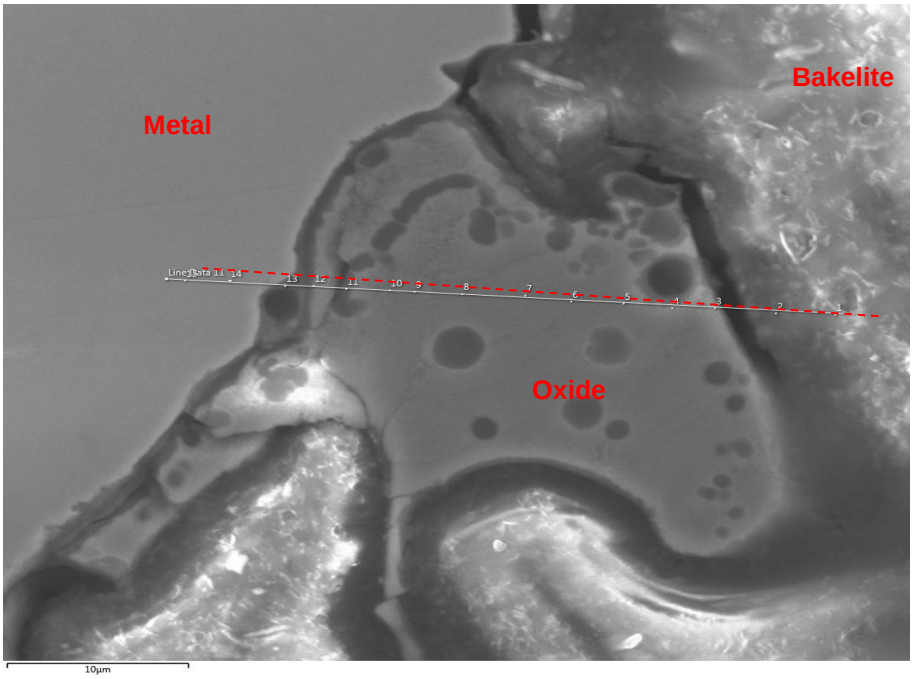


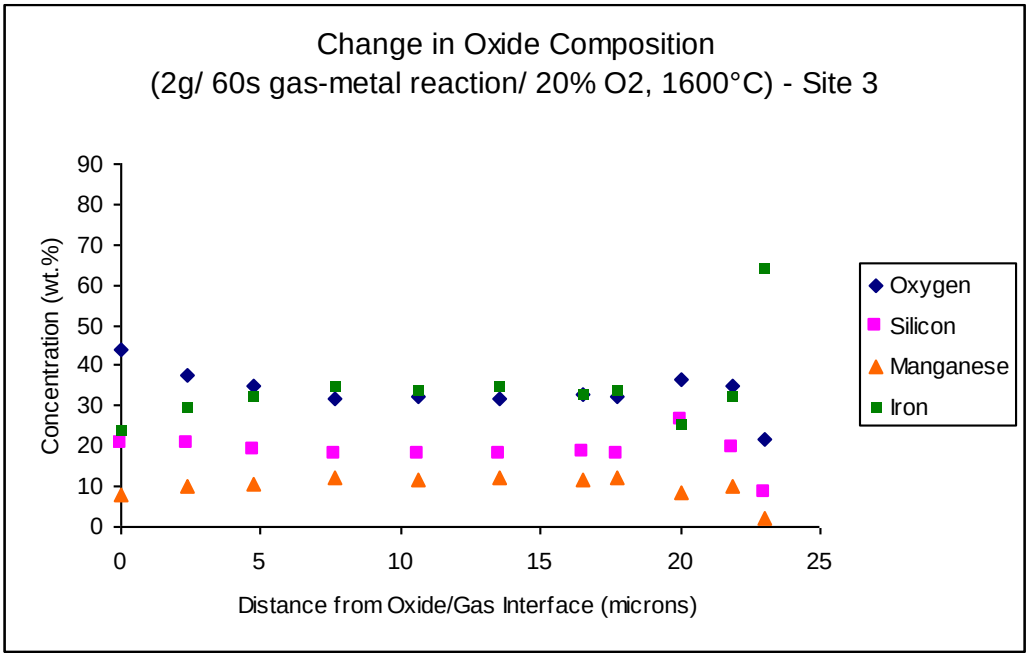


Figure 56: BSE/X-EDS image of surface oxide for 2g HM sample at 60s reaction time and change of oxide composition along its width (Run 8) – Site 3

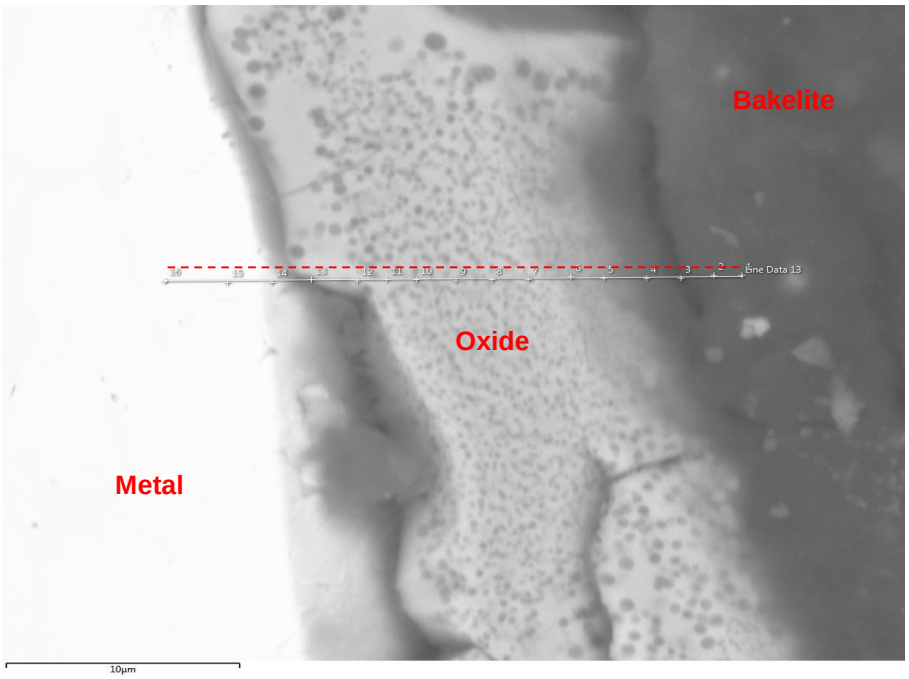


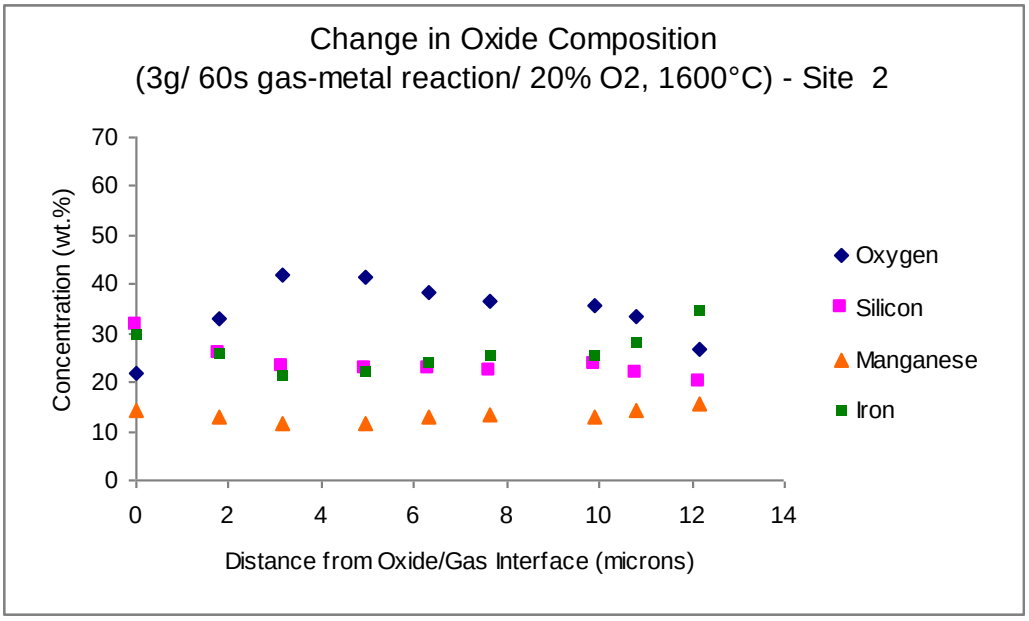


Figure 57: BSE/X-EDS image of surface oxide for 3g HM sample at 60s reaction time and change of oxide composition along its width (Run 9) – Site 2

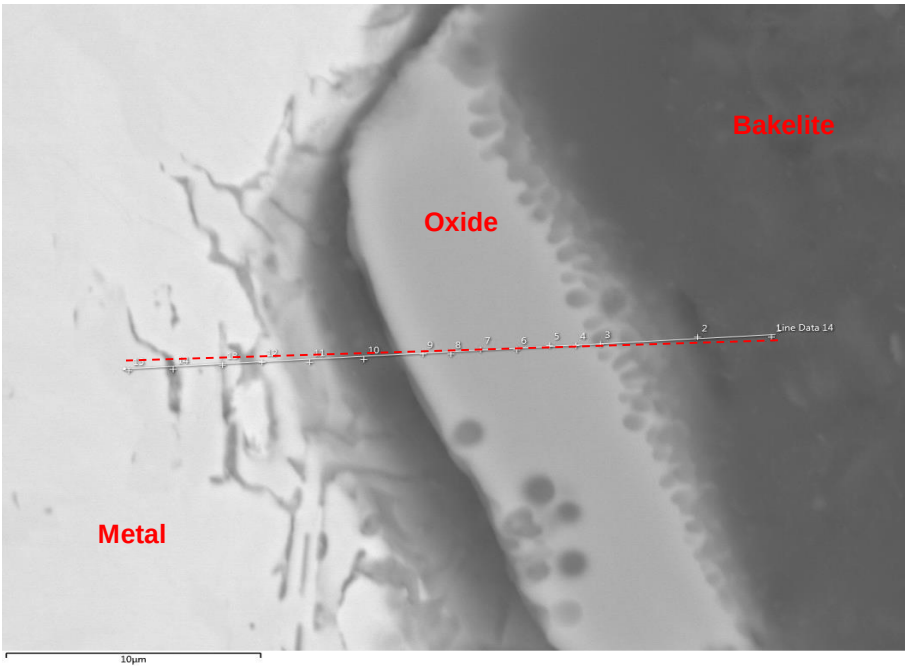


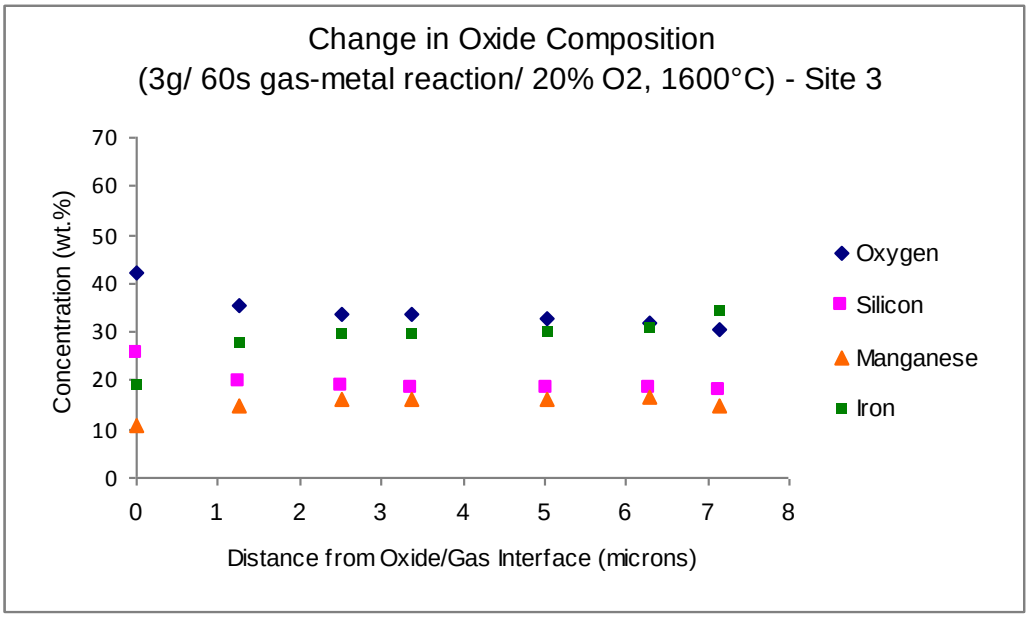


Figure 58: BSE/X-EDS image of surface oxide for 3g HM sample at 60s reaction time and change of oxide composition along its width (Run 9) – Site 3

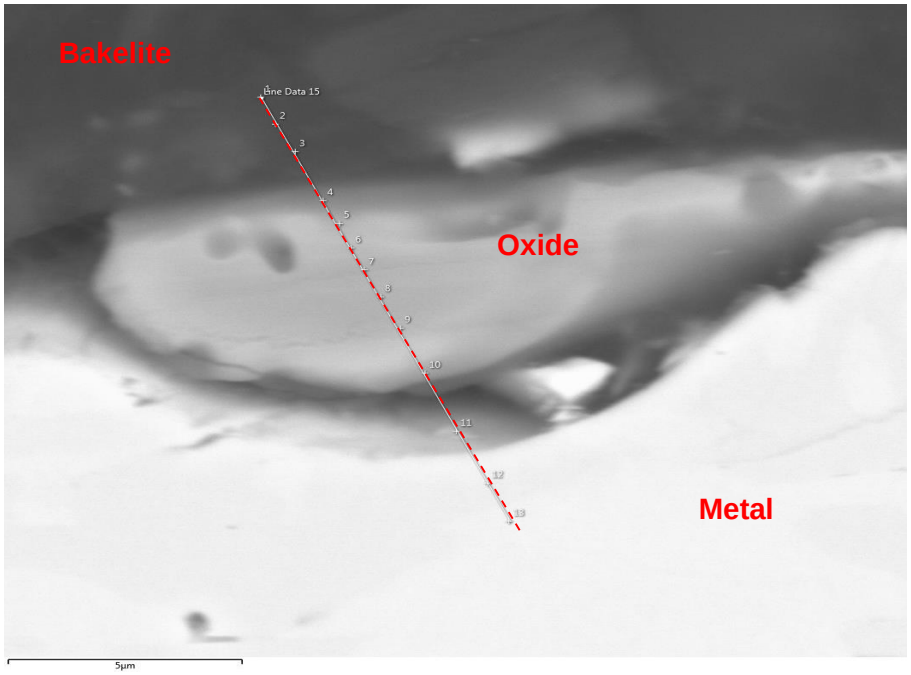


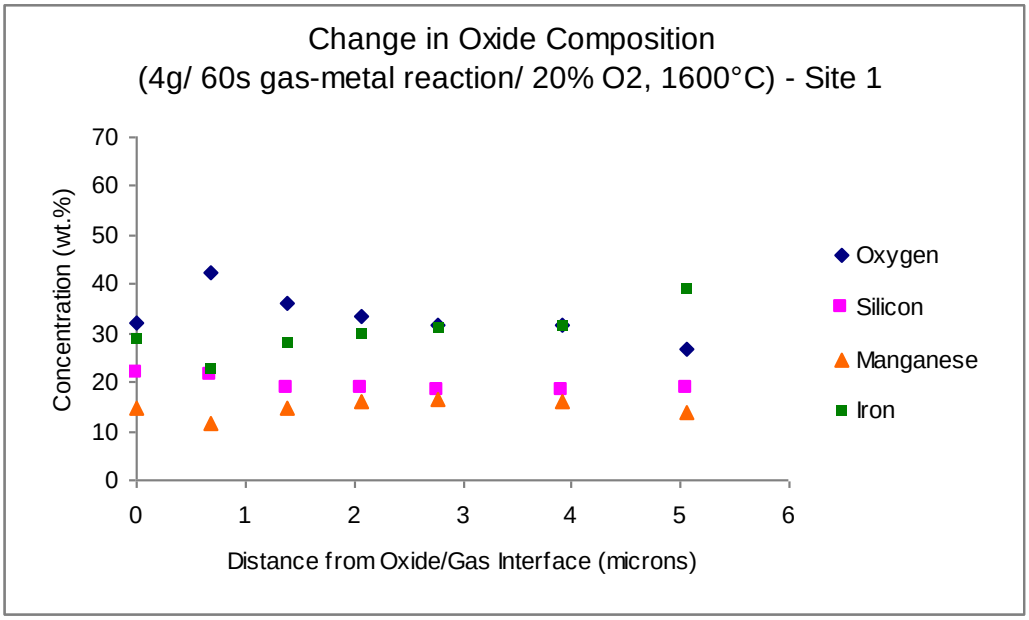


Figure 59: BSE/X-EDS image of surface oxide for 4g HM sample at 60s reaction time and change of oxide composition along its width (Run 10) – Site 1

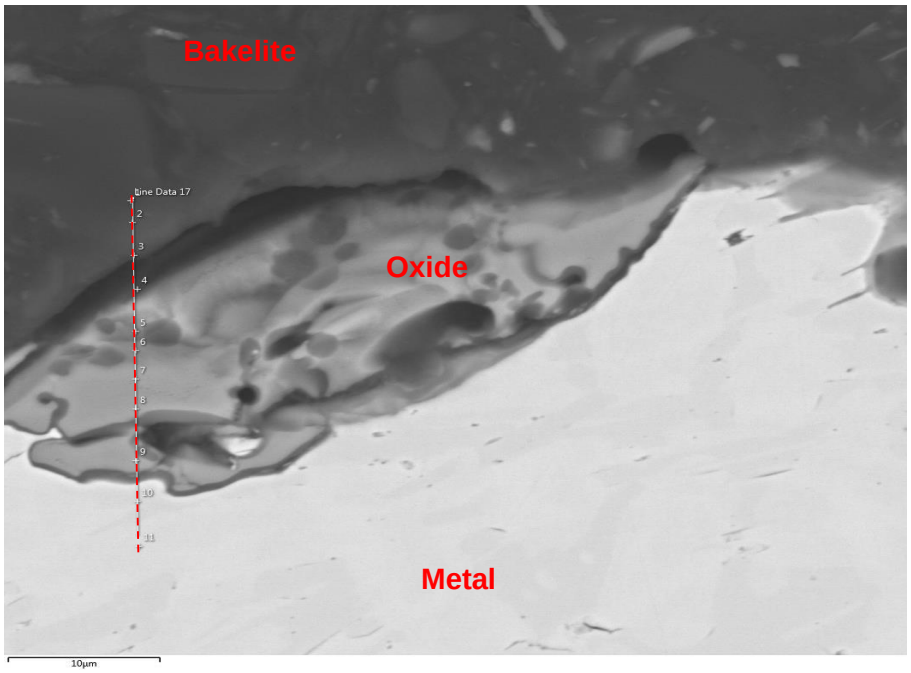


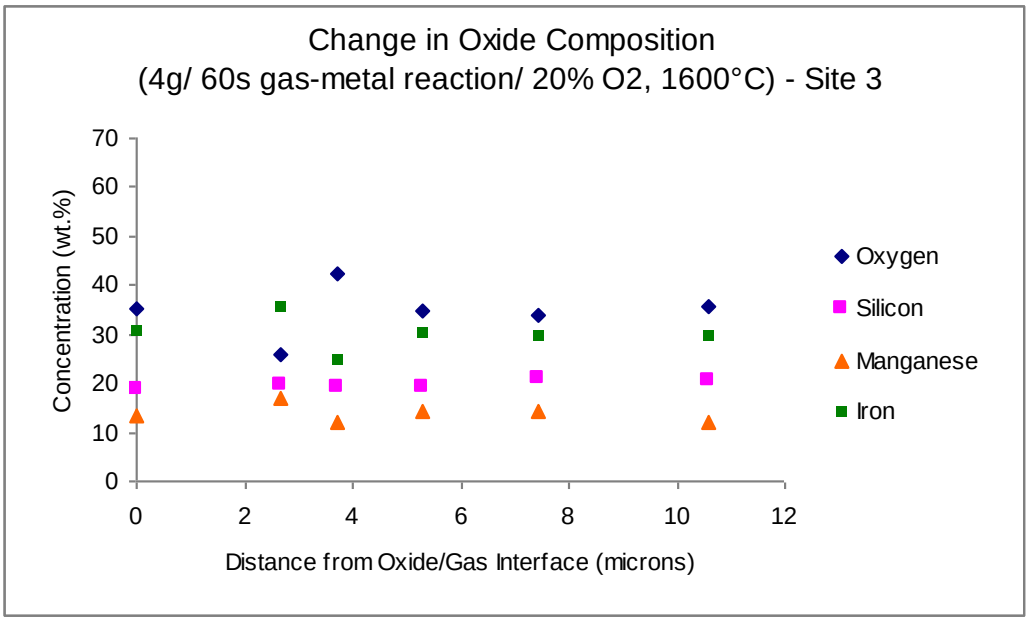


Figure 60: BSE/X-EDS image of surface oxide for 4g HM sample at 60s reaction time and change of oxide composition along its width (Run 10) – Site 3

Although the thickness of the oxides at the metal surface varied as did the shape of the oxides, which were at times bands and at other times more like globules, there was no apparent relation between droplet size and oxide thickness. Whilst there might have been a relation considering the change in reaction surface area, perhaps this was affected by surface turbulence caused by gas evolution from the metal which in turn could have affected the shape of the oxide phases. Irrespective of the droplet size, the oxides had relatively similar elemental compositions which stayed constant throughout the width of the oxide phase.

The hypothesis of there being a dependence of oxide thickness on droplet size was disproved therefore a relationship between oxide thickness and droplet size was not observed in this study. Assuming rapid metal phase mass transfer as argued by El Kaddah [74], the effect of having different bulk volumes can be dismissed as the metal surface was replenished with elements from the bulk phase quick enough to prevent delays in oxidation reaction procedure.

Having further observed a dependence of decarburisation on droplet size in the study by Baker [63] where the average change (1.50 wt.% dC/dt) of a 3mm diameter Fe-3.3-4.9 wt%C sample was over twice that of a 4mm diameter sample (0.60 wt.% dC/dt), and after also observing the same dependence through stationary levitation experiments of the present investigation; with lower HM carbon concentration measured for smaller droplets, given the dependence on HM carbon reaching a critical level before further metalloid removal, a difference in oxide growth rate might be expected for droplets of various sizes such as those of this particular study. It must be noted however that the above discussed studies used Fe-C alloys and not HM and as such different thermodynamic and kinetic relationships may be expected.

However, considering that the critical carbon level was not reached at the maximum reaction time of 60 seconds, it can be understood why similar concentration of oxide elements were found within the oxides for different sized droplets. Decarburisation proceeded with rapid surface decarburisation; which was measured to occur at a faster rate for smaller HM droplets, therefore limiting oxygen distribution to other elements such as silicon and manganese, hence preventing further oxidation occurring. Also, whilst Radzilowski [72, 75] proposed the possibility of high levels of silicon within the oxide phase acting to increase oxide passivity therefore restricting the diffusion of oxygen from the

gas phase to the metal surface to facilitate surface oxidation reactions, in this study, given that parts of the metal surface remained bare as the oxides were observed (both during the reaction procedure and surface analysis procedure) to only partially cover the metal surface, it is inconclusive whether oxide passivity was influential on oxygen up-take and hence oxide formation/growth.

Sun & Pehlke [51, 52] argued that, were the oxide at the surface to increase in viscosity, diffusion in the oxide layer may become rate controlling whilst See & Warner [70] also noted the controlling effect of oxide viscosity on reaction kinetics. With respect to the present study, because the metal temperature increased with reaction time, the proposed effect of oxide viscosity would have diminished although silica content in the liquid oxides ranged from 0 wt.% to >30 wt.%; a wide enough range certain to affect development of Si-O network even though there was no direct correlation between oxide silica content, reaction time and reaction temperature.

Were oxide viscosity to be an overriding factor on the other hand, reactions of lower gas phase oxygen content and larger droplet may have recorded the lowest oxide viscosity due to the slower rate of decarburisation and hence less output of exothermic heat which would slow down the heating of the oxide and consequently delay transfer of oxygen to the metal surface. However, further support that oxygen diffusion through the oxide was not the definitive rate controlling step is given by Baker [63] who stated that for the slag to become passive and presumably viscous due to its increased uptake of silicon and development of Si-O networks, initial metal Si content needed to exceed 3 wt.% which is a magnitude of order greater than the concentrations of the HM samples used in this study.

#### 4.3.3.3. Effect of Droplet Weight/Size on Oxide Composition Thickness (with slag)

When low liquidus slag was introduced into the reaction system, whilst bulk phosphorus levels remained unchanged, phosphorus transfer between metal and slag was evident. Figure 61 shows an oxide particle within a wide oxide phase submerged beneath the metal surface of HM sample of Run 11. By taking line and point scans across the region, oxide elements including phosphorus was measured and mapped by X-EDS. A concentration gradient existed within the segregated region as silicon, manganese, phosphorus and oxygen were at their highest concentration in the middle, and at their lowest at the edge; the inverse was true for iron concentrations.

Table 23: Concentration of elements across oxide phase for 2g HM sample reacted for 60 seconds under 20% $O_2$:80% He and basic slag (Refers to Fig. 61)

| **Site 2** | | **Element Concentration (wt.%)** | | | | | | | | | | |
|---|---|---|---|---|---|---|---|---|---|---|---|---|
| **Spectrum Label** | **Actual Distance (µm)** | **O** | **Mg** | **Al** | **Si** | **P** | **S** | **Ca** | **Ti** | **Mn** | **Fe** | **Total** |
| 6 | 0 | 11.23 | 0.23 | 0 | 1.93 | 2.01 | 0.13 | 0.14 | 0 | 0.51 | 83.83 | 100 |
| 7 | 0.96 | 21.93 | 0 | 0 | 4.26 | 4.76 | 0.11 | 0 | 0 | 1.38 | 67.56 | 100 |
| 8 | 1.92 | 29.13 | 0 | 0 | 5.9 | 6.99 | 0.21 | 0 | 0 | 2.11 | 55.67 | 100 |
| 9 | 3.84 | 32.12 | 0 | 0.2 | 6.39 | 7.49 | 0.19 | 0 | 0 | 2.24 | 51.36 | 100 |
| 10 | 4.8 | 31.87 | 0 | 0.81 | 5.91 | 6.87 | 0.3 | 0 | 0 | 1.9 | 52.33 | 100 |
| 11 | 5.76 | 25.62 | 0 | 0.17 | 4.46 | 5.17 | 0.25 | 0 | 0 | 1.43 | 62.9 | 100 |

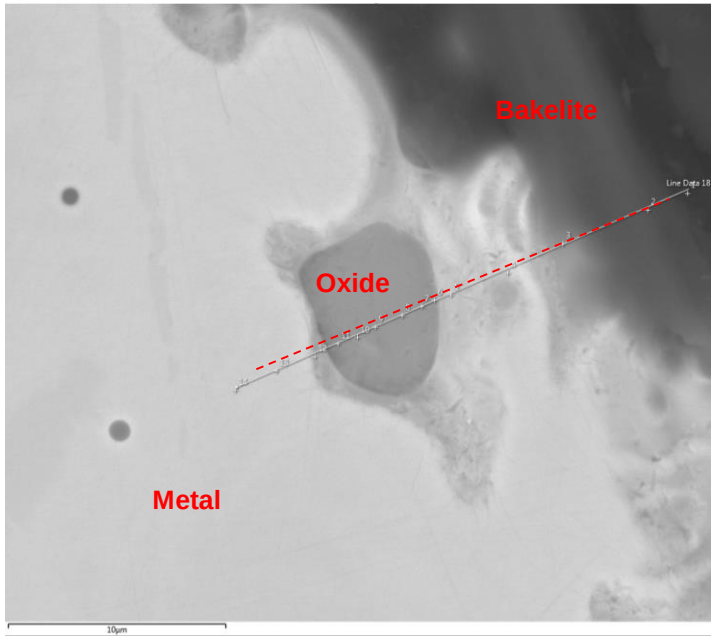


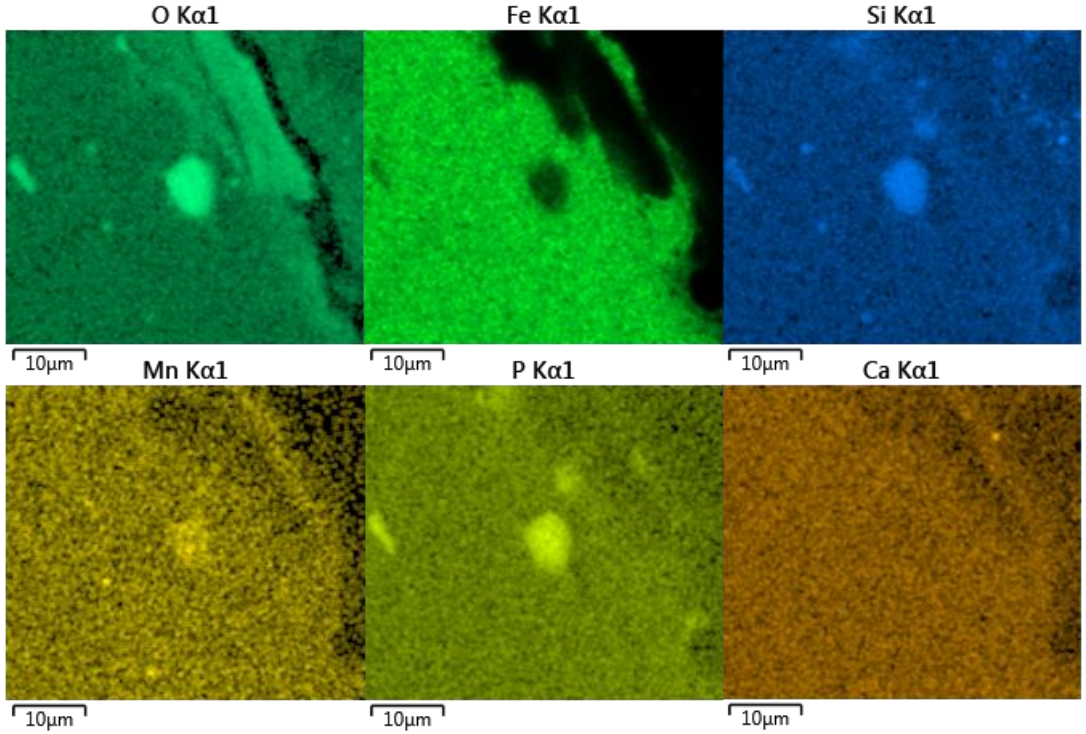


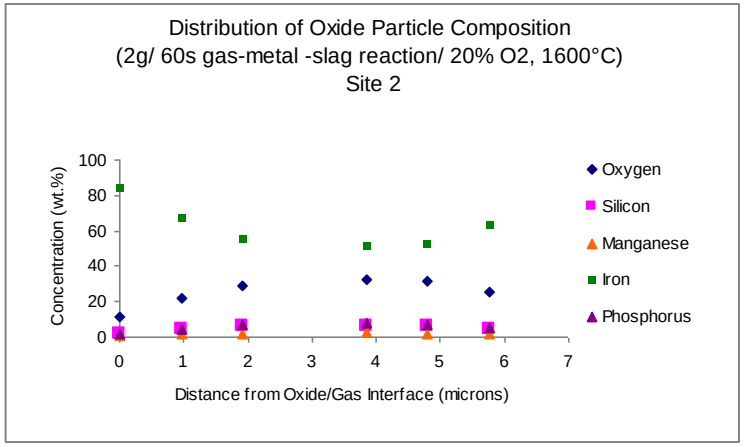


Figure 61: BSE/X-EDS mapped high phosphorus oxide and distribution of elements within oxide phase for 2g HM sample reacted for 60s under 20% $O_2$: 80% He and basic slag

Table 24: Concentration of elements across high phosphorus region in oxide phase for 3g HM sample reacted for 60s under 20% $O_2$:80% He and basic slag (Refers to Fig. 62)

| Sample | | O (wt.%) | Si (wt.%) | P (wt.%) | Mn (wt.%) | Fe (wt.%) |
|---|---|---|---|---|---|---|
| **a)** | **12 - Site 2** | 25.31 | 5.17 | 5.29 | 5.06 | 58.67 |

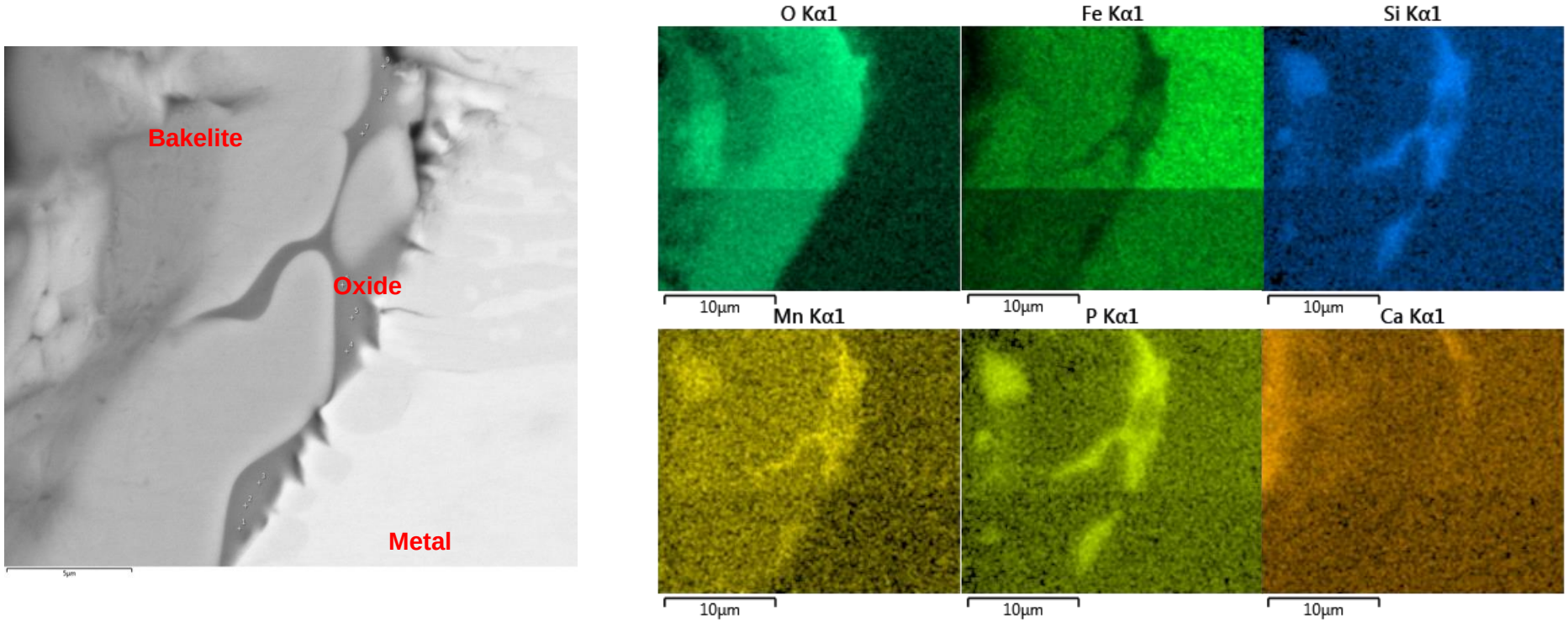


Figure 62: BSE/X-EDS image of network of liquid oxide/metal at HM droplet surface, and penetration of oxide subsurface (Run 12)

Table 25: Concentration of elements across high phosphorus region in oxide phase for 4g HM sample reacted for 60s under 20% $O_2$:80% He and basic slag (Refers to Fig. 63)

| Sample | | O (wt.%) | Si (wt.%) | P (wt.%) | Mn (wt.%) | Fe (wt.%) |
|---|---|---|---|---|---|---|
| **b)** | **13 - Site 3** | 23.20 | 5.07 | 1.52 | 8.53 | 61.33 |

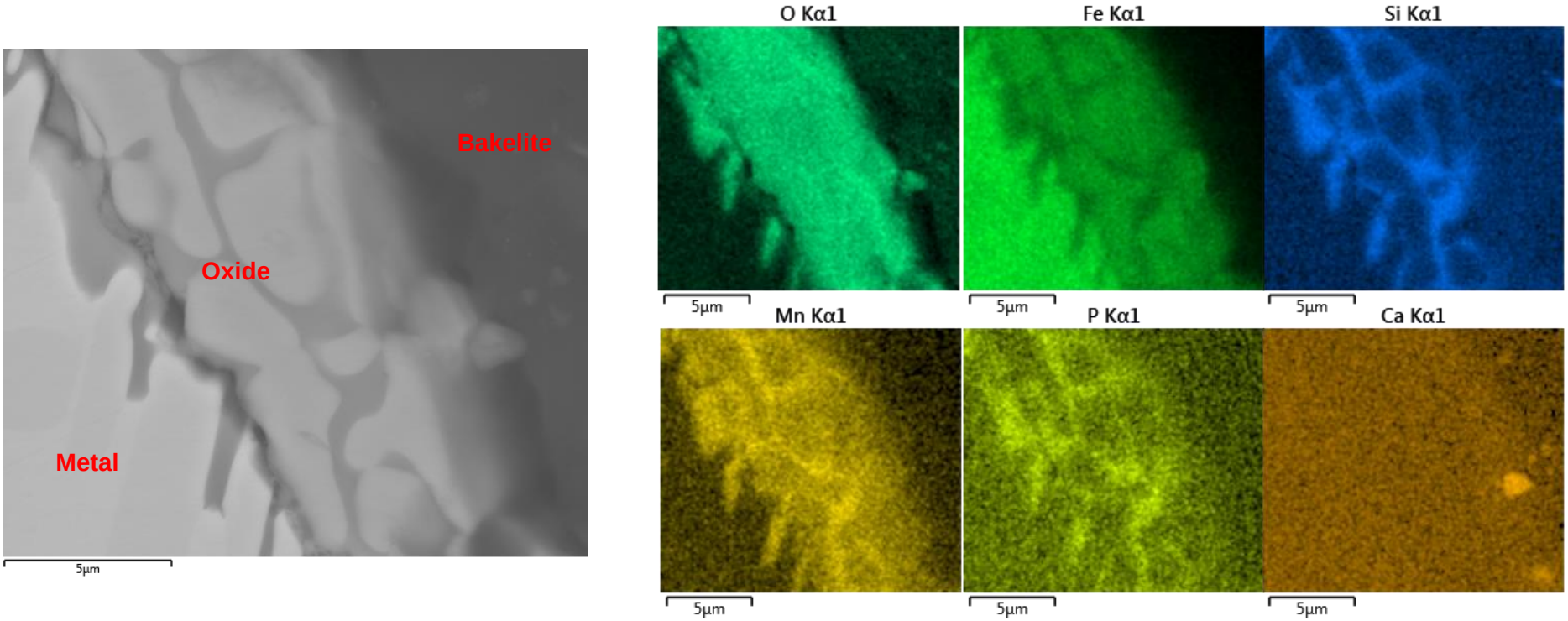


Figure 63: BSE/X-EDS image of network of liquid oxide/metal at HM droplet surface, and penetration of oxide subsurface (Run 13)

Phosphorus concentrations within the oxide reached levels up to 7.49 wt.% in comparison to levels of less than 0.5 wt.% in the liquid oxide surrounding the phosphorus-rich oxide volume; the distinct difference in phosphorus concentration is best displayed on the composition maps. For all droplet sizes, the liquid oxide at the metal surface entrained into the metal and as such, an oxide network formed at the subsurface (Figure 62), making it difficult to measure distribution of oxide composition. For this reason, only point scans were collected and compared with respect to droplet weight/size. The network of liquid oxide at the metal surface coupled with penetration of the oxides subsurface was seen for the sample of Run 13 (Figure 63) also. Phosphorus concentration measured across the oxide averaged at 1.52 wt.% which was significantly lower than the levels measured for the smaller size droplets.

Having gathered from the study by Jahanshahi [49] that HM dephosphorisation does not occur by vaporisation of volatile phosphorus species when undergoing gas/metal reaction, and further concluding that dephosphorisation did not take place within the experiments where CaO was introduced into the system due to poor CaO dissolution, the hypothesis of dephosphorisation occurring with the aid of low liquidus basic synthetic slag was proposed and whilst phosphorus was observed to reside in the slag, it is not believed to be associated with a particular slag phase, but instead likely to be a segregated phase.

### 4.4 Control Experiments

Having established the errors (Table 13) associated with the analytical techniques used in the current study, initial repeat experiments were conducted under controlled conditions similar to that of the main set of experiments documented within this chapter. The purpose of these repeat experiments was to determine the variance (random error) between results specifically credited to experimental procedure given that all conditions the samples were subjected to and the analysis technique were similar for each sample piece within its repeated group.

#### 4.4.1 Experiment Technique Control Test: Metal/gas Stationary Levitation

2g (+/-0.1g) HM samples underwent stationary levitation reaction under 20% oxygen atmosphere diluted with 80% high purity helium gas (their purities are listed in Table 12). As shown in the typical temperature profile (Figure 64) measured by the two colour pyrometer, the molten HM was stabilised at the initial reaction temperature of 1600°C (+/-16°C based on errors of the pyrometer), before introducing oxygen into the reaction

chamber. After 60 seconds (+/-1second) reaction time between the metal and gas, the samples were water quenched and either analysed by ICP-MS or combustion analysis to determine the final composition and identify the extent of any variance between the results.

Due to the size of the quenched HM sample (< 2g), a single HM sample could not be analysed by both ICP-MS and combustion analysis, therefore the test was repeated 8 times with 4 samples analysed by ICP-MS and 4 by combustion analysis technique. A further consideration is that whilst power being introduced to the electromagnetic coil was controlled manually using a remote control, the change in power was dictated by the temperature being measured by the two colour pyrometer. Given the error; +/-16°C (+/-1% of measured temperature), associated with the pyrometer, the input power to achieve stable temperature ranged between 402V – 432V; the variance may well be accounted for by the error associated with the pyrometer or as discussed in Chapter 4 - Section 4.1.1, the variance may also be due to the non-optimised coil design.

A summary of controlled parameters and analytical results from bulk analysis techniques (combustion analysis and ICP-MS) is listed in Table 26.

Table 26: Experimental variables and results for controlled stationary levitation experiments of 2g HM droplets of 4.98 wt.% C, 0.30 wt.% Si, 0.36 wt.% Mn and 0.09 wt.% P under 20% $O_2$:80% He gas atmosphere

| **Reaction gases** | **Sample** | **Weight (g)** | **Power (V)** | **Frequency (kHz)** | **Concentration (wt.%)** | | | |
|---|---|---|---|---|---|---|---|---|
| | | | | | **C** | **Si** | **Mn** | **P** |
| 20% $O_2$ (1.5LPM) 80% He (6LPM) | 1 | 2.02 | 404 | 114 | 2.47 | - | - | - |
| | 2 | 2.05 | 404 | 114 | 2.08 | - | - | - |
| | 3 | 1.92 | 429 | 114 | 1.89 | - | - | - |
| | 4 | 1.92 | 418 | 114 | 2.14 | - | - | - |
| | 5 | 2.02 | 418 | 114 | - | 0.28 | 0.24 | 0.09 |
| | 6 | 2.00 | 402 | 114 | - | 0.30 | 0.24 | 0.09 |
| | 7 | 2.05 | 432 | 114 | - | 0.29 | 0.25 | 0.09 |
| | 8 | 1.99 | 432 | 114 | - | 0.31 | 0.19 | 0.09 |

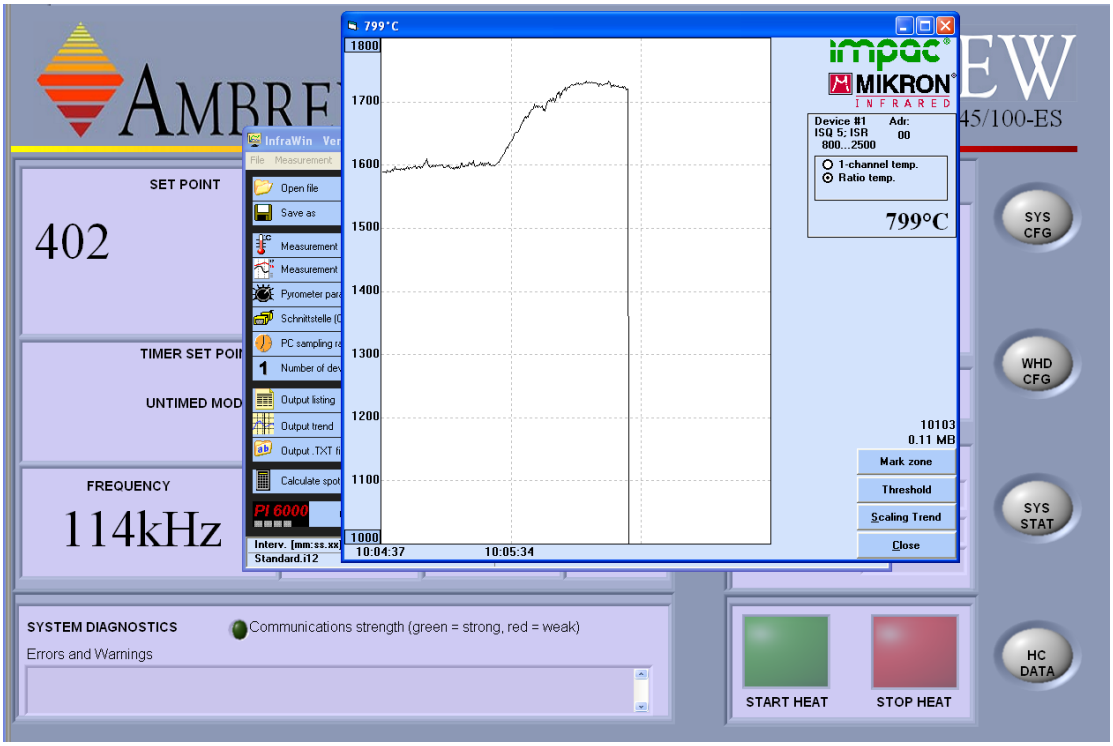


Figure 64: Typical temperature profile for HM sample undergoing stationary levitation melting (Sample 6)

The mean carbon concentration from the four repeated test was 2.15wt.% (+/-0.26wt.%), whilst much smaller mean values of experimental error was calculated for silicon (0.30wt.% +/-0.02wt.%), manganese (0.23wt.% +/-0.04wt.%). Phosphorus levels remained unchanged at 0.09wt.% for each of the four repeated experiments conducted. The random error; which was involved in the repeated measurements has been calculated for carbon, silicon and manganese using the following formulas. The mean value of the measured results is expressed as:

$$\bar{x} = \frac{1}{N}\sum_{i}^{N} x_i \tag{79}$$

where $N$ is the number of repeats and $x_i$ is the value of each individual repeat. The standard deviation ($\sigma_x$) of the individual measurements (Equation 80) and standard deviation of the mean (Equation 81) is expressed as such:

$$\sigma_x = \sqrt{\frac{1}{N-1}\sum(x_i - \bar{x})^2} \tag{80}$$

$$\sigma_{\bar{x}} = \frac{\sigma_x}{\sqrt{N}} \tag{81}$$

The random error ($\delta$) can therefore be calculated as such:

$$\delta_{\bar{x}} = \frac{\sigma_{\bar{x}}}{\bar{x}} x100\% \tag{82}$$

Based on the results of the controlled repeated experiments, Table 27 lists both the random errors and analytical errors representative of this study.

Table 27: Summary of errors

| | **Carbon** | **Silicon** | **Manganese** | **Phosphorus** |
|---|---|---|---|---|
| **Random error (% of final value)** | 11.26 | 4.38 | 11.77 | 0 |
| **Analytical error (+/- wt.%)** | 0.1 | 0.03 | 0.03 | 0.01 |

Efforts have been made to minimise systematic errors such as use of calibrated two colour pyrometer, cleaning the pyrometer viewing window before each experiment, and ensuring the furnace was gas tight especially at connection points by using silicon grease and gas bubble spray.

### 4.4.2 Experiment Technique Control Test: Metal/gas Free-fall Levitation

A separate set of controlled experiments involved levitation melting 2g (+/-0.1g) HM samples under inert atmosphere (100% Ar) until reaction temperature of 1600°C (+/-16°C) had been reached. After which, the EM coil was de-energised and the molten droplet fell through a 1m long reaction tube filled with 30% oxygen (0.75LPM) diluted with 70% high purity helium (1.75LPM) flowing upwards through the tube. A typical temperature profile is presented in Figure 65. As the droplets were to be discharged upon

reaching 1600°C and given the difficulty in stabilising droplet temperature as experienced in stationary levitation experiments, the droplet was immediately discharged from the coil once the target temperature had been reached. The change of gradient approaching the 1600°C point as illustrated on the plot, represents the use of temperature control measures such as increasing inert gas flow in the levitation melting chamber or varying the supply power to the coil to allow for a much more gradual approach to the target temperature which improved the likelihood of discharging the droplet from the coil at the right time.

Table 28: Variables and results for controlled free fall levitation experiments of 2g HM droplets of 4.98 wt.% C, 0.30 wt.% Si, 0.36 wt.% Mn and 0.09 wt.% P under 20%$O_2$:80% He gas atmosphere

| Reaction gases | Sample | Weight (g) | Power (V) | Frequency (kHz) | C (wt.%) |
|---|---|---|---|---|---|
| 30% $O_2$ (0.75LPM) | 1 | 2.02 | 399 | 114 | 4.74 |
| | 2 | 1.99 | 344 | 114 | 4.89 |
| 70% He (1.75LPM) | 3 | 2.00 | 374 | 114 | 4.85 |

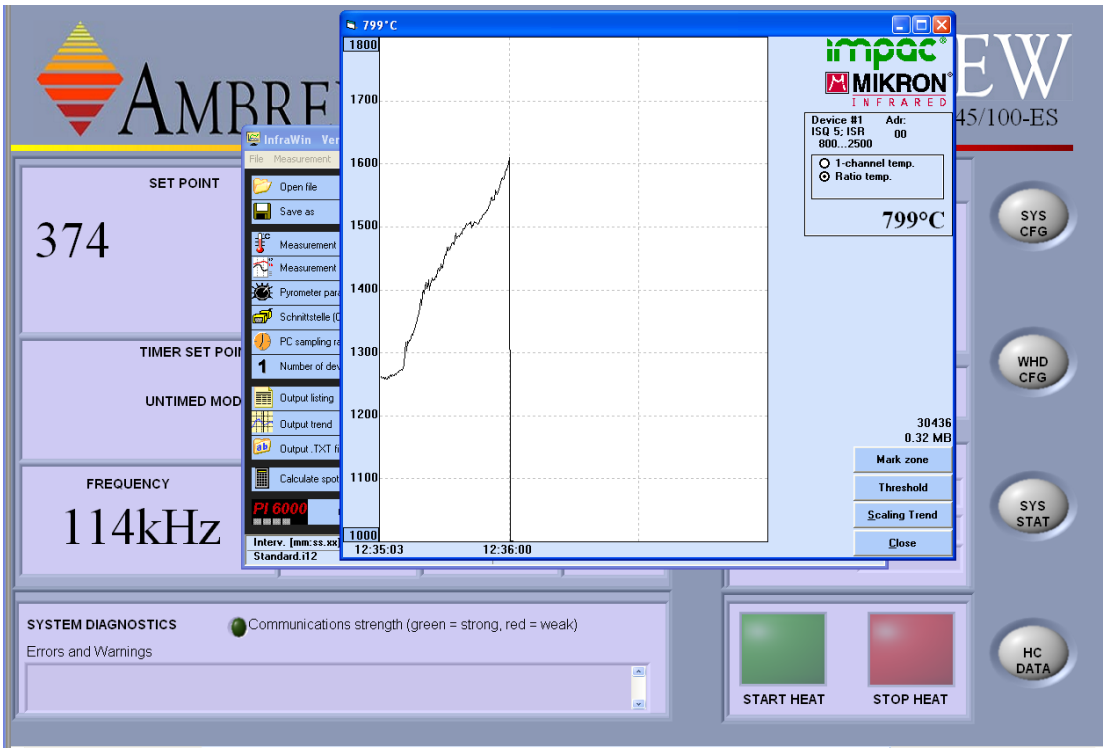


Figure 65: Typical temperature profile for HM sample undergoing free fall levitation melting (Sample 3)

Table 28 summarises the parameters and the analytical results. The repeated samples were analysed for carbon via combustion analysis. Considering that the free fall levitation technique is markedly different to stationary technique and given the short reaction time of 0.32 seconds, coupled with the fact that over an extended time period decarburisation was the most dominant reaction in the stationary technique, only carbon analysis was conducted for the free fall controlled experiments as this was thought to undergo greater composition change compared to other elements. The random error for carbon was calculated using the same method as in the first set of controlled experiments; the random error value for carbon for free fall levitation technique was +/-1.61%.

### 4.5 Summary of Results & Discussion

After gathering knowledge and design consideration of levitation melting apparatus used in an array of studies (Chapter 2 – Section 2.6), a levitation melting apparatus was designed, commissioned and applied (Chapter 4 – Section 4.1) to investigate the kinetics of oxidation steelmaking reaction. Also, combustion analysis, ICP-MS, X-EDS and EPMA technique have been applied to investigate the kinetics of oxidation steelmaking reactions of blast furnace HM. A series of HM levitation experiments were conducted under oxidising atmospheres of 10-30% $O_2$ and with slag making materials such as lime and synthetic slag. The rate of decarburisation was found to be influenced by changes in gas phase oxygen content suggesting the reaction was gas phase mass transfer controlled in agreement with several researchers [50-56, 63-65].

Faster rate of decarburisation was experienced with smaller HM droplets and increased gas phase oxygen content whilst the main method of decarburisation was observed to be subsurface decarburisation. Whilst silicon and manganese oxidation was pronounced in the early stages of the gas/metal reactions, it was limited once carbon oxidation became dominant, nevertheless liquid oxides were observed to form at the metal surface and upon introduction of basic synthetic slag, the HM silicon and manganese levels dropped significantly due to increased oxygen availability associated with the oxygen from the slag, i.e. the free oxygen ions associated with CaO. Phosphorus content was also measured within the synthetic slag but as HM phosphorus content remained unchanged, evidently dephosphorising conditions were not optimised within the current setup. It was established that it was thermodynamically unfavourable for $P_2O_5$ to form in its pure state, hence the lack of dephosphorisation in a gas-metal reaction. Whilst free oxygen associated with CaO favours dephosphorisation through formation of phosphate ion,

initially basic slag had its basicity lowered due to rapid mixture of acidic oxides ($S_iO_2$ and MnO) and basicity was not maintained through replenishment of CaO hence limited dephosphorisation. Liquid oxides detected at the metal surface were composed primarily of oxides of Si, Mn and Fe and whilst oxide composition remained relatively unchanged with reaction time, oxide growth occurred with reaction time but was not influenced by droplet size. Furthermore, the effect of droplet size was evident and the change in decarburisation increased with smaller droplet size, due to larger reaction surface area, and a correlation between droplet size and rate of mass transfer was established. Also, a mass transfer rate equation was also used to quantify the effect of droplet size on rate of reaction.

Placing the present experimental results in the context of the proposed dephosphorisation pre-treatment process (presented in Figure 17), the inability to significantly dephosphorise HM droplets which were exposed to an oxidising and basic atmosphere for an extended period of time beyond what would be experienced in the pre-treatment (although perhaps conditions would be more optimised), clearly demonstrates that the idea of dephosphorising HM droplets whilst falling (one pass) through the reactor would be constrained by the insufficient time for fluxing of lime or slag making material. The lack of fluxed basic slag at the droplet surface coupled with the insufficient contact time during the fall further suggests that if significant levels of dephosphorisation is to take place, it is most likely to occur within the collection ladle at the bottom of the furnace; even then, without a mean of agitating the bulk metal and slag to maximise mixing and reaction contact area, it remains questionable whether refining practice would be much improved compared to the established BOS practice where oxygen injection allows for mixing and sustained droplet generation seen to drive overall metal dephosphorisation [3].

# 5. Conclusions

The present study set out to investigate the feasibility of dephosphorising HM droplets under controlled oxidising and basic conditions in line with the HM dephosphorisation pre-treatment process proposed by Tata Steel R&D. Other oxidation steelmaking reactions (silicon, manganese and iron oxidation) were also studied under similar controlled conditions in view of understanding the relationship between the various oxidation reactions and its effect on overall reaction kinetics. The experimental findings and observation of the current study have been presented and discussed in Chapter 4. The conclusions of this study are as follows:

- HM dephosphorisation did not take place during either free fall (0.32s) or stationary (<60s) levitation reaction when standard grade Singleton Birch lime or basic synthetic slag was introduced onto the HM surface. This is believed to be down to the inability of lime and sufficient slag to flux into the existing surface liquid oxide due to short reaction/contact time resulting in lack of free oxygen from the slag. This coupled with higher temperatures at which high capacity phosphorus phases (i.e. C2S) are unstable may have also contributed to the lack of phosphorus transfer from the metal to the oxide/slag phase. The impact of this finding is acknowledgement that the time taken for the droplet to fall down the reaction column of the proposed dephosphorisation pre-treatment process is insufficient to warrant significant dephosphorisation.
- In line with BOS converter practice, silicon and manganese oxidation was dominant over decarburisation in the initial stages of oxidation reaction, therefore forming an early acidic oxide potentially suitable for fluxing of lime. During which period, decarburisation rate was slower but increased with time as conditions for favourable decarburisation (high temperature caused by exothermic oxidation reactions) occurred.
- For gas/metal reactions, oxides formed at the metal surface consisting of silicon, manganese, and iron. Having used X-EDS images of the metal/oxide interface to measure the oxide thickness and concentration distribution (Chapter 4 – Section 4.3.3), it is conclusive that growth of these oxides was partly influenced by reaction time (the longer the reaction time the wider the oxide band), but as with the concentration of the elements within the oxide, it was not influenced by droplet size or gas phase oxygen content. An appreciation for the size range of droplets within the BOS converter (through statistical study – Appendix 1 and IMPHOS

study [3, 84]) has been gained whilst the experimental results of the present investigation; notably that of oxide formation and growth, improves steelmakers knowledge of the effect of HM droplets on steelmaking refining reactions (i.e. large interfacial reaction area results in greater refining compared to bulk bath therefore driving the change in bulk bath concentrations). This knowledge will compliment steelmaker's extensive knowledge about bulk metal/slag reaction behaviour.

- With respect to carbon reaction, the rate of reaction was controlled by mass transfer of oxygen within the gas phase in agreement to various researchers [50-56, 63-65]. The lack of droplet explosion and limited/no porosity within the reacted HM droplets coupled with the observed constant rate of HM decarburisation suggested that sub surface decarburisation did not occur as the critical carbon level proposed by several researchers [51, 53, 53] was not reached.
- From the work done on analysing droplet size distribution of droplet in a slag/metal emulsion within a 6-tonne pilot scale BOS converter emulsion (Appendix 1), the results correlated well with the study by Millman [14] and further agreed with other researchers [20, 21, 13] by obeying the Rosin-Rammler-Sperling distribution function.
- Now that the newly designed apparatus is fully functional, and improved understanding of its limitations has been gained directly through this study, it presents an added method for conducting laboratory scale steelmaking reactions; especially ones where sample contamination is to be minimised – this particularly proving advantageous over traditional crucible techniques.

# 6. Recommendation of Future Work

- A significant amount of time has been spent designing the apparatus (Chapter 2 – Section 2.6 and Chapter 4 – Section 4.1) which has constrained experimental and analytical efforts. Therefore the present study may be presented as a prerequisite for a more detailed HM droplet study with a much more focused and robust experimental structure that includes more repeated experiments for confidence of accuracy.
- If dephosphorisation remains the focus of future studies, it is recommended that the work moves away from 'free-fall' levitation experiments and moves towards crucible droplet/slag experiments where contact time between the metal and slag is maximised, slag basicity is maintained and with analytical tools such as X-ray fluorescence [10] and confocal microscopy [102], real time analysis of reaction behaviour and metal/slag interaction may be monitored.
- The coils used in the present study dictated the initial reaction temperature of 1600°C as this was the lowest temperature around which droplet stability through power control and inert gas cooling could be achieved. At this temperature, the study has focused on oxidation of carbon, silicon, manganese and dephosphorisation; although temperature conditions for the latter were perhaps not optimised given that rapid dephosphorisation occurs in the initial stages of BOS process where HM temperature is still relatively low (1200°C - 1400°C). With this in mind, the design of a 'low temperature coil' which can achieve good droplet stability for the study of HM droplet dephosphorisation should be considered. Design considerations (Chapter 4 – Section 4.1) from this study can therefore be used as a platform for continued work.
- Several of the levitation melting studies reviewed in Chapter 2 – Section 2.5.3 had the molten droplet contained within a small, narrow volume; in most cases a silica quartz tube with the EM coil mounted externally. An advantage of this set-up would have been tighter control of gas flow (and presumably less use also) allowing for improved temperature control. Further studies may therefore wish to consider using smaller levitation chamber volumes as the incoming gas would be much more concentrated to the molten sample. The underlying benefit of this is envisaged to be improved temperature control of droplet. If the EM coil is still to remain mounted within the chamber as was the case in the present investigation, then the size of the chamber is most likely to be influenced by the size of the coil, which again is affected by the size of the sample (as the aim is to minimise the

free volume between the sample and the inside of the coil in order to maximise induction).

- Whilst MgO was added to the synthetic slag to prevent crucible erosion, MgO is noted to slow down the process of dephosphorisation. In future studies, the use of platinum crucibles should be considered to prevent slag contamination and its influence of reaction behaviour
- The combustion analysed carbon levels in all the samples of this study indicate substantial amounts of cementite-ferrite intergrowth would be present within the microstructure. In order to further distinguish between the carbon levels within HM samples which have reacted for various times, contrasting of the images of the intergrowth could be carried out.
- In the present study, fumes expelled from the molten droplet was assumed to be Fe and Mn due to their low vaporisation pressure, however fume samples were not collected. Future studies may wish to collect the fume samples to distinguish how much of the manganese removed from the HM was down to vaporisation (gas phase mass transfer) and mass phase transfer between the metal and slag/oxide.
- Whilst surface analysis techniques such as X-EDS and EPMA were applied within this study, the shape of the samples were distorted from their original shape upon hitting the bottom of the water quench pot. Application of in-situ gas cooling (by inert gas) may preserve the droplets' original shape and provide a much more representative distribution of elements across the metal and slag/oxide cross section.
- Whilst able to analyse a large volume of samples by X-EDS technique (Chapter 4 - Section 4.3.3), only a few could be analysed by EPMA. This is an area where further work can be done. The analytical error associated with EPMA technique is +/- 0.007wt.% therefore offering greater accuracy of results than X-EDS analysis technique.
- EPMA line scans can be extended beyond 100µm to determine the depth of surface deficiency of HM elements helping to quantitatively define the 'metal surface', 'metal subsurface' and 'bulk metal'. Perhaps this should be done for 60s reacted droplet where there would be stark contrast between subsurface and bulk metal composition as observed in the current study (Chapter 4 – Section 4.3.2, Figure 47).

## 7. References


1. B. DeO & R. Boom, “Fundamentals of Steelmaking Metallurgy”, Prentice Hall International, New York, 1993, p62
2. C. Barnes, "Steelmaking and Continuous Casting Technical Training Course: Basic Oxygen Steelmaking Theory and Practice", Materials Processing Institute, Teesside Technology Centre, United Kingdom, June 2014, p1-6
3. M.S. Millman, A. Kapilasharami, M. Bramming and D. Malmberg, "IMPHOS: Improving Phosphorus Refining", Research Programme of the Research Fund for Coal and Steel, (2009), p1-206
4. Subagyo, G.A Brooks, K.S. Coley, “Interfacial Area in Top Blown Oxygen Steelmaking”, Ironmaking Conference Proceedings, (2002), p837-850
5. R.C. Urquhart and W.G. Davenport, “Foams and Emulsion in Oxygen Steelmaking”, Canadian Metallurgical Quarterly, 12(1973), p507-516
6. N. Standish and Q.L He, “Drop generation due to Impinging and the Effect of Bottom Blowing in the Steelmaking Vessel”, ISIJ International, 29(1989)6, p455-461
7. N.A. Molloy, "Impinging Jet Flow in a Two-Phase System: The Basic Flow Pattern", Journal of the Iron and Steel Institute, (1970), p943-950
8. R. Li and R.L Harris, Pyrometallurgy 95 Conference Proceedings, IMM, London (1995), p107
9. Subagyo, G.A. Brooks, K.S. Coley and G.A. Irons, “Generation of Droplets in Slag-Metal Emulsions through Top Gas Blowing”, ISIJ International, 43(2003)7, p983-989
10. E. Chen and K. Coley, “Kinetic Study of Droplet Swelling in BOF Steelmaking”, Ironmaking and Steelmaking, 37(2010), p541-545
11. N. Dogan, G.A. Brooks, M.A. Rhamdhani, “Analysis of Bloated Droplet Theory using Steelmaking Process Model”, 39th Australian Chemical Conference, (2011), p1-14
12. H.W. Meyer, “Oxygen Steelmaking: Its Control and Future”, Journal of Iron and Steel Institute, 207(1969), p781- 789
13. C. Cicutti, M. Valdez, T. Perez, J. Petroni, A. Gomez, R. Donayo and L. Ferro, "Study of Slag-Metal Reactions in an LD-LBE Converter", p1-17
14. S. Millman, A. Overbosch, M Bramming, D, Malmberg, “IMPHOS: Improving Phosphorus Refining”, Tata Steel Research, Development and Technology, Middlesbrough, 2009, p36-47
15. D. Price, "An Investigation into the Chemistry and Kinetics of LD Steelmaking", Ph.D Thesis, Brunel University, (1972), p11
16. O.K. Tokovoi, A.I. Stroganov and D.Ya. Povolotskii, Steel USSR, 2(1972), p116-117

17. R.F. Block, A. Masui and G. Stolzenberg, “Physical Processes in the Top Blown Oxygen Converter”, Arch Eisenhuttenwes, 44 (1973), p357-361
18. W. Resch, “Kinetics of P Removal During O Top-Blowing Processes for P-Rich Fe”, Ph.D. Thesis, Technical University, Clausthal, 1976
19. V.I Baptizmanskii, V.B. Okhotskii, K.S. Prosvirin, G.A. Shchedrin, Yu.A. Ardelyan and A.G. Velichko, “Investigation of the Physico-chemical Processes in the Reaction Zone with Oxygen Injection of the Metal ”Steel USSR, 7(1977), p329-331
20. S.C. Koria and K.W. Lange, “A New Approach to Investigate the Drop Size Distribution in Basic Oxygen Steelmaking”, Metallurgical Transaction B, 15B(1984), p109-116
21. S.C. Koria and K.W. Lange, “Estimation of Drop Sizes in Impinging Jet Steelmaking Processes”, Ironmaking and Steelmaking, 13(1986), p236-240
22. S.C. Koria and K.W. Lange, “Disintegration of Iron-Carbon Drop by High-Velocity Gas Jet”, Ironmaking and Steelmaking, 10(1983), p160-168
23. Nordqvist, A. Tilliander, K. Grönlund, G. Runnsjö and P. Jönsson, “Characterisation of Metal Droplets Sampled During Top Lance Blowing”, Ironmaking and Steelmaking, 2009, 36, p421-431
24. E. Zinngrebe, “Size Distributions IMPHOS Foam”, Tata Steel Research, Development and Technology, Ijmuiden, 2008, p1-16
25. Mineral Technology International Inc, http://www.mineraltech.com/MODSIM/ModsimTraining/Module2/TechnicalNotes2.pdf, (accessed on 26.01.2013)
26. I. Brezani and F. Zelenak, “Improving the effectivity of work with Rosin-Rammler diagram by using MATLAB GUI tool”, Acta Montanistica Slovaca, 15(2010), p152-157
27. B. Monaghan, “The Kinetics of Liquid Iron Dephosphorisation Using Lime Based Slags”, Ph.D Thesis, University of Strathclyde, 1996, p108-128
28. T. Gare and G. Hazeldean, "Basic Oxygen Steelmaking: Decarburisation of Binary Fe-C Droplets and Ternary Fe-C-X Droplets in Ferruginous Slags", Ironmaking & Steelmaking, 8(1981)4, p169-181
29. B. Monaghan, “The Kinetics of Liquid Iron Dephosphorisation Using Lime Based Slags”, Ph.D Thesis, University of Strathclyde, 1996, p51
30. K. Mills, M. Allibert, H. Gaye et al, “Phosphate Capacities”, Slag Atlas: 2nd Edition, Stahl Eisen, (1995), p12

31. H. Preßlinger, K. Antlinger, K. Klepp and H. Hiebler, "Microanalytical Assessment of Solidified Slags in view of Steel Dephosphorization", Steel Research, 68(1997)12, p520-527
32. H. Preßlinger, M. Mayr and R. Apfolterer, "Quantitative Phase Evaluation of Converter Slags", Steel Research, 70(1999)6, p209-214
33. J.Waligora, D. Bulteel, P. Degrugilliers et al, "Chemical and Mineralogical Characterizations of LD Converter Steel Slags: A Multi-analytical Techniques Approach", Materials Characterization,61(2010), p39-48
34. E. Maxl, H. Hiebler, H. Preßlinger and K. Antlinger, "Microanalytical Investigations of Oxidizing Slags with Special COnsideration of Phosphorus- and Sulphur-containing Phases", ISIJ International, 33(1993)1, p88-97
35. J. Wrampelmeyer, S. Dimitrov and D. Janke, "Dephosphorization Equilibria between Pure Molten Iron and CaO-Saturated $FeO_n$-CaO-$SiO_2$ and $FeO_n$-CaO-$Al_2O_3$ Slags", Steel Research, 60(1989)12, p539-549
36. A. Bergman and A. Gustafsson, "On the Relation between Optical Basicity and Phosphorus Capacity of Complex Slags", Steel Research, 59(1988)7, p281-288
37. H. Flood, K. Grjotheim, "Thermodynamic Calculation of Slag Equilibria", Journal of the Iron and Steel Institute, (1952), p64-70
38. T. Winkler and J. Chipman, "An Equilibrium Study of the Distribution of Phosphorus between Liquid Iron and Basic Slags", Transactions of the Society of AIME, 167(1946), p111-133
39. C. Manning and R. Fruehan, “The Rate of the Phosphorus Reaction between Liquid Iron and Slag”, Metallurgical And materials Transactions B, 44B(2013), p37-44
40. K. Mori, S. Doi, T. Kaneko and Y. Kawai, “Rate of Transfer of Phosphorus between Metal and Slag”, Transactions ISIJ, 18(1978)5, p261-268
41. M. Nasu, K. Mills, B. Monaghan, A. Jakobsson and S. Seetharaman, “Effect of Slag/Metal Interfacial tension on Kinetics of Dephosphorisation”, Ironmaking and Steelmaking, 26(1999)5, p353-357
42. B. Monaghan, R. Pomfret and K. Coley, “The Kinetics of Dephosphorisation of Carbon-Saturated Iron Using an Oxidising Slag”, Metallurgical and Materials Transactions B, 29B(1998), p111-118
43. K. Mori, Y. Fukami and Y. Kawai, “Rate of Dephosphorisation of Liquid Iron-Carbon Alloys by Molten Slags”, Transactions ISIJ, 28(1988), p315-318

44. K. Balajiva, A. Quarrell and P. Vajragupta, "A laboratory Investigation of the Phosphorus Reaction in the Basic Steelmaking Process", Journal of the Iron and Steel Institute, 153(1946)1, p115-145
45. P. Wei, M. Sano, M. Hirasawa and K. Mori, “Kinetics of Phosphorus Transfer between Iron Oxide Containing Slag and Molten iron of High Carbon Concentration under Ar-$O_2$ Atmosphere”, ISIJ International, 33(1993)4, p479-487
46. P. Wei, M. Sano, M. Hirasawa, K. Mori, "Kinetics of Carbon Oxidation Reaction between Molten Iron of High Carbon Concentration and Iron Oxide Containing Slag", ISIJ International, 31(1991)4, p358-365
47. H. Gaye and P. Riboud, "Oxidation Kinetics of Iron Alloy Drops in Oxidising Slags", Metallurgical Transactions B, 8(1977)2, p409-415
48. G. Murthy, Y. Sadawa and J. Elliot, "Reduction of FeO Dissolved in CaO-$SiO_2$-$Al_2O_3$ Slags by Fe-C Droplets", Ironmaking & Steelmaking, 20(1993)3, p179-190
49. S. Jahanshahi and J. Jeffes, "Vaportization of Iron-Phosphorus Alloys in Gases of Various Oxygen Potentials", Ironmaking and Steelmaking, 10(1983)4, p155-159
50. R. Kaplan and W. Philbrook, "Kinetics of Gaseous Oxidation of Binary and Ternary Alloys of Liquid Iron", Transactions of the Metallurgical Society of AIME, 245(1969)10, p2195-2204
51. H. Sun and R. D. Pehlke, "Kinetics of Oxidation of Carbon in Liquid Iron-Carbon-Silicon-Manganese-Sulfur Alloys by Carbon Dioxide in Nitrogen", Metallurgical and Materials Transactions B, 26B(1995), p335-344
52. H. Sun and R.D Pehlke, "Modelling and Experimental Study of Gaseous Oxidation of Liquid Iron Alloys", Metallurgical and Materials Transaction B, 27B(1996), p855-864
53. D. Widlund, D.S. Sarma and P.G. Jonsson, “Studies on Decarburisation of Levitated Fe-C-Si alloy Droplets”, ISIJ International 46(2006), p1149-1157
54. L.A. Baker, N.A Warner and A.E Jenkins, “Kinetics of Decarburisation of Liquid Iron in an Oxidising Atmosphere Using Levitation Technique”, Transactions of the Metallurgical Society of AIME, 230(1964), p1228-1235
55. L.A. Baker, N.A Warner and A.E Jenkins, “Decarburisation of a Levitated Iron Droplet in Oxygen”, Transactions of the Metallurgical Society of AIME, 239(1967), p857-864
56. R. Baker and R. Ward, “Reaction of an Iron Carbon Droplet during Free Fall through Oxygen”, Journal of the Iron and Steel Institute, 205(1967), p714-717

57. M.E. Watkins, "Calcium Modification of Surface Oxides Formed on Levitated Iron and Steel Alloy Droplets and Related Surface Tension Phenomena", Ph.D Thesis, The Ohio State University, 1987, p1-179
58. S. Sagardia and R. Segsworth, "Electromagnetic Levitation Melting of Large Conduction Loads", IEEE Transaction Industry Applications, 1A-13(1977)1, p49-52
59. V. Bojarevics, K. Pericleous, "AC & DC Magnetic Levitation and Semi-Levitation Modelling", International Scientific Colloquium, Hannover, (2003), p99
60. B. Li, "The Magnetothermal Phenomena in Electromagnetic Levitation Processes", International Journal of Engineering Science, 31(1993)2, p201-220
61. D. King, "Ambrell Limited: Ekoheat Operation and Maintenance Instructions", Revision N, (2012)
62. S. Jahanshahi and J. Jeffes, "Design of Coils for Levitating Droplets of Metals with Improved Temperature Control Characteristics", Transactions of the Institution of Mining and Metallurgy, Section C: Mineral Processing and Extractive Metallurgy, 90(1981), p138-141
63. R. Baker, "Oxidation Studies of Molten iron Alloy drops", Journal of the Iron and Steel Institute, 1967, p634-641
64. P. Distin, G. Hallett and F. Richardson, "Some Reactions between Drops of Iron and Flowing Gases", Journal of Iron and Steel Institute, 206(1968), p821-833
65. P. Roddis, "Mechanism of Decarburisation of Iron Carbon Alloy Drops Falling through an Oxidising Gas", Journal of the Iron and Steel Institute, 211(1973), p53-58
66. H.G. Lee and Y.K. Rao, "Rate of Decarburisation of Iron-Carbon Melts: Part 1. Experimental Determination of the Effect of Sulfur", Metallurgical and Materials Transactions B, 13B(1982), p403-409
67. N.J. Simento, P.C. Hayes and H.G Lee, "Decarburisation Kinetics of Fe-C-S Droplets with $H_2O$", ISIJ International, 38(1998), p690-696
68. N.J. Simento, H.G Lee and P.C. Hayes, "Decarburisation of Liquid Fe-C-S Drops Using Multiple Oxidants of $O_2$, $CO_2$ and $H_2O$", ISIJ International, 39(1999), p1217-1223
69. D.B. Caryll and R.G. Ward, "Study of Slag-Metal Equilibria by Levitation Melting: Application to the Fe-Mn-O System", Journal of the Iron and Steel Institute, (1967), p28-31
70. J.B. See and N.A. Warner, "Reactions of Iron Alloy Drops in Free Fall through Oxidising Gases", Journal of the Iron and Steel Institute, (1973), p44-52

71. D.G. Robertson and A.E Jenkins, "Heterogeneous Kinetics at Elevated Temperatures and Pressures", G.R Belton and W.L Worrell Edition, Plenum Press, (1970), p393-408
72. R.H. Radzilowski and R.D. Pehlke, "Gaseous Oxygen Absorption by Molten Iron and Some Fe-Al, Fe-Si, Fe-Ti and Fe-V Alloys", Metallurgical and Materials Transaction B, 10B(1979), p341-348
73. V.T. Burtsev, V.G. Glebovskiy, A.Yu. Polyakov, A.M. Samarin, "Distribution of Sulphur and Oxygen between Iron and a Lime-Alumina Slag during Levitation Melting", Chernaya Metallurgiya (1962), 13-18
74. N.H El-Kaddah and D.G.C. Robertson, "The Kinetics of Gas-Liquid Metal Reactions Involving Levitated Drops. Carburisation and Decarburisation of Molten iron in CO-$CO_2$ Gas Mixtures at High Pressures", Metallurgical Transaction B, 9B(1978), p191-199
75. R.H. Radzilowski, "Kinetics of Gaseous Absorption by Molten Iron and Some iron Alloys", PhD Thesis, University of Michigan, 1977, p23-35
76. S. Zinn and S. Semiatin, "Coil design and Fabrication: Basic Design and Modifications", Heat Treating, (1988), p32-41
77. B. Harris and A. Jenkins, "Controlled Atmosphere Levitation System", Journal of Scientific Instruments, 36(1959), p238240
78. P. Distin, S. Whiteway and C. Masson, "Solubility of Oxygen in Liquid Iron from 1785°C to 1960°C. A New Technique for the Study of Slag-Metal Equilibria", Canadian Metallurgical Quarterly, 10(1971)1, p13-18
79. H Gaye and J. Lehmann, "Slag Atlas", 2nd Edition, Verein Deutscher Eisenhuttenleute, (1995), p274
80. J. Schoop, W. Resch and G. Mahn, "Reactions Occurring during the Oxygen Top-Blown process and calculation of Metallurgical Control Parameters", Ironmaking and Steelmaking 2(1978), p72-79
81. S. Seetharaman, "Fundamentals of Metallurgy", Woodhead Publishing, England, Cambridge, (2008), p6
82. Y.K. Rao, "Stoichiometry and Thermodynamics of Metallurgical Processes", Cambridge University Press, London, 1985, p883-895
83. E.T. Turkdogan, P. Grieveson and L.S. Darken, "The formation of Iron Oxide Fume" Journal of Metals, 14(1962), p521-526

84. S. Millman, A. Overbosch, A. Kapilashrami, D. Malmberg and M Bramming, “Some Observations on BOS Refining”, Tata Steel Research, Development and Technology, Middlesbrough, 2012, p1-5
85. Mathematics and Statistics Help (MASH), "The Normal Distribution", The University of Sheffield, http://www.mash.dept.shef.ac.uk/shef-only/39_1_norm_dist.pdf (accessed 25.04.2015)
86. A. Fields, "Discovering Statistics using SPSS", 3rd Edition, Sage Publications, London, (2009), p43-45 and p144
87. F. Ji, M. Rhamdhani, Subagyo, M. Barati, K.S. Coley, G.A. Brooks, G.A Irons and S. Nightingale, Proceedings of the Mills Symposium, Volume 1, IoM, London, UK (2002), p247
88. G. Brooks, Y. Pan, Subagyo, K. Coley, "Modelling of Trajectory and Residence Time of Metal Droplets in Slag-Metal-Gas Emulsions in Oxygen Steelmaking", Metallurgical and Materials Transactions B, 36B(2005), p529-533
89. G. Ehrlich, “The Mechanism of Chemisorption on Metals”, Journal of Physics and Chemistry of Solids, 1(1956)1, p3-13
90. M.J. Rhydderch, "Spray Steelmaking", Journal of Iron and Steel Institute, (1967), p814-817
91. J. Pears and E. Davies, "The Application of Pre-refining for Steelmaking Processes", International Symposium on Recent Developments in Iron and Steelmaking with Special Reference to Indian Conditions, Jamshedpur, (1963), p31-39
92. J. Pears and J Pearson, “Spray Refining of Molten Pig Iron”, Physical chemistry of Steelmaking, Proceedings of Open Hearth Steel Conference, (1962), p458-470
93. D.R.G. Davies, M.J. Rhydderch and L.J. Shaw, “Spray Steelmaking at Millom”, Journal of Iron and Steel Institute, (1967), p810-813
94. S.Y. Kitamura, K. Yonezawa, Y. Ogawa and N. Sasaki, “Improvement of Reaction efficiency in Hot Metal Dephosphorisation”, Ironmaking and Steelmaking, 2002, 29, p121-1245.
95. S. Ishihara, ""Pre-treatment of Hot Metal", International Iron and Steel Institute, Johannesburg, 1, 1984, p8-25
96. T. Zhi-hong, L Ben-hai, Z. Xiao-Ming and J. Zhong-Hang, “Double Slag Operation Dephosphorisation in BOF for Producing Low Phosphorus Steel”, Journal of Iron and Steel Research International, 2009, 16, p6-14

97. J. Perez, R. Donayo, A. Gomez, A. Data and W. Balante, "Decrease of Fume Emissions in the Converter by New Process for High Silicon and- Phosphorus Hot Metal", Iron and Steel Technology, 2012, p68-75
98. P. Coheur, “On the LD-AC and LD-KALDO Processes”, C.N.R.M, 1996
99. A.F. Jessop, “Operation of the LD/AC Plant at Lysaght’s Scunthorpe Works, Steel Times”, 1966
100. Corby Works, “The LD/AC Steelmaking Plant at Corby”, Iron and Steel, 1966
101. G.C.R. Mathieson, “The Unique Engineering Problems of LDAC Steelmaking”, Journal of The Iron and Steel Institute, 1968
102. S. Seetharaman, “Application of Confocal Scanning Laser Microscopy to Steel Research”, Proceedings of the 3rd International Congress on the Science and Technology of Steelmaking, United States, (2005), p797-810
103. S. Sabah and G. Brooks, “Splash Distribution in Oxygen Steelmaking”, Metallurgical and Materials Transactions B, 46(2015)2, p863-872
104. Eltra Elemental Analyser, “Carbon/Sulfur Analyser CS800 – CS2000”, Technical Data Brochure, file:///C:/Users/Efosa/Downloads/brochure_cs-800_cs-2000_en.pdf (accessed 23.08.2015)
105. P.D. Desal, “Thermodynamic Properties of Manganese and Molybdenum”, The Journal of Physical Chemistry, 16(1987)1, p97

# Appendix 1: Study of Metal Droplet Size Distribution and Population Density in 6-tonne BOS Converter Emulsion

## A.1. Introduction

As discussed in Chapter 2 - Section 2.3, metal droplets in the BOS converter provide a large interfacial (reaction) area and therefore are greatly refined compared to bulk bath metal especially in the early stages of blow where the metal is rich in impurity elements such as silicon and phosphorus (carried through from the raw materials via the blast furnace), as well as carbon at initial levels of between 4 - 4.5 wt.%C. As displayed in Table 4, several converter based studies have also been conducted where a range of droplet sizes has been measured and whilst the range of droplets sizes may be influenced by factors such as sampling technique and sampling location, in each study, a size distribution ranging from the micron scale is apparent.

Although these studies have been reviewed and summarised (in Table 4), this particular section focuses exclusively on IMPHOS (Improving Phosphorus Refining) investigation which was conducted as a RFCS (Research Fund for Coal & Steel) project by Tata Steel that aimed to improve the understanding of reactions within the BOS converter with special emphasis on dephosphorisation through pilot scale plant trials. The reason why special focus is afforded to this study is because it forms the basis of the statistical work conducted in the current research, as raw data from IMPHOS imaged processed emulsion samples were used to determine droplet size distribution and its correlation with the Rosin-Rammler-Sperling (RRS) distribution function.

In the IMPHOS study, 25 heats were processed and in each of these heats, sampling of the bulk bath metal, slag and emulsion occurred simultaneously using a specially designed lance which allowed for sampling at 7 different heights within the 6t BOS converter at 2 minutes intervals for the duration of blow (~18 minutes). A new sampling lance was used for every heat and sampling stage. A critical feature of this assembly was that the reactions and dynamic state of all three areas of the BOS could be interpreted relative to each other, therefore offering an improved holistic view of refining reactions occurring at any stage within the blow procedure. The main conclusions of IMPHOS are comprehensively reviewed in the literature review (Chapter 2), but in light of the fact that this particular section of the current research focuses on statistical analysis (i.e. size distribution, population density) of metal droplets sampled from the emulsion of

IMPHOS heats, the key findings from the IMPHOS research with respect to this were as follows:

- High frequency of droplets had diameters ranging between 16 - 40µm (Note: 16µm was the analytical limit)
- At the early stages of blow, metal droplets were greatly refined compared to bulk bath metal whilst at the end of blow element concentration levels were similar
- Smaller HM droplets (<500µm) were more refined than larger droplets
- Metal droplets had a high circulation (between the bulk bath and emulsion) rate of 5% to 10% per second of the overall metal (tap) weight during the major part of blow [84]
- Droplets consisted of porosity proposed to have formed during solidification

The limited metal droplet size distribution analysis conducted by Millman [14] and Zinngrebe [24] only spanned to plotting (on a series of histograms) the droplet size distribution of image processed fragments recovered from the sample cups of 2 of the 25 sampled heats (S1837 and S1840), and even then, only plotting the metal droplet size distribution representative of only 1 of 5 available sample pots (sample level) that sampled within the emulsion layer. From these series of plots with a bin of 20µm, it was clear that there was a large fraction of droplets of less than 40µm diameter for both heats, although going by the higher frequency of larger diameter droplets (> 40µm) for the analysed S1837 heat compared to S1840 heat, the analysed pot may have been at a lower level hence constituting the reduced distribution of droplet size for heat S1837.

Having identified potential scope for building on this work, further statistical analysis with respect to metal droplets in the emulsion was conducted for the same heats as these offered the most complete set of data sourced from the image processed raw data. The present study builds on the IMPHOS work on statistical analysis of metal droplets in the emulsion by determining the effect of emulsion height on the droplet size distribution and population density through analysing raw data for sample pots at 4 different levels within the emulsion layer.

Whilst metal size distribution has already been reported by IMPHOS, the present work extends this by considering the population density of these droplets within the surrounding emulsion area for samples collected at a particular emulsion level at different

blow times. A wider bin number (100µm) was also used to account for the presence of larger droplets (>400µm) not considered in the IMPHOS work, hence offering more of a focus on macro scale droplets; indicative of HM droplet sizes (2-4mm) used in the levitation melting experiments detailed in Chapter 3. The present statistical study further aimed at extending the limited interpretation given by IMPHOS on its relation between metal droplet size distribution and the RRS function. This is addressed in the present study with the current set of analysed samples and is further discussed in relation to the blowing number ($N_B$) proposed by Subagyo [4, 9].

## A.2 Method

### A.2.1 Sample Collection Method

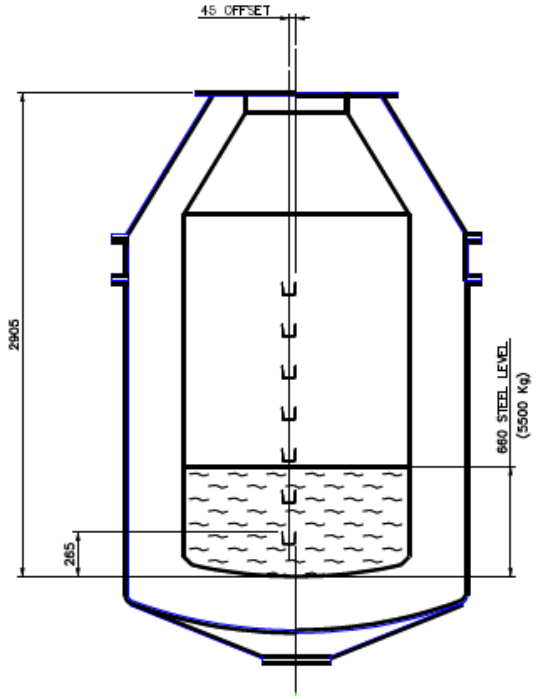


Figure A.1: BOS Converter sampling lance [19]

Steelmaking project IMPHOS (Improving Phosphorus Refining) was designed as a comprehensive examination of the Basic Oxygen Steelmaking (BOS) process, with special emphasis on the behaviour of phosphorus [12]. The approach was as follows: every two minutes through the oxygen blow, up to seven converter samples from the bulk metal bath and the slag/metal emulsion were collected simultaneously. The sample collection method used a custom-designed sampling lance and lance delivery system, Figure A.1. The sampling lance was positioned on a vertical away from the (single) oxygen jet impact zone and contained seven lidded-sampling pots. The high thermal mass of each sampling

pot ensured that the retrieved samples were rapidly cooled. The 1st lidded-sampling pot was located in the bulk metal bath; the 2nd and 3rd were positioned around the quiescent bulk metal/slag interface; and pots 4-7 were sited at selected heights within the slag/metal emulsion. For the automated sampling procedure, a robotic arm selected a new sampling lance from a rotating cassette assembly, lifted it out and then presented it to the converter. The sampling lance was then driven rapidly into position at which time all the sampling pot lids opened simultaneously and remained open for 3 seconds before rapidly closing. The robotic arm then immediately lifted the sampling lance out of the BOS converter and returned it into the rotating cassette assembly for short-term storage. This procedure was repeated 8 times (every 2 minutes) during each converter blow.

### A.2.2 Image Processing Method

The determination of metal droplet parameter was conducted using image analysis software (Zeiss AxioVision 4.6 microscope software). The procedure was done before the commencement of this current investigation, therefore it must be noted that the author of this report is not responsible for developing the raw data used in this statistical study. Nevertheless, the procedure which was adopted for the determination of metal droplet parameter is detailed below and is further documented in its respective literature [3].

- Slag pieces from a representative heat were mounted and polished
- Colour images of the microstructure were captured using an Olympus Vanox T met. Microscope with Fujifilm HC 300Z digital camera using Photoshop/TWAIN
- The captured images were stitched together. Care was taken to retain the image resolution
- The stitched photos were ‘image enhanced’ to counteract any variability in the luminosity of the surrounding resin and areas of buried/ poorly resolved slag (Figure A.2a and A.2b)
- These images were then transferred to another PC for image analysis using Zeiss KS300 software. A macro was developed to threshold the image for Fe particle parameters and total area occupied, and to derive the total area of the lump. The data were stored in a Word document which was later transferred to another PC for the results spreadsheets to be prepared.
- If the quality of threshold was found to be inadequate (particularly for the voids, where the range of greys tended to vary from one part of the lump to another), an iterative process was used to further Photoshop-process the image.

a) Before processing

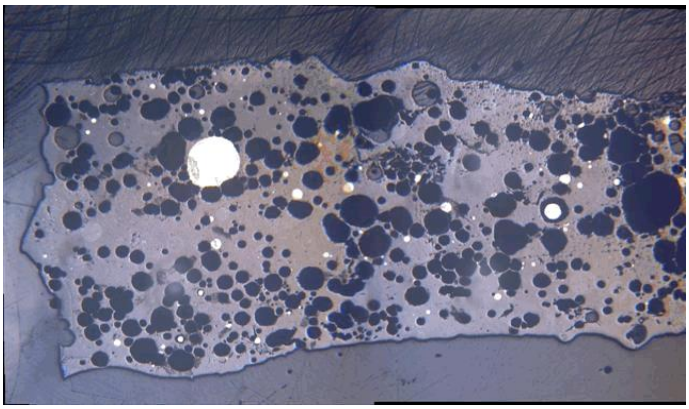

b) After processing

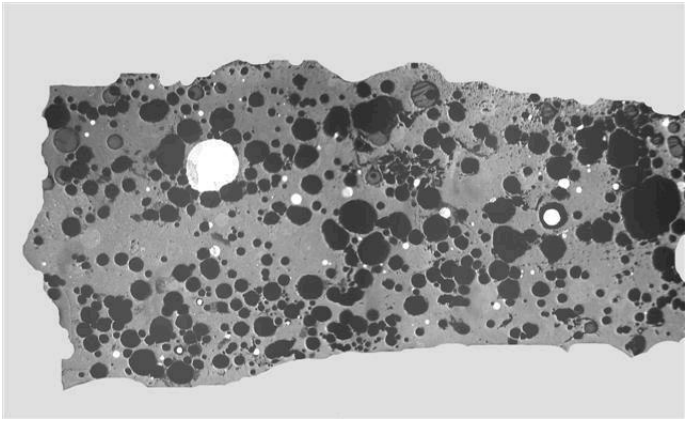

Figure A.2a and A.2b: Fragment of quenched emulsion sample, a) before and b) after image enhancement [19]

*Note that 16µm was the analytical limit of the image processing software, hence the minimum droplet size which could be obtained.*

### A.2.3 Statistical Analysis Method

Sigma Plot 12.0 (Statistical Software Package) was used to carry out a Shapiro-Wilk test for normality on raw data produced from the image analysed samples in order to determine whether the droplet size distribution followed a Normal/Gaussian distribution curve. The null hypothesis for the test stated that the droplet sizes were normally distributed and as such, if the calculated *p*-value was less than the critical value of $p = 0.05$ then the null hypothesis was rejected as the droplet size distribution did not display normal distribution [85]. The method was however biased towards sample size as $p<0.05$ values could easily be obtained for larger sample sizes from small deviations from normality [86].

Key outputs from the computed calculation included the mean droplet size (Equation A.1) within each population (sample group) which basically presents an estimate of average droplet size in the population and standard deviation (Equation A.2); so how closely related are the size of each individual droplet to the calculated mean of the population; with large standard deviation suggesting that the measured sample sizes are distant from the mean value.

$$\bar{X} = \frac{\sum_{i=1}^{n} x_i}{n} \tag{A.1}$$

$$s = \sqrt{\frac{\sum (x_i - \bar{x})^2}{N-1}} \tag{A.2}$$

$$CI_{LB} = \bar{X} - \left( \frac{z_{1-p}}{2} xSE \right) \tag{A.3}$$

$$CI_{UB} = \bar{X} - \left( \frac{z_{1-p}}{2} - SE \right) \tag{A.4}$$

95% ($p = 0.05$) and 99% ($p = 0.01$) confidence interval for each population was also calculated as these represent boundaries within which the true mean value is likely to fall into. The lower and upper boundary confidence intervals were computed using Equation A.3 and A.4. This statistical tool effectively acts as a method for assessing the accuracy

of the calculated sample means because if the confidence interval is small then the true mean is close to the sample mean therefore the sample mean is a true representation of the sample population. However if the confidence interval is wide then the sample mean could be much different to the true mean, in which case, the calculated sample mean is likely to be a bad representation of the sample population. [86]

### A.3 Results & Discussion

Whilst it is apparent from Figure A.3 and A.4 that droplet size distribution for samples collected in heats S1837 and S1840 were non-parametric; Gaussian distribution was not obeyed, to statistically confirm this, Shapiro-Wilk normality test was conducted using Sigma Plot 12.0 statistical software. The S1837 samples analysed in this study were collected at 2 minutes interval between 8 and 16 minutes of blow, therefore each of the 5 sample population underwent separate normality tests. The S1840 samples analysed in this study however were sampled 8 minutes into blowing procedure and at 4 different emulsion heights. Similarly, these 4 sample populations underwent 4 separate normality test. For both these test, the P-value (the estimated probability that the distribution is normal) was set at 0.05. The raw data for both these heats (comprising 9 sample population in total) were imported into 2 Sigma Plot 12.0 software from Microsoft Excel and computed; the results of which are displayed in Table A.1 and Table A.2. The results explicitly shows that the data is non parametric and having failed the normality test, suggests that there is a significant variance between the actual and expected Gaussian type 'bell' distribution result.

Table 29: Heat S1837 Normality test

| Sample Population | Blow Time | Emulsion Level | Population Size | P-value | Result |
|---|---|---|---|---|---|
| S1837_4_4 | 8 | 4 | 442 | $P < 0.05$ | Failed |
| S1837_5_4 | 10 | 4 | 418 | $P < 0.05$ | Failed |
| S1837_6_4 | 12 | 4 | 686 | $P < 0.05$ | Failed |
| S1837_7_4 | 14 | 4 | 1010 | $P < 0.05$ | Failed |
| S1837_8_4 | 16 | 4 | 524 | $P < 0.05$ | Failed |

Table 30: Heat S1840 Normality test

| Sample Population | Blow Time | Emulsion Level | Population Size | P-value | Result |
|---|---|---|---|---|---|
| S1840_4_4 | 8 | 4 | 1822 | $P < 0.05$ | Failed |
| S1840_4_5 | 8 | 5 | 3688 | $P < 0.05$ | Failed |
| S1840_4_6 | 8 | 6 | 1709 | $P < 0.05$ | Failed |
| S1840_4_7 | 8 | 7 | 3027 | $P < 0.05$ | Failed |

## A.3.1 Droplet Size Distribution - BOS Experimental Heat S1837

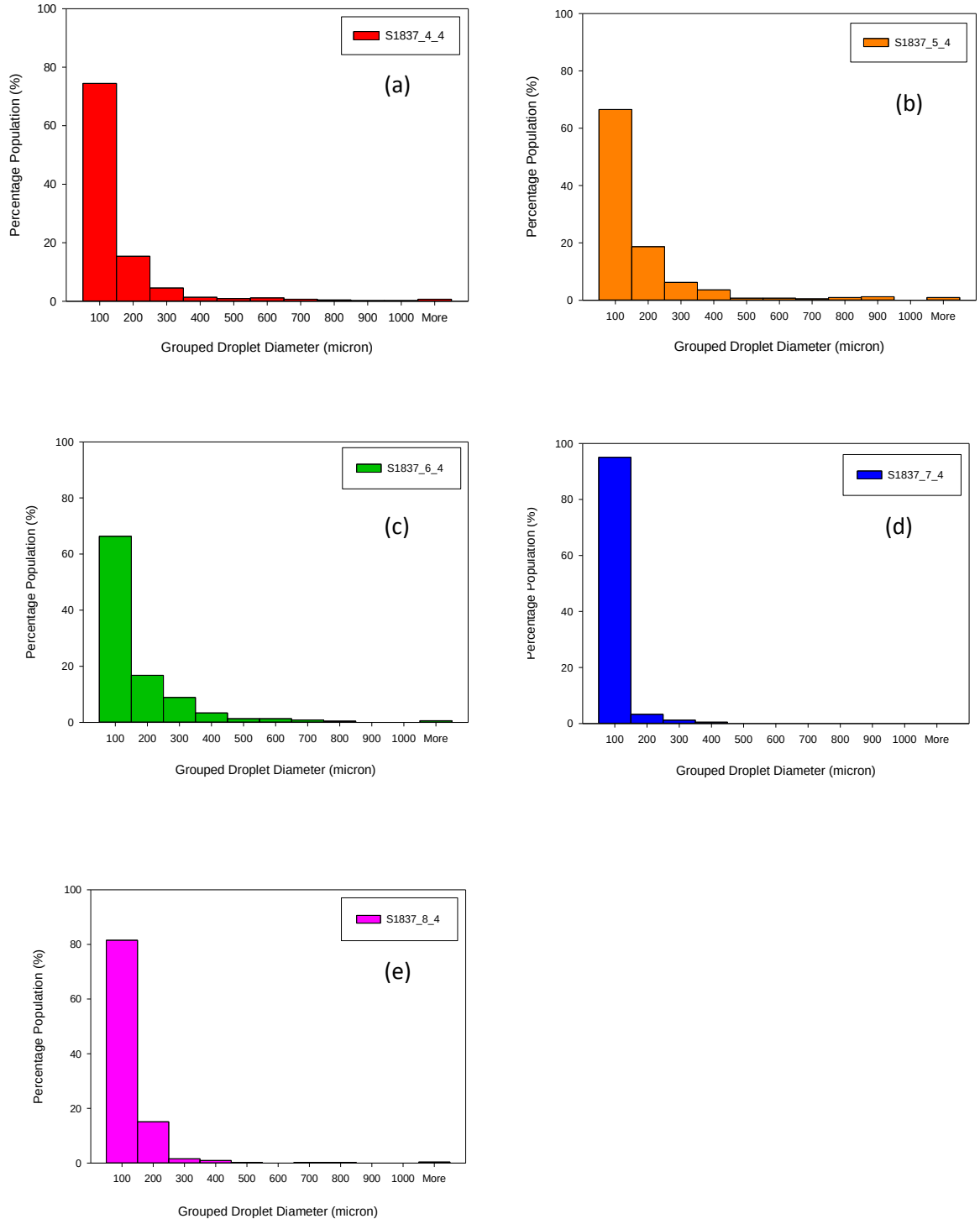


Figure A.3a-e: Heat S1837 droplet size distribution as a function of blow time

Droplet size distribution for experimental BOS heats S1837 was statistically analysed as a function of blow time. For this particular analysis, samples from pot 5 only, were used

because there was more readily available raw data for samples collected at the corresponding emulsion level than other emulsion levels. Figure A.3a-e illustrates the percentage population for droplets with diameters that fall within a particular class. Statistical outputs such as the mean droplet size, standard deviation and confidence intervals were also computed and are presented in Table A.3.

Table 31: S1837 Droplet size distribution

| | **S1837_4_4** | **S1837_5_4** | **S1837_6_4** | **S1837_7_4** | **S1837_8_4** |
|---|---|---|---|---|---|
| **Sample size** | 442 | 418 | 686 | 1010 | 524 |
| **Mean (µm)** | 98 | 139 | 122 | 42 | 75 |
| **Median (µm)** | 47 | 61 | 57 | 31 | 51 |
| **Minimum Diameter (µm)** | 16 | 16 | 21 | 23 | 22 |
| **Maximum Diameter (µm)** | 1597 | 6363 | 3306 | 366 | 1293 |
| **Standard Deviation** | 163 | 376 | 207 | 38 | 99 |
| **Standard Error** | 8 | 18 | 8 | 1 | 4 |
| **95% Conf** | 15 | 36 | 16 | 2 | 8 |
| **99% Conf** | 20 | 48 | 20 | 3 | 11 |

The sample size of the 5 sample population (pots) is different as the emulsion fragments that made up the 5 sample populations had varying amounts of metal droplets within it. Clearly the most number of droplets was counted for the sample collected at 14 minutes of blow (sample S1837_7_4) and this sample population also recorded the smallest mean diameter droplet 42µm. The wide range of droplet size measured within each of the 5 population group and the significant differences between these droplet sizes and the mean droplet diameter is reflected by the large standard deviation recorded for each population group. Samples collected at 10 and 12 minutes of blowing measured the largest standard deviation which may be expected given that these two population groups also recorded droplets with the maximum diameters of 6363µm and 3306µm respectively. Given the relatively small confidence interval calculated for 95% confidence level for both sample S1837_7_4 (+/- 2µm) and S1837_8_4 (+/- 8µm), this suggest that the calculated mean of 42µm and 75µm is close to the true mean and therefore the calculated mean is a true representation of the sample population. Similar level of confidence is also calculated for the 99% confidence level.

The highest number of droplets per unit area (Table A.4) was recorded at 8 minutes into the blowing procedure suggesting that this was the time at which high percentage of droplets resided within the emulsion hence increased interfacial reaction area. Lance height was maintained at 160cm above the bath level from 5 to 17 minutes into the blow suggesting that difference in droplet population between the sample groups were not influenced by the lance height which further suggests that changes in the physical properties of metal, slag and emulsion were responsible for the number of droplets generated as argued by Subagyo [4, 9]

Table 32: S1837 Droplets per unit area

| | **S1837_4_4** | **S1837_5_4** | **S1837_6_4** | **S1837_7_4** | **S1837_8_4** |
|---|---|---|---|---|---|
| **No. of Droplets Sampled** | 442 | 418 | 686 | 1010 | 524 |
| **Sampled Area (μm$^2$)** | 113 | 463 | 279 | 453 | 534 |
| **No. of Droplet per Unit Area** (rounded to the nearest 1) | 4 | 1 | 2 | 2 | 1 |

### A.3.2 Droplet Size Distribution - BOS Experimental Heat S1840

Samples of experimental BOS heat S1840 were collected at emulsion levels (pots) 4, 5, 6 and 7, each at 8 minutes of blow.

Of the 4 samples population group, 3 has relatively similar mean droplet diameters of 28, 30 and 31 for samples collected at levels 5, 6 and 7 within the emulsion layer and the same population groups had the least measured standard deviation. Sample S1840_4_7 had the lowest standard deviation of +/- 26μm of the 4 sampled population groups and also recorded the smallest confidence interval for 95% and 99% confidence level both of which were +/-1μm. The calculated confidence interval of +/-1μm infers that the true mean value will fall within the confidence interval with 99% confidence. Maximum measured droplet diameter decreased with increased emulsion level as sample S1840_4_7 (corresponding to the highest sampled emulsion level) recorded the lowest maximum

droplet diameter of 337µm compared to the three preceding lower emulsion levels which registered maximum droplet diameters of 579µm, 1030µm and 1744µm respectively.

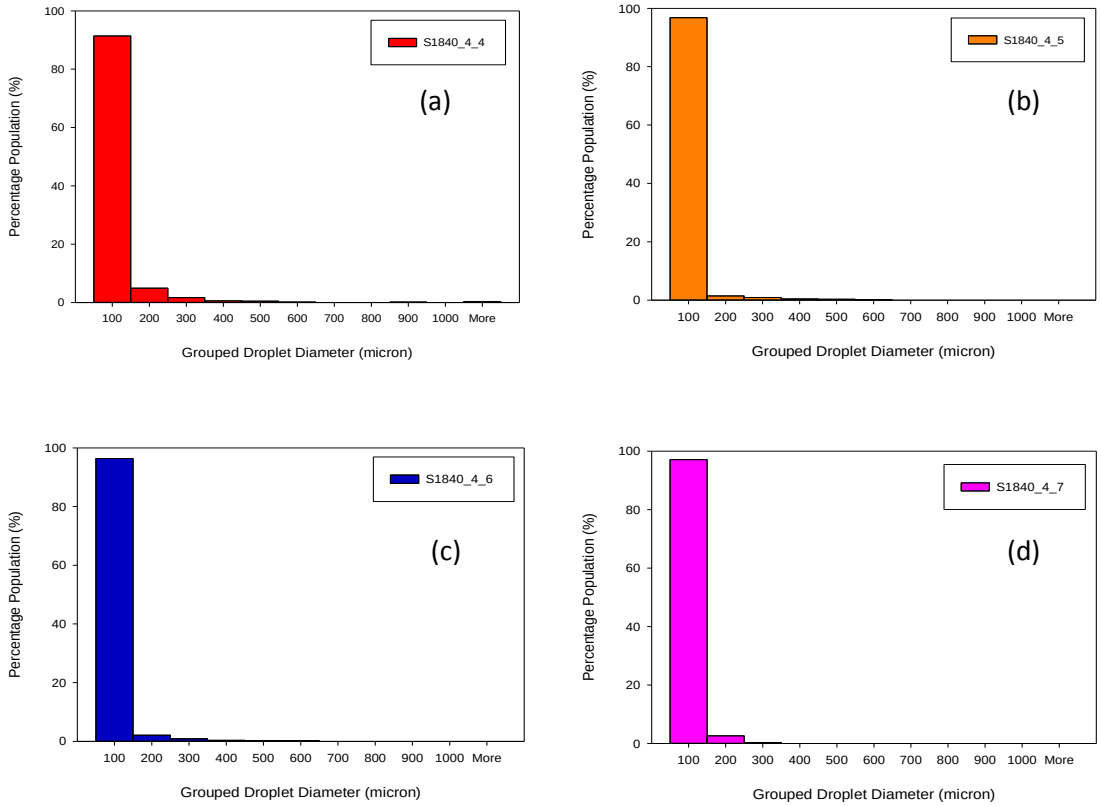


Figure A.4a-d: Heat S1840 droplet size distribution as a function of emulsion height

Table 33: S1840 Droplet size distribution

| | S1840_4_4 | S1840_4_5 | S1840_4_6 | S1840_4_7 |
|---|---|---|---|---|
| **Sample size** | 1822 | 3688 | 1709 | 3027 |
| **Minimum Diameter (µ)** | 162 | 16 | 16 | 16 |
| **Maximum Diameter (µ)** | 1744 | 1030 | 579 | 337 |
| **Mean (µ)** | 50 | 28 | 30 | 31 |
| **Median (µ)** | 22 | 19 | 19 | 23 |
| **Standard Deviation** | 107 | 49 | 43 | 26 |
| **Standard Error** | 3 | 1 | 1 | 0.48 |
| **95% Conf** | 5 | 2 | 2 | 1 |
| **99% Conf** | 7 | 2 | 3 | 1 |

As shown in Table A.6, the most number of droplets per unit area of sampled emulsion for S1840 heat at 8 minutes blow time was measured for the sample which was collected at level 5 within the emulsion layer – 8 droplets per unit area. Equally so, less droplets per unit area was recorded for samples collected at lower and high emulsion levels. Assuming that all droplets generated in the jet impact zone made up the entire metal volume in the emulsion, and further assuming that the number of droplets within the sampled emulsion area offered a good representation of droplet distribution within the emulsion, then it can be stated that a larger population of generated droplets resided between level 5 and 6 compared to any other region of the emulsion and the average size of these droplets was between 28µm and 30µm.

Table 34: S1840 Droplets per unit area

| | **S1840_4_4** | **S1840_4_5** | **S1840_4_6** | **S1840_4_7** |
|---|---|---|---|---|
| **No. of Droplets Sampled** | 1822 | 3688 | 1709 | 3027 |
| **Sampled Area (µm$^2$)** | 444 | 490 | 317 | 562 |
| **No. of Droplet per Unit Area** (rounded to the nearest 1) | 4 | 8 | 5 | 5 |

## A.4. Analysis of Result & Discussion

### A.4.1 Droplet Size Distribution

BOS emulsion has been sampled within 2 heats (S1837 and S1840) to determine the effect of blow time and emulsion level on metal droplet size distribution and population density of these droplets within the emulsion volume. Whilst the mean droplet size calculated for heat S1837 at level 4 and at 8 minutes blow time was bigger than that samples for heat S1840 at level 4 and 8 minutes blow time, the number of droplet per unit area within their respective emulsion was similar (4 droplets per unit area) suggesting that similar level of droplet generation within the jet impact zone occurred.

The findings of this study validates the calculated droplet size distribution for these two specific heats within the IMPHOS study [14], whilst also correlating well with that of other researchers as shown in Table 4. The droplet size range from converter studies by Meyer [12] and Cicutti [13] agree well with each other, but a significantly wider size range (at a point in time) was found within the present converter study. The measured metal droplet

size range from this study may be restricted to a minimum droplet size value of 16μm due to the analytical limit of the image analysis process.

Contrary to the results of this study whereby the majority of sampled emulsion metal droplet population had diameters less than 100μm or more specifically <40μm according to the histograms of size distribution presented by IMPHOS [14], the minimum droplet size measured from other converter studies [12, 13, 17] were higher, and ranged from 150μm-500μm. Although Koria and Lange [20] dismissed the significance of sampling procedure on droplet size distribution, this may be considered as one of the underlying factors contributing to such discrepancies between the highlighted converter studies. In comparison to the above discussed converter studies, it is arguable that the applied sampling technique in the present investigation provided a better representation of BOS emulsion metal droplet size distribution. Factors such as the immediate proximity of the sampling lance to the jet impact zone, coupled with the discovery of finer droplet sizes (not documented by previous converter studies [12, 13, 17]) further supports this argument.

Converter sampling methods such as 'tilting' [18] may interrupt the dynamic state of the BOS steelmaking process, whilst collection of 'splashed/ejected' droplets [12] from the converter tap hole may also lead to non-representative droplet size distributions, as the droplets sampled via this method were likely to be characteristic of a particular period of blow associated with when emulsion height was highest within the converter; an event usually linked with the highest rate of slag/metal emulsion decarburisation. Other factors such as droplet swelling, iron oxidation, droplet coalescence and disintegration may have also determined the final droplet sizes and hence the droplet size distribution.

Microstructures of the slag/metal emulsion for similar experimental BOS heats to that of this study were reported in work done by Zinngrebe [24] and Millman [14, 84]. Metal droplets and spherical voids were seen in image processed emulsion fragments such as those displayed in Figure A.2a and A.2b. In some cases, the metal droplets were smaller than the void it occupied, indicating that the droplet may have contracted from an initial larger diameter size presumably equal to the diameter of the void, constituted by a period of droplet swelling and contraction during a respective decarburisation procedure; a phenomenon experienced by metal droplets in a gaseous environment as documented by several researchers [55, 56, 63-66]. Also, ‘larger’ metal droplets were surrounded by pockets of voids, indicating that gases (i.e. CO) may have evolved from the metal surface. In

relation to the present statistical study, sampling of the BOS converter at a particular time could have correspond to a particular stage of droplet swelling or contraction, therefore the image processed emulsion fragments only gave an instantaneous profile of droplet size distribution.

Considering the dynamic nature of the BOS converter and high metal circulation rate (up to 5-10% of overall metal weight per second [84]) between the bulk metal and slag/metal emulsion, it is conceivable to hypothesise that a significant proportion of the initially generated droplets from the oxygen jet impact zone coalesced or disintegrated having collided during temporary suspension in the slag/metal emulsion, which may have led to the changes in the final droplet size compared to its initial size. Support for this argument is given by the finding of macro-scale metal droplets within the sampled emulsion fragments, with droplet diameters of up to 6000μm being registered and the detection of droplets of diameters less than 16μm unable to be detected due to the 16μm analytical limit of the image processor.

The size of the majority sampled metal droplets was below 100μm regardless of sampling time and emulsion position. However, with a wide range of droplet sizes sampled (16μm-6363μm), this lays further support to the argument of droplet coalescing and disintegrating but without real-time visual analytical tool, differentiating between these droplet generation methods may prove difficult. Nevertheless, having determined the metal droplet size distribution of a different IMPHOS heat (S1841) to that of this study by means of a Population Density Function (PDF), Zinngrebe [24] proposed the droplet size distribution were likely related to actual process dynamics at the time and location of sampling, although factors such as quench gradient (between the slag/metal emulsion and the sample collection vessel) needed to be taken into account.

### A.4.2 Droplet Size Distribution in Relation to Rosin-Rammler-Sperling Function

Figure A.5a and A.5b are plots of cumulative weight (R) percent of droplets above a certain droplet size, against the upper limit of droplet class diameter (d) for slag/metal emulsion samples of experimental BOS heats S1837 and S1840 respectively.

(a)

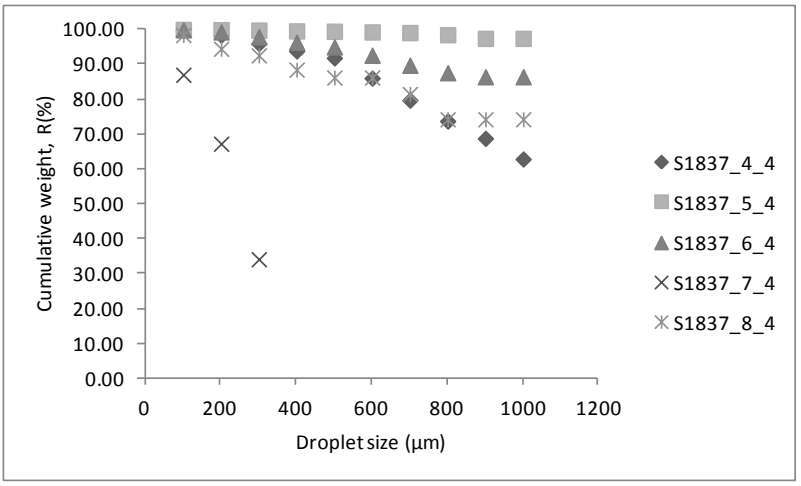


(b)

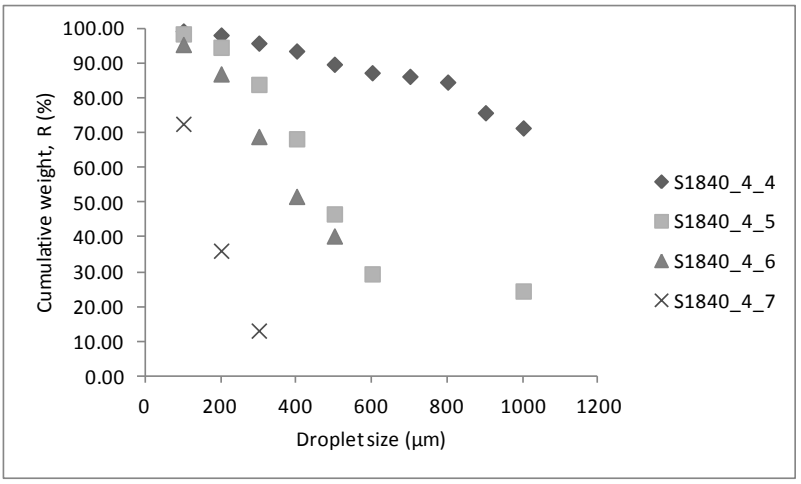


Figure A.5: RRS droplet size distribution for heat a) S1837 and b) S1840

It is clearly shown in Figures A.5a and A.5b that the droplet size distribution when sampled as a function of blow time (heat S1837) or emulsion level (heat S1840) obeyed the RRS distribution function. This agrees well with results from other studies [13, 20].

(a)

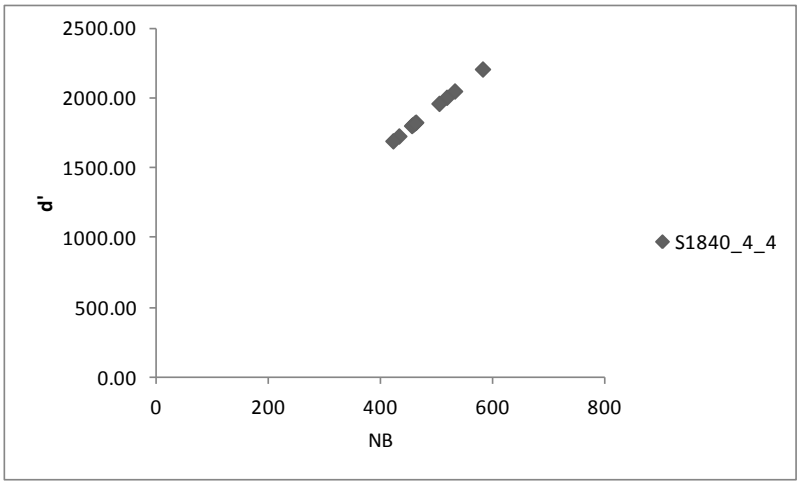


(b)

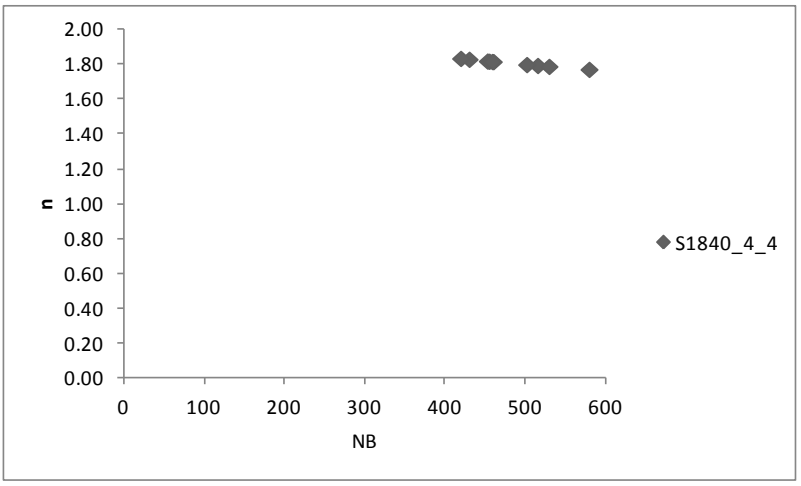


Figure A.6: Effect of blowing number on RSS distribution parameters *d'* (a) *and n* (b) for heat S1840_4_4

*n* = Distribution parameter- measure of spread of particle sizes (dimensionless)

*d'* = Size parameter – mean particle size corresponding to R = 36.8% (mm)

Parameter *n* and *d'* were calculated using the least squared method, and as in the study by Subagyo[9], plotted against the blowing number to determine its effects on the RRS distribution (Figure A.6a and A.6b). The results suggest that the size parameter *d'* is highly dependent on blowing number as NB increased as the value of this parameter increased with increasing blow number whilst there appeared to be little or no dependency in blowing number by the distribution parameter *n*. These findings are in good agreement with Subagyo [9] and Koria and Lange [57] who observed the same relationship between their blowing number and RSS distribution parameters *d'* and *n*. For the present study, *n* values of 1.74 (+/-0.54) were obtained which is in good agreement with Subagyo [9] (*n* = 1.26 +/-0.43) and Koria and Lange [57] (*n* = 1.26), where

(a)

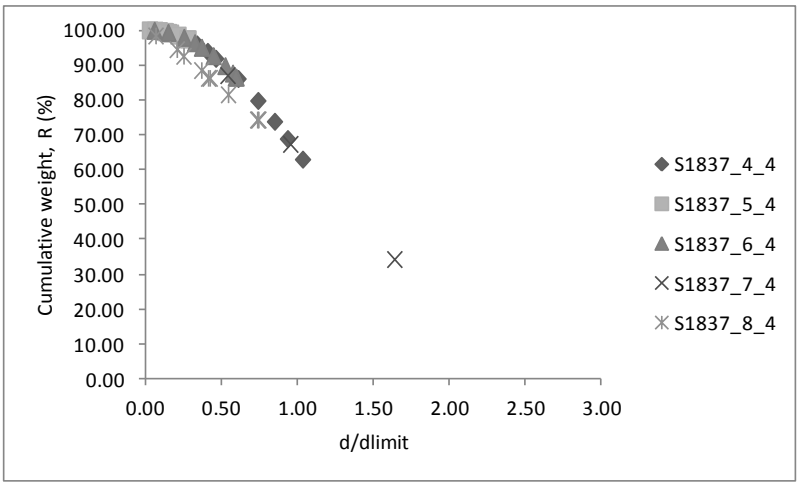


(b)

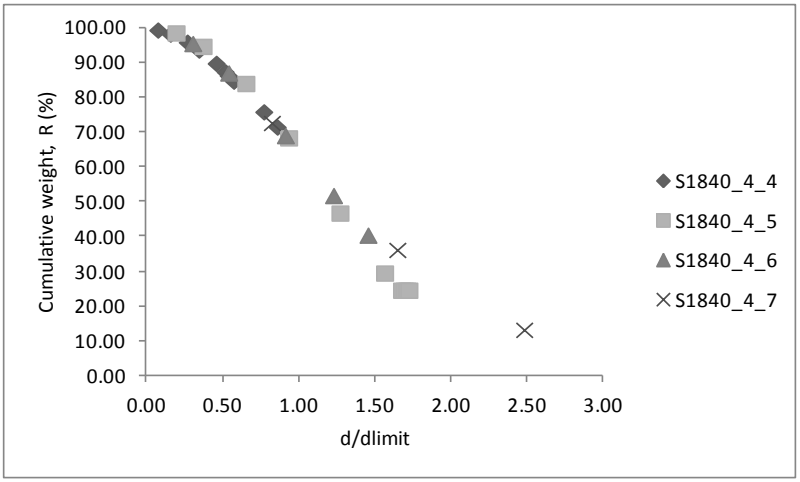


Figure A.7: Cumulative weight percent against the ratio of class diameter to limiting droplet diameter, for heat a) S1837 and b) S1840

Figure A.7a and A.7b shows the dimensionless representation of the cumulative weight percent (R) against the ratio of class diameter to limiting diameter ($d/d_{limit}$) for sample S1837 and S1840 respectively. The absolute droplet size sampled (d), were eliminated and represented by $d_{limit}$; defined as the smallest absolute droplet size achievable during blow corresponding to R = 0.1% (Equation A.5). It followed that despite changing d', the characteristics of the droplet size distribution remained the same, as long as the distribution exponent (n) was identical [64], and RRS distribution function was obeyed.

$$d_{limit} = d'\left(\frac{3}{\log e}\right)^{1/n} \qquad \text{(A.5)}$$

Where, e = 100/R and R = 0.1%

### A.5. Further Considerations

Through IMPHOS study conducted by Millman et al [3] metal droplets within the emulsion have been proven to drive fast initial refining reactions such as dephosphorisation and decarburisation as metal droplets offered a larger reaction surface area than the bulk bath metal hence increased reaction area. The present statistical study on the droplet size distribution of two (S1837 and S1840) of the 25 heats shows a wide range of metal droplets exist within the emulsion yet this is in agreement with other plant based studies [12, 13, 15]. The droplet size distribution follows the RRS distribution function and was in agreement with Cicutti [13] (Figure A.8) and Koria & Lange [20, 21].

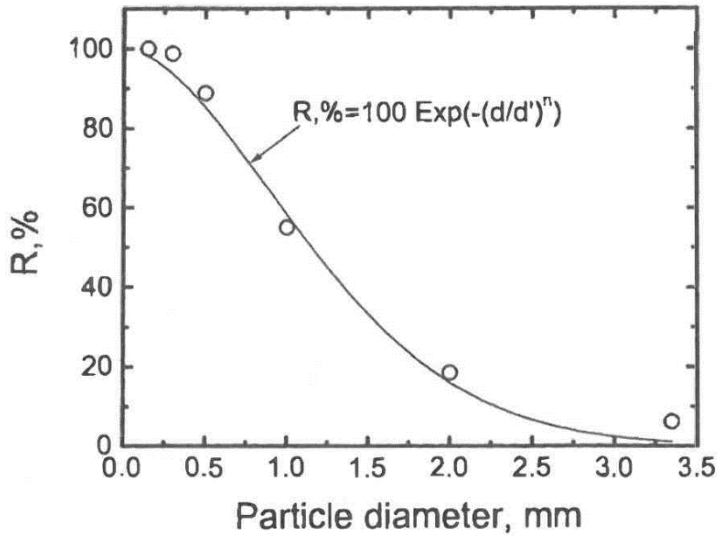


Figure A.8: RRS metal droplet distribution [6]

The majority of droplets sampled within the emulsion had diameters less than 100µm and considering that large generated droplets ejected into the emulsion are initially heavier than smaller droplets it follows that the larger droplets would have a shorter residency time within the emulsion compared to the smaller/lighter metal droplets. Also, considering that smaller droplets comprise large interfacial area, these are more likely to 'swell' and reduce in density quicker than larger droplets due to increased oxygen diffusion and CO bubble nucleation within the metal, hence smaller droplets suspend in the emulsion for longer periods of time. Although the majority of metal droplets sampled by Koria and Lange [20] were without cavities, the same cannot be said for the droplets within this present investigation, due to the more dynamic nature and scale of the BOS converter compared to their laboratory scale studies.

For these reasons, it follows that smaller droplets within the emulsion are more likely to be captured than larger droplets as proposed by Subagyo [4] and measured in the present study. Whilst Ji [87] further proposed that if droplets of similar diameter had identical residency time then the residence time can simplified, Brooks [88] argues otherwise as droplets of similar diameter may vary in density due to the amount of gas (CO) within the metal, and therefore vary in their residence time. The latter argument by Brooks is believed to be true for droplet behaviour within the BOS converter emulsion such as that of the IMPHOS study.

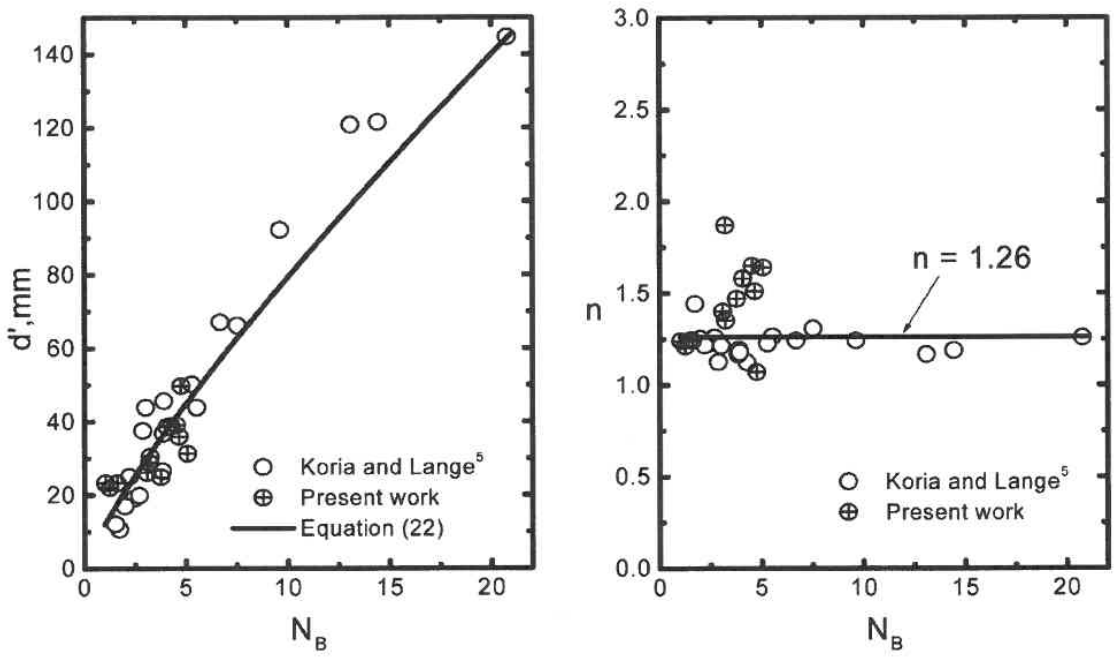


Figure A.9: Effect of blowing number of RRS distribution parameters *d'* and *n* [9]

A relationship between droplet generation and droplet size distribution has also been found in the present study using the blowing number proposed by Subagyo [9] and further measured by Koria & Lange [20, 21]. Whilst the blowing number of this study is significantly higher than that proposed by Subagyo, similar conclusions can still be made with respect to droplet generation and size distribution; as blowing number increased, the size parameter (*d'*) increases also. As reported by Standish and He [6], this is caused by transition of droplet generation mechanism from 'dropping' to 'swarming' expressed through the nominal Weber number.

## A.6. Summary

Metal droplets in slag/metal emulsion contribute significantly to refining reactions in a BOS converter because they provide a large surface area of reaction. By collecting samples within a 6 tonne converter using a specially designed sampling system [14], this study has measured droplet size distribution at different time of blow and at different emulsion heights whilst population density of droplets within the emulsion has also been determined. The highest amount of droplet per unit area was sampled at level 5 within the emulsion with an overall mean droplet size of 28µm (+/- 2µm 99% confidence level) indicating that the majority of droplets were ejected at a peak height between sampling pots 5 and 6.

The majority of sampled metal droplets had diameters less than 100µm correlating with initial IMPHOS findings and a droplet size range of 16µm to over 6000µm measured correlates well with other plant studies listed in Table 4. In agreement with Subagyo [9], Koria & Lange [20, 21] and Millman [14] the droplet size distribution follows the Rosin-Rammler-Sperling (RSS) distribution function which has further been related with the blowing number proposed by Subagyo to show that a relationship exist between the size distribution parameter (*d'*) and blowing number.